

# LOAN DOCUMENT

PHOTOGRAPH THIS SHEET

DTIC ACCESSION NUMBER

LEVEL

INVENTORY

AFRL-ML-TY-TR-2001-0051

DOCUMENT IDENTIFICATION

9 NOV 2001

**DISTRIBUTION STATEMENT A**  
Approved for Public Release  
Distribution Unlimited

DISTRIBUTION STATEMENT

ACCESSION FOR	
NTIS	GRAM
DTIC	TRAC
UNANNOUNCED	
JUSTIFICATION	
BY	
DISTRIBUTION/	
AVAILABILITY CODES	
DISTRIBUTION	AVAILABILITY AND/OR SPECIAL
A-1	

DISTRIBUTION STAMP

DATE ACCESSIONED

DATE RETURNED

20020626 107

DATE RECEIVED IN DTIC

REGISTERED OR CERTIFIED NUMBER

PHOTOGRAPH THIS SHEET AND RETURN TO DTIC-FDAC

H  
A  
N  
D  
L  
E  
  
W  
I  
T  
H  
  
C  
A  
R  
E

**AFRL-ML-TY-TR-2001-0051**



# **Laser Ionization Detection (LID) and Photoemissive (PE) Ion Mobility Spectrometry (IMS) Development**

**Orven F. Swenson**

**North Dakota State University  
1301 12th Avenue, N.  
Fargo, ND 58105-3400**

**Approved for Public Release; Distribution Unlimited**

**AIR FORCE RESEARCH LABORATORY  
MATERIALS & MANUFACTURING DIRECTORATE  
AIR EXPEDITIONARY FORCES TECHNOLOGIES DIVISION  
139 BARNES DRIVE, STE 2  
TYNDALL AFB FL 32403-5323**

*AQ402-09-1985*

## NOTICES

USING GOVERNMENT DRAWINGS, SPECIFICATIONS, OR OTHER DATA INCLUDED IN THIS DOCUMENT FOR ANY PURPOSE OTHER THAN GOVERNMENT PROCUREMENT DOES NOT IN ANY WAY OBLIGATE THE US GOVERNMENT. THE FACT THAT THE GOVERNMENT FORMULATED OR SUPPLIED THE DRAWINGS, SPECIFICATIONS, OR OTHER DATA DOES NOT LICENSE THE HOLDER OR ANY OTHER PERSON OR CORPORATION; OR CONVEY ANY RIGHTS OR PERMISSION TO MANUFACTURE, USE, OR SELL ANY PATENTED INVENTION THAT MAY RELATE TO THEM.

THIS REPORT IS RELEASABLE TO THE NATIONAL TECHNICAL INFORMATION SERVICE  
5285 PORT ROYAL RD.

SPRINGFIELD VA 22 161

TELEPHONE 703 487 4650; 703 4874639 (TDD for the hearing-impaired)

E-MAIL [orders@ntis.fedworld.gov](mailto:orders@ntis.fedworld.gov)

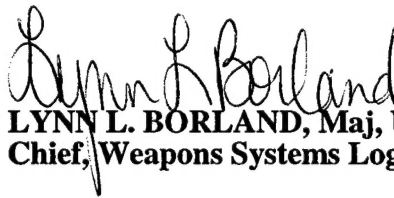
WWW <http://www.ntis.gov/index.html>

AT NTIS, IT WILL BE AVAILABLE TO THE GENERAL PUBLIC, INCLUDING FOREIGN NATIONS.

THIS TECHNICAL REPORT HAS BEEN REVIEWED AND IS APPROVED FOR PUBLICATION.



**MICHAEL J. CALIDONNA, Capt, USAF**  
Program Manager



**LYNN L. BORLAND, Maj, USAF, BSC**  
Chief, Weapons Systems Logistics Branch



**DONALD R. HUCKLE, JR., Colonel, USAF**  
Chief, Air Expeditionary Forces Technologies Division

Do not return copies of this report unless contractual obligations or notice on a specific document requires its return.

REPORT DOCUMENTATION PAGE			Form Approved OMB No. 0704-0188	
Public reporting burden for this collection of information is estimated to average 1 hour per response, including the time for reviewing instructions, searching existing data sources, gathering and maintaining the data needed, and completing and reviewing the collection of information. Send comments regarding this burden estimate or any other aspect of this collection of information, including suggestions for reducing this burden, to Washington Headquarters Services, Directorate for Information Operations and Reports, 1215 Jefferson Davis Highway, Suite 1204, Arlington, VA 22202-4302, and to the Office of Management and Budget, Paperwork Reduction Project (0704-0188), Washington, DC 20503.				
1. AGENCY USE ONLY (Leave blank)		2. REPORT DATE 9 November 2001		3. REPORT TYPE AND DATES COVERED Final Report, 13 Feb 1998 - 15 Aug 2001
4. TITLE AND SUBTITLE Laser Ionization Detection (LID) and Photoemissive (PE) Ion Mobility Spectrometry (IMS) Development			5. FUNDING NUMBERS C - F08637-98-C-6003 PE - 62202F JON - 1900E28A	
6. AUTHOR(S) Orven F. Swenson				
7. PERFORMING ORGANIZATION NAME(S) AND ADDRESS(ES) North Dakota State University 1301 12th Avenue, N. Fargo, ND 58105-3400			8. PERFORMING ORGANIZATION REPORT NUMBER	
9. SPONSORING/MONITORING AGENCY NAME(S) AND ADDRESS(ES) Air Force Research Laboratory Air Expeditionary Forces Technologies Division (AFRL/MLQ) 139 Barnes Drive, Suite 2 Tyndall AFB FL 32403-5323			10. SPONSORING/MONITORING AGENCY REPORT NUMBER  AFRL-ML-TY-TR-2001-0051	
11. SUPPLEMENTARY NOTES Contracting Officer's Technical Representative: Mr. Bruce J. Nielsen				
12a. DISTRIBUTION AVAILABILITY STATEMENT Approved for public release; distribution unlimited			12b. DISTRIBUTION CODE  A	
13. ABSTRACT (Maximum 200 words) Significant advances are reported in the detection of trace analytes in ambient air by laser ionization detection and photoemissive ion mobility spectrometry. A numerical model was developed that describes the behavior of laser-produced ions in an applied electric field and the subsequent induced current flow in an external detection circuit between the biased electrodes. The modeling and extensive measurements on parallel-plate and cylindrical electrodes resulted in a novel hemishperical cell geometry in which the cathode is a wire on a ceramic base (actually the wire will be positioned in a small depression in the base) and the anode is a half-cylinder of metal wire. This design minimizes noise generated by scattered ultraviolet light, allows a very small detection volume, is readily flash heated to eliminate memory effects, provides a peak in the induced current that makes it easier to extract temporal data, and is easily manufactured. Very narrow features were demonstrated in a laser ionization spectral study for molecules as large as indene even at room temperature under ambient pressure conditions. The narrowness of these features means that on-and-off-resonance measurements to separate out background LID signals are very feasible. A combined LI-IMS was demonstrated as an effective approach for speciation in ambient pressure air. An alternative ionization approach of photoemissive electron capture combined with IMS was demonstrated as a promising technique for detecting electronegative species such as explosives molecules.				
14. SUBJECT TERMS Laser ionization detection; Ion mobility spectrometry; Photoemissive; Indene			15. NUMBER OF PAGES 45	
			16. PRICE CODE	
17. SECURITY CLASSIFICATION OF REPORT  UNCLASS	18. SECURITY CLASSIFICATION OF THIS PAGE  UNCLASS	19. SECURITY CLASSIFICATION OF ABSTRACT  UNCLASS	20. LIMITATION OF ABSTRACT  UL	



## **PREFACE**

This report was prepared by North Dakota State University, 1301 12<sup>th</sup> Avenue, Fargo, ND 58105, AFRL Contract F08637-98-C-6003, for the Air Force Research Laboratory, Air Expeditionary Forces Technologies Division (AFRL/MLQ), 139 Barnes Drive, Suite 2, Tyndall Air Force Base, Florida 32403-5323.

This final report describes research conducted on laser ionization detection and photoemissive ion mobility spectrometry of trace molecules in ambient pressure air. The research was conducted in the Physics Department at North Dakota State University. The following graduate and undergraduate students were involved in various aspects of the research: Christopher Walls, Maxwell Lucci, Feng Hong, Joseph Carriere, Matthew Hillman, Christopher Raabe, Al Meidinger, Ben Meier, and Paul Seifert.

The author wishes to acknowledge scientific advice and assistance by Dr. Greg Gillispie on many aspects of the research and technical assistance from Harlan Isensee.

The work was performed between February 1998 and August 2001. The AFRL/MLQ project manager was Mr. Bruce J. Nielsen.



## **EXECUTIVE SUMMARY**

### **A. OBJECTIVE**

The purpose of this research effort was to develop and demonstrate capabilities for trace detection of analyte molecules in ambient pressure air. The principle goals were fourfold:

- Laser ionization detection (LID) temporal waveform study.
- Expanding the number of molecules in the LID spectral database.
- Combined laser ionization-ion mobility spectrometry (LI-IMS) for deconvolution of mixtures.
- Photoemissive ion mobility spectrometry (PE-IMS) development.

### **B. BACKGROUND**

Laser ionization and electron capture have been demonstrated to be effective methods of selectively ionizing neutral molecules. Once ionized, these ions can be very efficiently detected electronically. A common drawback for most analytical techniques is that they cannot be performed in ambient pressure air and require delicate instrumentation that makes field detection cumbersome. Our laser ionization detection and photoemissive ion mobility spectrometry approaches provide selective, sensitive detection of trace hazardous analytes under ambient field conditions.

### **C. SCOPE**

This report presents results of four independent but linked studies on the detection of trace analytes in ambient air via ionization and subsequent electronic detection. The first study included extensive measurements of the sub-nanoamp currents induced in an external detection circuit by drifting ions with parallel plate, cylindrical and half-cylindrical electrode configurations. The drifting ion distributions and consequent induced currents were numerically modeled for the parallel-plate and cylindrical configurations.

The second study was to extend the spectral data base of gas phase species that could be detected by ambient air LID. The focus was on a high resolution study of trace levels of indene in ambient air.

The third study combined LI with a simple ion mobility drift tube. Results were limited due to problems with the tunable second harmonic dye laser and the limitations of the drift tube.

The fourth study on photoemissive ion mobility spectrometry included generation of free electrons by ultraviolet illumination of a thin gold film on a fused silica window and detection of  $\text{Cl}^-$  anions created by the dissociative electron attachment by chlorinated molecules. This effort was in conjunction with a complementary Strategic Environmental Research and Development Program (SERDP) subcontract SC-98C6009 to Dakota Technologies, Inc.

### **D. METHODOLOGY**

The measurements were all made in the laboratory using trace mixtures generated by injecting head space of the analytes into a volume of ambient pressure air or carrier gas.

### **E. RESULTS**

Within experimental error, the parallel plate and cylindrical configurations provide equivalent detectivity. The cylindrical approach has the advantage of providing an induced current peak for the ion

of interest while the oppositely charged ion waveform can be shaped as a nearly flat baseline. The photoelectric effect can be significantly reduced in the cylindrical or semi-cylindrical case by passing the ionizing laser beam next to the negatively charged outer cylinder. The surface area of the positive electrode, that emits photoelectrons due to absorbed scattered light, is minimized by reducing the diameter of the collecting wire. These results led to the development of a novel hemispherical cell geometry that was thoroughly characterized.

Laser ionization spectral results were obtained for indole and indene with the emphasis on indene. The 1+1 and 2+2 resonance enhanced multiphoton ionization (REMPI) spectra of gas phase indene near the origin of the first electronic transition at 287.9 nm are reported in ambient air. The spectra were acquired to help assess options for on- and off-resonance REMPI, similar in concept to differential absorbance LIDAR (DIAL) and differential optical absorbance spectroscopy (DOAS). The 1+1 REMPI spectrum for indene at 50 ppbv concentration in air compares well with published high resolution absorbance spectra obtained for much longer pathlength and higher sample concentration. Extensive sequence band structure is observed near the origin. The rotational contours of the origin and sequence bands consist of a narrow, nearly symmetric feature accompanied by a lower intensity broad sideband shading to the red.

Analytical calibration curves to determine a limit of detection (LOD) were not attempted for indene, but the LOD is obviously very low, probably in the very low parts-per-trillion. The 1+1 REMPI spectra shown were acquired for an indene concentration of 50 ppbv in air. After the laser power was reduced to the point that the REMPI signal was more than 1000 times smaller, the signal-to-noise ratio is still at least 25:1. Presumably, a 1000-fold reduction in concentration to 50 ppt while maintaining full laser power would have the same effect on the signal amplitude and signal-to-noise as the laser power reduction. An accurate measurement of the LOD requires careful procedures to reliably prepare such low concentration samples. Moreover, our interest lies more in the LOD for a real-world sample, that could have other LID-active species in the same wavelength region. Indene was detected in the headspace over the multicomponent mixtures of coal tar and creosote.

Two-dimensional laser ionization data were obtained for a number of aromatic molecules demonstrating the efficacy of laser ionization-ion mobility spectrometry. Analytes can be clearly distinguished by contour plots of the laser ionization wavelength versus the ion drift times. The study was limited because the drift tube did not have a counter-flowing carrier gas or the ability to heat it during data acquisition.

Photoemissively generated free electrons were effectively generated and used to detect the trace chlorocarbons TCE and PCE in nitrogen. Because we used a static cell, problems arose that hindered the resolution of chloride ions from oxygen anions when the detection was attempted in air. Instead of using separate, flowing drift and carrier gases that would prevent dispersion of analyte into the drift region, we introduced analyte and permitted it to diffuse throughout the cell. As a result, the ion-molecule reaction chemistry that generates chloride ions in the presence of oxygen occurs throughout the drift region and our ion mobility spectra contain front-end shoulders. This coupled with the fact that oxygen anion and chloride anion drift times are not significantly different prevented their resolution in the short, 2 cm drift distance used.

## F. CONCLUSIONS

A numerical model was developed that describes the behavior of laser-produced ions in an applied electric field and the subsequent induced current flow in an external circuit between the biased electrodes. The modeling and extensive measurements on parallel-plate and cylindrical electrodes resulted in a novel hemispherical cell geometry in which the cathode is a wire on a ceramic base (the wire may be

positioned in a small depression in the base or a narrow conducting film used) and the anode is a half-cylinder of conducting material. This design minimizes noise generated by scattered ultraviolet light, allows a very small detection volume, is readily flash heated to eliminate memory effects, provides a peak in the induced current that makes it easier to extract temporal data, and is easily manufactured.

The spectral study was part of a long-term project to examine the suitability of LID for real-time analysis of aromatic hydrocarbons in air. We demonstrated that very narrow features can be seen for molecules as large as indene even at room temperature under ambient pressure conditions. The narrowness of these features means that on-and off-resonance measurements to separate out background REMPI signals are very feasible. Detection of indene in the headspace of coal tar was also demonstrated. Data have also been acquired for indole and for phenanthrene at its room temperature vapor pressure (ca. 200 ppbv). While these have broader features than indene, combined with IMS the wavelength features can positively identify these molecules as well.

The combined LI-IMS was demonstrated as an effective approach for speciation in ambient pressure air. The drift tube needs to have a counterflowing carrier gas, either nitrogen or dry air, to prevent reactions and water clustering in the drift region. The device must also be heatable during operation.

This work has demonstrated real-time detection of chlorinated aliphatic compounds using a photoemissive-ionization ion mobility detector. Detection in ambient air was hindered because oxygen anion and chloride ion mobilities are too similar to distinguish with our low-resolution instrument. However, improvements to the design such as incorporation of a drift tube and counter-flowing drift gas or addition of oxygen discriminating devices would permit very sensitive detection of these compounds in air. Although we have only detailed the detection of chlorinated solvents, the PE-IMS is applicable to the detection of a wide variety of electron-attaching vapors. Among these are the nitro-containing explosives, many pesticides, and several lachrymators.

## G. RECOMMENDATIONS

The very successful numerical modeling of the ion drift should be extended to include space charge effects. This will allow experimental data to be curve fit using an optimization routine to determine effective parameters such as the ion mobilities and drift coefficients. These parameters in turn will identify the drifting ions. Chemometric techniques also need to be developed to combine the waveform temporal data with wavelength data to provide two-dimensional speciation of mixtures.

Highly sensitive LID detection of trace levels of indene at ppbv levels in ambient air has been demonstrated. The technology should be commercialized for the detection of indene in the headspace over multicomponent mixtures such as coal tar, creosote, etc. The commercial instrumentation presently exists for this application with a change of ionization laser wavelength (Dakota Technologies, Inc., Fargo, ND). The LID spectral data-base needs to be completed for the rest of the EPA priority PAH pollutants.

The application of the PE-IMS for chlorinated species in air is limited by the interference of oxygen anions in the drift spectra. However, since nitroaromatic molecules are not expected to dissociate upon electron attachment, the oxygen interference for detecting explosives should be avoidable by designing a counter-flowing air or nitrogen drift tube similar to those used in a commercial IMS. Ion mobility spectrometry is presently the industry standard for field measurements of nitroaromatic explosives. The efficient detection of the nitroaromatic p-nitrotoluene by PE electron capture has been demonstrated in nitrogen and P-5 gas in our laboratory. The application of PE-IMS combined with laser desorption to the detection of explosives definitely warrants further development.

Another promising application of the PE-IMS is as a very sensitive fast gas chromatograph detector. By combining a PE-IMS with a low resolution fast GC, real-time analysis with high sensitivity and high resolution appears possible through the use of chemometrics applied to the two-dimensional data. Separation of the oxygen by the fast GC would eliminate PE-IMS interference problems.

The literature on the photoelectric effect suggests that the photoemitter can be made significantly more efficient. Nearly all these studies were made in ultrahigh vacuum to avoid the effects of molecules adsorbed on the emitting surface. Since our approach requires operating at ambient pressure, these studies should be repeated under operational conditions. The photoelectric effect literature indicates parametric studies of thin film thickness, thin film material, applied bias, and ultraviolet wavelength and polarization would have high payoff. The potential of using the recently available diode pumped microlasers as the ultraviolet source for photoemission makes the PE-IMS extremely attractive.

## TABLE OF CONTENTS

Preface .....	iii
Executive Summary .....	v
A. Objective .....	v
B. Background .....	v
C. Scope .....	v
D. Methodology .....	v
E. Results .....	v
F. Conclusions .....	vi
G. Recommendations .....	vii
Table of Contents .....	ix
List of Figures .....	x
Section I Introduction .....	1
A. Objective .....	1
B. Background .....	1
C. Scope/Approach .....	1
1. LID Temporal Waveform Study .....	1
2. LID Spectral Database .....	2
3. LI-IMS .....	2
4. PE-IMS .....	2
Section II LID Temporal Waveforms .....	3
A. Background .....	3
B. Parallel Plate Waveforms .....	3
C. Cylindrical Waveforms .....	9
D. Half-Cylinder Waveforms .....	15
Section III LID Aromatic Spectra .....	24
A. Background .....	24
B. Summary of Results .....	24
Section IV LID Ion Mobility Spectrometry .....	25
A. Background .....	25
B. Two-Dimensional Laser Ionization Data .....	25
Section V Photoemissive Ion Mobility Spectrometry .....	31
A. Background .....	31
B. Summary of Results .....	32
References .....	33
Appendix A, Masters Thesis by Feng Hong, "Modeling of Ion Drift in an Applied Electric Field in Ambient Pressure Air," July 2001	
Appendix B, Masters Thesis by Maxwell Ryan Lucci, "Resonance Enhanced Multiphoton Ionization Spectroscopy of Indene at Ambient Conditions," June 1999	
Appendix C, Draft Masters Thesis by Christopher J. Walls, "Photoemissive Ion Mobility Spectrometry for Detection of Chlorinated Vapors," May 2002	

## LIST OF FIGURES

Figure 1. Styrene parallel plate waveforms, +300 V bias, as the laser beam is moved away from the collector electrode (repeller at positive bias, collector at ground).....	4
Figure 2. Total charge collected as function of position between parallel plates, 300 V bias.....	4
Figure 3. Styrene LID waveforms, -300 V bias, as the laser beam is moved away from the collector electrode (repeller at negative bias, collector at ground).....	5
Figure 4. Total charge collected as function of position between parallel plates, -300 V bias .....	5
Figure 5. Styrene LID waveforms, +50 V bias, as the laser beam is moved away from the collector electrode (repeller at positive bias, collector at ground).....	6
Figure 6. Styrene LID waveforms, +100 V bias, as the laser beam is moved away from the collector electrode (repeller at positive bias, collector at ground).....	6
Figure 7. Styrene LID waveforms, +900 V bias, as the laser beam is moved away from the collector electrode (repeller at positive bias, collector at ground).....	7
Figure 8. Styrene LID waveforms as the bias is varied from 10 to 100 V (repeller at positive bias, collector at ground) with the laser beam centered between the electrodes.....	7
Figure 9. Styrene LID waveforms as the bias is varied from 50 to 1000 V (repeller at positive bias, collector at ground) with the laser beam centered between the electrodes.....	8
Figure 10. Representative LID waveforms for acetaldehyde in air at 363.5 nm. ....	9
Figure 11. Cylindrical electrode LID waveforms as a function of distance from the collection wire (cylinder at +300 V, collector wire at ground to collect positive ions.) .....	10
Figure 12. Styrene LID waveforms, +300 V bias, as the laser beam is moved across the diameter of the cylinder (cylinder at positive bias, collector wire at ground). ....	10
Figure 13. Total styrene LID charge collected across cylindrical cell with cylinder biased at +300 V. ....	11
Figure 14. Laser pulse energy transmitted through cylindrical LID cell of Figure 13. ....	11
Figure 15. Cylindrical electrode LID waveforms as a function of distance from the collection wire (cylinder at -300 V, collector wire at ground to collect anions.) .....	12
Figure 16. Styrene LID waveforms, -300 V bias, as the laser beam is moved across the diameter of the cylinder (cylinder at negative bias, collector wire at ground). ....	12
Figure 17. Total styrene LID charge collected across cylindrical cell with cylinder biased at -300 V. ....	13
Figure 18. Laser pulse energy transmitted through cylindrical LID cell of Figure 17. ....	13
Figure 19. LID waveforms for cylindrical electrodes at midpoint between wire and cylinder as a function of voltage applied to the cell.....	14
Figure 20. Interpolated styrene LID waveforms, midpoint between wire and cylinder, as the voltage is increased to 1000 V. ....	14
Figure 21. Total charge plot of styrene ionization at the midpoint between the wire and cylinder as the applied bias is varied. ....	15
Figure 22. Collection wire at negative bias. A1 and A4: laser beam hitting cylinder at the ceramic; A2 and A3: laser beam just missing the ceramic half way between the wire and cylinder; A: laser hitting the collection wire. Indene (190 ppbv) in air.....	16
Figure 23. Collection wire at positive bias. A1 and A4: laser beam hitting cylinder at the ceramic; A2 and A3: laser beam just missing the ceramic half way between the wire and cylinder; A: laser hitting the collection wire. Indene (190 ppbv) in air.....	16
Figure 24. Collection wire at negative bias. A: laser hitting the collection wire; C: half way between the wire and cylinder; D: just missing the cylinder; E: hitting the cylinder. Indene (190 ppbv) in air. ...	17
Figure 25. Collection wire at negative bias. A: laser hitting the collection wire; C: half way between the wire and cylinder; D: just missing the cylinder; E: hitting the cylinder. Waveforms normalized to maximum current.....	18
Figure 26. Collection wire at positive bias. A: laser hitting the collection wire; C: half way between the wire and cylinder; D: just missing the cylinder; E: hitting the cylinder. Indene (190 ppbv) in air. ...	18



Figure 27. Collection wire at positive bias. A: laser hitting the collection wire; C: half way between the wire and cylinder; D: just missing the cylinder; E: hitting the cylinder. Waveforms are normalized.	19
Figure 28. Position C half way between the wire and the cylinder. The dashed is the waveform for the collection wire negatively biased and solid line for the wire positively biased.	19
Figure 29. Position D just missing the cylinder. The dashed is the waveform for the collection wire negatively biased and solid line for the wire positively biased.	20
Figure 30. Collection wire at negative bias with laser beam at position D. Styrene (150 ppbv) in air.	20
Figure 31. Collection wire at negative bias with laser beam at position D. Styrene (150 ppbv) in air.	21
Figure 32. Collection wire at negative bias with laser beam at position D. Styrene (150 ppbv) in nitrogen.	21
Figure 33. Collection wire at negative bias with laser beam at position D. Styrene (150 ppbv) in nitrogen.	22
Figure 34. Collection wire at negative bias with laser beam at position D. Styrene (150 ppbv) in P-5 (5% methane in argon).	22
Figure 35. Collection wire at negative bias with laser beam at position D. Styrene (150 ppbv) in P-5 (5% methane in argon).	23
Figure 36. Collection wire at negative bias with laser beam at position D. Styrene (150 ppbv) in argon.	23
Figure 37. LI-IMS schematic.	26
Figure 38. LI-IMS waveforms for different applied biases in the drift region.	26
Figure 39. Total charge collected versus drift electric field.	27
Figure 40. Two-dimensional LI-IMS plot for 100 ppbv styrene in air.	27
Figure 41. Two-dimensional LI-IMS plot for 20 ppbv aniline in air.	28
Figure 42. Two-dimensional LI-IMS plot for 30 ppbv aniline and 100 ppbv styrene in air.	28
Figure 43. Two-dimensional LI-IMS plot for 1 ppbv methylnaphthalene in air.	29
Figure 44. Two-dimensional LI-IMS plot for 13 ppbv naphthalene	29
Figure 45. Two-dimensional LI-IMS plot for 9.0 ppbv naphthalene and 0.73 ppbv methylnaphthalene.	30

## SECTION I INTRODUCTION

### A. OBJECTIVE

The objective of this project was to develop and demonstrate capabilities for trace detection of analyte molecules in ambient pressure air. The principle goals were fourfold:

- Laser ionization detection (LID) temporal waveform study.
- Expanding the number of molecules in the LID spectral database.
- Combined laser ionization-ion mobility spectrometry (LI-IMS) for deconvolution of mixtures.
- Photoemissive ion mobility spectrometry (PE-IMS) development.

### B. BACKGROUND

Our LID and PE-IMS techniques have several common features:

1. Charged species are generated by pulsed photoprocesses and then drawn to a collector by an electric field.
2. The ions are collected at atmospheric pressure (and generally ambient) conditions.
3. The ion drift times are long compared to the time scale over which the ions are generated.
4. The ion drift times (or equivalently, the ion mobilities) provide a means of chemical identification.

Neither the LID nor the PE-IMS techniques are completely new; however, our approach is notable because it emphasizes practical applications and operation under realistic field conditions. For example, LID, commonly referred to as resonance enhanced multiphoton ionization (REMPI), spectrometry is a popular laboratory technique; however, most of the work has been performed with supersonically cooled samples. The mass resolution of the LID generated ions can be achieved with time-of-flight mass spectrometry (TOF-MS). However, supersonic cooling and TOF-MS require high vacuum conditions making them incompatible with field implementations. It is interesting to note the common misconception that LID ion collection requires high vacuum conditions. We have extensively demonstrated effective LID measurements for a considerable range of different carrier gases and pressures. Ion mobility spectrometry (IMS) is a well-known gas phase detection method (Eiceman, 1994), but commercial instruments invariably use radioactive sources that have significant deficiencies. Lubman and coworkers (Lubman, 1983, Kolaitis, 1986) have measured and tabulated mobilities of ions generated by LI, but they typically used fixed wavelength excitation at 266 nm and therefore did not take advantage of the spectral resolution. We are the first to introduce a tunable laser source and to consider the ion mobility aspects in the specific context of LID ion generation. Schechter (Schechter, 1992) and Ogawa (Ogawa, 1992) have discussed the temporal waveforms associated with collecting LID-generated ions at parallel plate electrodes; however, we have much more clearly demonstrated the ion dynamics taking place that will provide significantly more information. The PE-IMS technique (Begley, 1991) was presented in the literature by Simmonds group, but no follow-up work has been published. No data were presented for the two most obvious applications, detection of chlorinated solvents and nitro-organics (i.e., explosives). This research has resulted in three masters degree theses, that are attached, as well as a number of undergraduate research projects whose results are included in this report. A background description for each of the four areas is included in its respective section.

### C. SCOPE/APPROACH

#### 1. LID Temporal Waveform Study

The induced current resulting from drifting LI generated ions was measured for three electrode configurations: parallel plates, cylindrical and half-cylindrical. These configurations were studied extensively as a function of laser beam position and applied bias. Measurements were made primarily in

ambient pressure air but comparison measurements were included in nitrogen, argon and P5 gases. The induced current was also numerically modeled for the parallel plate and cylindrical cases permitting a definitive analysis of the features in the ion current waveforms. The numerical modeling was the basis of an NDSU Physics Department Master's degree thesis that is included as attachment A.

## **2. LID Spectral Database**

The LID spectrometry was limited primarily to a study of indene in ambient pressure air. This study comprises an NDSU Chemistry Department Master's degree thesis that is included as attachment B.

## **3. LI-IMS**

The laser ionization-ion mobility spectrometry study involved acquisition of temporal waveforms as the wavelength of the ionizing laser was scanned in a simple drift tube with an aperture grid. These data are then plotted as two-dimensional data that provide signatures of the detected analyte. This study was limited by not having a cell with counter-flowing nitrogen to prevent reactions in the drift region or heating during data acquisition. The approach was clearly demonstrated but requires further development.

## **4. PE-IMS**

The photoemissive ion mobility spectrometry included generation of free electrons by ultraviolet illumination of a thin gold film on a fused silica window and detection of  $\text{Cl}^-$  anions created by the dissociative attachment by chlorinated molecules. The results from this contract are presented in an NDSU Chemistry Department Master's degree thesis that is included as attachment C. This effort was in conjunction with a complementary Strategic Environmental Research and Development Program (SERDP) subcontract SC-98C6009 to Dakota Technologies, Inc.

## SECTION II LID TEMPORAL WAVEFORMS

### A. BACKGROUND

The ambient pressure LID temporal waveform phenomenon can be interpreted as the creation of electron-positive ion pairs that drift through an electric field as they collide with the ambient gas molecules. When a molecule reaches its ionization continuum by photon absorption, it liberates an electron and leaves behind a positive molecular ion. In our experiments, these charged species are efficiently collected and detected at biased electrodes. When a charged particle moves between the electrodes, it induces changing charges on the electrode surfaces resulting in a current between the electrodes that is monitored. The cations approaching the negative electrode and the anions approaching the positive electrode are both recorded in the external circuit as a positive current flowing from the negative electrode to the positive electrode. A parallel plate configuration is the easiest to build and interpret because the electric field is constant between the plates. This configuration was used for most of our previous work, but it yields waveforms that consist of ion current plateaus as seen in Figure 1. Additional selectivity is available from ambient pressure LID via the molecule specific ion mobilities by measuring the drift time. In a cylindrical configuration a peak in the current as a function of time is produced as observed in Figure 11. The shift in this peak due to differing drift times for different species is easier to determine than the edge of the parallel plate plateau. Consequently, we undertook this study to compare the efficacy of the cylindrical configuration compared to the proven parallel plate configuration for LID detection. The properties of the parallel plate detector are detailed in Section B, the properties of the cylindrical configuration are explored in Section C and the results of a new design, the half-cylinder, are given in Section D. Numerical modeling of both the parallel and cylindrical geometries is presented in Appendix A.

### B. PARALLEL PLATE WAVEFORMS

Waveforms were acquired using a LID cell configured with copper parallel plate electrodes 2 cm in diameter separated by 1 cm. The flow system was purged with dry compressed air and 5  $\mu$ L of styrene headspace was injected into the 5 L flask to give a concentration of approximately 10 ppbv in atmospheric pressure air. The rhodamine dye laser was tuned to the styrene resonance at 287.5 nm and a variable high voltage supply was used to bias the electrodes. The waveforms were acquired with a Tektronix 2440 digital oscilloscope and downloaded to the PC through the GPIB. The LID cell was mounted on a translation stage and moved with a micrometer to adjust the distance of the parallel laser beam from the collector electrode. The cell was moved in intervals of 1 mm between the electrodes to acquire the waveforms shown in Figure 1 taken with a positive bias of 300 V (300 V/cm drift field). For the first waveform, at 1 mm from the collector, the positive styrene molecules travel only 1 mm to reach the negative (ground) collector while the anions (electrons captured by oxygen) must travel 9 mm to reach the positive repeller electrode. Consequently, the fast peak in this case is due to the cations and the delayed plateau to the anions. As the ionizing laser beam is moved away from the collector, the positive ions travel further and the anions less until the distances they travel are reversed corresponding to the last waveform shown in Figure 1. In this case the fast peak corresponds to the anions and the delayed plateau to the cations. Because the anions travel faster than the positive ions, the waveforms are not symmetric. When the laser beam is in the center, the cations and anions drift the same distance although the anions will reach their electrode a little sooner because of their higher drift velocity. Even when the ionizing laser beam is in the center between the electrodes, the current is seen to drop after its initial rise creating a sharp initial peak. This can be explained by the space charge effect of the overlapping negative and positive ion swarms (see Appendix A) causing a decreasing total electric field (the applied external field plus the field due to the oppositely charged ions). As the swarms separate, their effect on each other becomes negligible and total electric field once again becomes the applied external field.

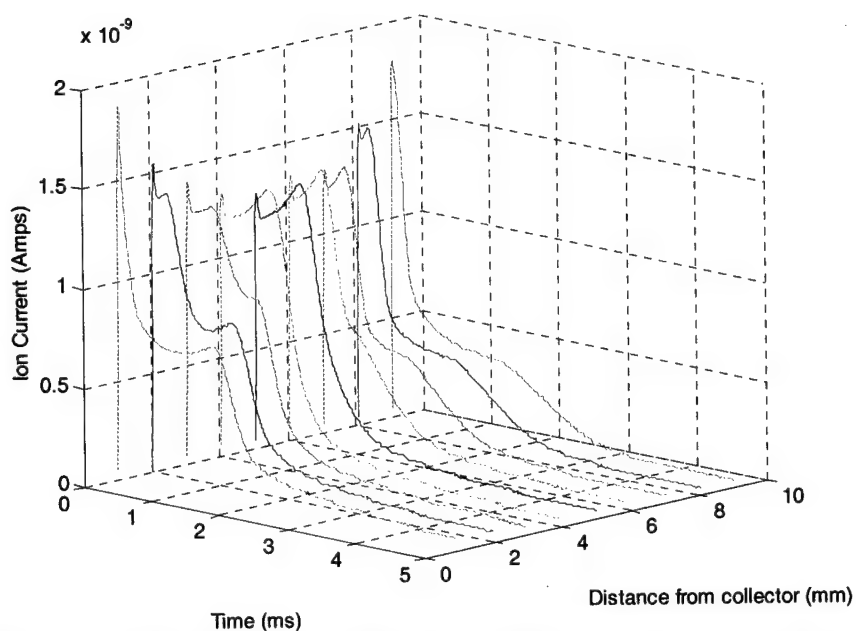


Figure 1. Styrene parallel plate waveforms, +300 V bias, as the laser beam is moved away from the collector electrode (repeller at positive bias, collector at ground).

To evaluate if charge was collected as efficiently at all positions, the waveforms of Figure 1 were integrated to yield the total charge collected for the respective laser beam position relative to the collector electrode.

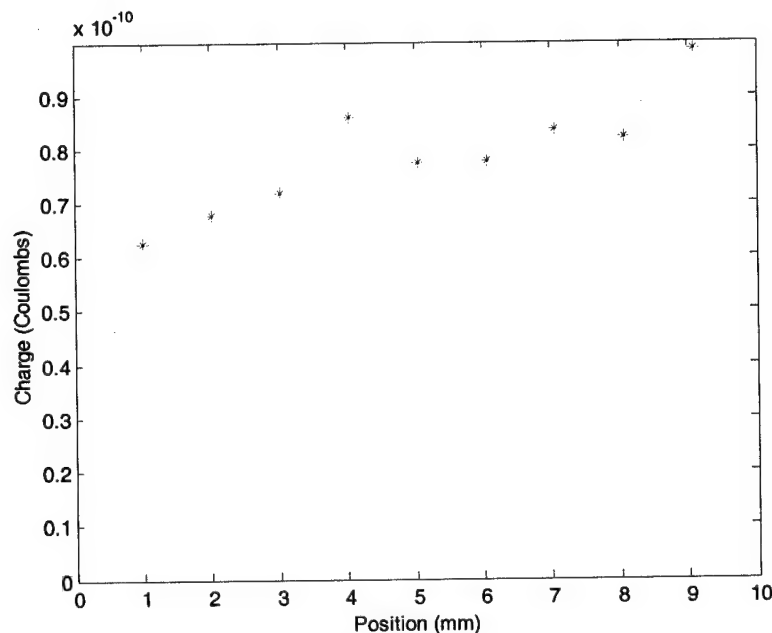


Figure 2. Total charge collected as function of position between parallel plates, 300 V bias.

The procedure was repeated with a -300 V bias resulting in the waveforms in Figure 3 being reversed as expected. The total charge collected as shown in Figure 4 is nearly identical to that for positive bias and suggests that any variations are geometry related.

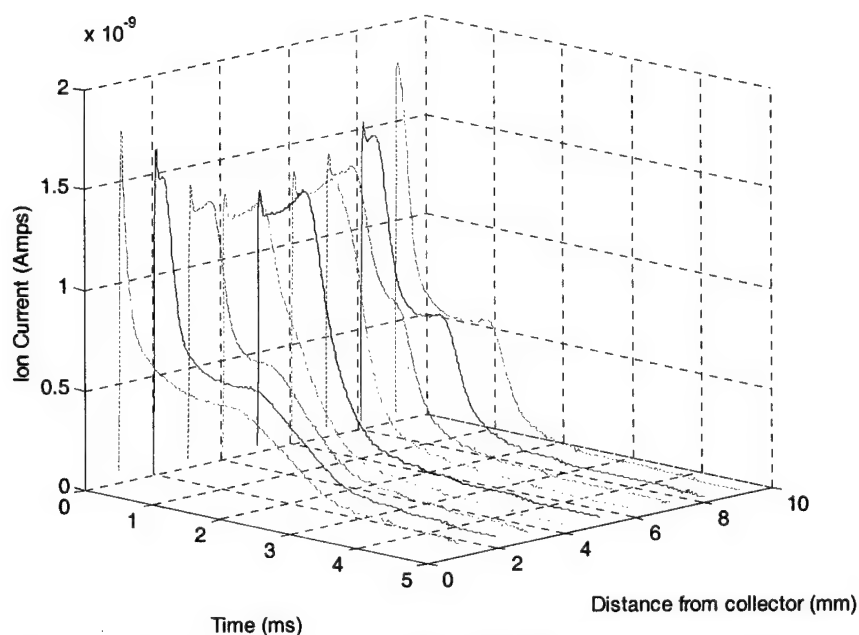


Figure 3. Styrene LID waveforms, -300 V bias, as the laser beam is moved away from the collector electrode (repeller at negative bias, collector at ground).

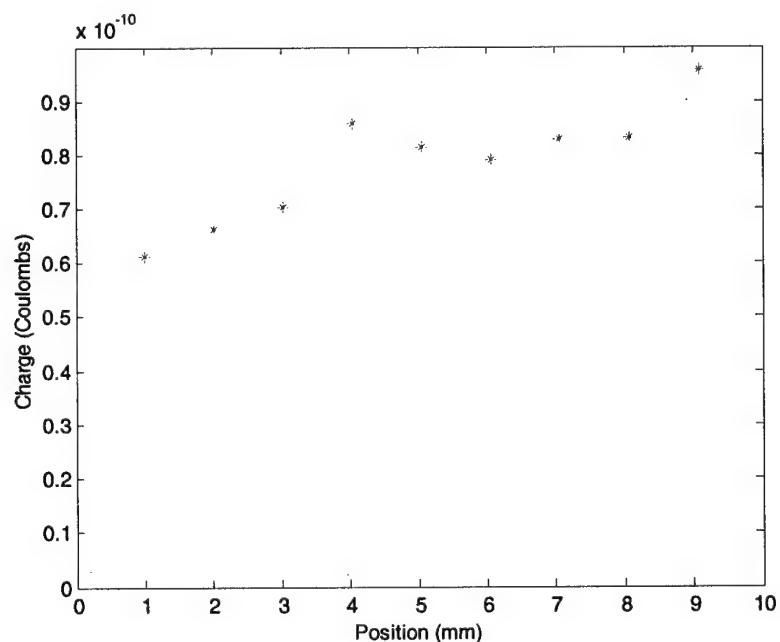


Figure 4. Total charge collected as function of position between parallel plates, -300 V bias

The acquisitions were then done at different positive bias voltages as shown in Figure 5, Figure 6, and Figure 7. The waveforms are very similar except that the drift time decreases with increasing bias (drift field). Note that the time scales are different for Figure 1, Figure 5, Figure 6, and Figure 7 that were taken under identical conditions except that the positive bias was increased.

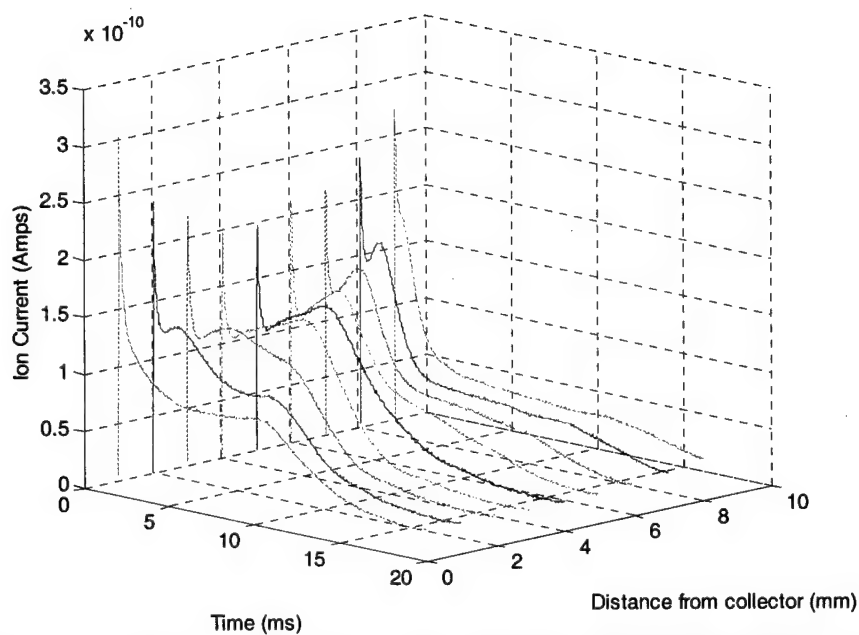


Figure 5. Styrene LID waveforms, +50 V bias, as the laser beam is moved away from the collector electrode (repeller at positive bias, collector at ground).

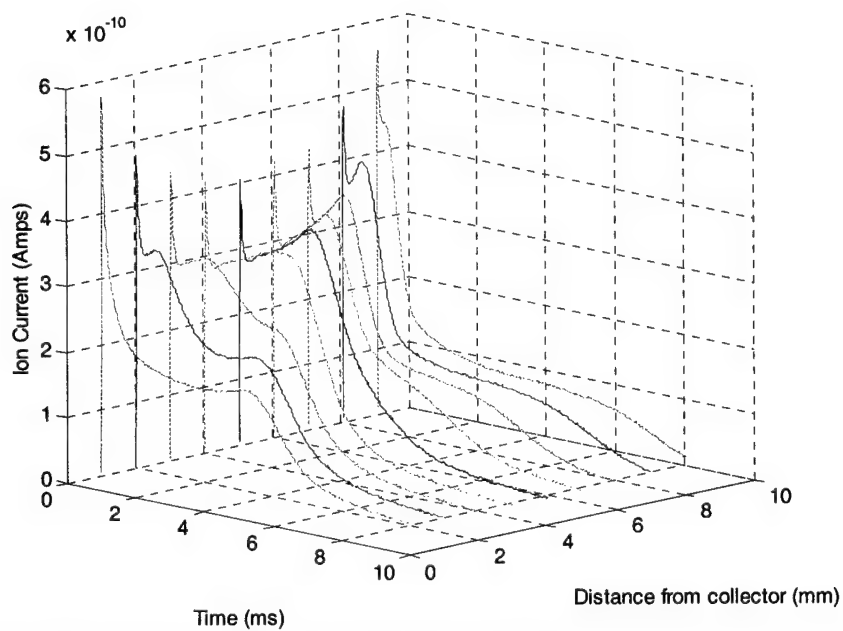


Figure 6. Styrene LID waveforms, +100 V bias, as the laser beam is moved away from the collector electrode (repeller at positive bias, collector at ground).

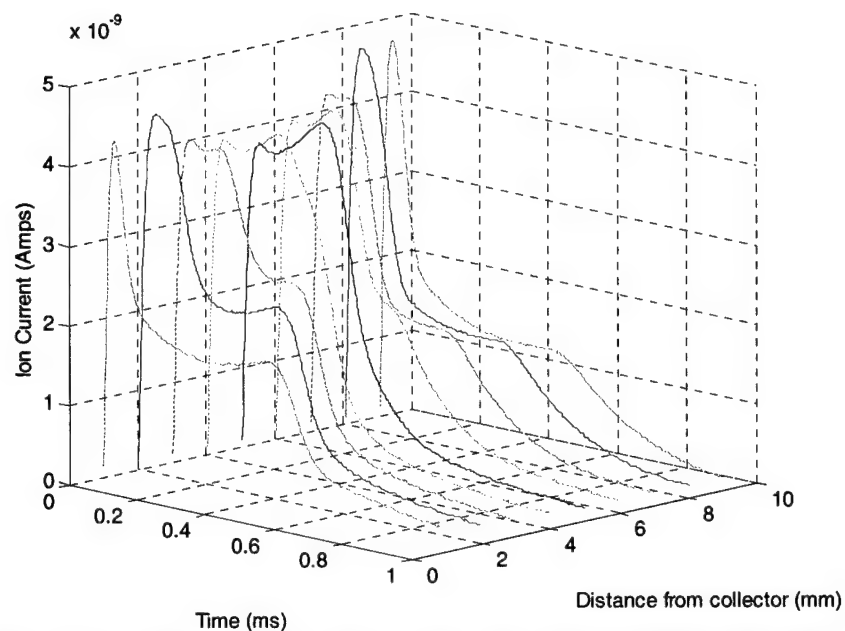


Figure 7. Styrene LID waveforms, +900 V bias, as the laser beam is moved away from the collector electrode (repeller at positive bias, collector at ground).

To better observe the effects of varying the bias on the waveform, two sequences were taken in which the laser beam was centered between the electrodes and the bias varied. A mesh plot of the first sequence in which the voltage was varied from 10 to 100 V in steps of 10 V is shown in Figure 8.

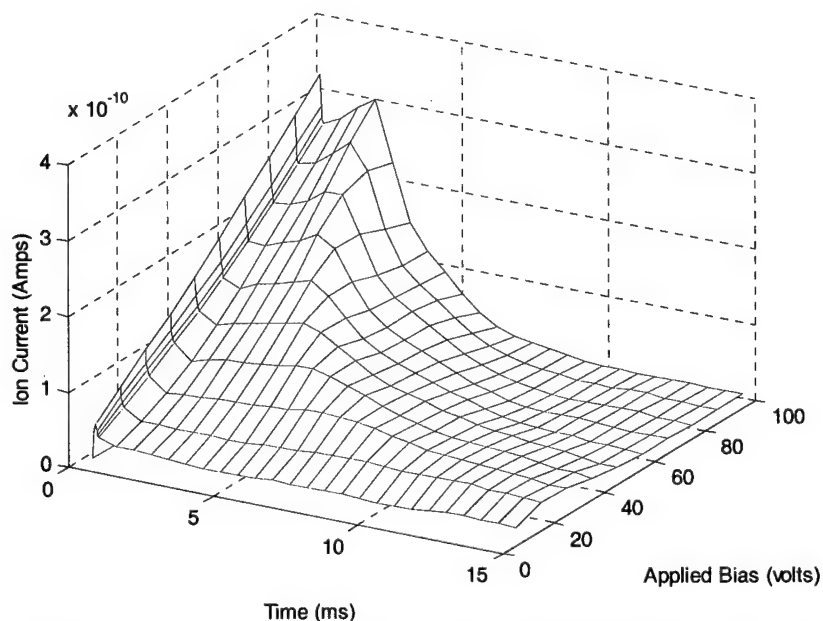


Figure 8. Styrene LID waveforms as the bias is varied from 10 to 100 V (repeller at positive bias, collector at ground) with the laser beam centered between the electrodes.



The second mesh plot in Figure 9 shows the waveform variation as the voltage was varied from 50 to 1000 V in steps of 50 and then 100 V. Note the change in time scale and that the peak current has changed by an order of magnitude from Figure 8.

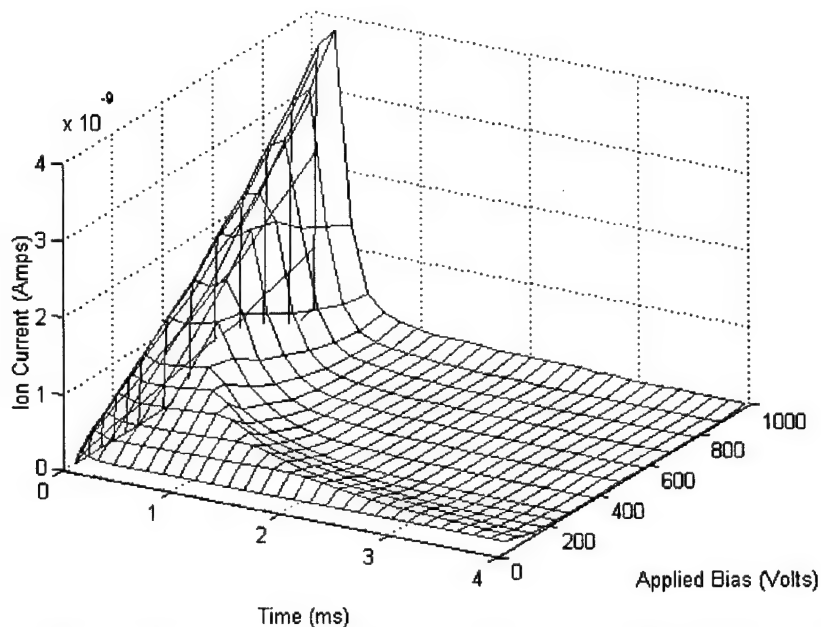


Figure 9. Styrene LID waveforms as the bias is varied from 50 to 1000 V (repeller at positive bias, collector at ground) with the laser beam centered between the electrodes

The temporal width of the waveforms typically remains the same while the current increases proportionately with concentration. However, atypical temporal broadening with concentration was observed for acetaldehyde (Swenson 1999). A pulsed Ti:sapphire laser was tuned on the acetaldehyde origin peak at 363.5 nm and the ionization current monitored as acetaldehyde diluted  $1:10^5$  in methanol was injected into a 5 L closed system. As indicated in Figure 10, the waveforms get progressively lengthened in time as the concentration increases indicating a decrease in the mobilities of the ions. This is in contrast to a constant temporal shape with concentration that we have observed in other analytes. For a given concentration, the temporal shape of the acetaldehyde waveforms did not change with wavelength. This behavior is indicative of clustering of the acetaldehyde molecules with each other or with other molecules. Further studies of this effect are clearly warranted.

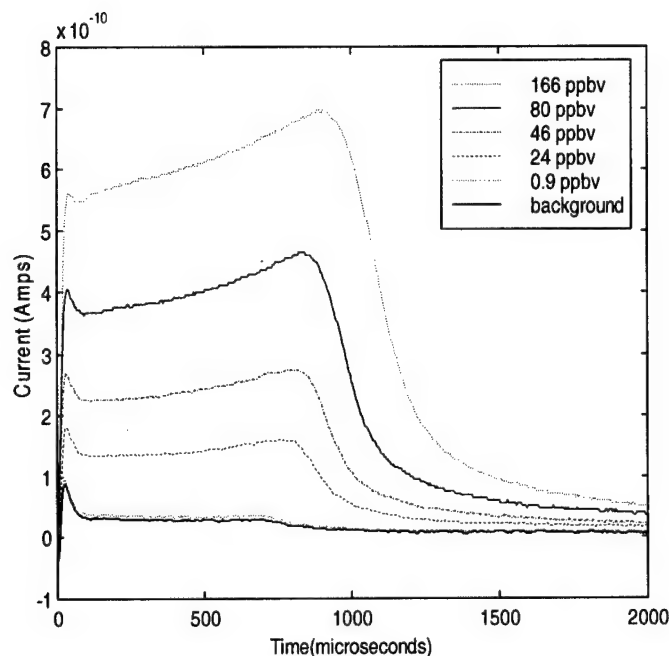


Figure 10. Representative LID waveforms for acetaldehyde in air at 363.5 nm.

### C. CYLINDRICAL WAVEFORMS

Waveforms were acquired using a LID cell configured with a copper cylinder electrode (2.6 cm long and 1.1 cm inside diameter) and a 1 mm diameter copper wire electrode through the center of the cylinder. The variable high voltage supply was connected to the outer cylindrical pipe and the central collection wire was connected to the pre-amp (ground). The flow system contained laboratory air and 5  $\mu$ L of styrene headspace was injected into the 5 L flask to give a concentration of approximately 10 ppbv in atmospheric pressure air. The rhodamine dye laser was tuned to the styrene resonance at 287.5 nm. The waveforms were acquired with a Tektronix 2440 digital oscilloscope and downloaded to the PC through the GPIB. The LID cell was mounted on vertical/horizontal translation stages and moved with micrometers to adjust the distance of the parallel laser beam from the wire collector electrode. The cell was moved in small increments so that the laser beam sampled across the diameter of the cylinder. The laser beam hit the collection wire when the beam was aimed through the center.

Waveforms acquired with a positive 300 volt bias are shown in Figure 11. For the first waveform, at 1 mm from the collector, the positive styrene molecules travel only 1 mm to reach the negative (ground) collector while the anions (electrons captured by oxygen) must travel to the positive cylindrical electrode. Consequently, the fast peak in this case is due to the cations and the anions are delayed. Because the electric field varies inversely with distance from the collection wire in the cylindrical case, the ions traveling to the collection wire are well defined. The current of oppositely charge ions traveling to the cylinder is stretched out in time and effectively produces a flat baseline (see Appendix A). As the ionizing laser beam is moved away from the collector, the positive ions travel further and the current peak due to positive ions nearing the collection wire is delayed in time. The laser beam was moved in small increments across the diameter of the cylinder as indicated in Figure 12 where the collection wire in the cylinder center is located at 0. The total charge collected at each position was determined by integrating the current for each waveform and is displayed in Figure 13. The drops in collected charge match the laser beam being blocked by the outer cylinder and the center collection wire as seen by comparing the collected charge with the transmitted laser pulse energy shown in Figure 14.

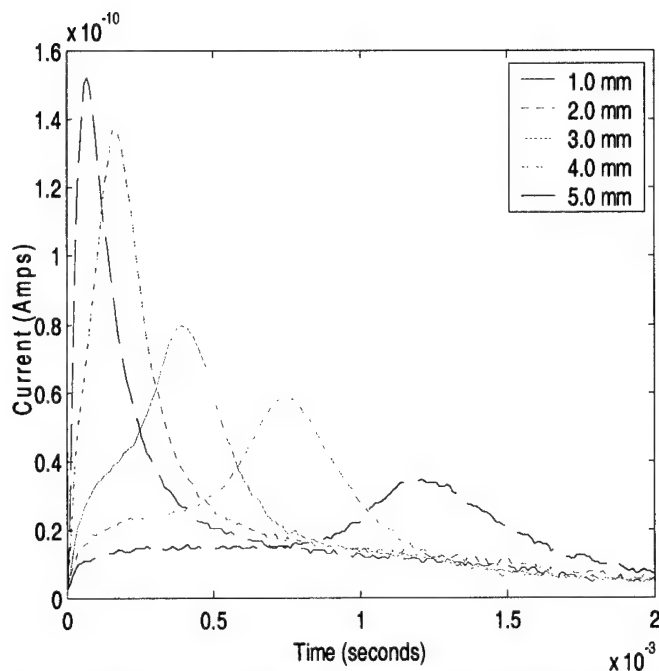


Figure 11. Cylindrical electrode LID waveforms as a function of distance from the collection wire (cylinder at +300 V, collector wire at ground to collect positive ions.)

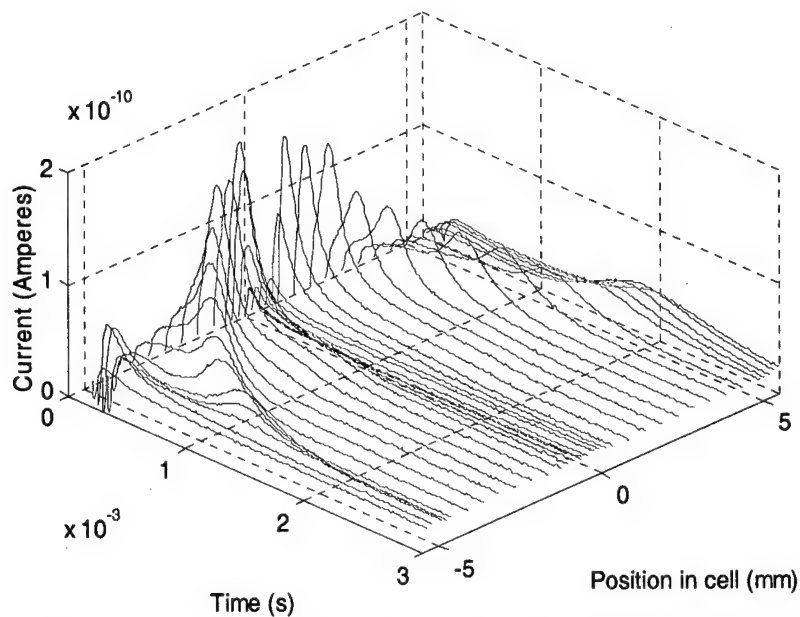


Figure 12. Styrene LID waveforms, +300 V bias, as the laser beam is moved across the diameter of the cylinder (cylinder at positive bias, collector wire at ground).

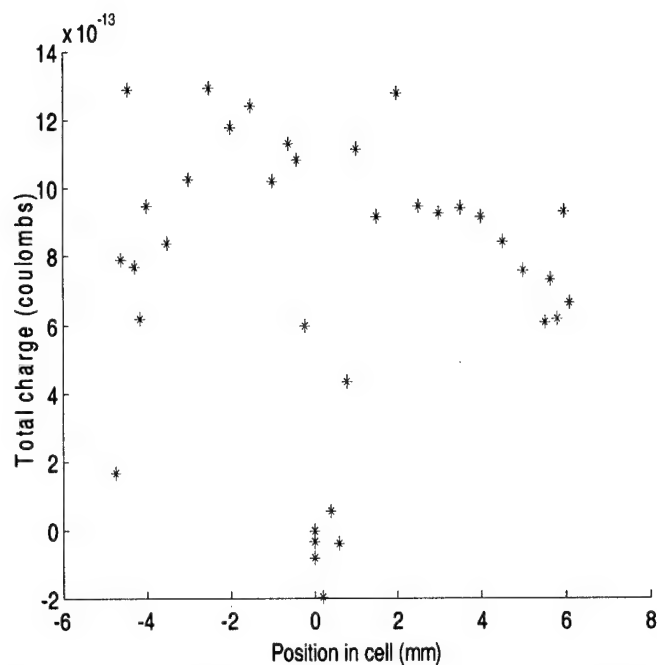


Figure 13. Total styrene LID charge collected across cylindrical cell with cylinder biased at +300

V.

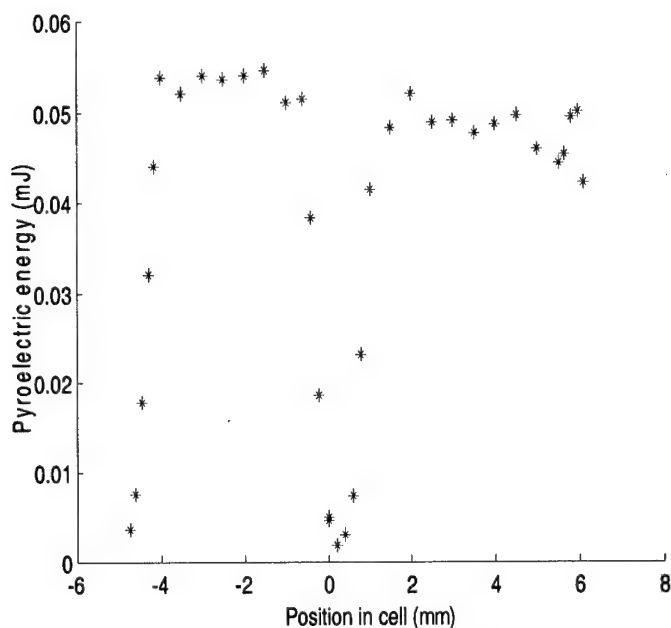


Figure 14. Laser pulse energy transmitted through cylindrical LID cell of Figure 13.

The procedure was repeated with a  $-300$  V bias resulting in the waveforms in Figure 15. The composite of waveforms as a function of position is shown in Figure 16. Large currents were detected as the laser beam struck the negatively biased cylinder due to the photoelectric effect. This is clearly reflected in the total charge collected shown in Figure 17 along with the corresponding laser energy transmitted given in Figure 18.

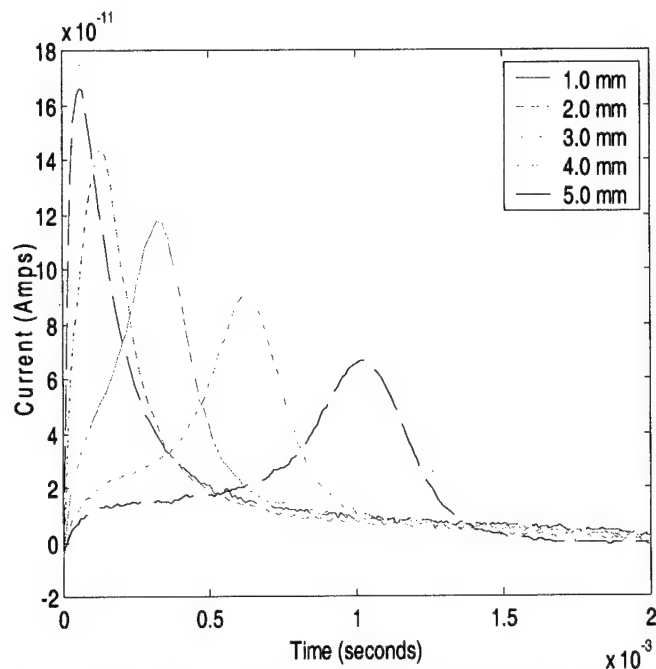


Figure 15. Cylindrical electrode LID waveforms as a function of distance from the collection wire (cylinder at -300 V, collector wire at ground to collect anions.)

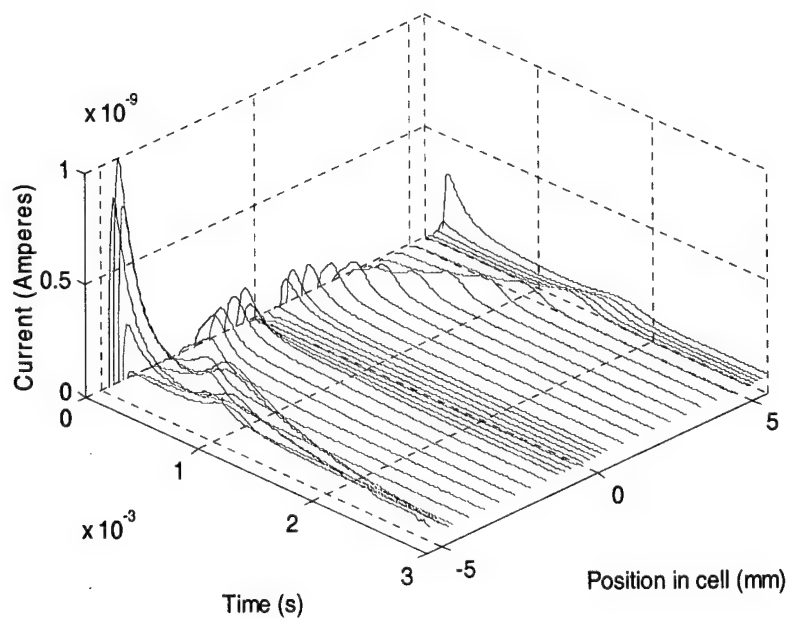


Figure 16. Styrene LID waveforms, -300 V bias, as the laser beam is moved across the diameter of the cylinder (cylinder at negative bias, collector wire at ground).

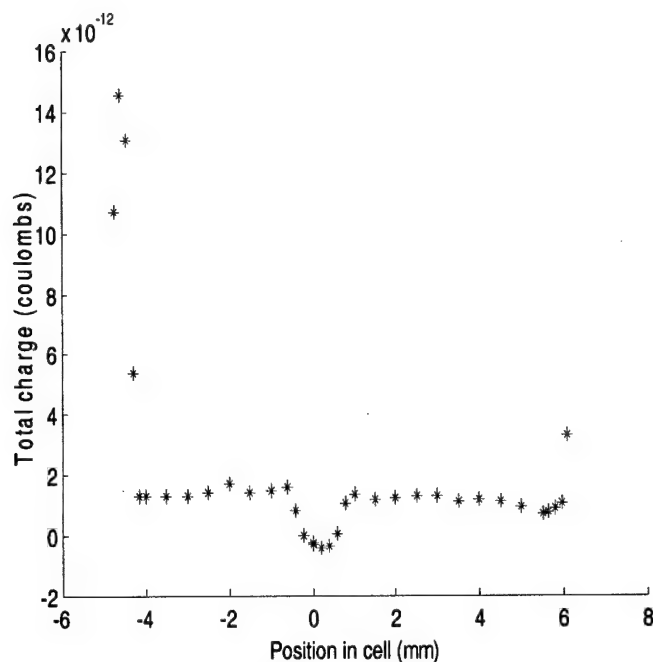


Figure 17. Total styrene LID charge collected across cylindrical cell with cylinder biased at -300 V.

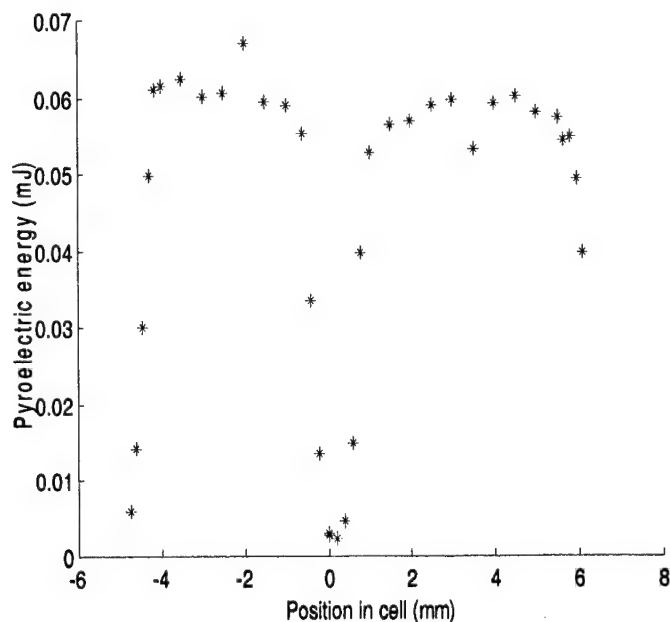


Figure 18. Laser pulse energy transmitted through cylindrical LID cell of Figure 17.

The bias voltage was also varied with the laser beam in a fixed position relative to the collection wire. The results for the laser beam midway between the cylinder and the collection wire is given in Figure 19. As expected the higher the bias, the faster the ions drift and the peaks are shifted to shorter times.

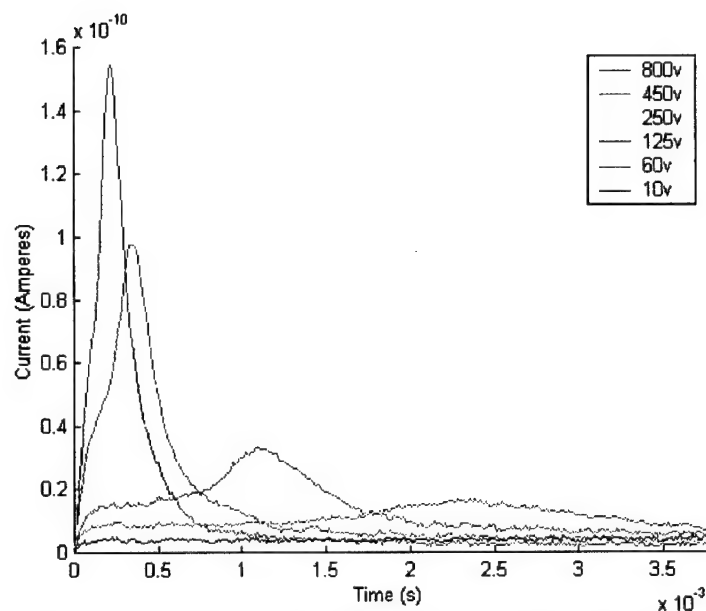


Figure 19. LID waveforms for cylindrical electrodes at midpoint between wire and cylinder as a function of voltage applied to the cell.

An interpolated plot is presented in Figure 20. The corresponding total charge as a function of bias is shown in Figure 21. The implication is that above some voltage, approximately 50 V for this configuration, the collection efficiency is nearly independent of bias. This means that the voltage can be adjusted to place the ion current peak at a convenient drift time.

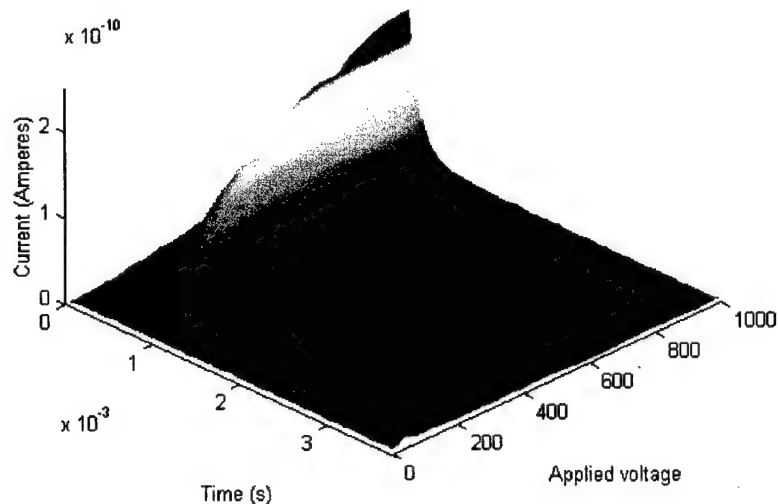


Figure 20. Interpolated styrene LID waveforms, midpoint between wire and cylinder, as the voltage is increased to 1000 V.

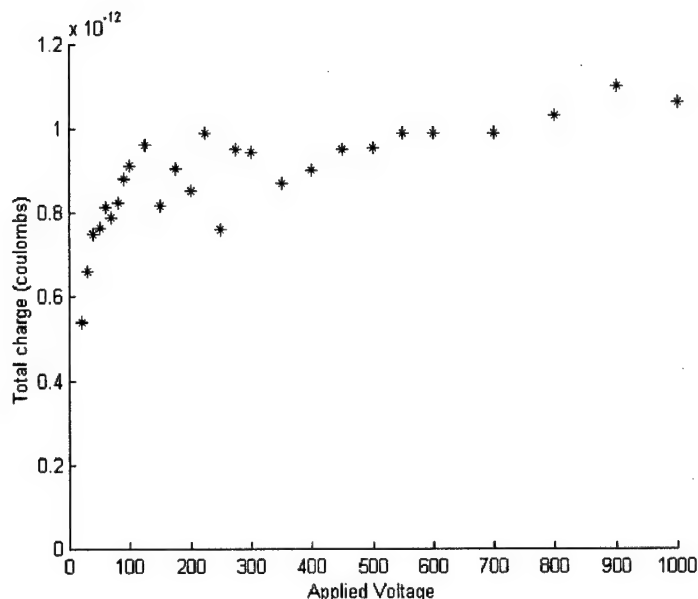


Figure 21. Total charge plot of styrene ionization at the midpoint between the wire and cylinder as the applied bias is varied.

Similar results were obtained with the collection wire biased to collect anions and over a range of laser beam positions. In addition, large currents were detected as the laser beam struck the negatively biased cylinder due to the photoelectric effect. Within experimental error, the cylindrical and parallel plate configurations produced similar total charge detection for the same laser beam and analyte concentration. The cylindrical configuration was shown to work effectively over a wide range of drift distances and applied bias.

#### D. HALF-CYLINDER WAVEFORMS

The positive results from the cylindrical configuration led us to develop a hemispherical cell geometry that minimizes photoemission due scattered light striking the negative electrode while providing peaked ion current waveforms. The collection electrode is a wire mounted on a ceramic base and the repeller electrode is a 4.9 mm inside diameter, 11.6 mm long half-cylinder of copper. Figure 22 shows waveforms obtained from such a cell containing indene vapor (190 ppbv) in air at ambient pressure as a function of position along the ceramic relative to the collection wire. The laser was tuned to 288 nm and a 300 V battery was used to bias the electrodes.

The largest and fastest peak was obtained at position A with the laser beam striking the end of the collection wire, which nearly blocked the entire beam. The peak for position A is over one order of magnitude larger than at positions A1 and A4 and over three times the magnitudes at positions A2 and A3. In both cases A1 and A4, the beam was striking the cylinder. The very large magnitude suggests that the peak at A must be predominantly due to photoelectric-effect electrons from the negatively biased collection wire rather than ionization of indene. The 288 nm light should not be energetic enough for photoemission from copper, so we are likely seeing a 2-photon effect (Smith, 1962, Teich, 1964, Logothetis, 1967). Since the cylinder is symmetric, one would expect the same results on both sides. Since the cylinder is positively biased, there should be no photoemission from the cylinder (positions A1 and A4) and little ionization of indene since most of the beam is blocked, which corresponds to what is observed.



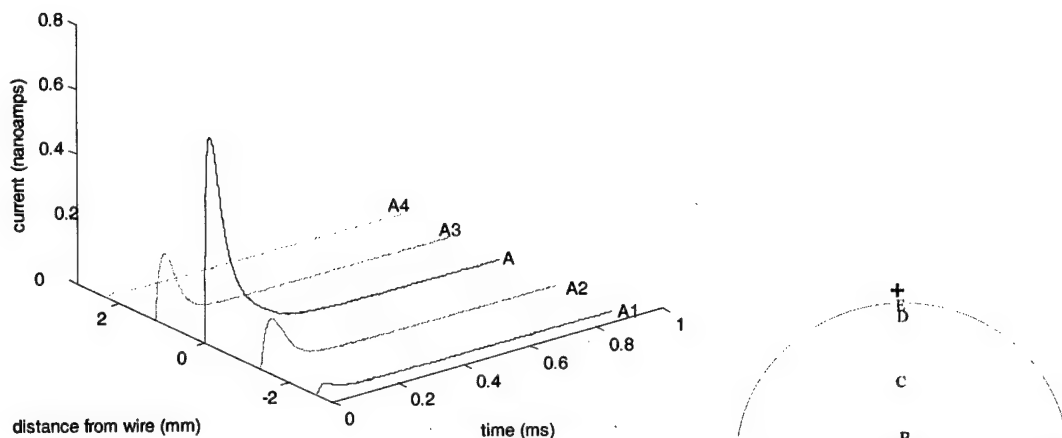


Figure 22. Collection wire at negative bias. A1 and A4: laser beam hitting cylinder at the ceramic; A2 and A3: laser beam just missing the ceramic half way between the wire and cylinder; A: laser hitting the collection wire. Indene (190 ppbv) in air.

Figure 23 shows the same situation with the bias reversed, i.e. the oxygen anions are now being collected at the collection wire. With the cylinder at negative bias, positions A1 and A4 are dominated by photoemission. A1 and A4 must again correspond to the emission of the photoelectrons rather than the collection of the anions at the wire since they are much faster than the anions from A2 and A3 traveling to the wire. There should be little or no photoemission from the collection wire for situation A as is observed. A should be negatively charged anions traveling to the wire and should be prompter than A2 and A3 which appears the case. A is much smaller than A2 or A3 probably because the beam was largely blocked by the wire therefore few ions were created along the wire.

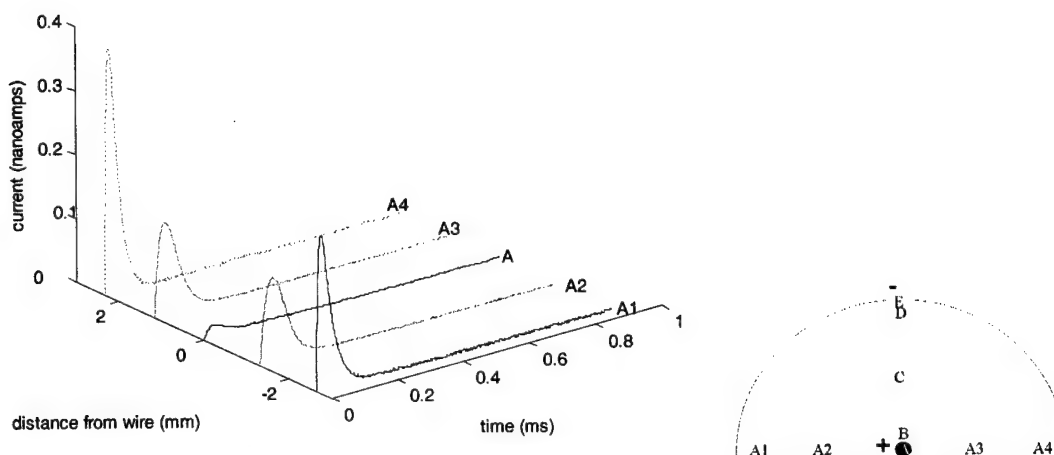


Figure 23. Collection wire at positive bias. A1 and A4: laser beam hitting cylinder at the ceramic; A2 and A3: laser beam just missing the ceramic half way between the wire and cylinder; A: laser hitting the collection wire. Indene (190 ppbv) in air.

Figure 24 and Figure 25 correspond to positions vertical to the ceramic plane. Again there is a large photoemission peak at position A. In Figure 24 the peak for A must be dominated by the photoemitted electrons that presumably are captured by oxygen molecules and the consequent anions drift to the cylinder. From numerical modeling, this should be a broad, flat curve. The fact that instead, a prompt large peak is observed confirms that it corresponds to current flowing through the external detector circuit to make up the deficiency of photo-electrons leaving the wire. If this is the case, the pulse shape of waveform A should represent the response time of the electronics. The time dependence of the four waveforms is presented in Figure 25 where the waveforms are normalized to their peak current value. Since C is faster than D, they appear to correspond to the positive indene ions traveling to the collection wire. Following this argument, the peak in E would correspond to the positive indene ions traveling to the collection wire. The leading shoulders on D and E then correspond to the anions traveling to the cylinder since they have a much shorter distance to travel. The farther the anions have to travel, the smaller the magnitude and broader the corresponding current waveform contribution.

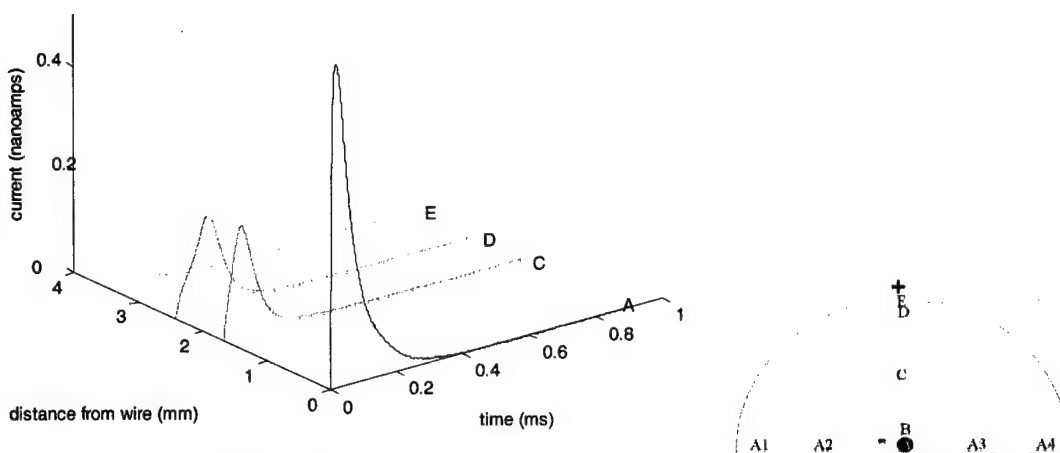


Figure 24. Collection wire at negative bias. A: laser hitting the collection wire; C: half way between the wire and cylinder; D: just missing the cylinder; E: hitting the cylinder. Indene (190 ppbv) in air.

Figure 26 and Figure 27 correspond to positions vertical to the ceramic plane with the collection wire at positive bias. Now the large photoemission peak should correspond to position E. In Figure 26 the peak for E must be dominated by the electrons photoemitted from the half-cylinder that presumably are captured by anions and drift to the collection wire. The fact that the peak for E is prompter than for A (see Figure 27) reinforces that it corresponds to current flowing through the circuit to make up the deficiency due to electrons leaving the cylinder. The spread out part of E may correspond to the anions reaching the collection wire. Since C is again faster than D, they correspond to the negative anions traveling to the collection wire. The prompt peak in A could correspond to photoelectrons being emitted by the scattered light hitting the cylinder and the tail by the negative ions traveling to the collection wire and/or positive ions traveling to the cylinder.

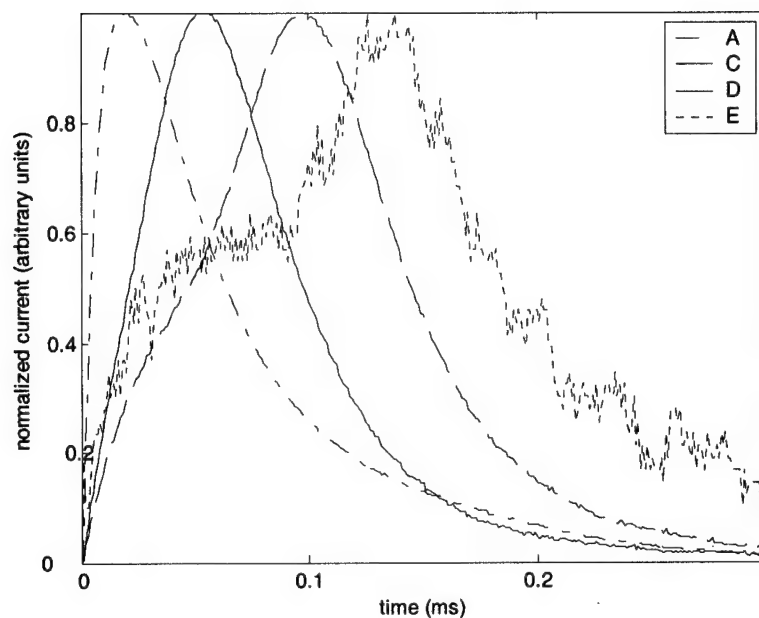


Figure 25. Collection wire at negative bias. A: laser hitting the collection wire; C: half way between the wire and cylinder; D: just missing the cylinder; E: hitting the cylinder. Waveforms normalized to maximum current.

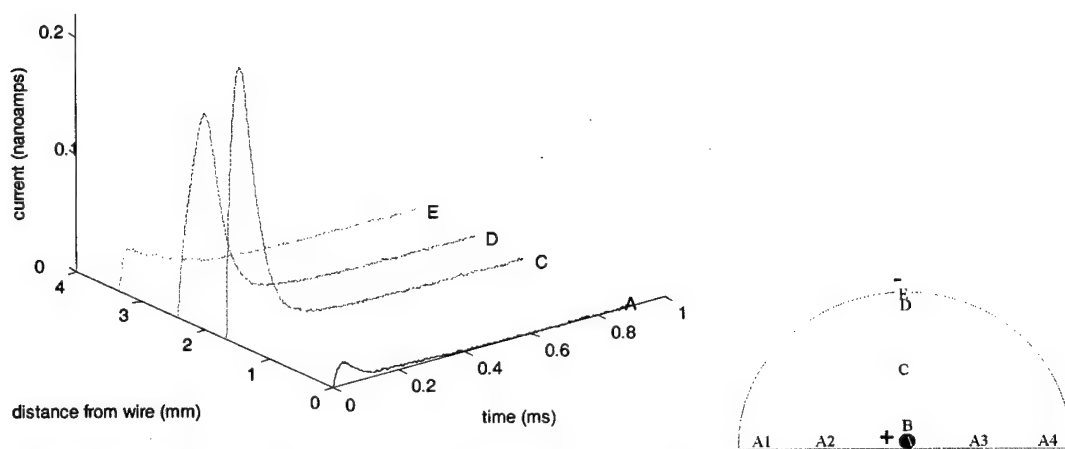


Figure 26. Collection wire at positive bias. A: laser hitting the collection wire; C: half way between the wire and cylinder; D: just missing the cylinder; E: hitting the cylinder. Indene (190 ppbv) in air.

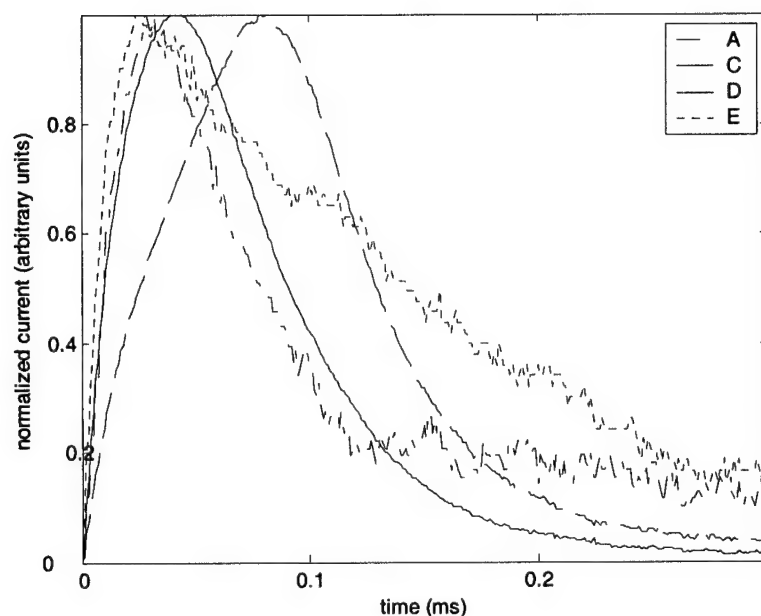


Figure 27. Collection wire at positive bias. A: laser hitting the collection wire; C: half way between the wire and cylinder; D: just missing the cylinder; E: hitting the cylinder. Waveforms are normalized.

Figure 28 and Figure 29 compare waveforms from Figure 24 and Figure 26 for the same position (C and D) with the bias reversed. These results are consistent with the cations traveling slower than the anions.

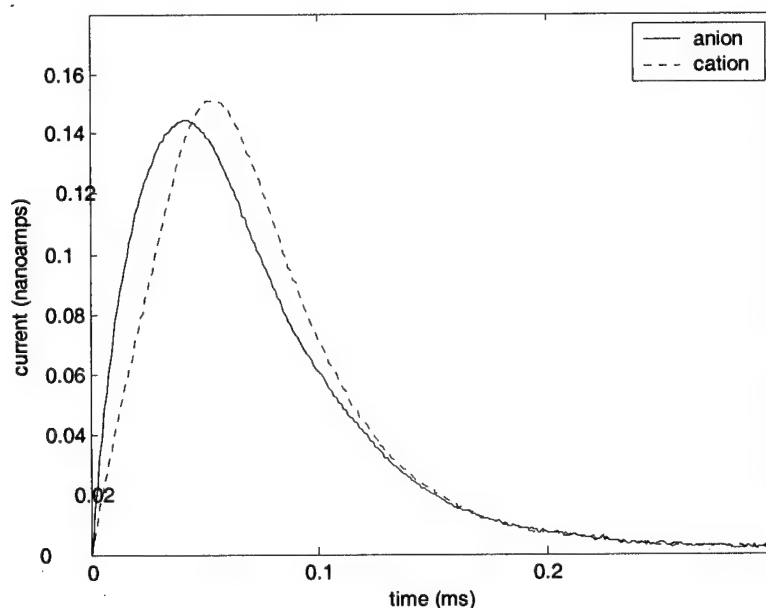


Figure 28. Position C half way between the wire and the cylinder. The dashed is the waveform for the collection wire negatively biased and solid line for the wire positively biased.

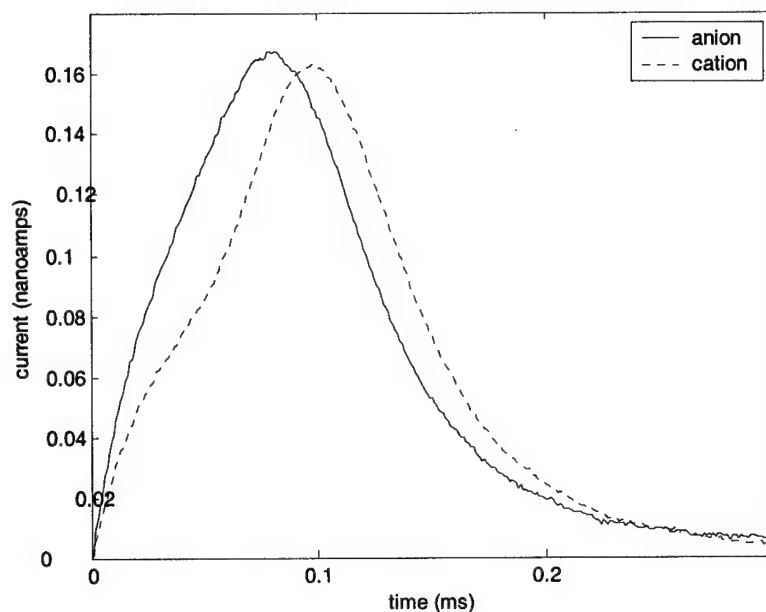


Figure 29. Position D just missing the cylinder. The dashed is the waveform for the collection wire negatively biased and solid line for the wire positively biased.

These results indicate that the preferred configuration for the detection of positively charged parent molecule ions generated by laser ionization is with the laser beam at position D just missing the positively charged cylinder. Scattered light striking the cylinder will not generate photo-emitted electrons and the collection wire presents a very small cross-section for absorbing scattered light. As indicated in Figure 30, the applied bias can be adjusted for the desired drift time for the peak. There is obviously a trade-off between increasing the drift time for better resolution and the spreading of the ion swarm.

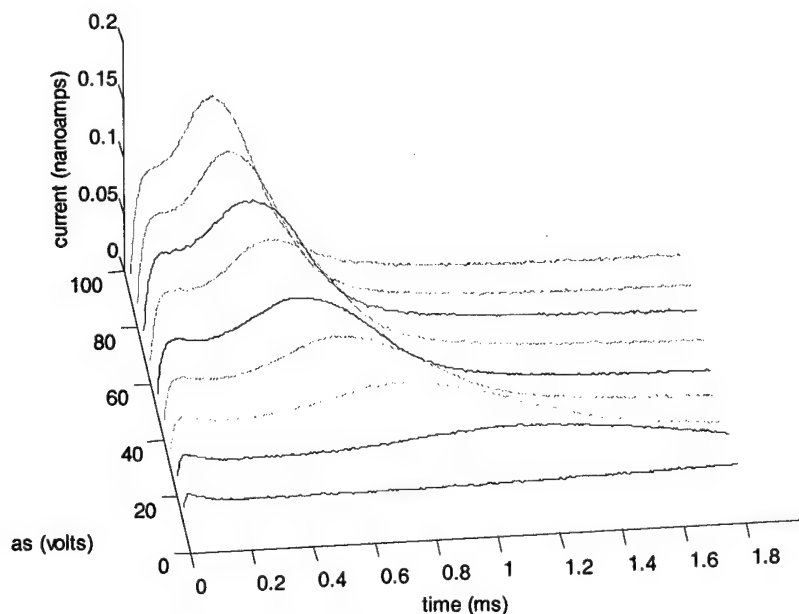


Figure 30. Collection wire at negative bias with laser beam at position D. Styrene (150 ppbv) in air.

The integrated area under the waveforms of Figure 30 yields the total collected ionization current and is given in Figure 31. The integrated charge for 10, 20 and 30 V biases is significantly decreased because part of the waveform was cut-off due to the storage oscilloscope time scale setting. Otherwise, there is little difference in collection efficiency for the different biases.

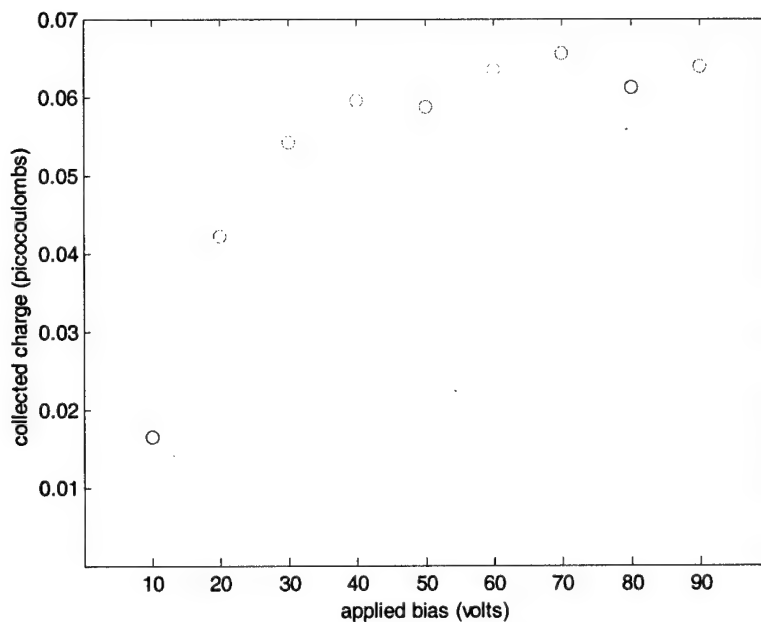


Figure 31. Collection wire at negative bias with laser beam at position D. Styrene (150 ppbv) in air.

Because this detector configuration has high potential for a selective gas chromatograph detector, it was evaluated for the possible carrier gases nitrogen, P-5 (5% methane in argon), and argon.

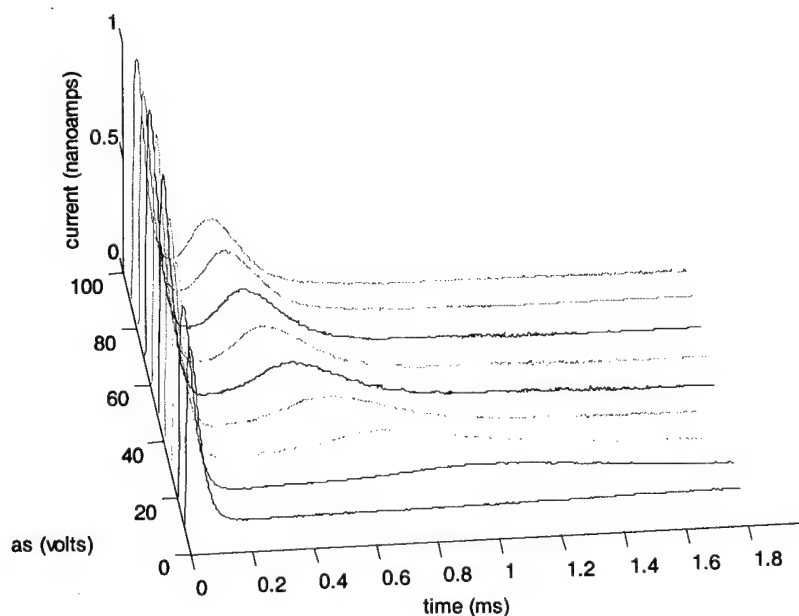


Figure 32. Collection wire at negative bias with laser beam at position D. Styrene (150 ppbv) in nitrogen.

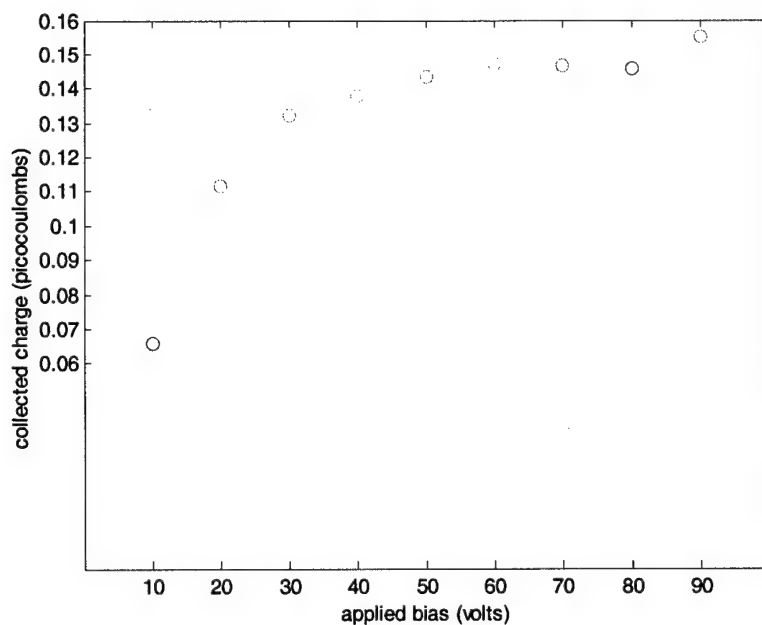


Figure 33. Collection wire at negative bias with laser beam at position D. Styrene (150 ppbv) in nitrogen.

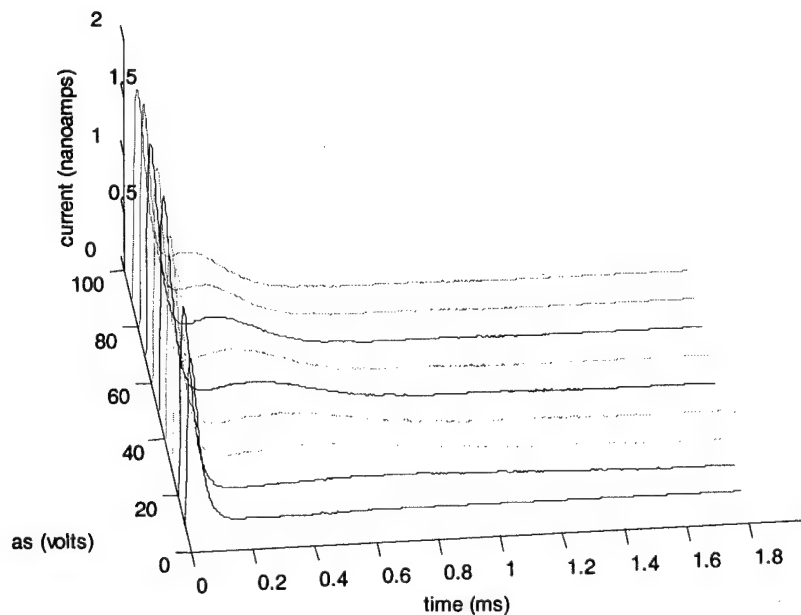


Figure 34. Collection wire at negative bias with laser beam at position D. Styrene (150 ppbv) in P-5 (5% methane in argon).

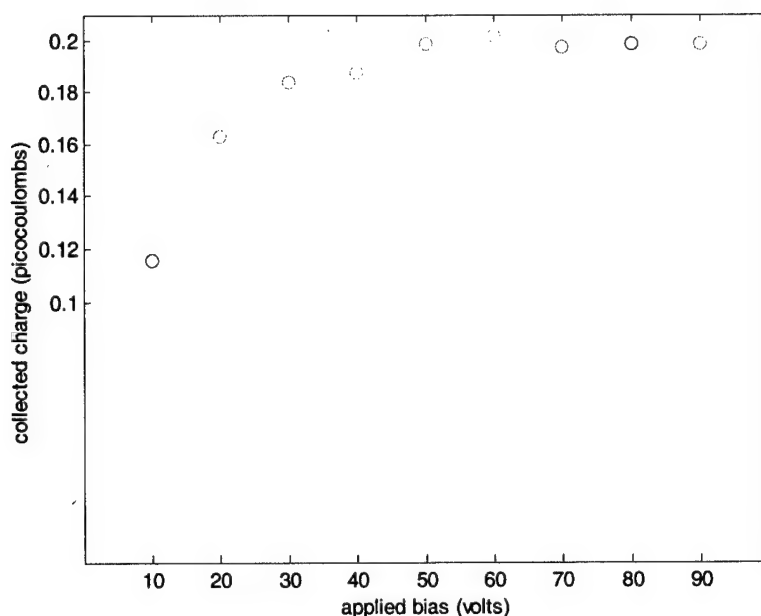


Figure 35. Collection wire at negative bias with laser beam at position D. Styrene (150 ppbv) in P-5 (5% methane in argon).

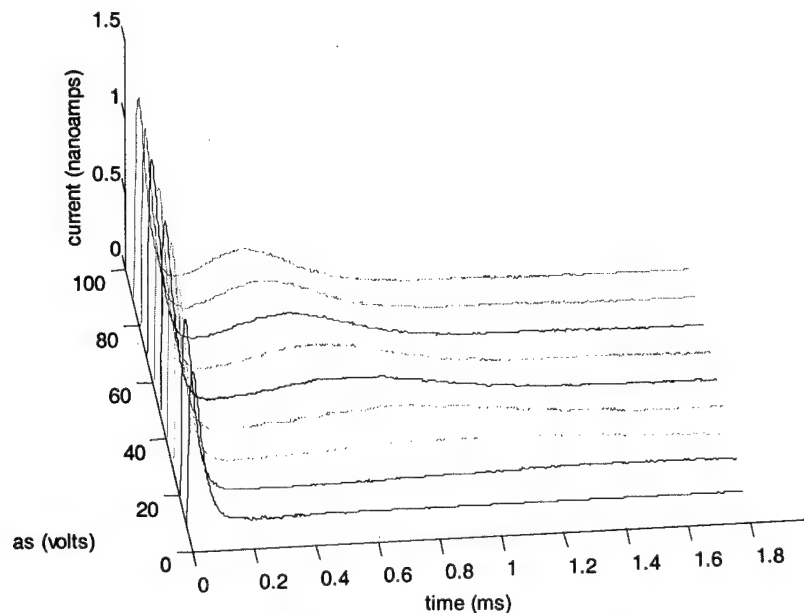


Figure 36. Collection wire at negative bias with laser beam at position D. Styrene (150 ppbv) in argon.

As is obvious from these results, the novel hemispherical detector with the ionizing laser beam passing near the half-cylinder anode provides a number of advantages. The photoelectric effect due to scattered light being absorbed by the negative electrode is essentially eliminated. The sample volume can be minimized while still generating a peaked induced ion current that will be ideal for lock-in or sample-and-hold detection. The hemisphere can be made larger if longer drift times are desired to provide low resolution speciation by ion mobility. The cylinder on ceramic design is also easy to fabricate.



### SECTION III LID AROMATIC SPECTRA

#### A. BACKGROUND

Substantial progress was achieved during previous research including LID spectra of aniline, styrene, (Swenson, 1996) acetaldehyde (Swenson, 1999) and benzene, toluene, ethylbenzene, and xylenes (BTEX) (Gillispie, 1999, Swenson, 1996, 1998) at the  $<1$  ppbv level via 1+1 resonance-enhanced multiphoton ionization in atmospheric pressure room air. There are many different gas phase species that could be detected by LID, and the need exists to identify the most appropriate target species, the optimal spectral ranges, and possible interferences. The focus of this segment of the effort was to increase the database of ambient pressure LID spectra for the polycyclic aromatic hydrocarbons EPA priority pollutants. The main thrust ended up being a high resolution study of indene (Lucci, 1999) as a Chemistry Department thesis that is at Attachment B. The experimental setup and procedures are detailed in Attachment B.

#### B. SUMMARY OF RESULTS

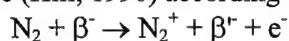
Max Lucci's results on indene were presented at Photonics East (Lucci, 1999) as well as his thesis at Attachment B. This work demonstrated that very narrow features can be seen for molecules as large as indene even at room temperature under ambient pressure conditions. The narrowness of these features means that on- and off-resonance measurements to separate out background LID signals are very feasible for real-time analysis of aromatic hydrocarbons in air.

## SECTION IV LID ION MOBILITY SPECTROMETRY

### A. BACKGROUND

Since the temporal waveforms that we obtain in our ambient pressure LID detection provide an ion mobility spectrum, this opens a new avenue for ion speciation. We are aware of three groups (Gormally, 1991, Kolaitis, 1986, Clark, 1995) that have published laser MPI coupled with a conventional ion mobility drift tube (ca. 14 cm drift region vs. 1 cm in our parallel plate LID cell). These groups have used single wavelength nonresonant MPI, typically the fourth harmonic of Nd:YAG at 266 nm. Both room temperature LID and IMS give low resolution speciation when compared to techniques such as high vacuum jet expansion LID mass spectrometry. However, by acquiring both LID and IMS data simultaneously and applying multivariate analysis of the multimode data, very high resolution speciation should be attainable. At the same time, the convenience of ambient pressure, real-time acquisition is possible with much higher sensitivity since the sample is not diluted by introducing it into a high vacuum.

In the conventional IMS, the beta particle ( $\beta^-$ ) emitted from a radioactive  $^{63}\text{Ni}$  foil is used as the ionization source (Hill, 1990) according to the process:



where  $\beta^-$  is a beta particle that has lost some of its initial energy. The  $\text{N}_2^+$  ion begins a series of ion-molecule reactions with trace amounts of  $\text{H}_2\text{O}$ ,  $\text{NH}_3$ ,  $\text{NO}$ , and the target analyte. These reactant ions undergo further ion-molecule reactions with neutral gas-phase analytes to produce the analyte product ions of interest. Similarly, the thermal electrons,  $\text{e}^-$ , are captured by  $\text{O}_2$  and result in the negative reactant clusters,  $(\text{H}_2\text{O})_n\text{O}_2^-$  or  $(\text{H}_2\text{O})_n(\text{CO}_2)_m\text{O}_2^-$  and negative analyte product ions are produced by ion-molecule reactions. The ions are accelerated by an electric field and quickly come to an average ion velocity due to collisions with the drift gas molecules. Each ion will have a unique average velocity characterized by its reduced mobility. The drift time to reach the collector electrode is inversely proportional to the reduced mobility of the ion and the ratio of its drift time to the drift time of a calibrant gas is used to identify the analyte.

Since the radioactive source continuously generates ions, an electronic grid gate shutter must be used at the inlet of the drift tube in order to time the travel of the ions down the drift tube. This adds electronics and a large number of ions are lost in traveling through the grid shutter. These problems are eliminated by LID. In addition, LID adds wavelength speciation to produce two-dimensional data (wavelength and ion mobility). The LID elimination of the radioactive ionization source normally used with conventional IMS and with it the nuclear regulatory requirements alone justifies pursuing this nonradioactive source. We demonstrated the feasibility of this approach by generating two-dimensional data for a number of aromatic species.

### B. TWO-DIMENSIONAL LASER IONIZATION DATA

Our parallel plate LID cell was modified by adding a drift tube consisting of five rings from a Camac IMS with a gold plated grid in front of the collector plate as shown in Figure 37. The separation between the drift-tube rings and between the repeller and first ring and the last ring and the grid was approximately 8 mm. The ionizing laser beam was passed parallel to the positive repeller electrode. The LI-IMS was operated at room temperature and atmospheric pressure. Analyte headspace was injected into a 5 L flask of atmospheric pressure air and circulated through the ionization cell. A Nd:YAG pumped dye laser operating at 50 Hz was scanned to selectively ionize the analyte molecules. The positive ions drift through the tube to the collector electrode. After they pass through the aperture grid they induce a current to flow between the aperture grid and collector electrode. Because this is a narrow gap, a sharp (relative to parallel plate waveforms) induced current peak is produced. Both the current intensity and time relative to the laser pulse are recorded. These waveforms were then corrected for variations in laser pulse energy and are plotted versus wavelength and drift time.

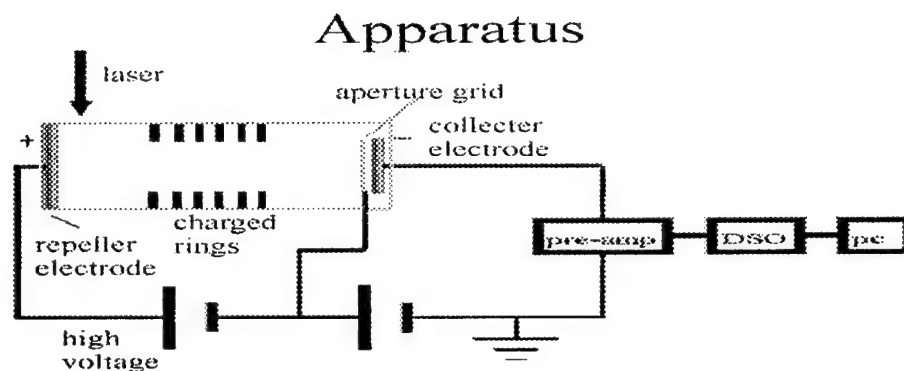


Figure 37. LI-IMS schematic.

Since the drift time is determined by the applied bias, the LI-IMS response to varying total applied biases was established. The drift tube rings were connected by  $300\text{ k}\Omega$  resistors. A lower applied bias results in longer drift times and greater separation between ions with different mobilities but also results in spreading of the ion swarm. The results in Figure 38 were recorded with  $100\text{ ppbv}$  styrene in air with a laser wavelength of  $287.75\text{ nm}$ . The potential between the aperture grid and the collector electrode was held at  $350\text{ V}$  by varying the resistance between the grid and ground as the total potential across the rings was varied from  $2000\text{ V}$  to  $1300\text{ V}$ , decreasing by increments of  $100\text{ V}$ . The total charge collected was determined by integrating the area under the waveforms of Figure 38 and the results are presented in Figure 39. A bias of  $1600\text{ V}$  was selected and maintained between the repeller and grid ( $4.8\text{ cm}$  separation) producing an average drift region electric field of  $333\text{ V/cm}$  for all measurements reported below. A bias of  $350\text{ V}$  was maintained between the grid and collector corresponding to approximately a  $3500\text{ V/cm}$  electric field.

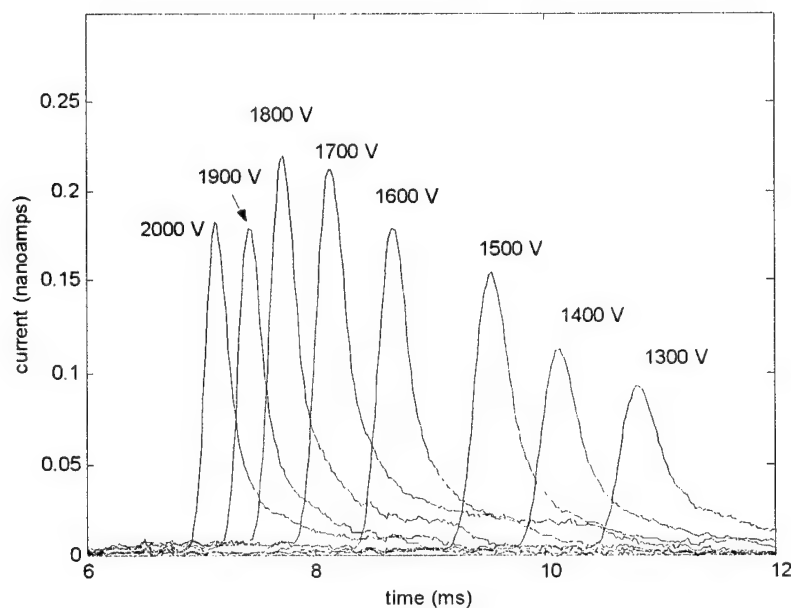


Figure 38. LI-IMS waveforms for different applied biases in the drift region.

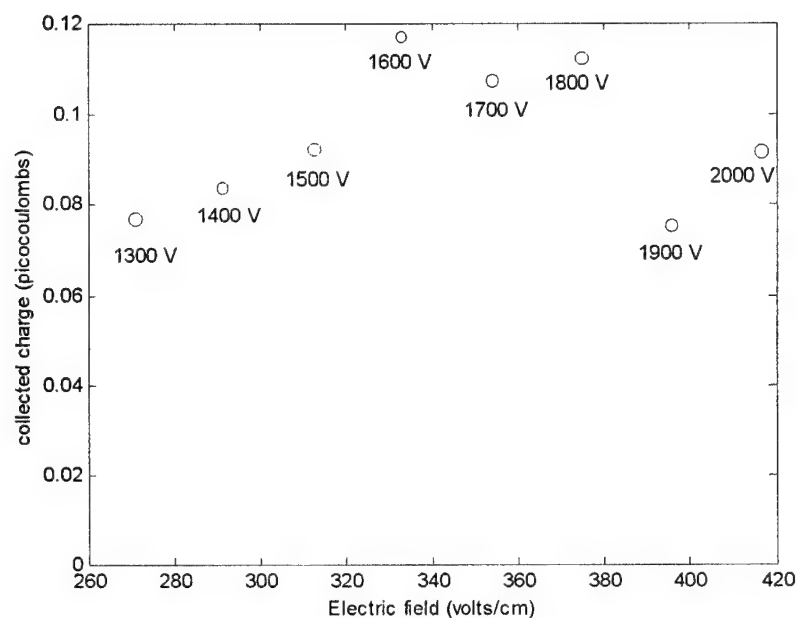


Figure 39. Total charge collected versus drift electric field.

We generated two-dimensional plots (drift time vs ionization wavelength) for styrene in Figure 40 and aniline in Figure 41. These 2-D plots represent a unique fingerprint that can identify the presence of the molecule. The signatures of styrene and aniline are clearly identified in the 2-D plot for a mixture of 30 ppbv aniline and 100 ppbv styrene in Figure 42. The drift times have shifted between measurements probably because the laser beam was not located in an identical position. The measurements were made on separate days and the cell removed to bake it out between measurements.

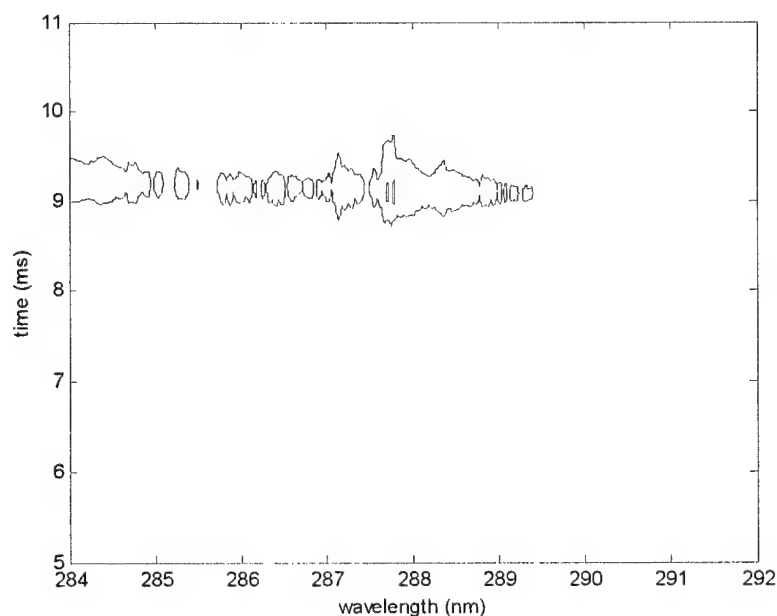


Figure 40. Two-dimensional LI-IMS plot for 100 ppbv styrene in air.

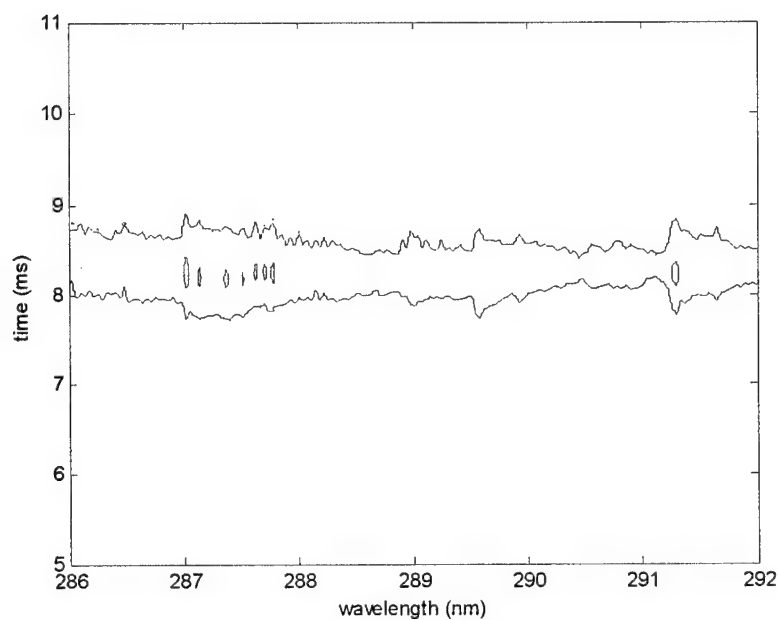


Figure 41. Two-dimensional LI-IMS plot for 20 ppbv aniline in air.

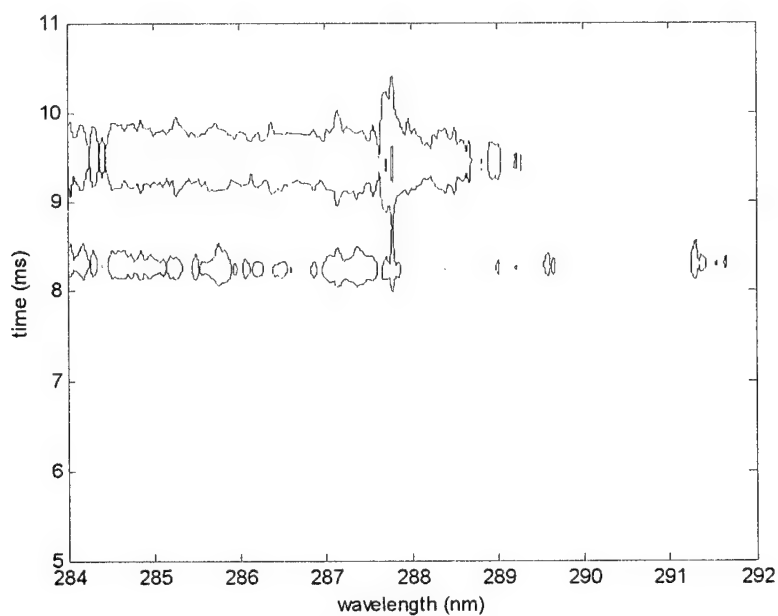


Figure 42. Two-dimensional LI-IMS plot for 30 ppbv aniline and 100 ppbv styrene in air.

Similarly two-dimensional data were obtained for methylnaphthalene in Figure 43 and naphthalene in Figure 44. While they have similar mobilities and very broad absorption spectra, the two can easily be distinguished in a mixture shown in Figure 45.

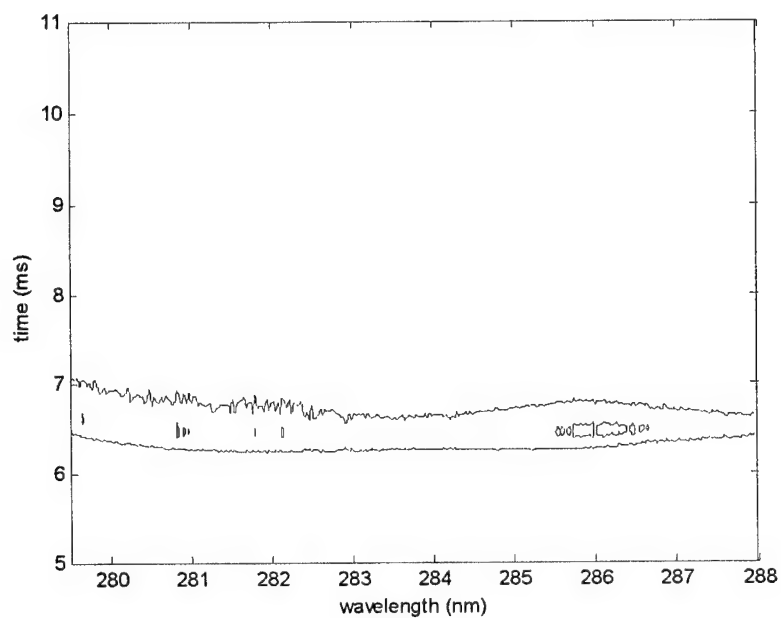


Figure 43. Two-dimensional LI-IMS plot for 1 ppbv methylanthalene in air.

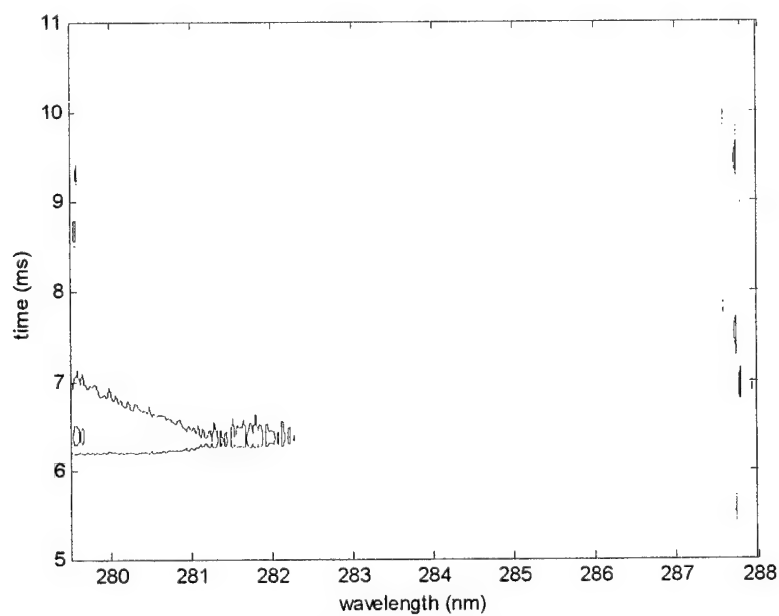


Figure 44. Two-dimensional LI-IMS plot for 13 ppbv naphthalene

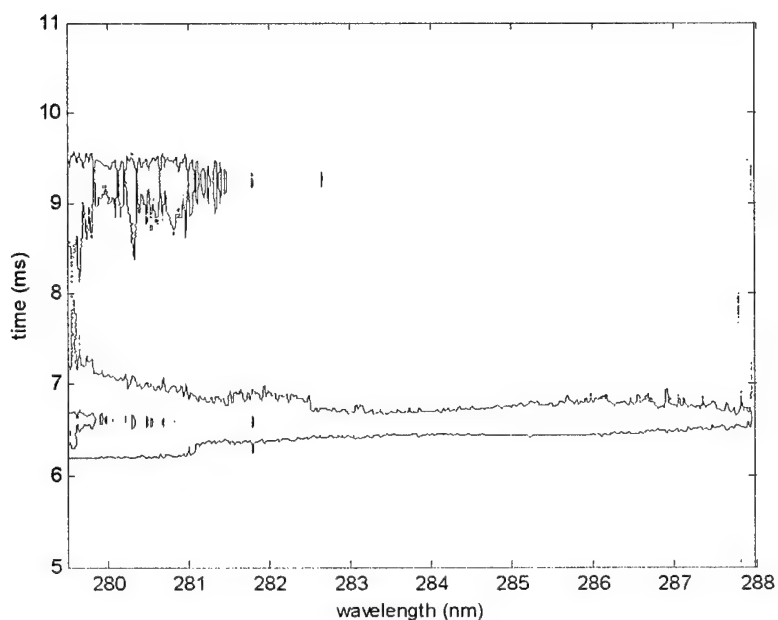


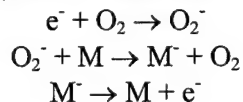
Figure 45. Two-dimensional LI-IMS plot for 9.0 ppbv naphthalene and 0.73 ppbv methylnaphthalene.

These preliminary results demonstrate the excellent potential for two-dimensional (drift time versus ionization wavelength) diagnostics for the identification of aromatics in ambient air. A number of improvements are required in the device. A counter-flowing dry air or nitrogen drift region similar to those in a commercial IMS is needed and the device should be bakeable in situ to remove adsorbed analytes. Apertures or other techniques need to be incorporated to insure that the laser beam location is identical. Finally, chemometric analysis needs to be developed to identify molecules in complex mixtures.

## SECTION V PHOTOEMISSIVE ION MOBILITY SPECTROMETRY

### A. BACKGROUND

The use of photoemitted electrons from thin metallic films exposed to ultraviolet light as the source of thermal electrons in an electron-capture detector, eliminating the need for the radioactive  $^{63}\text{Ni}$  emitter was previously reported (Simmonds, 1987). Besides the elimination of the regulatory requirement of the radioactive source, a number of benefits are reaped by using photoemitted electrons: part of the current measured in conventional IMS is due to the migration of positive ions to the anode and this complication is eliminated by eliminating the positive ions; elimination of the positive ions prevents the large electron-positive ion recombination in the reaction region; and the chemical processes within the detection cell are simplified considerably if positive ions are absent making interpretation of the measured signal more straightforward. In air, the photoemitted electrons start with a maximum energy of only 0.4 eV and very rapidly acquire a mean electronic energy at 293 K equal or close to  $3/2 kT$  (0.037 eV). Consequently, no positive ions or energized radicals are produced. Simmonds et al. subsequently extended the photoemissive electron concept to ion mobility detectors (Begley, 1991). In addition to the ECD benefits, the ion mobility spectrometer shutter grid at the entrance of the drift tube and its associated gating electronics are eliminated. In their design, they used a fused silica window with a thin gold layer with a work function of *ca.* 4.5 eV as the photoemissive source. The ultraviolet light from a pulsed xenon lamp placed on the other side of the window generates thermal electrons,  $e^-$ , by the photoelectric effect. Since the electrons are generated as a pulse, the starting grid shutter is eliminated. With air as the sample and drift gas, the photoemissive electron IMS performed comparable to a conventional radioactive  $^{63}\text{Ni}$  emitter IMS. In air, the thermal electrons will travel only *ca.*  $1.2 \times 10^{-2}$  cm before conversion to an  $\text{O}_2^-$  reactant ion. The target compound M is ionized by the following system of reactions:



They found that where oxygen is present, the ion mobility resolution is effectively unchanged at oxygen concentrations in excess of 6% and decreases as the oxygen content is decreased due to free electrons traveling further distances before being attached to oxygen. The photoemissive IMS was demonstrated for acetylacetone, benzoylacetone and benzoquinone.

Alastair Clark et al. (Clark, 1995) have demonstrated the electron capture-IMS approach using LID instead of the photoelectric effect to produce the free electrons. They showed that the LID IMS spectra was very similar to the  $^{63}\text{Ni}$  IMS spectra for 2,4-DNT, 2,4,6-TNT, PETN, and RDX but with slightly poorer resolution. The emphasis of their approach appears to have been to use the photo-dissociation/fragmentation of the explosive molecules and subsequent LID ionization of NO in the 225-227 nm range; however, no signals in addition to the background signal were observed in the positive ion mode for the explosives. They then tried the negative ion mode using a rather inefficient means to generate electrons, namely three-photon LID of  $\text{O}_2$  at 225.0 nm, that produces both positive oxygen ions and low energy electrons. The free electrons attached to neutral oxygen molecules producing  $\text{O}_2^-$  that subsequently reacted with the explosives in the manner in which we are proposing. Our photo-emissive approach produces copious numbers of electrons compared to the number they could produce via LID. Also their work was done in a conventional IMS with the LID ionization occurring 4 mm from the ion gate in a region of variable electric field. In our photoemissive approach we create the anions in the plane of the thin film coating in very large numbers without the electronic shutter grid losses, which is expected to result in higher resolution than the conventional IMS.



Our PE-IMS methodology has evolved from ground-breaking results (Swenson, 1996, Swenson, Nov 1996) on the detection of organics in air with resonance enhanced multiphoton ionization (LID) under atmospheric pressure. Because the LID process of interest to us occurs under ambient conditions, the ions thus created diffuse through the air rather than traveling by free flight in a vacuum, as is the case for time-of-flight instruments. The electrons attach to the oxygen that is abundantly present in the cell and form  $O_2^-$ , which can further react with atmospheric constituents to form clusters of the peroxide anion with water and carbon dioxide (Eiceman, 1994). All of these anions are collected at the positive electrode after diffusing through the air, in contrast to the free electrons collected in the early MPI cell experiments reported in the literature. As in a conventional IMS, the time interval for the ion to reach the collector is inversely proportional to its ion mobility, that can be related to a more fundamental parameter, the reduced mobility. Ion mobility spectrometers using a radioactive ionization source are used extensively for detecting explosives using the negative ion mode. Because the reaction region and the positive ions are eliminated in our scheme as well as the large losses to ion shutters, we should ultimately attain higher sensitivity.

## B. SUMMARY OF RESULTS

Christopher Wall's results on PE-ECD were presented at Photonics East (Walls, 1999) as well as in his draft thesis at Attachment C. Results of complementary work will be reported under Strategic Environmental Research and Development Program (SERDP) subcontract SC-98C6009 to Dakota Technologies, Inc.

## REFERENCES

- Begley, P., Corbin, R., Foulger, B. E., and Simmonds, P. G., "Photoemissive ionisation source for ion mobility detectors," *J. Chromat.*, **588**, 239-249 (1991).
- Clark, Alastair, Robert M. Deas, Constaninos Kosmidis, Kenneth W. D. Ledingham, Archibald Marshall and Ravi P. Singhal, "Explosives vapour identification in ion mobility spectrometry using a tunable laser ionisation source: a comparison with conventional  $^{63}\text{Ni}$  ionisation," *Proceedings of the 6th International Symposium on Advanced Nuclear Energy Research: innovative laser technologies in nuclear energy*, pp 521-529, Japan Atomic Energy Research Institute (1995).
- Eiceman, Gary A. and Zeev Karpas, *Ion Mobility Spectrometry*, CRC Press, Boca Raton, 1994.
- Gillispie, G. D., M. R. Lucci, O. F. Swenson, and J. L. Klingfus, "Compound identification in multicomponent mixtures via REMPI at ambient conditions," *Solid State Lasers VIII*, Richard Scheps, ed. SPIE Vol. 3613, pp. 75-82 (1999).
- Gormally, John and Julie Phillips, "The performance of an ion mobility spectrometer for use with laser ionization," *Int. J. of Mass Spectr. and Ion Processes*, **107**, 441-451 (1991).
- Hill, Herbert H., Jr., William F. Siems, Robert H. St. Louis, and Dennis G. McMinn, "Ion Mobility Spectrometry," *Anal. Chem.*, **62**, 1201A-1209A (1990).
- Kolaitis, Leonidas and David M. Lubman, "Atmospheric pressure ionization mass spectrometry with laser-produced ions," *Anal. Chem.*, **58**, 1993-2001 (1986).
- Logothetis, E. M. and P. L. Hartman, "Three-photon photoelectric effect in gold," *Phys. Rev. Lett.* **18**, 581-583 (1967).
- Lubman, David M. and Mel N. Kronick, "Wavelength-selective ionization of organic compounds in an ion mobility spectrometer," *Anal. Chem.*, **55**, 867-873 (1983).
- Lucci, M. R., O. F. Swenson, and G. D. Gillispie, "Chemical Vapor Detection in Ambient Air via REMPI," *Electro-Optic, Integrated Optic, and Electronic Technologies for On-Line Chemical Process Monitoring*, M Fallahi, R J Nordstrom, T R Todd, eds. SPIE Vol. 3537, pp. 150-157 (1999).
- Ogawa, Teiichiro, To-oru Yasuda, and Hirofumi Kawazumi, "Laser Two-Photon Ionization Detection of Aromatic Molecules on a Metal Surface in Ambient Air," *Anal. Chem.*, **64**, 2787-2796 (1992).
- Schechter, Israel, Hartmut Schroder, and Karl L. Kompa, "Quantitative Laser Mass Analysis by Time Resolution of the Ion-Induced Voltage in Multiphoton Ionization Processes," *Anal. Chem.*, **64**, 2787-2796 (1992).
- Simmonds, P. G., "Electron-Capture Detector with a Photoemissive Electron Source," *J. Chromat.*, **399**, 149-164 (1987).
- Smith, R. L., "Two-Photon Photoelectric Effect," *Physical Review*, **128**, 2225-2229 (1962).

Swenson, O. F., G. D. Gillispie, and C. J. Walls, "Detection of Organic Compounds by Ambient Pressure MPI," *Trends in Optics and Photonics Series (TOPS), Volume 8, Environmental Monitoring and Instrumentation*, pp.20-24, Optical Society of America (1996).

Swenson, O. F., G. D. Gillispie, W. F. Cooper, and M. A. Dvorak, "Real-Time Detection of Volatile Aromatic Hydrocarbons in Groundwater and Soil," *Trends in Optics and Photonics Series (TOPS), Volume 8, Environmental Monitoring and Instrumentation*, Optical Society of America (1996).

Swenson, O. F., and G. D. Gillispie, "REMPI detection of volatile aromatic hydrocarbons in ambient air," *Advanced Technologies for Environmental Monitoring and Remediation*, T. Vo-Dinh ed., SPIE Vol. 2835, pp. 144-152 (Nov 1996).

Swenson, O. F., J. P. Carriere, H. Isensee, G. D. Gillispie, W. F. Cooper, M. A. Dvorak, "Real-time monitoring of BTEX in air via ambient-pressure MPI," *Methods for Ultrasensitive Detection*, Bryan L. Fearey, ed. SPIE Vol. 3270, pp.216-225 (1998).

Swenson, O. F., J. A. Williams, R. Wells, T. Tipton, S. Baxley, and S. Markgraf, "Ambient pressure REMPI monitoring of acetaldehyde production during the breakdown of ethyl-3-ethoxypropionate (EEP)," *Advanced Sensors and Monitors for Process Industries and the Environment*, W A de Groot, ed. SPIE Vol. 3535, pp 244-252 (1999).

Teich, M. C., J. M. Schroeer, and G. J. Wolga, "Double-Quantum Photoelectric Emission from Sodium Metal," *Phys. Rev. Lett.*, **13**, 611-614 (1964).

Walls, C. J., O. F. Swenson, and G. D. Gillispie, "Real-time monitoring of chlorinated aliphatic compounds in air using ion mobility spectrometry with photoemissive electron sources," T Vo-Dinh, R L Spellicy, eds. SPIE Vol. 3534, pp. 290-298 (1999).

## APPENDIX A

MODELING OF ION DRIFT IN AN APPLIED ELECTRIC  
FIELD IN AMBIENT PRESSURE AIR  
FOR LASER IONIZATION  
DETECTION APPLICATIONS

A Thesis  
Submitted to the Graduate Faculty  
of the  
North Dakota State University  
of Agriculture and Applied Science

By  
Feng Hong

In Partial Fulfillment of the Requirements  
for the Degree of  
MASTER OF SCIENCE

Major Department:  
Physics

July 2001

Fargo, North Dakota

**North Dakota State University**  
**Graduate School**

---

**Title**

MODELING OF ION DRIFT IN AN APPLIED ELECTRIC  
FIELD IN AMBIENT PRESSURE AIR  
FOR LASER IONIZATION  
DETECTION APPLICATIONS

**By**

Feng Hong

The Supervisory Committee certifies that this **disquisition** complies with North Dakota State University's regulations and meets the accepted standards for the degree of

**MASTER OF SCIENCE**

**SUPERVISORY COMMITTEE:**

Dr. Orven F. Swenson

Chair

Dr. Douglas Kurtze

Dr. Richard Hammond

Dr. Wayne Reitz

Dr. William Slanger

Approved by Department Chair:

Date

Signature

## ABSTRACT

Hong, Feng, M.S., Department of Physics, College of Science and Mathematics, North Dakota State University, July 2001. Modeling of Ion Drift in an Applied Electric Field in Ambient Pressure Air for Laser Ionization Detection Applications. Major Professor: Dr. Orven F. Swenson.

A numerical model that describes the behavior of laser-produced ions in an applied electric field and the subsequent induced current flow in an external circuit between the biased electrodes was developed. The numerical solutions provide a picture of the laser-generated charge distribution moving between the parallel plate or cylindrical electrodes as well as the measured induced current behavior with time. First, a numerical model was established to describe the distribution and dynamics of positive and negative ions between parallel plate or cylindrical electrodes. The model was simplified by considering an ideal situation of a low pressure reduced electric field ( $E/P$ ) between infinite electrode configurations, neglecting the influence of the electric field created by the charged particles in the ion swarm itself and the ion diffusion current contribution; however, it showed good agreement with experimental results.

## ACKNOWLEDGMENTS

I would like to thank my adviser, Orven F. Swenson for supervising this research. Although studying and doing research was hard work, it was very pleasant because I felt Dr. Swenson's respect and belief in me as a future scientist. I appreciate the many ideas and suggestions he made with respect to the research constituting this thesis. I am really amazed with his detail as well as ability of organization, and I really tried to learn to be like him. Dr. Orven Swenson has taught me to search for an understanding of the physical concepts behind the experiments, and has given me constant guidance and encouragement.

I would like to express special gratitude to Dr. Kurtze for many extremely useful discussions and guiding suggestions related to this research, and for his devotion to teaching and doing research together with the students. I am very grateful to Dr. Richard Hammond for help in my work and studies at NDSU.

My special thanks to Atkins Scott, Terry Pilling, and Chris Walls, graduate students of the Physics and the Chemistry Departments, for discussions and help on various topics. I am grateful also to Mrs. Patty Hartsoch, who is the secretary in the Physics Department, for making my life as a student easier. Thanks also to the faculty, staff, and graduate students of the Physics Department for assistance.

Above all, I would like to thank my wife and my daughter, Yimei Zhu and Hong Hong, for coming with me to the United States and being by my side during all joys and troubles; and my father and mother who brought me up with a love for science.

Finally, I acknowledge The Air Force Research Laboratory for its financial support.



## TABLE OF CONTENTS

ABSTRACT.....	iii
ACKNOWLEDGMENTS.....	iv
LIST OF FIGURES.....	vii
1. INTRODUCTION.....	1
1.1. Laser Ionization Detection (LID) Instrumentation.....	1
1.2. Background.....	2
2. NUMERICAL MODELING FOR PARALLEL CONFIGURATION.....	6
2.1. The Reduction of Three Dimensions to One.....	7
2.2. Influence of an Applied Field on Laser-Induced Ions.....	7
2.3. Effect of Laser-Produced Ions on the Field and the External Circuit.....	10
2.4. Numerical Modeling.....	13
2.5. Analytical vs Numerical Results.....	25
2.6. Comparison of Numerical Results to Experimental Waveforms.....	31
3. NUMERICAL MODELING FOR CYLINDER.....	33
3.1. Electric Field.....	34
3.2. Continuity and Diffusion Equation.....	37
3.3. Positive and Negative Ion Profiles for Laser-Produced Charges.....	38
3.4. The Current Induced by Laser-Produced Charges.....	42
3.5. Comparison of Numerical Results to Experimental Waveforms.....	50

4. DISCUSSION AND CONCLUSION.....	60
4.1. Discussion.....	60
4.2. Conclusion.....	63
REFERENCES CITED.....	65
APPENDIX A. ANALYTICAL SOLUTIONS OF EQS. 2.16 AND 2.17.....	67
APPENDIX B. NUMERICAL SOLUTIONS OF EQS. 2.16 AND 2.17.....	71
B.1. Consistency.....	71
APPENDIX C. SOURCE CODE FOR PARALLEL PLATES.....	74
C.1. Code Written in C++.....	74
C.2. Code Written in Matlab.....	79
APPENDIX D. SOURCE CODE FOR CYLINDRICAL PLATES.....	83
APPENDIX E. INDUCED CHARGES ON PARALLEL PLATES.....	99
E.1. Green Reciprocity Theorem.....	99
E.2. Induced Charges.....	100

## LIST OF FIGURES

<u>Figure</u>	<u>Page</u>
1.1. Schematic of experimental apparatus.....	2
1.2. Positive ions drift to the cathode while negative ions move toward the anode, inducing the current in the external circuit.....	4
2.1. A cross section of the three-dimensional parallel plate electrodes.....	8
2.2. A schematic diagram that illustrates the flow of current in the external circuit connecting two parallel plate electrodes when a charge is caused to move in a direction perpendicular to the planes.....	11
2.3. The image charge model for charge induction.....	12
2.4. The time evolution of the positive and negative ion distributions.....	15
2.5. The time evolution of three current profiles induced by the positive ions, the negative ions, and both of them at the laser positions of 0.202 cm and 0.404 cm.....	18
2.6. The time evolution of three current profiles induced by the positive ions, the negative ions, and both of them at the laser positions of 0.505 cm and 0.606 cm.....	19
2.7. The finite difference grid in the solution region.....	20
2.8. The time evolution of the positive and negative ion distributions computed numerically.....	23
2.9. Total induced currents computed analytically and numerically with voltage 300 V for the initial laser position of 0.202 cm and 0.404 cm.....	26
2.10. Total induced currents computed analytically and numerically with voltage 300 V for the initial laser position of 0.505 cm and 0.606 cm.....	27
2.11. The current induced by the positive ions changes with the positive ion mobility in the top figure.....	28

2.12. The current induced by the positive ions changes with the diffusion coefficient for positive ions in the top figure.....	29
2.13. The total ion current changes with the laser width at the laser position of 0.505 cm with voltage 300 V.....	30
2.14. Total induced currents computed numerically and measured at ambient pressure with voltage 300 V for the initial laser position of 0.202 cm and 0.404 cm.....	31
2.15. Total induced currents computed numerically and measured at ambient pressure with voltage 300 V for the initial laser position of 0.505 cm and 0.606 cm.....	32
3.1. Cylindrical configuration.....	33
3.2. A cross-section of the three-dimensional geometry.....	34
3.3. A cross-section of a coaxial cylindrical electrode.....	36
3.4. A cross-section of the three-dimensional geometry.....	39
3.5. Distribution of the electric fields and the potentials.....	44
3.6. The positive ion and negative ion currents computed numerically at initial laser position of 1 mm are shown in the top figure.....	51
3.7. The positive ion and negative ion currents computed numerically at initial laser position of 2 mm are shown in the top figure.....	53
3.8. The positive ion and negative ion currents computed numerically at initial laser position of 3 mm are shown in the top figure.....	54
3.9. The positive ion and negative ion currents computed numerically at initial laser position of 4 mm are shown in the top figure.....	55
3.10. The positive ion and negative ion currents computed numerically at initial laser position of 4.5 mm are shown in the top figure.....	56
3.11. Same as Figure 3.7 showing the influence of choosing different diffusion coefficients on the induced current.....	57
3.12. Same as Figure 3.7 showing the influence of choosing different mobilities on the induced current.....	57
3.13. The influence of choosing different laser widths on the induced current.....	58

4.1. This figure compares the total induced current calculated numerically to that measured at ambient pressure with a 300 V bias for the initial laser position of 5.05 mm.....	62
E.1. Two situations.....	101

# CHAPTER 1

## INTRODUCTION

Gaseous trace components play important roles in a variety of chemical and physical processes. In terms of environmental concerns, it is important to describe and understand the production, transport, transformation, and removal of substances from the atmosphere.<sup>1</sup> In the *Laser Ionization Detection (LID)* technique,<sup>2</sup> an electric field is applied across the volume of interaction to separate the charges created by laser illumination. The current induced by these moving charges can then be efficiently detected electronically. This thesis focuses on investigating the behavior of the laser-produced ions in atmospheric pressure air in an applied electric field and the subsequent induced current flow in an external circuit between the biased electrodes. The numerical solutions provide a “motion picture” of the laser-generated charge distribution moving between both parallel and cylindrical plates as well as the measured induced current behavior with time.

### 1.1. Laser Ionization Detection (LID) Instrumentation

The LID instrumentation shown in Figure 1.1. is very simple.<sup>1</sup> An LID waveform is generated by measuring the current induced by the laser-produced charged particles in the space between the electrodes. The current waveforms were acquired using the LID cell configured either with parallel copper electrodes 2.0 cm in diameter with a separation of 1.0 cm, or with a 1.0 mm diameter wire axially positioned in a 2.6 cm long and 1.1 cm inside diameter cylindrical copper tube. A 300 V battery was used to bias the electrodes with one electrode connected through

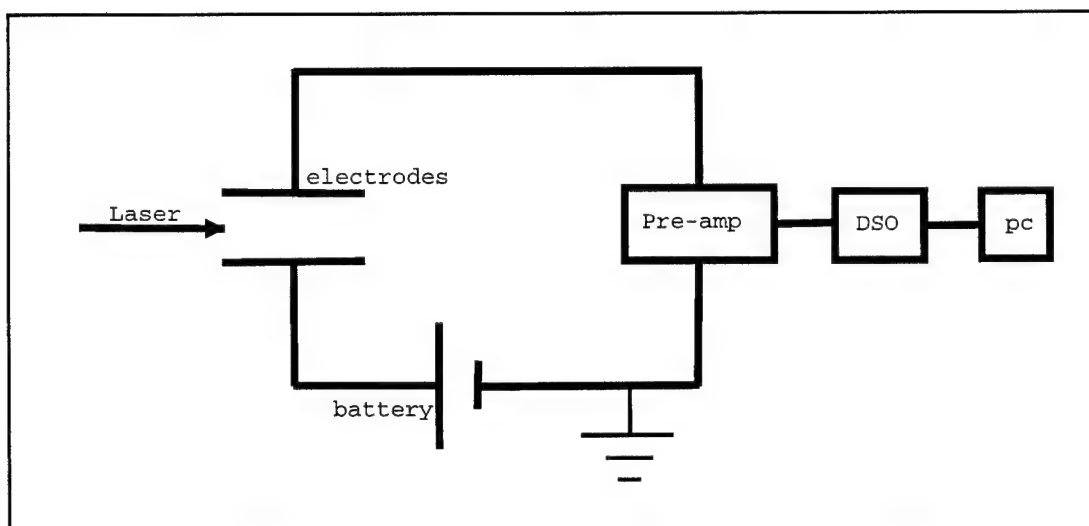


Figure 1.1. Schematic of experimental apparatus.

a pre-amplifier to ground. The gas flow system contained ambient pressure laboratory air, and 5  $\mu\text{L}$  of styrene headspace was injected into the 5 L flask to give a concentration of approximately 10 ppbv in atmospheric pressure air. The frequency doubled rhodamine dye laser was tuned to the styrene resonance at 287.5 nm. The pulsed electrical signal from the pre-amplifier was fed to a Tektronix 2440 digital storage oscilloscope (DSO) that displays and digitizes the ion current intensity vs. time waveform to 1024 data points. The waveforms were then downloaded to a personal computer. The LID cell was mounted on a horizontal translation stage and moved with a micrometer to adjust the distance of the parallel laser beam from the grounded electrode.

## 1.2. Background

Analysis and modeling of the ions and the current produced by an LID event in an external electric field is based on understanding the physical and chemical processes of gas conduction. Most previous research in gas conduction has focused on the analysis of why and how gas conduction occurs; measuring ion and electron drift

velocities, diffusion coefficients, and mobilities,<sup>3,4</sup> and deriving the mathematical model for ions and electrons drifting in a gas in a uniform electric field from the continuity equation.<sup>2,5</sup> This paper also studied the circuit current produced by the motion of ions in a gas by considering the image charges in the electrodes.<sup>5</sup> L. G. H. Huxley solved a mathematical model for a group of electrons drifting between plane parallel electrodes using the continuity equation for the number density of electrons as a function of space and time.<sup>6</sup>

The goal of this work is to model the behavior of laser-produced ions and the current induced by this behavior in a gas between two electrodes. The temporal ion current waveforms produced by LID in atmospheric pressure can be interpreted as the creation of electron-positive ion pairs that drift through an electric field as they collide with the ambient gas molecules.<sup>7</sup> When a molecule or an atom reaches its ionization continuum by photon absorption, it liberates an electron and leaves behind a positive molecule ion. When free electrons are available, they may attach themselves to neutral atoms or molecules, and negative ions, called anions, are formed. Gases with one or two electrons deficient in their outer shell or molecules of two (or more) atoms,<sup>7,8</sup> such as  $O_2$ , tend to easily attach electrons. The three-body attachment coefficients of  $N_2$  and  $O_2$  at 300K for the reaction  $e^- + O_2 + S \rightarrow O_2^- + S^{(*)} + \text{energy}$  are  $0.1 \times 10^{-30} \text{ cm}^6 \text{ s}^{-1}$  and  $2 \times 10^{-30} \text{ cm}^6 \text{ s}^{-1}$ , respectively.<sup>9</sup> The time scale for electron attachment based on this process is then approximately 17 ns. In our model, we assume that the free electrons immediately attach to the abundant oxygen molecules to form  $O_2^-$  relative to the drift time of ions which is hundreds of microseconds. These charged species are efficiently collected at biased electrodes after diffusing through the air. When a charged particle moves between two electrodes, it induces changing charges on the electrode surface, resulting in a current between electrodes that is monitored by the pre-amplifier. The induced current appears as soon as the charge is created and starts moving and continues until the



charged particles strike the electrodes shown in Figure 1.2. The cations approaching the negative electrode and anions approaching the positive electrode are both recorded as a positive current flowing from the negative electrode to the positive electrode. These ions move in opposite directions in response to the electric field but produce current contributions of the same sign.

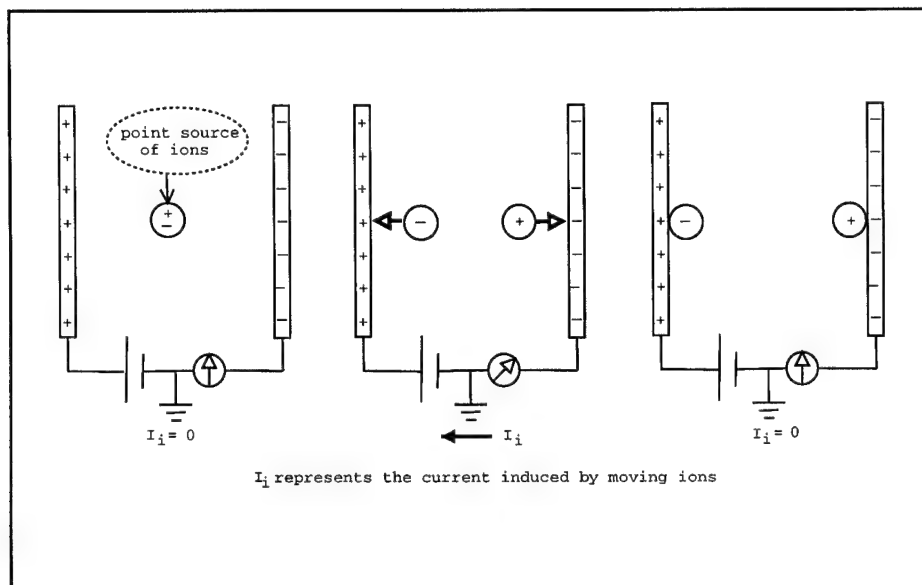


Figure 1.2. Positive ions drift to the cathode while negative ions move toward the anode, inducing the current in the external circuit. The current begins at the time the charge starts to travel and ends when the charge encounters an electrode.<sup>5</sup>

In this work, we assume an ideal situation of a low pressure reduced electric field ( $E/P$ ,  $E$  - electric field and  $P$  - gas pressure) between the electrodes. As  $E/P$  is low, the energy gained in a single flight is low for a given atom or molecule;<sup>7,8</sup> therefore, it is reasonable to neglect ionization due to collisions. In addition, the applied electric field will remove most of the charges from the interaction region very quickly. Consequently, the electric field will limit ionization and recombination (the

neutralization of ionized particles) from occurring at any significant rate. At room temperature, the thermal ionization is so small that we can ignore it. We also neglect the influence of the electric fields created by the charged particles in the ion swarm itself (space charge); however, the model shows good agreement with experimental results for low ionization concentrations.

In Chapter 2, we build the mathematical model, a second-order nonlinear partial differential equation via the continuity equation, for the transport of positive and negative ions produced by the laser. The analytical and numerical solutions, the charge number densities, to this second-order partial differential equation are given for two infinite parallel electrodes. At the end of this chapter, we provide the comparison of the analytical to numerical solutions as well as the numerical results to the experimental results. In Chapter 3, we use an approach similar to that utilized in Chapter 2 to compute the charge number densities,  $n_+(\mathbf{r}, t)$  and  $n_-(\mathbf{r}, t)$ , and then solve for the current induced by laser-generated ions between two infinite cylindrical electrodes. Under the parallel configuration, we treat the electric field as a constant since the influence of the electric field created by laser-produced ions in a gas is neglected. However, the electric field is not constant but a function of position, angle, and time between two electrodes under the cylindrical situation. The remainder of this chapter compares the theoretical results and the experimental waveforms. Chapter 4 gives a brief discussion of the results. Conclusions and suggestions for future work are also given.

## CHAPTER 2

### NUMERICAL MODELING FOR PARALLEL FOR CONFIGURATION

In this chapter, we model the behavior of laser-induced ions in a gas between two biased electrodes and the current generated by this behavior. The model is based on solving the continuity equation analytically and numerically for the distributions of positive and negative ions produced by laser illumination. In this chapter, we use the parallel electrode configuration, and in Chapter 3, we compute the same equation in the cylindrical electrode configuration. Once we know the distributions of ions, we can proceed to calculate the current induced by these ions. We use the following notation and variables throughout this work:

$E$  = external electric field, assumed constant and uniform between two parallel plates;

$v_+, v_-$  = drift velocities of positive and negative ions;

$n_+, n_-$  = densities of positive and negative ions;

$\mu_+, \mu_-$  = mobilities of positive and negative ions, assumed constant;

$D_+, D_-$  = diffusion coefficients of positive and negative ions, assumed constant;

$e \approx -1.602 \cdot 10^{-19} \text{ C}$  = electron charge;

$V_0$  = voltage applied to electrodes;

$x_l$  or  $r_{las}$  = initial position of laser in parallel and cylindrical configurations, respectively;

$L_0$  = distance between two electrodes;

$\sigma$  = width of laser-induced ion distribution, assumed equal to that of laser pulse;

$i_+$  and  $i_-$  = current created by laser-induced positive and negative ions;

$i$  = total current equal to  $i_+ + i_-$ ;

## 2.1. The Reduction of Three Dimensions to One

For modeling the motion of the distributions of laser-induced positive and negative ions in a gas, the mathematical description of this motion is simplified by reducing three dimensions to one under the assumption that the parallel electrodes are infinite.<sup>5</sup> All vector quantities, such as electric field and ion drift velocities, are treated as scalar quantities with the sign denoting their directions. Figure 2.1 shows a two-dimensional edge view of three-dimensional parallel plate electrodes. After the passage of time, charged particles have moved to the positions of  $l_+$  and  $l_-$ . The laser-induced ions between two parallel plates will create their own electric fields superimposed on the external electric field. For simplicity, the electric field generated by laser-induced ions will be neglected because of the low ion number density under normal experimental conditions. The laser ionization is also assumed to create equal Gaussian distributions of anions and cations, at time  $t = 0$ , that broaden with time, mainly owing to the effect of diffusion.

$$n_{\pm}(x, 0) = c_0 e^{\frac{-4(x-x_l)^2}{\sigma^2}}, \quad (2.1)$$

where  $\sigma$  is the width of charge distribution at  $t = 0$  and  $c_0$  is the amplitude of the ion distribution at  $t = 0$ .

## 2.2. Influence of an Applied Field on Laser-Induced Ions

When the external electric field is applied to a gas in which ions are present, an electric force acts on each one of them. Due to the electric forces, the ions are accelerated. If they move in a complete vacuum, the velocities can reach very high values.<sup>7,8</sup> However, in a gas at sufficiently high pressure (e.g., ambient pressure), the

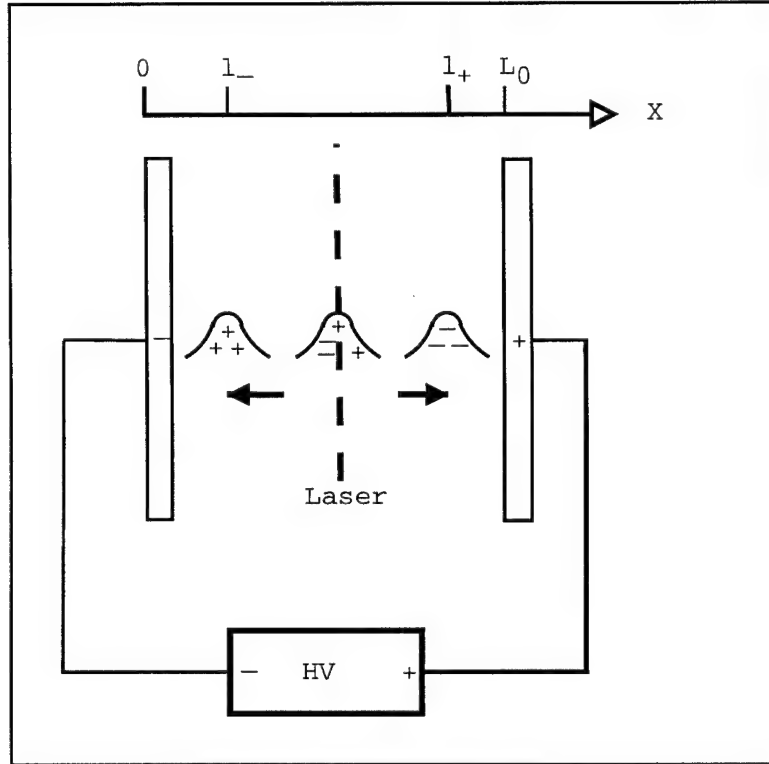


Figure 2.1. A cross section of the three-dimensional parallel plate electrodes. Parallel plate electrodes are at  $x = 0$  and  $x = L_0$ . A laser is used to create an equal number density of positive and negative ions centered at  $x_l$  at the initial time. Then, positive and negative ions move in opposite directions due to the influence of the external electric field. HV stands for high voltage source.

accelerated ions lose their energies by collisions with gas molecules and reach a terminal velocity, called drift velocity.<sup>7</sup> The mobility,  $\mu_+$ , of an ion is defined as the ratio of its drift velocity<sup>3,5,8</sup> in the electric field direction to the magnitude of the electric field.<sup>5</sup> Thus, for any positive ion or negative ion in a gas, the mobility is

$$\mu_+ = \frac{v_+}{E} \text{ m}^2/\text{V-sec} \quad (2.2)$$

or

$$\mu_- = \frac{v_-}{E} \text{ m}^2/\text{V-sec} \quad (2.3)$$

The mobility of charged particles in a variety of gases under the influence of an external electric field has been studied extensively, theoretically and experimentally.<sup>3,7</sup> Since the goal of this work is only to build a mathematical model for describing the behavior of the laser-induced charged particles and the current due to this behavior, calculation and measurement of the mobility is not covered in this thesis. For simplicity, we treat the mobilities of positive and negative ions as constants.

The laser pulse width is typically 5-10 ns, so the creation of electron-positive ion pairs can be considered to occur instantly relative to the drift times of ions. The theory for electron drift motion in a gas within an external electric field is much more complicated than for ions,<sup>13</sup> mainly because the mass of electrons is much less than that of ions; that is, the mobility of electrons is much greater than that of ions. Electronegative gas molecules with one or two electrons deficient in their outer shell, such as  $O_2$ , tend to easily attach electrons.<sup>14</sup> Therefore, in this thesis, we study the movement of negative ions ( $O_2^-$ ) and their contribution to the induced current instead of electrons.

### 2.3. Effect of Laser-Produced Ions on the Field and the External Circuit

When the production of positive and negative ions occurs due to laser illumination, the external electric field immediately separates these ions, positive ions move toward the cathode and negative ions to the anode. An additional electric field is induced because of these ions in the space between the two electrodes called space charge. Thus, in Eqs. 2.2 and 2.3,  $\mathbf{E}$  should be equal to the superposition of the external electric field and the electric field generated by space charges. However, under the condition mentioned at the beginning of this chapter, the electric field produced by laser-induced ions is small enough that we can ignore it relative to the applied electric field. Figure 2.2 illustrates the induced flow of current in the external circuit. For the sake of simplicity, only a single positive point charge is shown. This positive ion is forced to move toward the cathode. The negative induced charges on the surface of the cathode increase and decrease on the opposite electrode-anode. This process is accompanied by the flow of charge in the external circuit. A similar argument obviously applies to a negative ion. We will calculate this current analytically and numerically by using the continuity equation in Section 2.4.

The relationship between the electric field,  $\mathbf{E}$ , and the potential,  $V$ , is given by<sup>10</sup>

$$\mathbf{E} = -\nabla V. \quad (2.4)$$

If there were no free charge in the space between two electrodes, then the Laplace Equation would be

$$\nabla \cdot \mathbf{E} = -\nabla^2 V = 0. \quad (2.5)$$

For one dimension, Eq. 2.5 simplifies to

$$\frac{dE}{dx} = -\frac{d^2V}{dx^2} = 0. \quad (2.6)$$

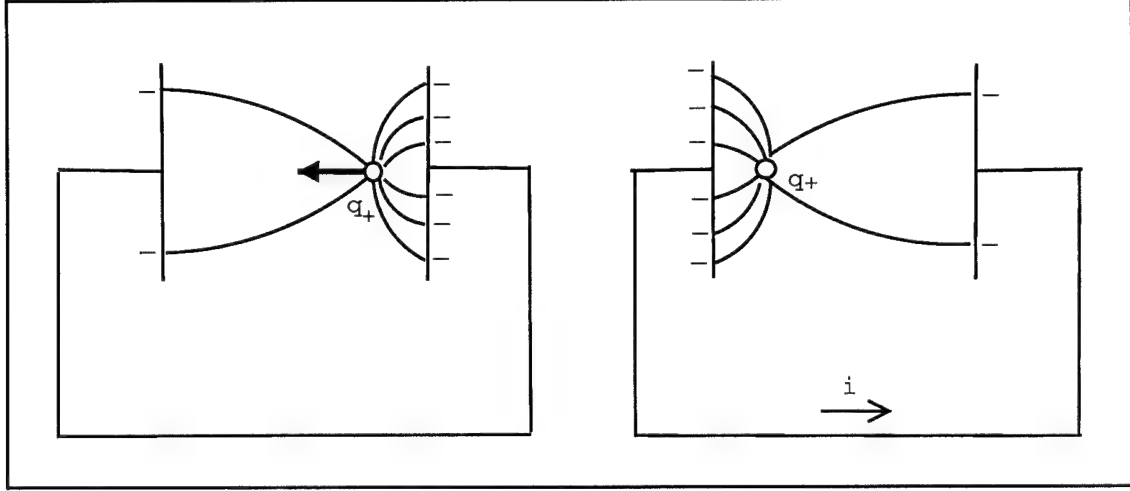


Figure 2.2. A schematic diagram that illustrates the flow of current in the external circuit connecting two parallel plate electrodes when a charge is caused to move in a direction perpendicular to the planes.

With the boundary conditions  $V=0$  at  $x=0$  and  $V = V_0$  at  $x = L_0$  (shown in Figure 2.1), the solution to Eq. 2.6 is

$$\begin{aligned} E &= -\frac{V_0}{L_0} \\ V &= \frac{xV_0}{L_0}. \end{aligned} \tag{2.7}$$

Our choice of origin causes the value of  $E$  to always be negative.

In order to determine the current induced by laser-created ions, we first calculate the surface charges induced on the two electrodes. For simplicity, we consider the case with only one point charge between two parallel plates. Figure 2.3 shows a positive point charge at position  $x_Q$ . We refer to the plate at  $x = 0$  as the cathode and the plate at  $x = L_0$  as the anode. The positive point charge,  $q$ , results in the two first-order negative image charges,  $q_1$  and  $q_2$ , located behind two parallel plates at  $x_1 = -x_Q$  and  $x_2 = 2L_0 - x_Q$ , respectively. The induced charges on both the cathode and the anode were given by using the Green Reciprocity Theorem (as explained in



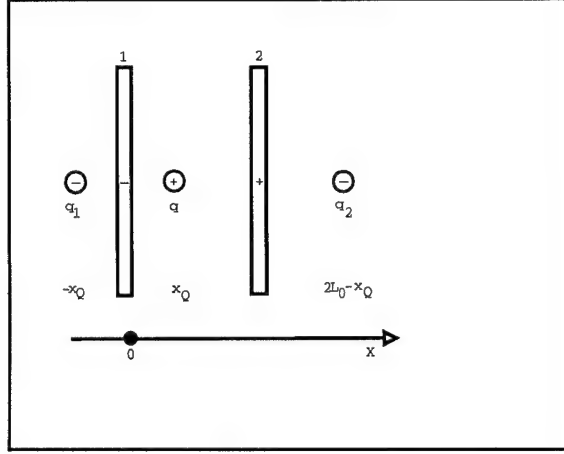


Figure 2.3. The image charge model for charge induction.

Appendix E):

$$\begin{aligned} q_1 &= -q \left( \frac{L_0 - x_Q}{L_0} \right) \\ q_2 &= -q \left( \frac{x_Q}{L_0} \right), \end{aligned} \tag{2.8}$$

where  $q_1$  is the charge induced on the cathode,  $q_2$  is the charge induced on the anode, and  $x_Q$  is the initial position of point charge  $q$ . The surface charges,  $q_1$  and  $q_2$ , induced on the two parallel plates are a function of the position,  $x_Q$ , of the positive point charge. In other words,  $q_1$  and  $q_2$  change with the position of charge,  $q$ . As point charge  $q$  moves, an induced current flows in the external circuit connecting the two electrodes. By differentiating Eq. 2.8 with respect to time, the current of the cathode and anode is then

$$\begin{aligned} i_1 &= \frac{dq_1}{dt} = \frac{q}{L_0} \left( \frac{dx_Q}{dt} \right) \\ i_2 &= \frac{dq_2}{dt} = -\frac{q}{L_0} \left( \frac{dx_Q}{dt} \right), \end{aligned} \tag{2.9}$$

where  $dx_Q/dt$  is the drift velocity of the positive point charge from electrode 2 to

electrode 1 shown in Figure 2.3. According to Eqs. 2.2 and 2.3, Eq. 2.9 is now written

$$\begin{aligned} i_1 &= \frac{q}{L_0} \left( \frac{dx_Q}{dt} \right) = \frac{q}{L_0} v_+ = \left( \frac{q}{L_0} \right) \mu_+ E, \\ i_2 &= -\frac{q}{L_0} \left( \frac{dx_Q}{dt} \right) = -\frac{q}{L_0} v_+ = -\left( \frac{q}{L_0} \right) \mu_+ E. \end{aligned} \quad (2.10)$$

In this case, the drift velocities of positive and negative ions are constant due to the fact that the electric field and mobilities are treated as constants.<sup>13</sup> The current that the electric field and mobilities are treated as constants begins at the time the charge starts to travel and ends when the charge encounters an electrode.<sup>5</sup>

## 2.4. Numerical Modeling

The continuity equation<sup>6,10,11</sup> governs the time dependence of the charge density,  $\rho$ , at each point in the space between two electrodes. The general relationship for charge is given by the continuity equation,

$$\nabla \cdot \mathbf{J}_{\pm} + \frac{\partial \rho_{\pm}}{\partial t} = 0, \quad (2.11)$$

where  $\mathbf{J}$  is the current density.  $\mathbf{J}$  can be described in terms of the drift motion due to the external electric field and diffusion. Both charged and neutral particles move from a region of high density to a region of low density. The current density for positive ions,  $\mathbf{J}_+$ , is represented by<sup>10</sup>

$$\mathbf{J}_+ = -eD_+ \nabla n_+ + e\mu_+ n_+ \mathbf{E}. \quad (2.12)$$

For one dimension, Eq. 2.12 becomes

$$J_+ = -eD_+ \nabla n_+ + e\mu_+ n_+ E, \quad (2.13)$$

where

$$\nabla n_+ = \frac{\partial n_+}{\partial x}. \quad (2.14)$$

Substituting Eq. 2.14 into Eq. 2.13, we obtain

$$J_+ = -eD_+ \frac{\partial n_+}{\partial x} + e\mu_+ n_+ E. \quad (2.15)$$

By inserting Eq. 2.15 into Eq. 2.11, the continuity equations for the positive and negative ions become

$$\frac{\partial n_+}{\partial t} = -\frac{\partial}{\partial x} \left( +\mu_+ E n_+ - D_+ \frac{\partial n_+}{\partial x} \right) \quad (2.16)$$

$$\frac{\partial n_-}{\partial t} = -\frac{\partial}{\partial x} \left( -\mu_- E n_- - D_- \frac{\partial n_-}{\partial x} \right), \quad (2.17)$$

where ion recombination and ionization<sup>7</sup> due to collisions have been neglected, and the direction of the external electric field is opposite to the  $x$  axis shown in Figure 2.1.

Eqs. 2.16 and 2.17 are solved analytically (Appendix A) to give the charge densities as functions of time and position.

$$n_+(x, t) = \frac{c_0 \sigma}{\sqrt{\sigma^2 + 16D_+ t}} e^{-\frac{4(x-x_l - \mu_+ E t)^2}{\sigma^2 + 16D_+ t}} \quad (2.18)$$

and

$$n_-(x, t) = \frac{c_0 \sigma}{\sqrt{\sigma^2 + 16D_- t}} e^{-\frac{4(x-x_l + \mu_- E t)^2}{\sigma^2 + 16D_- t}}, \quad (2.19)$$

where  $c_0$  is the amplitude of the initial charge distribution. Figure 2.4 shows several positive and negative ion profiles at different particular times for an initial ion charge distribution centered at  $x_l = 0.404$  cm with a width  $\sigma = 0.1$  cm. During the movement of the positive ions towards the cathode and the negative ions towards the anode, both the positive ion and the negative ion distributions expand, and their

amplitudes decrease due to diffusion. It is obvious that the distribution *broadens* as it moves, consequently decreasing in amplitude due to the fact that the integral (or charge) is constant. When ions reach either the cathode or the anode, since we assume that the boundary conditions require that charge density be zero in the electrodes, the ions appear to traverse the cathode or the anode as if it were “transparent”<sup>5</sup> to them as shown in Figure 2.4. We choose  $\mu_+ = 1.36 \text{ volt}^{-1} \text{ cm}^2 \text{ sec}^{-1}$ ,  $\mu_- = 1.82 \text{ volt}^{-1} \text{ cm}^2 \text{ sec}^{-1}$ ,  $D_+ = 0.032 \text{ cm}^2 \text{ sec}^{-1}$ , and  $D_- = 0.040 \text{ cm}^2 \text{ sec}^{-1}$  for both analytical and numerical calculations for the parallel plate electrodes.<sup>6,12</sup>

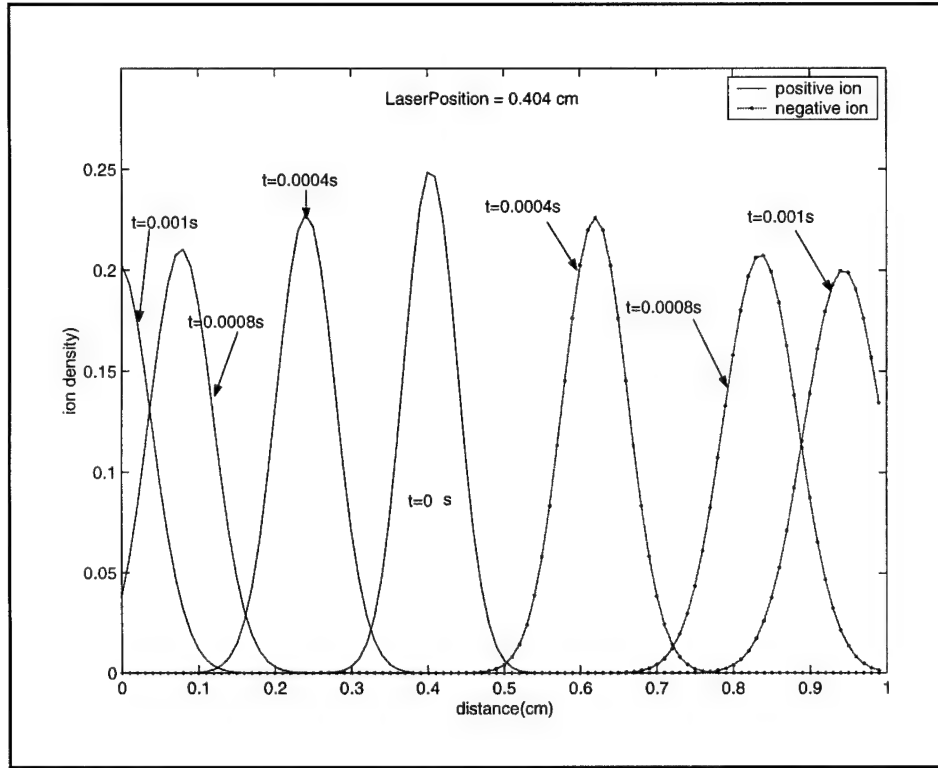


Figure 2.4. The time evolution of the positive and negative ion distributions. The amplitude of the initial ion number density,  $c_0$ , is 0.25. We choose  $\mu_+ = 1.36 \text{ volt}^{-1} \text{ cm}^2 \text{ sec}^{-1}$ ,  $\mu_- = 1.82 \text{ volt}^{-1} \text{ cm}^2 \text{ sec}^{-1}$ ,  $D_+ = 0.032 \text{ cm}^2 \text{ sec}^{-1}$ , and  $D_- = 0.040 \text{ cm}^2 \text{ sec}^{-1}$ .

In Section 2.3., the current induced by a single point charge was calculated, giving the induced current proportional to the charge times the electric field and mobility (shown in Eq. 2.10). Since the charge is now a charge distribution rather than a single point charge, it is apparent that the current induced by a positive charge distribution is an integral over the space between the two parallel plates (from 0 to  $L_0$ ).

$$i_+(t) = \frac{\mu_+ E}{L_0} \int_0^{L_0} e n_+(x, t) dx. \quad (2.20)$$

Substituting Eq. 2.18,  $n_+(x, t)$ , into Eq. 2.20, we obtain

$$i_+(t) = \frac{\mu_+ E}{L_0} \frac{c_0 \sigma}{\sqrt{\sigma^2 + 8D_+ t}} \int_0^{L_0} e^{-\frac{4(x-x_l-\mu_+ Et)^2}{\sigma^2 + 16D_+ t}} dx. \quad (2.21)$$

Let  $y = \frac{2(x-x_l-\mu_+ Et)}{\sqrt{\sigma^2 + 16D_+ t}}$ , then  $i_+(t)$  becomes

$$\begin{aligned} i_+ &= \frac{\mu_+ E e \sigma c_0}{2L_0} \int_{\frac{2(-x_l-\mu_+ Et)}{\sqrt{\sigma^2 + 16D_+ t}}}^{\frac{2(L_0-x_l-\mu_+ Et)}{\sqrt{\sigma^2 + 16D_+ t}}} e^{-y^2} dy \\ &= \frac{\mu_+ E e \sigma \sqrt{\pi}}{4L_0} \left[ \operatorname{erf} \left( \frac{2(L_0 - x_l - \mu_+ Et)}{\sqrt{\sigma^2 + 16D_+ t}} \right) - \operatorname{erf} \left( \frac{2(-x_l - \mu_+ Et)}{\sqrt{\sigma^2 + 16D_+ t}} \right) \right]. \end{aligned} \quad (2.22)$$

Similarly, the current induced by the negative ions is given by

$$i_- = \frac{\mu_- E e \sigma c_0 \sqrt{\pi}}{4L_0} \left[ \operatorname{erf} \left( \frac{2(L_0 - x_l + \mu_- Et)}{\sqrt{\sigma^2 + 16D_- t}} \right) - \operatorname{erf} \left( \frac{2(-x_l + \mu_- Et)}{\sqrt{\sigma^2 + 16D_- t}} \right) \right]. \quad (2.23)$$

The total current induced by laser-produced positive and negative ions is

$$\begin{aligned} i &= i_+ + i_- \\ &= \frac{\mu_+ E e \sigma c_0 \sqrt{\pi}}{4L_0} \left( \operatorname{erf} \left( \frac{2(L_0 - x_l - \mu_+ Et)}{\sqrt{\sigma^2 + 16D_+ t}} \right) - \operatorname{erf} \left( \frac{2(-x_l - \mu_+ Et)}{\sqrt{\sigma^2 + 16D_+ t}} \right) \right) \\ &\quad + \frac{\mu_- E e \sigma c_0 \sqrt{\pi}}{4L_0} \left( \operatorname{erf} \left( \frac{2(L_0 - x_l + \mu_- Et)}{\sqrt{\sigma^2 + 16D_- t}} \right) - \operatorname{erf} \left( \frac{2(-x_l + \mu_- Et)}{\sqrt{\sigma^2 + 16D_- t}} \right) \right). \end{aligned} \quad (2.24)$$

Figures 2.5 and 2.6 show the total induced current corresponding to four different initial laser positions of 0.202 cm, 0.404 cm, 0.505 cm, and 0.606 cm. For the first waveform at 0.202 cm from the grounded electrode, the positive styrene molecules travel 0.202 cm to reach the negative (grounded) collector while the negative oxygen molecules (electrons captured by oxygen) must travel 0.798 cm to the positive electrode. The mobility of the positive ion is less than that of the negative ion,<sup>6,12</sup> but they are comparable. Consequently, the current induced by the negative ions is delayed in time, and the negative ion current is greater than the positive ion current due to that fact that the mobility is proportional to the drift velocity. As the laser beam moves further from the grounded electrode, the delay of the negative ions is reduced.

Now we use the numerical method to solve Eqs. 2.16 and 2.17 for charge distributions created by the laser and then obtain the time dependence induced current. The solution domain in  $x - t$  space is covered by a rectangular grid, with grid spacing of  $\Delta x$  and  $\Delta t$  in the  $x$  and  $t$  directions, respectively, the values of  $\Delta x$  and  $\Delta t$  being assumed uniform. The grid consists of the set of lines parallel to the  $t$ -axis, given by  $x_j = j \Delta x$ , and the set of lines parallel to the  $x$ -axis, given by  $t_k = k \Delta t$ , as shown in Figure 2.7. Finite difference methods<sup>11,13,14,15</sup> which determine approximately the values of  $n_{\pm}(x, t)$  at interior points will be developed. These points, with coordinates  $(x_j, t_k)$ , are called grid-points and are denoted  $(j, k)$ . Those points on the boundary of the edge grid-points, that is, those for which  $j = 0$  or  $k = 0$ , are called boundary grid-points. The following notation will be used for the value of  $n_{\pm}(x, t)$  and its derivatives at the  $(j, k)$  grid-point:

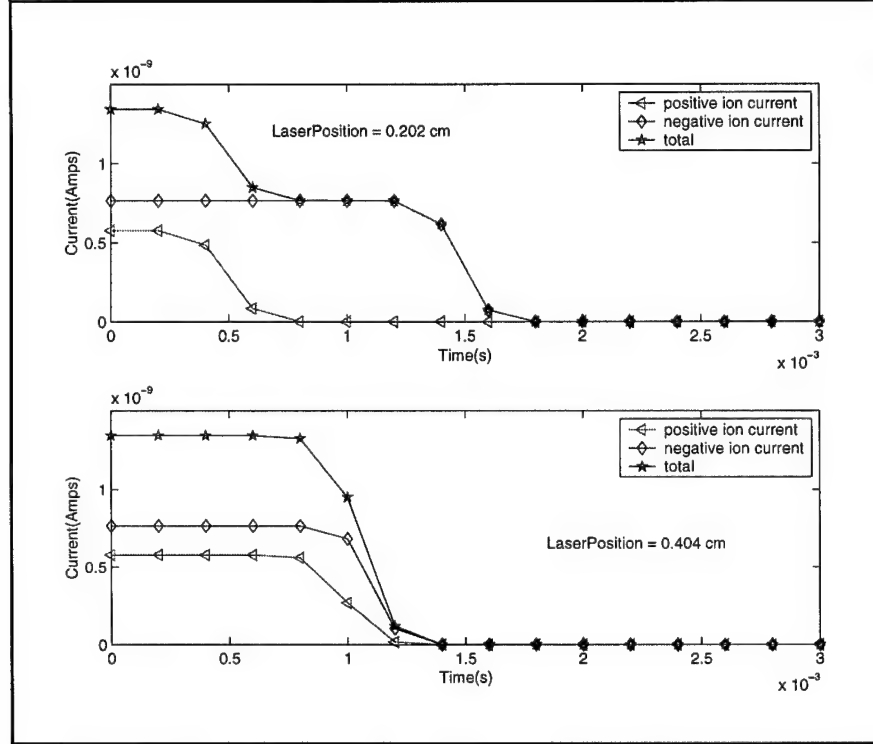


Figure 2.5. The time evolution of three current profiles induced by the positive ions, the negative ions, and both of them at the laser positions of 0.202 cm and 0.404 cm. The amplitude of the initial ion number density,  $c_0$ , is 0.25. We choose  $\mu_+ = 1.36 \text{ volt}^{-1} \text{ cm}^2 \text{ sec}^{-1}$ ,  $\mu_- = 1.82 \text{ volt}^{-1} \text{ cm}^2 \text{ sec}^{-1}$ ,  $D_+ = 0.032 \text{ cm}^2 \text{ sec}^{-1}$ , and  $D_- = 0.040 \text{ cm}^2$ .

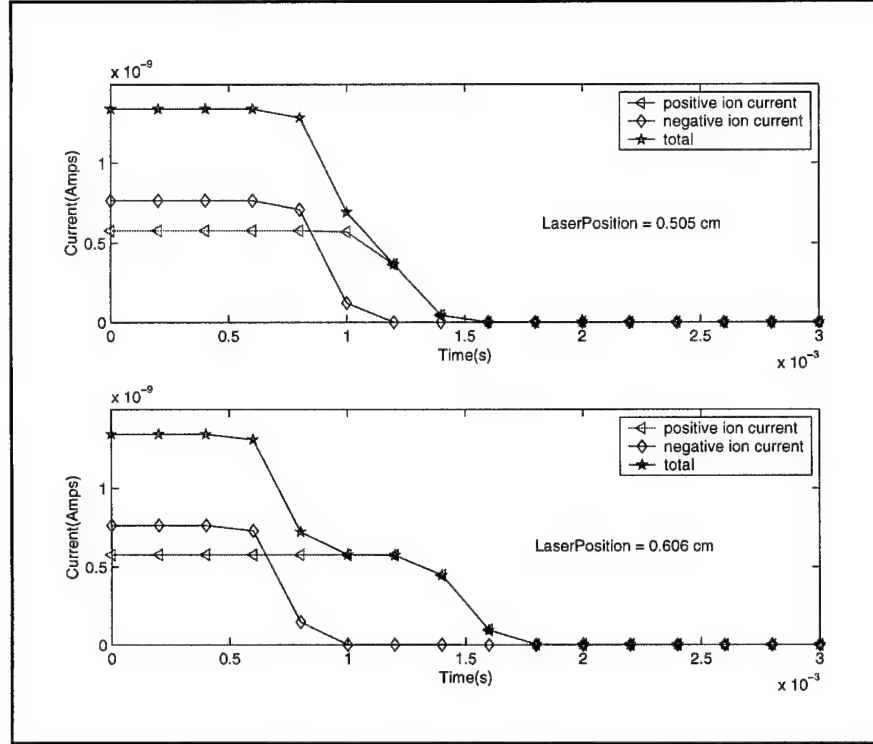


Figure 2.6. The time evolution of three current profiles induced by the positive ions, the negative ions, and both of them at the laser positions of 0.505 cm and 0.606 cm. The amplitude of the initial ion number density,  $c_0$ , is 0.25. We choose  $\mu_+ = 1.36 \text{ volt}^{-1} \text{ cm}^2 \text{ sec}^{-1}$ ,  $\mu_- = 1.82 \text{ volt}^{-1} \text{ cm}^2 \text{ sec}^{-1}$ ,  $D_+ = 0.032 \text{ cm}^2 \text{ sec}^{-1}$ , and  $D_- = 0.040 \text{ cm}^2$ .



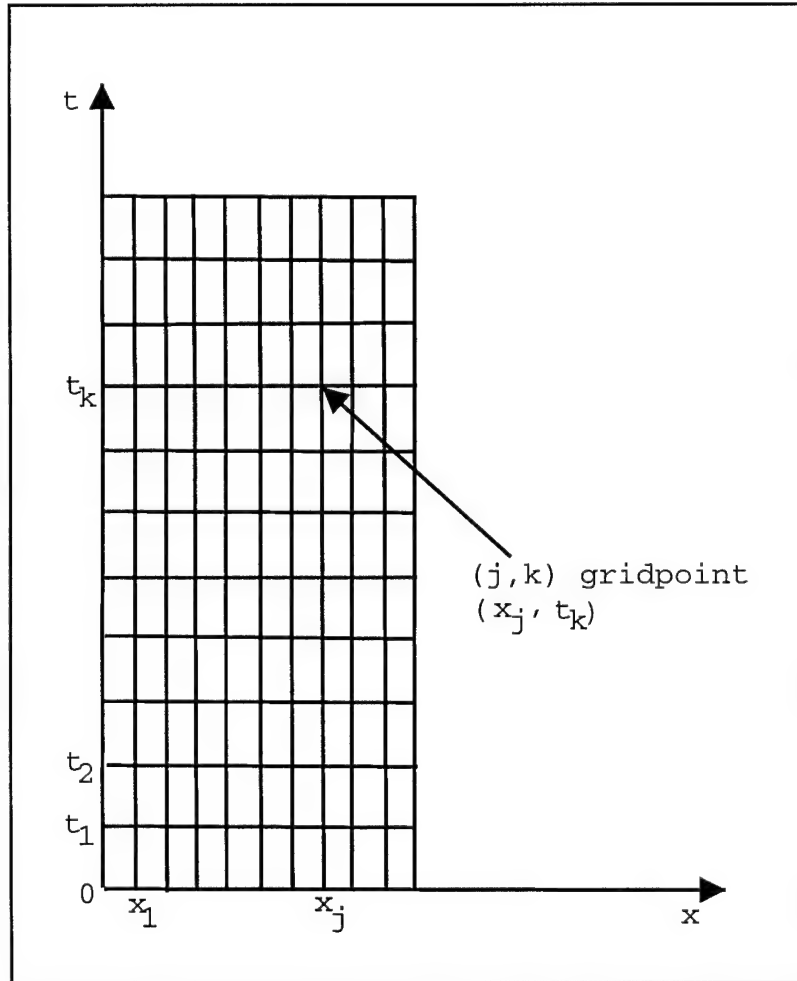


Figure 2.7. The finite difference grid in the solution region.

$$\begin{aligned}
n_{\pm} |^k_j &= n_{\pm}(x_j, t_k), \\
\frac{\partial n_{\pm}}{\partial t} |^k_j &= \frac{\partial n_{\pm}(x_j, t_k)}{\partial t}, \\
\frac{\partial n_{\pm}}{\partial x} |^k_j &= \frac{\partial n_{\pm}(x_j, t_k)}{\partial x}, \\
\frac{\partial^2 n_{\pm}}{\partial x^2} |^k_j &= \frac{\partial^2 n_{\pm}(x_j, t_k)}{\partial x^2}.
\end{aligned} \tag{2.25}$$

Note that the superscript  $k$  indicates the time level and the subscript  $j$  indicates the space level. One way of approximating the value of  $\frac{\partial n_{\pm}}{\partial t}$  and  $\frac{\partial n_{\pm}}{\partial x}$  at the  $(j, k)$  grid-point is by using a Taylor series expansion of  $n_{\pm}$  about the  $(j, k)$  grid-point.

$$\frac{\partial n_{\pm}}{\partial t} |^k_j = \frac{n_{\pm} |^{k+1}_j - n_{\pm} |^k_j}{\Delta t} + 0((\Delta t)) \tag{2.26}$$

and

$$\frac{\partial n_{\pm}}{\partial x} |^k_j = \frac{n_{\pm} |^k_{j+1} - n_{\pm} |^k_{j-1}}{2 \Delta x} + 0((\Delta x)^2) \tag{2.27}$$

These equations lead to the forward difference approximation<sup>14,15,16</sup> to the first-order time derivative and the central difference approximation to the first-order spatial derivative<sup>11,18</sup>

$$\frac{\partial n_{\pm}}{\partial t} |^k_j \simeq \frac{n_{\pm} |^{k+1}_j - n_{\pm} |^k_j}{\Delta t} \tag{2.28}$$

$$\frac{\partial n_{\pm}}{\partial x} |^k_j \simeq \frac{n_{\pm} |^k_{j+1} - n_{\pm} |^k_{j-1}}{2 \Delta x} \tag{2.29}$$

The errors in using the right side of Eqs. 2.30 and 2.31 for the values of  $\frac{\partial n_{\pm}}{\partial t}$  and  $\frac{\partial n_{\pm}}{\partial x}$  are  $0((\Delta t))$  and  $0((\Delta x)^2)$ .

In a similar way, the central difference approximation<sup>14,15</sup> of the second-order spatial derivative can be derived

$$\frac{\partial^2 n_{\pm}}{\partial x^2} |^k_j = \frac{n_{\pm} |^k_{j+1} - 2n_{\pm} |^k_j + n_{\pm} |^k_{j-1}}{(\Delta x)^2} + 0((\Delta x)^2) \tag{2.30}$$

$$\frac{\partial^2 n_{\pm}}{\partial^2 x} \Big|_j^k \simeq \frac{n_{\pm} \Big|_{j+1}^k - 2n_{\pm} \Big|_j^k + n_{\pm} \Big|_{j-1}^k}{(\Delta x)^2}. \quad (2.31)$$

Consider Eq. 2.16 evaluated at the  $(j, k)$  grid-point; that is,

$$\frac{\partial n_+}{\partial t} \Big|_j^k + \mu_+ E \frac{\partial n_+}{\partial x} \Big|_j^k = D_+ \frac{\partial^2 n_+}{\partial^2 x} \Big|_j^k. \quad (2.32)$$

If the central difference form, Eq. 2.29, is used for the spatial derivative in the drift term with the forward difference form, Eq. 2.28, for the time derivative and the central difference form, Eq. 2.31, for the second-order derivative in the diffusion term, this equation becomes

$$\begin{aligned} \frac{n_+ \Big|_j^{k+1} - n_+ \Big|_j^k}{\Delta t} + 0((\Delta t)) + \mu_+ E \frac{n_+ \Big|_{j+1}^k - n_+ \Big|_{j-1}^k}{2 \Delta x} + 0((\Delta x)^2) \\ = D_+ \frac{n_+ \Big|_{j+1}^k - 2n_+ \Big|_j^k + n_+ \Big|_{j-1}^k}{(\Delta x)^2} + 0((\Delta x)^2). \end{aligned} \quad (2.33)$$

Dropping the terms of  $O[(\Delta t)^2, (\Delta t)(\Delta x)^2]$  from the above equation yields an explicit finite difference equation<sup>14,15,16</sup> which contributes an error of  $O[(\Delta t)^2, (\Delta t)(\Delta x)^2]$  to the discretization error (the difference between the true solution of the partial differential equation and the exact solution of the approximating finite difference equation) at each time step and can be used to solve Eqs. 2.16 and 2.17. This equation is

$$n_{\pm} \Big|_j^{k+1} = \left( S \pm \frac{1}{2} C \right) n_{\pm} \Big|_{j-1}^k + (1 - 2S) n_{\pm} \Big|_j^k + \left( S \mp \frac{1}{2} C \right) n_{\pm} \Big|_{j+1}^k, \quad (2.34)$$

where  $C = \frac{\mu_+ E \Delta t}{\Delta x}$  and  $S = \frac{D_+ \Delta t}{(\Delta x)^2}$ .

From Appendix B, the condition that makes the numerical solution to Eq. 2.34 consistent with Eqs. 2.16 and 2.17 is

$$\Delta t < \min \left( \frac{2D_+}{\mu_+^2 E^2}, \frac{2D_-}{\mu_-^2 E^2} \right). \quad (2.35)$$

A finite difference equation is regarded as being *consistent* with a partial differential equation if, when the grid spacing,  $\Delta t$  and  $\Delta x$ , goes to zero, the difference equation (Eq. 2.34) becomes the same as the partial differential equation at each point in the solution domain.<sup>13,14,15,18</sup> A formal consistency analysis will be discussed in Appendix B.

Appendix C contains the source-code listing of a program written with C++, based on Eq. 2.34. The program traces the time history of either positive ions or negative ions deposited as a Gaussian distribution at time  $t = 0$ . Figure 2.8 shows several positive and negative ion profiles at different particular times for an initial ion charge distribution centered at  $x_l = 0.404$  cm with a width  $\sigma = 0.1$  cm. How the

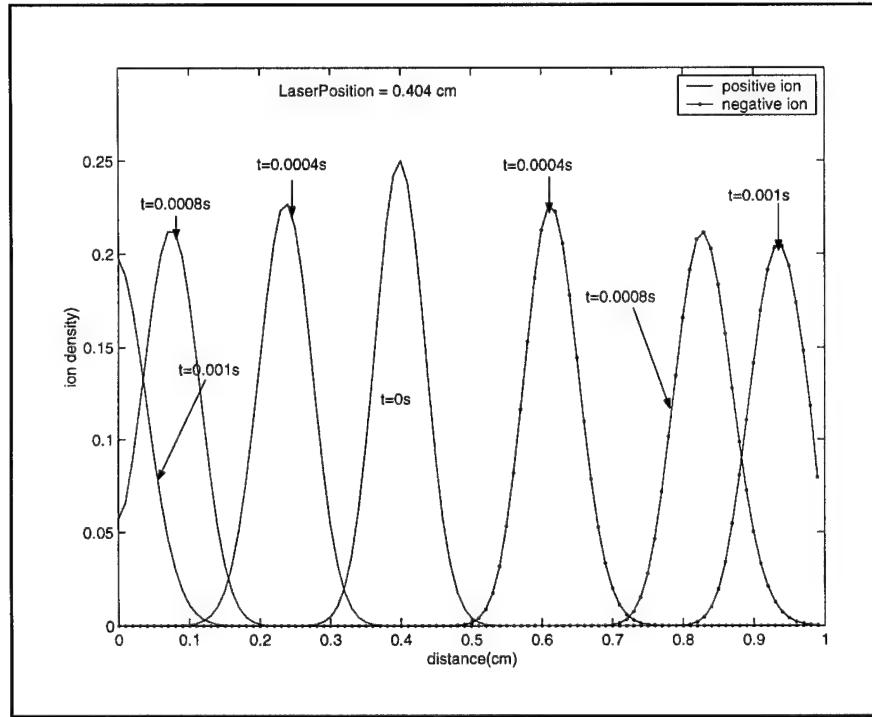


Figure 2.8. The time evolution of the positive and negative ion distributions computed numerically. The amplitude of the initial ion number density,  $c_0$ , is 0.25. We choose  $\mu_+ = 1.36$  volt<sup>-1</sup> cm<sup>2</sup> sec<sup>-1</sup>,  $\mu_- = 1.82$  volt<sup>-1</sup> cm<sup>2</sup> sec<sup>-1</sup>,  $D_+ = 0.032$  cm<sup>2</sup> sec<sup>-1</sup>, and  $D_- = 0.040$  cm<sup>2</sup>.

ion distribution changes with time is in the same manner as the ion distribution computed analytically, that is, the expansion and amplitude reduction of the ion distribution with time.

From Eq. 2.34, we derive the charge number densities,  $n_+(x, t)$  and  $n_-(x, t)$ , at each time step,  $\Delta t$ . By using Eq. 2.8, we can compute the induced charges on each electrode,  $q_{cathode}^+$ ,  $q_{anode}^+$ ,  $q_{cathode}^-$ , and  $q_{anode}^-$ , at  $t = k\Delta t$

$$\begin{aligned}
q_{cathode}^+|^k &= -e \sum_{j=1}^N \left(1 - \frac{j\Delta x}{L_0}\right) n_+|^k_j(\Delta x) \\
q_{anode}^+|^k &= -e \sum_{j=1}^N \left(\frac{j\Delta x}{L_0}\right) n_+|^k_j(\Delta x) \\
q_{cathode}^-|^k &= e \sum_{j=1}^N \left(1 - \frac{j\Delta x}{L_0}\right) n_-|^k_j(\Delta x) \\
q_{anode}^-|^k &= e \sum_{j=1}^N \left(\frac{j\Delta x}{L_0}\right) n_-|^k_j(\Delta x)
\end{aligned} \tag{2.36}$$

The currents flowing out from both the electrodes at  $t = k\Delta t$  are given

$$\begin{aligned}
i_{cathode}^+|^k &= \frac{q_{cathode}^+|^{k+1} - q_{cathode}^+|^k}{\Delta t} \\
&= \frac{e \sum_{j=1}^N (-n_+|^k_j + n_+|^{k+1}_j) \left(1 - \frac{j\Delta x}{L_0}\right)}{\Delta t} \\
i_{anode}^+|^k &= \frac{q_{anode}^+|^{k+1} - q_{anode}^+|^k}{\Delta t} \\
&= \frac{e \sum_{j=1}^N (-n_+|^k_j + n_+|^{k+1}_j) \left(\frac{j\Delta x}{L_0}\right)}{\Delta t}
\end{aligned} \tag{2.37}$$

and

$$\begin{aligned}
i_{cathode}^-|^k &= \frac{q_{cathode}^-|^k - q_{cathode}^-|^{k+1}}{\Delta x} \\
&= \frac{-e \sum_{j=1}^N (-n_-|^k + n_-|^k) \left(1 - \frac{j\Delta x}{L_0}\right)}{\Delta t} \\
i_{anode}^- &= \frac{q_{anode}^-|^k - q_{anode}^-|^{k+1}}{\Delta t} \\
&= \frac{-e \sum_{j=1}^N (-n_-|^k + n_-|^k) \left(\frac{j\Delta x}{L_0}\right)}{\Delta t}
\end{aligned} \tag{2.38}$$

Note that the current flowing out from the cathode is not equal to as well as in opposite sign of that coming out from the anode.

Finally, the total induced external current is given by the equation

$$\begin{aligned}
i_{total} &= i_{total}^+ - i_{total}^- \\
&= (i_{cathode}^+ - i_{anode}^+) - (i_{cathode}^- - i_{anode}^-)
\end{aligned} \tag{2.39}$$

## 2.5. Analytical vs Numerical Results

We solve Eqs. 2.16 and 2.17 for the laser-induced charge number densities,  $n_+$  and  $n_-$ , and then calculate the currents corresponding to these charges by using the analytical and numerical approaches. The analytical result is compared to the numerical result, with a 300 V battery used to bias the electrodes, at the initial laser positions of 2.02 mm, 4.04 mm, 5.05 mm, and 6.06 mm in Figures 2.9 and 2.10. It should be emphasized that, since the numerical approach<sup>15,18</sup> used in Section 2.4.2 decreases the effect of diffusion term by an amount  $\frac{1}{2}\mu_{\pm}^2 E^2 \Delta t \frac{\partial^2 n_{\pm}}{\partial^2 x}$  explained in detail in Appendix B and eventually causes an error, this additional term,  $\frac{1}{2}\mu_{\pm}^2 E^2 \Delta t$ , was added to the diffusion coefficients of the positive and negative ions, respectively.

Note that, since the laser width, the mobilities and diffusion coefficients for the positive as well as negative ions are uncertain, the values mentioned above are used

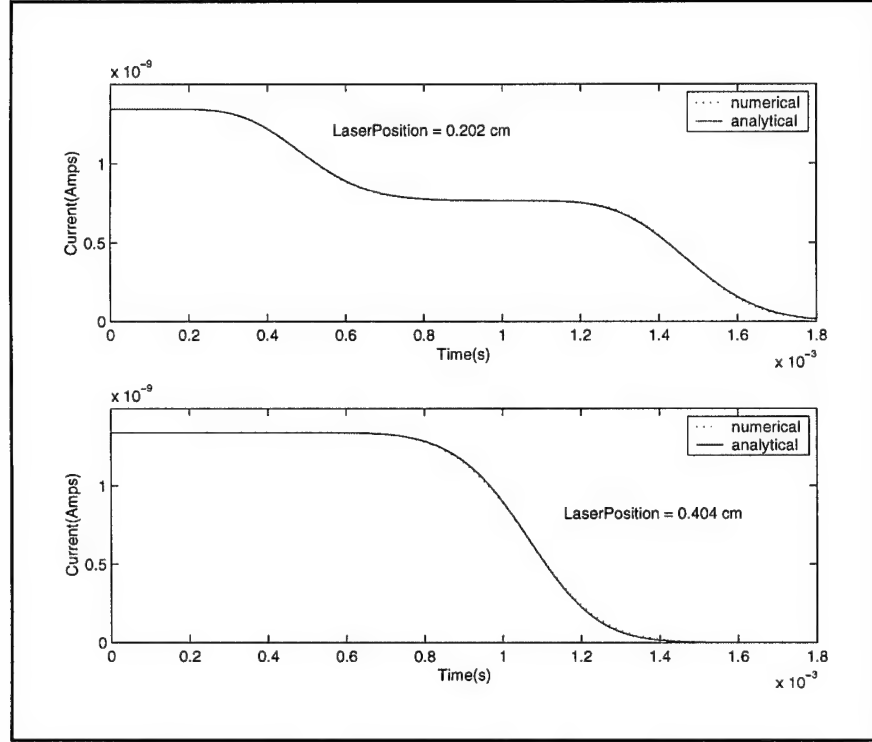


Figure 2.9. Total induced currents computed analytically and numerically with voltage 300 V for the initial laser position of 0.202 cm and 0.404 cm. The amplitude of the initial ion number density,  $c_0$ , is 0.25. We choose  $\mu_+ = 1.36 \text{ volt}^{-1} \text{ cm}^2 \text{ sec}^{-1}$ ,  $\mu_- = 1.82 \text{ volt}^{-1} \text{ cm}^2 \text{ sec}^{-1}$ ,  $D_+ = 0.032 \text{ cm}^2 \text{ sec}^{-1}$ , and  $D_- = 0.040 \text{ cm}^2$ .

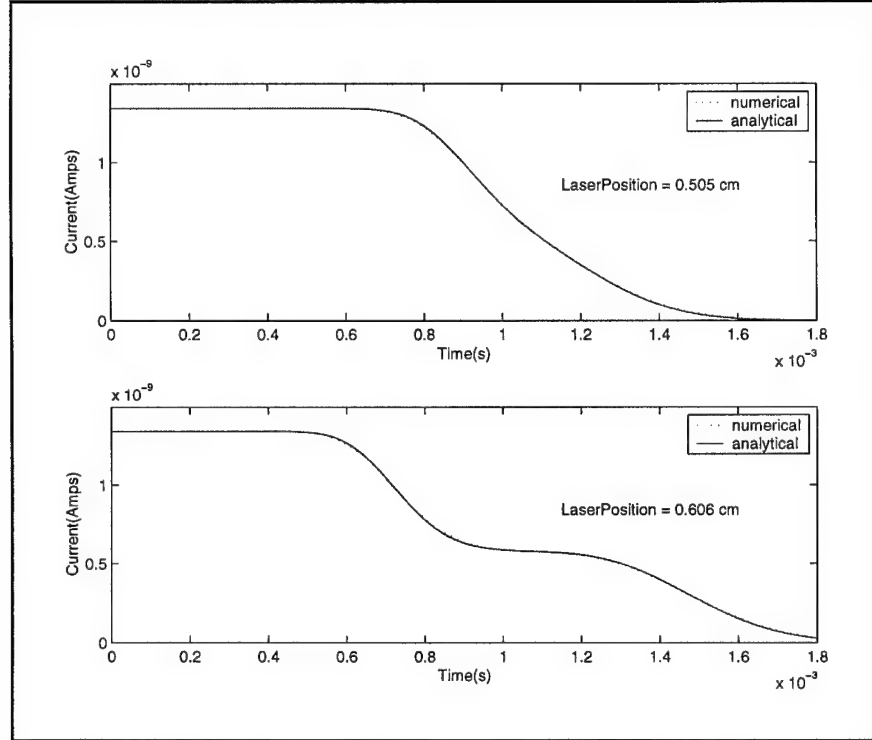


Figure 2.10. Total induced currents computed analytically and numerically with voltage 300 V for the initial laser position of 0.505 cm and 0.606 cm. The amplitude of the initial ion number density,  $c_0$ , is 0.25. We choose  $\mu_+ = 1.36 \text{ volt}^{-1} \text{ cm}^2 \text{ sec}^{-1}$ ,  $\mu_- = 1.82 \text{ volt}^{-1} \text{ cm}^2 \text{ sec}^{-1}$ ,  $D_+ = 0.032 \text{ cm}^2 \text{ sec}^{-1}$ , and  $D_- = 0.040 \text{ cm}^2$ .



to calculate and plot the figures related to these unknown parameters.

Figures 2.11-2.13 show the effect of varying the ion mobility and the diffusion coefficient of the positive ion. As a consequence of  $E$  being constant, the current induced by the ions is proportional to the ion mobility (Eq. 2.10). Therefore, an increase of the magnitude of the ion mobility will lead to a proportional increase in the induced current shown in Figure 2.11. It is seen in Figure 2.12 that increasing the diffusion coefficient affects the current slopes in such a way that the current slope increases with a decrease of the diffusion coefficient. Figure 2.13 shows that, when the laser width becomes larger, the slope of the positive ion current decreases.

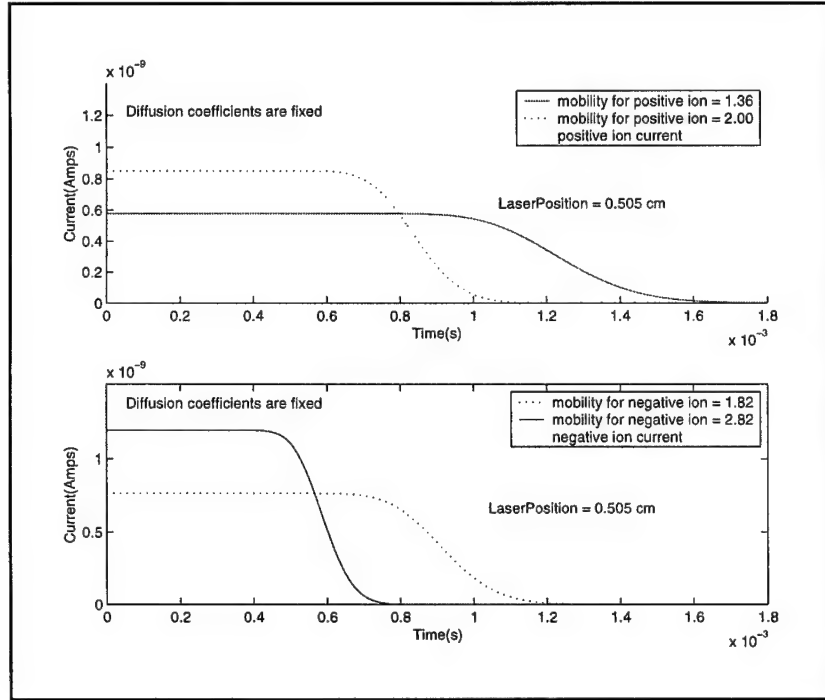


Figure 2.11. The current induced by the positive ions changes with the positive ion mobility in the top figure. The lower figure shows how the negative ion current changes with the negative ion mobility at the laser position of 5.05 mm with voltage 300 V. The amplitude of the initial ion number density,  $c_0$ , is 0.25.

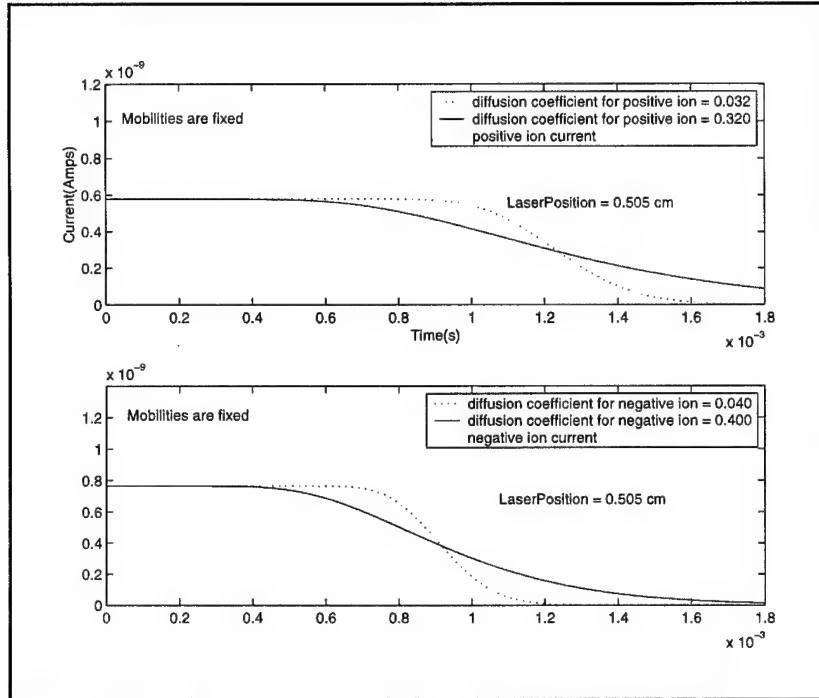


Figure 2.12. The current induced by the positive ions changes with the diffusion coefficient for positive ions in the top figure. The lower figure shows how the negative ion current changes with the diffusion coefficient for negative ions at the initial laser position of 0.505 cm with voltage 300 V. The amplitude of the initial ion number density,  $c_0$ , is 0.25.

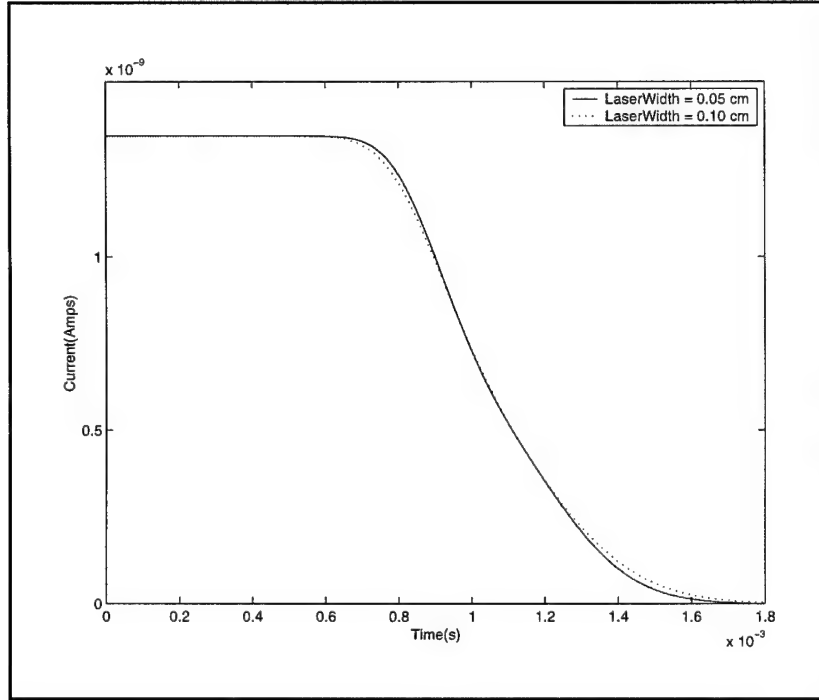


Figure 2.13. The total ion current changes with the laser width at the laser position of 0.505 cm with voltage 300 V. The total number of positive and negative ions is constant. We choose  $\mu_+ = 1.36 \text{ volt}^{-1} \text{ cm}^2 \text{ sec}^{-1}$ ,  $\mu_- = 1.82 \text{ volt}^{-1} \text{ cm}^2 \text{ sec}^{-1}$ ,  $D_+ = 0.032 \text{ cm}^2 \text{ sec}^{-1}$ , and  $D_- = 0.040 \text{ cm}^2$ .

## 2.6. Comparison of Numerical Results to Experimental Waveforms

Representative experimental waveforms and their corresponding numerical models are shown in Figures 2.14 and 2.15 for laser positions 0.202 cm, 0.404 cm, 0.505 cm, and 0.606 cm from the grounded electrode. For the first waveform at 0.202 cm from the grounded electrode, the positive styrene molecules travel only 0.202 cm to reach the negative (grounded) collector while the negative oxygen molecules (electrons captured by oxygen) must travel 0.798 cm to the positive electrode. We mentioned in

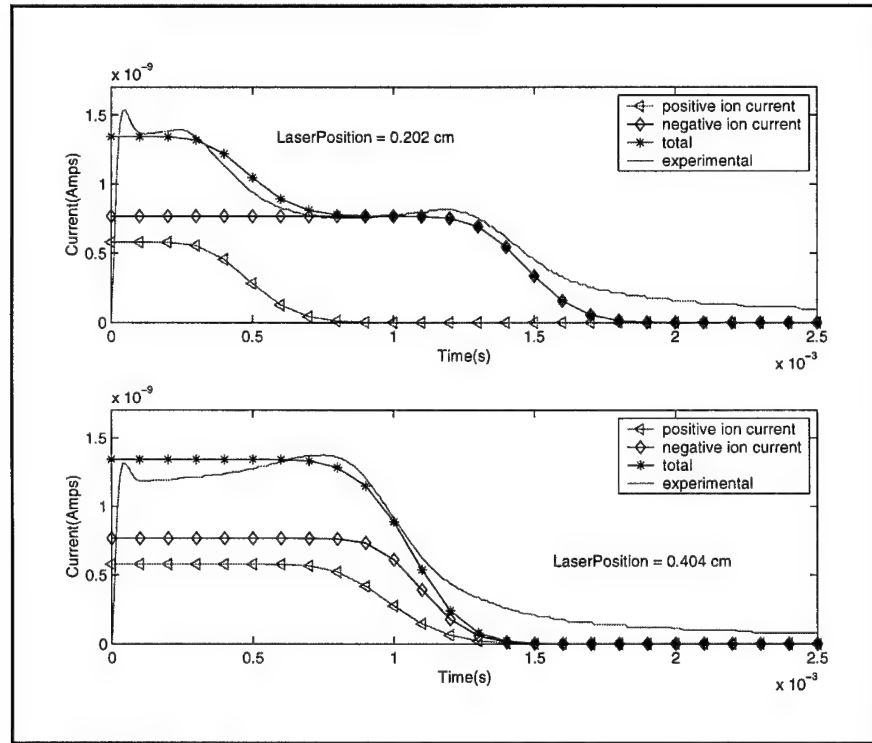


Figure 2.14. Total induced currents computed numerically and measured at ambient pressure with voltage 300 V for the initial laser position of 0.202 cm and 0.404 cm. The amplitude of the initial ion number density,  $c_0$ , is 0.25. We choose  $\mu_+ = 1.36 \text{ volt}^{-1} \text{ cm}^2 \text{ sec}^{-1}$ ,  $\mu_- = 1.82 \text{ volt}^{-1} \text{ cm}^2 \text{ sec}^{-1}$ ,  $D_+ = 0.032 \text{ cm}^2 \text{ sec}^{-1}$ , and  $D_- = 0.040 \text{ cm}^2$ .

Chapter 2 that, since the electric field and the mobilities of the positive and negative ions are regarded as constants, both the positive and negative currents are constant before the first negative ion strikes the positive electrode. Afterwards, the current decreases until the last ion reaches the positive electrode. As the ionizing laser beam is moved away from the negative electrode (grounded), the positive ions travel further, and the positive ion current is delayed in time.

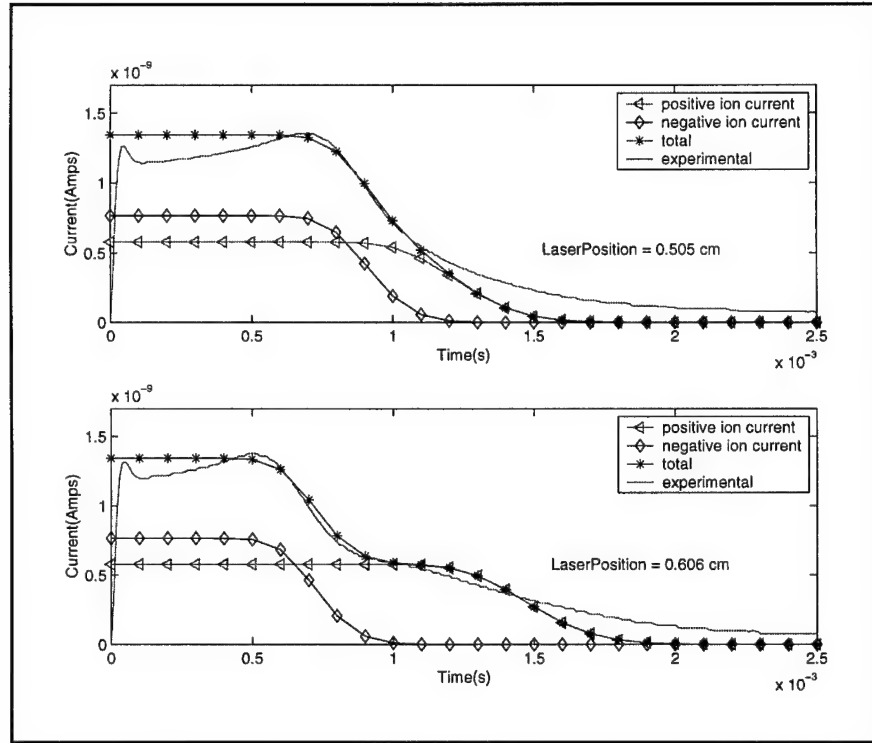


Figure 2.15. Total induced currents computed numerically and measured at ambient pressure with voltage 300 V for the initial laser position of 0.505 cm and 0.606 cm. The amplitude of the initial ion number density,  $c_0$ , is 0.25. We choose  $\mu_+ = 1.36 \text{ volt}^{-1} \text{ cm}^2 \text{ sec}^{-1}$ ,  $\mu_- = 1.82 \text{ volt}^{-1} \text{ cm}^2 \text{ sec}^{-1}$ ,  $D_+ = 0.032 \text{ cm}^2 \text{ sec}^{-1}$ , and  $D_- = 0.040 \text{ cm}^2$ .

## CHAPTER 3

### NUMERICAL MODELING FOR CYLINDER

In this chapter, we will establish the model for the behavior of laser-produced ions in an applied field and for the current induced in the external circuit by this behavior for cylindrical electrodes. Figure 3.1 represents the three-dimensional geometry of cylindrical plates. The cylindrical situation is more complicated than the parallel plates where the electric field is constant because the electric field under cylindrical electrodes is changing with position and time; that is, the velocities of moving charges vary with position between the cylinders. The assumptions that we will make here are the same as those that we used with the parallel configuration in Chapter 2. We solve Eqs. 2.16 and 2.17 with numerical methods.

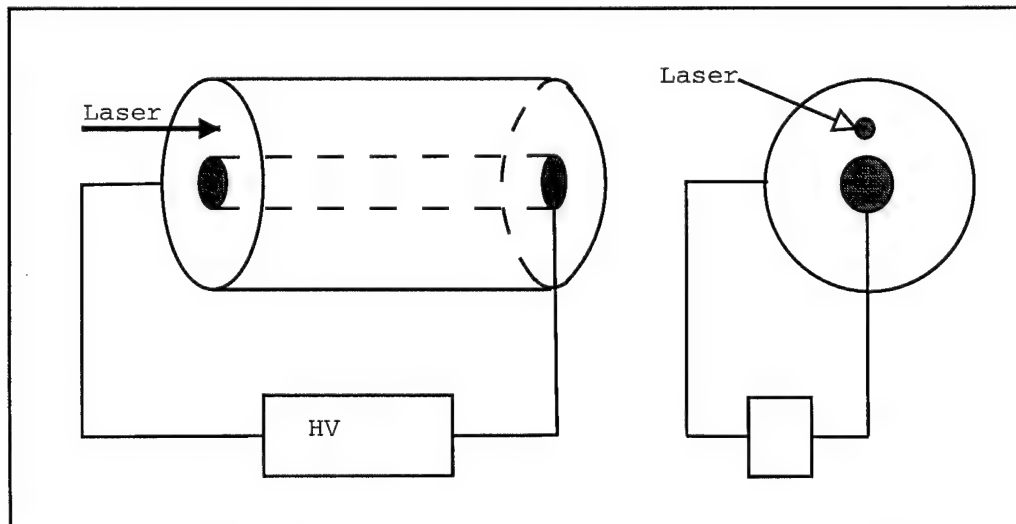


Figure 3.1. Cylindrical configuration.

### 3.1. Electric Field

Now, we compute the electric field for the cylindrical situation. Figure 3.2 represents a two-dimensional cross-section of the three-dimensional geometry between two cylindrical electrodes. Laplace's equation<sup>15</sup> for the scalar electric

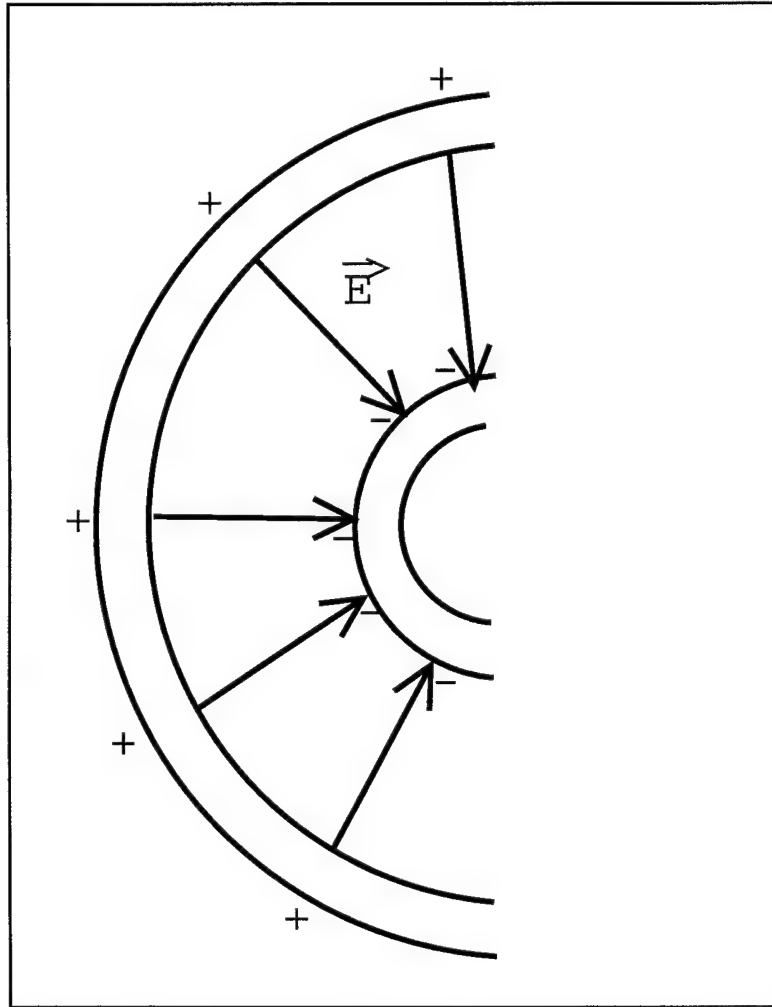


Figure 3.2. A cross-section of the three-dimensional geometry.

potential,  $V$ , in cylindrical coordinates is

$$\nabla^2 V = \frac{1}{r} \frac{\partial}{\partial r} \left( r \frac{\partial V}{\partial r} \right) + \frac{1}{r^2} \frac{\partial^2 V}{\partial \phi^2} + \frac{\partial^2 V}{\partial z^2} = 0. \quad (3.1)$$

In situations in which the length dimension of the cylindrical geometry is large in comparison to its radius, the associated field quantities may be considered to be approximately independent of  $z$ . In such cases,  $\frac{\partial^2 V}{\partial z^2} = 0$ , and Eq. 3.1 becomes the governing equation of a two-dimensional problem:

$$\frac{1}{r} \frac{\partial}{\partial r} \left( r \frac{\partial V}{\partial r} \right) + \frac{1}{r^2} \frac{\partial^2 V}{\partial \phi^2} = 0. \quad (3.2)$$

Applying the method of separation of variables, we assume a product solution

$$V(r, \phi) = R(r) \Phi(\phi), \quad (3.3)$$

where  $R(r)$  and  $\Phi(\phi)$  are, respectively, functions of  $r$  and  $\phi$ . By substituting the solution to Eq. 3.3 into Eq. 3.2, multiplying by  $r^2$ , and dividing by  $R(r) \Phi(\phi)$ , we have

$$\begin{aligned} \frac{r}{R(r)} \frac{d}{dr} \left[ r \frac{dR(r)}{dr} \right] &= k^2 \\ \frac{1}{\Phi(\phi)} \frac{d^2 \Phi(\phi)}{d\phi^2} &= -k^2. \end{aligned} \quad (3.4)$$

Figure 3.3 shows a cross-section of the coaxial cylindrical electrodes. We also assume no  $\phi$ -dependence ( $k = 0$ ) by symmetry. Eq. 3.4 then simplifies to

$$\frac{r}{R(r)} \frac{d}{dr} \left[ r \frac{dR(r)}{dr} \right] = 0 \quad (3.5)$$



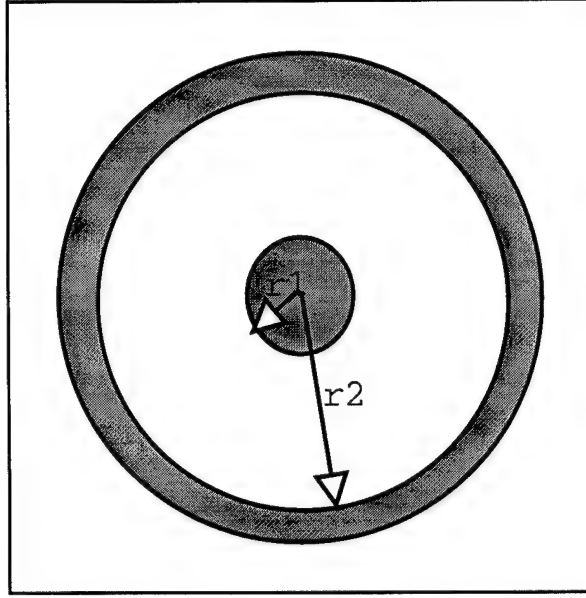


Figure 3.3. A cross-section of a coaxial cylindrical electrode.

By solving Eq. 3.5, we have a solution that is independent of either  $z$  or  $\phi$

$$V(r) = C_1 \ln r + C_2, \quad (3.6)$$

where the arbitrary constants,  $C_1$  and  $C_2$ , are determined from boundary conditions.

$$V(r_1) = 0 \quad (3.7)$$

$$V(r_2) = V_0.$$

Therefore, the electric field is

$$\mathbf{E}_r = -\nabla V = -\frac{V_0}{\left[ r \ln \left( \frac{r_2}{r_1} \right) \right]} \hat{r} = -\frac{C_0}{r} \hat{r}, \quad (3.8)$$

where  $C_0 = \frac{V_0}{\ln \left( \frac{r_2}{r_1} \right)}$ .

### 3.2. Continuity and Diffusion Equation

The continuity equations<sup>5,6</sup> regulating the time dependence of charge density at each point in the space between two cylindrical electrodes are now written

$$\frac{\partial \rho_{\pm}}{\partial t} = -\nabla \cdot \vec{J}_{\pm}, \quad (3.9)$$

where  $J_{\pm}$  are current densities (charges per square centimeter per second). The negative divergence of the current density, i.e., the charge flux into a volume element less the charge flux out of the same volume element, indicates the volumetric rate of number density increase due to non-uniform charge transport.<sup>6</sup>

The current density for the positive ions is represented as

$$\mathbf{J}_+ = -eD_+ \nabla n_+ + e\mu_+ n_+ \mathbf{E}, \quad (3.10)$$

where

$$\nabla n_+ = \frac{\partial n_+}{\partial r} \hat{r} + \frac{1}{r} \frac{\partial n_+}{\partial \phi} \hat{\phi}. \quad (3.11)$$

Substituting Eq. 3.11 into Eq. 3.10, we obtain

$$\mathbf{J}_+ = -eD_+ \frac{\partial n_+}{\partial r} \hat{r} - eD_+ \frac{1}{r} \frac{\partial n_+}{\partial \phi} \hat{\phi} + e\mu_+ n_+ \mathbf{E}, \quad (3.12)$$

where the first and second terms are diffusion terms that represent the tendency of any particle to migrate from a region of high density to a region of low density along  $r$  and  $\phi$  directions. Thus, the diffusional terms both have negative signs to indicate migration in the opposite direction to the density gradient, and the third term is the field transport term.<sup>7</sup>

The divergence of the current density is

$$\begin{aligned}
\nabla \cdot \mathbf{J}_+ &= \frac{1}{r} \frac{\partial}{\partial r} (r J_r) + \frac{1}{r} \frac{\partial J_\phi}{\partial \phi} \\
&= \frac{e}{r} \frac{\partial}{\partial r} \left[ r \left( -D_+ \frac{\partial n_+}{\partial r} + \mu_+ E_r n_+ \right) \right] - e \frac{D_+}{r} \frac{\partial}{\partial \phi} \left( \frac{1}{r} \frac{\partial n_+}{\partial \phi} \right) \\
&= -e D_+ \frac{\partial^2 n_+}{\partial r^2} - e \left( \frac{D_+ - \mu_+ C_0}{r} \right) \frac{\partial n_+}{\partial r} - \frac{e D_+}{r^2} \frac{\partial^2 n_+}{\partial \phi^2},
\end{aligned} \tag{3.13}$$

where  $C_0 = V_0 / \ln \left( \frac{r_2}{r_1} \right)$ . Eq. 3.9 becomes

$$\frac{\partial n_+}{\partial t} = D_+ \frac{\partial^2 n_+}{\partial r^2} + \left( \frac{D_+ - \mu_+ C_0}{r} \right) \frac{\partial n_+}{\partial r} + \frac{D_+}{r^2} \frac{\partial^2 n_+}{\partial \phi^2}. \tag{3.14}$$

The continuity equation for the negative ions is the same as that for the positive ions except for the direction of drift movement. Thus, the continuity equations are given by

$$\begin{aligned}
\frac{\partial n_+}{\partial t} &= D_+ \frac{\partial^2 n_+}{\partial r^2} + \left( \frac{k_+}{r} \right) \frac{\partial n_+}{\partial r} + \frac{D_+}{r^2} \frac{\partial^2 n_+}{\partial \phi^2} \\
\frac{\partial n_-}{\partial t} &= D_- \frac{\partial^2 n_-}{\partial r^2} + \left( \frac{k_-}{r} \right) \frac{\partial n_-}{\partial r} + \frac{D_-}{r^2} \frac{\partial^2 n_-}{\partial \phi^2},
\end{aligned} \tag{3.15}$$

where  $k_+ = D_+ - \mu_+ C_0$  and  $k_- = D_- + \mu_- C_0$ .

### 3.3. Positive and Negative Ion Profiles for Laser-Produced Charges

We make the assumption that laser ionization creates equal Gaussian distributions of positive and negative ions at time  $t = 0$ . Under the cylindrical coordinate system, the initial distributions of ions, shown in Figure 3.4, are given by

$$\begin{aligned}
n_\pm &= c_0 e^{-\frac{(\vec{r} - \vec{l})^2}{\sigma^2}} \\
&= c_0 e^{-\frac{(r^2 - 2lr \cos \phi + l^2)}{\sigma^2}},
\end{aligned} \tag{3.16}$$

where  $\vec{l} = \vec{r}_{las}$ , the center of the laser beam.

Now, we solve Eq. 3.15 using the finite difference method<sup>13,14,15</sup> in a similar way as we did in Chapter 2 for the parallel configuration. The following notation will be used for the value of  $n_{\pm}(r, \phi, t)$  and its derivatives at the  $(j, s, n)$  grid-point:

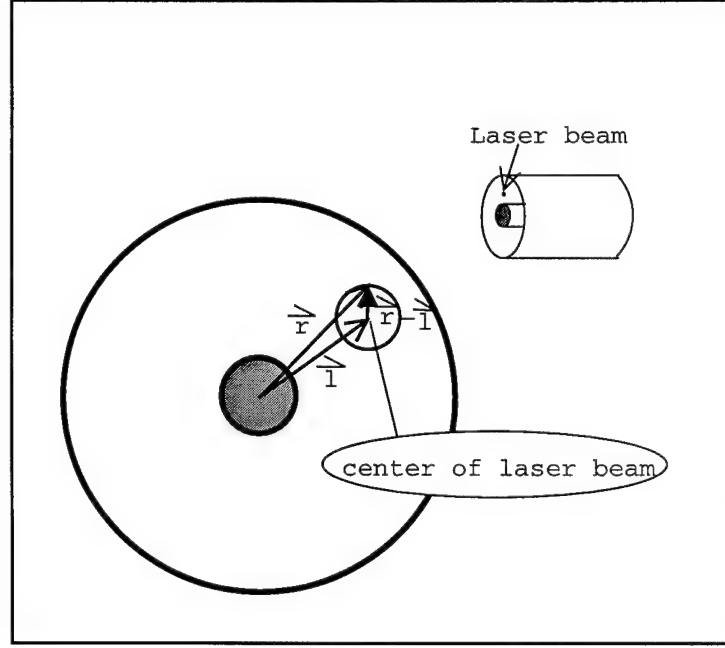


Figure 3.4. A cross-section of the three-dimensional geometry.

$$\begin{aligned}
 n_{\pm} |_{j,s}^n &= n_{\pm}(r_j, \phi_s, t_n), \\
 \frac{\partial n_{\pm}}{\partial t} |_{j,s}^n &= \frac{\partial n_{\pm}(r_j, \phi_s, t_n)}{\partial t}, \\
 \frac{\partial n_{\pm}}{\partial r} |_{j,s}^n &= \frac{\partial n_{\pm}(r_j, \phi_s, t_n)}{\partial r}, \\
 \frac{\partial^2 n_{\pm}}{\partial r^2} |_{j,s}^n &= \frac{\partial^2 n_{\pm}(r_j, \phi_s, t_n)}{\partial r^2},
 \end{aligned} \tag{3.17}$$

where  $r_j = j \triangle r$ ,  $\phi_s = s \triangle \theta$ , and  $t_n = n \triangle t$ .

We consider Eq. 3.15 evaluated at the  $(j, s, n)$  grid-point, where  $j$ ,  $s$ , and  $n$  are

position, angle, and time, respectively; that is,

$$\begin{aligned}\frac{\partial n_+}{\partial t} \Big|_{j,s}^n &= D_+ \frac{\partial^2 n_+}{\partial r^2} \Big|_{j,s}^n + \left( \frac{k_+}{r} \right) \frac{\partial n_+}{\partial r} \Big|_{j,s}^n + \frac{D_+}{r^2} \frac{\partial^2 n_+}{\partial \phi^2} \Big|_{j,s}^n \\ \frac{\partial n_-}{\partial t} \Big|_{j,s}^n &= D_- \frac{\partial^2 n_-}{\partial r^2} \Big|_{j,s}^n + \left( \frac{k_-}{r} \right) \frac{\partial n_-}{\partial r} \Big|_{j,s}^n + \frac{D_-}{r^2} \frac{\partial^2 n_-}{\partial \phi^2} \Big|_{j,s}^n.\end{aligned}\tag{3.18}$$

In the same way as in Chapter 2, the central difference approximation to the first-order spatial derivative<sup>14,15,18</sup> can be derived

$$\frac{\partial n_{\pm}}{\partial r} \Big|_{j,s}^n = \frac{n_{\pm} \Big|_{j+1,s}^n - n_{\pm} \Big|_{j-1,s}^n}{2 \Delta r} + O((\Delta r)^2).\tag{3.19}$$

The central difference approximation (finite difference) to the second-order spatial derivative<sup>14,15,18</sup> is based on the relation

$$\begin{aligned}\frac{\partial^2 n_{\pm}}{\partial r^2} \Big|_{j,s}^n &= \frac{n_{\pm} \Big|_{j+1,s}^n - 2n_{\pm} \Big|_{j,s}^n + n_{\pm} \Big|_{j-1,s}^n}{(\Delta r)^2} + O((\Delta r)^2) \\ \frac{\partial^2 n_{\pm}}{\partial \theta^2} \Big|_{j,s}^n &= \frac{n_{\pm} \Big|_{j,s+1}^n - 2n_{\pm} \Big|_{j,s}^n + n_{\pm} \Big|_{j,s-1}^n}{(\Delta \phi)^2} + O((\Delta \phi)^2).\end{aligned}\tag{3.20}$$

The forward difference approximation<sup>14,15,18</sup> to  $\frac{\partial n_{\pm}}{\partial t}$  at the  $(j, s, n)$  grid-point is

$$\frac{\partial n_{\pm}}{\partial t} \Big|_{j,s}^n = \frac{n_{\pm} \Big|_{j,s}^{n+1} - n_{\pm} \Big|_{j,s}^n}{\Delta t} + O((\Delta t)),\tag{3.21}$$

which leads to the forward difference approximation.

The reason why the central difference approximation is used here is that the error in using the central difference approximation for the values of the first- and second-order spatial derivatives is  $O((\Delta r)^2)$ , which is smaller than the error,  $O(\Delta r)$ , in using the forward difference approximation for  $\Delta r \ll 1$ .

Using Eqs. 3.19, 3.20, and 3.21, Eq. 3.18 becomes

$$\begin{aligned}
\frac{n_+ |_{j,s}^{n+1} - n_+ |_{j,s}^n}{\Delta t} + O((\Delta t)) &= D_+ \frac{n_+ |_{j+1,s}^n - 2n_+ |_{j,s}^n + n_+ |_{j-1,s}^n}{(\Delta r)^2} \\
&+ k_+ \left[ \frac{n_+ |_{j+1,s}^n - n_+ |_{j-1,s}^n}{2 \Delta r} \right] \frac{1}{r} |_{j,s}^n \\
&+ \frac{D_+}{r^2} |_{j,s}^n \left[ \frac{n_+ |_{j,s+1}^n - 2n_+ |_{j,s}^n + n_+ |_{j,s-1}^n}{(\Delta \phi)^2} \right] \\
&+ O((\Delta \phi)^2, (\Delta r)^2)
\end{aligned} \tag{3.22}$$

or

$$\begin{aligned}
\frac{n_- |_{j,s}^{n+1} - n_- |_{j,s}^n}{\Delta t} + O((\Delta t)) &= D_- \frac{n_- |_{j+1,s}^n - 2n_- |_{j,s}^n + n_- |_{j-1,s}^n}{(\Delta r)^2} \\
&+ k_- \left[ \frac{n_- |_{j+1,s}^n - n_- |_{j-1,s}^n}{2 \Delta r} \right] \frac{1}{r} |_{j,s}^n \\
&+ \frac{D_-}{r^2} |_{j,s}^n \left[ \frac{n_- |_{j,s+1}^n - 2n_- |_{j,s}^n + n_- |_{j,s-1}^n}{(\Delta \phi)^2} \right] \\
&+ O((\Delta \phi)^2, (\Delta r)^2).
\end{aligned} \tag{3.23}$$

By dropping the terms of  $O(\Delta t, (\Delta r)^2, (\Delta \phi)^2)$  from the above equation, an explicit finite difference equation,<sup>11,18</sup> which can be used to solve Eq. 3.18, is obtained. This equation is

$$\begin{aligned}
n_{\pm} |_{j,s}^{n+1} &\approx \left( S_r + \frac{C}{r_{j,s}^n} \right) n_{\pm} |_{j+1,s}^n + \left( S_r - \frac{C}{r_{j,s}^n} \right) n_{\pm} |_{j-1,s}^n \\
&+ \left( 1 - 2S_r - \frac{2S_{\phi}}{(r_{j,s}^n)^2} \right) n_{\pm} |_{j,s}^n + \frac{S_{\phi}}{(r_{j,s}^n)^2} (n_{\pm} |_{j,s+1}^n + n_{\pm} |_{j,s-1}^n),
\end{aligned} \tag{3.24}$$

where

$$\begin{aligned}
S_r &= \frac{D_{\pm} \Delta t}{(\Delta r)^2}, \\
S_{\phi} &= \frac{D_{\pm} \Delta t}{(\Delta \phi)^2}, \\
C &= \frac{k_{\pm} \Delta t}{2 (\Delta r)}.
\end{aligned} \tag{3.25}$$

Appendix D contains the source-listing of the Matlab program based on Eq. 3.18. This program is designed to trace the time history of both charged particles deposited as a Gaussian distribution and the current induced by the moving laser-produced ions in the space between two cylindrical electrodes. The user is asked by the program to supply the initial position and distribution width of the laser-produced charges. The program is written to accommodate positive and negative ions simultaneously, and the program writes output to “comma-separated variable” (filename.m) files for graphic display.

### 3.4. The Current Induced by Laser-Produced Charges

In this section, we focus on computing the current induced by the moving laser-produced charges using numerical methods. Now, we recall the Poisson equation<sup>10</sup>

$$\nabla^2 V = -\frac{\rho}{\epsilon_0}, \quad (3.26)$$

where  $\rho$  is the charge density,  $V$  is the electric potential, and  $\epsilon_0$  is the permittivity of free space. In the cylindrical coordinate system, Poisson’s equation becomes

$$\frac{1}{r} \frac{\partial}{\partial r} \left( r \frac{\partial V}{\partial r} \right) + \frac{1}{r^2} \frac{\partial^2 V}{\partial \phi^2} + \frac{\partial^2 V}{\partial z^2} = -\frac{e(n_+ - n_-)}{\epsilon_0}, \quad (3.27)$$

where we have used the number density of positive ions,  $n_+(cm^{-3})$ , and negative ions,  $n_-(cm^{-3})$ , along with the charge on a proton,  $e$ , in place of the charge density,  $\rho$ , of Eq. 3.26. If the length dimension of the cylindrical geometry is large in comparison to its radius, the associated field quantities may be considered to be approximately independent of  $z$ . Eq. 3.27 then becomes

$$\frac{1}{r} \frac{\partial}{\partial r} \left( r \frac{\partial V}{\partial r} \right) + \frac{1}{r^2} \frac{\partial^2 V}{\partial \phi^2} = -\frac{e(n_+ - n_-)}{\epsilon_0} \quad (3.28)$$

or

$$\frac{\partial^2 V}{\partial r^2} + \frac{1}{r} \frac{\partial V}{\partial r} + \frac{1}{r^2} \frac{\partial^2 V}{\partial \phi^2} = -\frac{e(n_+ - n_-)}{\epsilon_0} \quad (3.29)$$

The solution domain in  $r - \phi$  space is segmented by circle grids and radial lines since the potential and the magnitude of the electric field are dependent on the variables,  $\phi$  and  $r$ . The values of  $\Delta r$  and  $\Delta \phi$  are assumed uniform as shown in Figure 3.5. Consider Eq. 3.29 evaluated at the  $(j, s, n)$  grid-point; that is,

$$\frac{\partial^2 V}{\partial r^2} \Big|_{j,s}^n + \frac{1}{r} \frac{\partial V}{\partial r} \Big|_{j,s}^n + \frac{1}{r^2} \frac{\partial^2 V}{\partial \phi^2} \Big|_{j,s}^n = -\frac{e(n_+ \Big|_{j,s}^n - n_- \Big|_{j,s}^n)}{\epsilon_0}, \quad (3.30)$$

where  $j$ ,  $s$ , and  $n$  are given by  $r_j = j\Delta r$ ,  $s_\phi = s\Delta \phi$ , and  $t_n = n\Delta t$ , respectively. If the central difference approximation is used for both the first-order and the second-order derivatives,<sup>14,15</sup> the above equation becomes

$$\begin{aligned} & \frac{V \Big|_{j+1,s}^n - 2V \Big|_{j,s}^n + V \Big|_{j-1,s}^n}{(\Delta r)^2} + \frac{1}{r} \Big|_{j,s}^n \frac{V \Big|_{j+1,s}^n - V \Big|_{j-1,s}^n}{2(\Delta r)} \\ & + \frac{1}{r^2} \Big|_{j,s}^n \frac{V \Big|_{j,s+1}^n - 2V \Big|_{j,s}^n + V \Big|_{j,s-1}^n}{(\Delta \phi)^2} + O((\Delta r)^2, (\Delta \phi)^2) \\ & = -\frac{e(n_+ \Big|_{j,s}^n - n_- \Big|_{j,s}^n)}{\epsilon_0}. \end{aligned} \quad (3.31)$$

Note that the superscript  $n$  indicates the time level, and the subscripts  $j$  and  $s$  indicate the space and angle levels. We solve Eq. 3.30 for the distribution of the potentials between the two cylindrical electrodes and then calculate the distribution of the electric fields corresponding to these potentials. Figure 3.5 shows the distribution of both the electric fields and the potentials between two cylindrical electrodes.



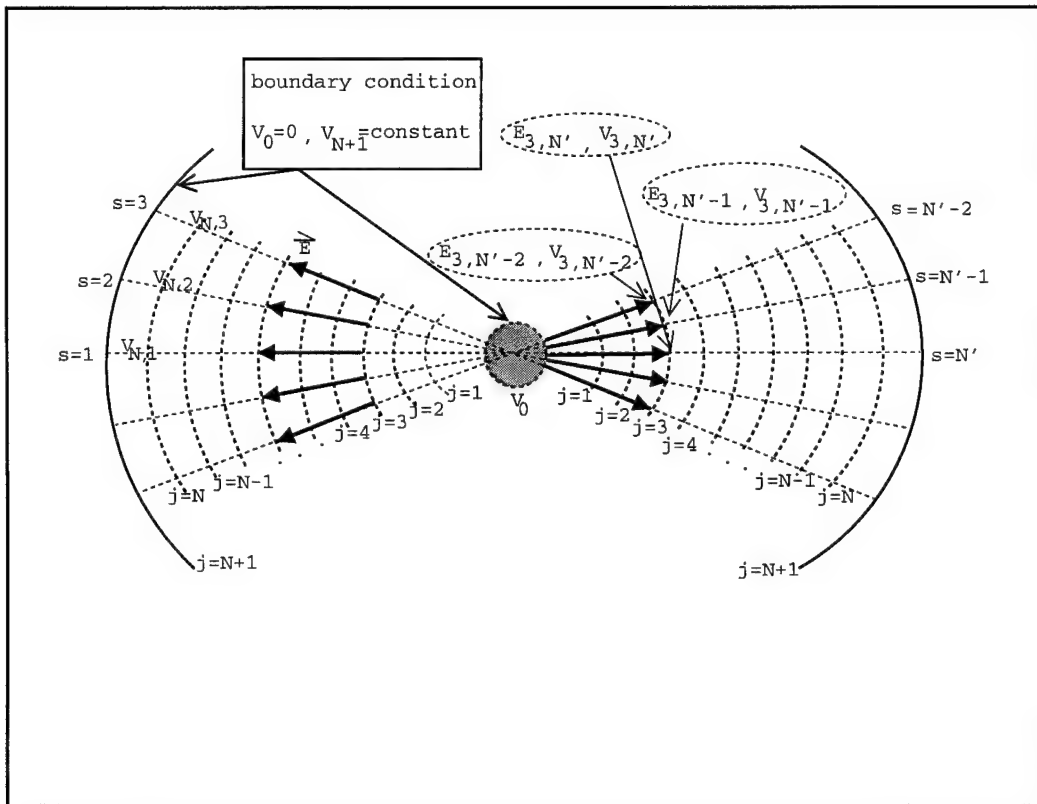


Figure 3.5. Distribution of the electric fields and the potentials.

By dropping the error term of  $O((\Delta r)^2, (\Delta \phi)^2)$ , Eq. 3.31 now becomes

$$\begin{aligned} & \frac{V|_{j+1,s}^n - 2V|_{j,s}^n + V|_{j-1,s}^n}{(\Delta r)^2} + \frac{1}{r} |_{j,s}^n \frac{V|_{j+1,s}^n - V|_{j-1,s}^n}{2(\Delta r)} \\ & + \frac{1}{r^2} |_{j,s}^n \frac{V|_{j,s+1}^n - 2V|_{j,s}^n + V|_{j,s-1}^n}{(\Delta \phi)^2} \\ & \approx -\frac{e(n_+ |_{j,s}^n - n_- |_{j,s}^n)}{\epsilon_0}. \end{aligned} \quad (3.32)$$

Multiply both sides of Eq. 3.32 by  $(\Delta r)^2$ ; substitute

$r|_{j,s}^n = r_1 + k\Delta r = (N_1 + k)\Delta r = j\Delta r$  into Eq. 3.32; and then obtain

$$\begin{aligned} & V|_{j+1,s}^n - 2V|_{j,s}^n + V|_{j-1,s}^n + \frac{V|_{j+1,s}^n - V|_{j-1,s}^n}{2j} + \frac{V|_{j,s+1}^n - 2V|_{j,s}^n + V|_{j,s-1}^n}{(j(\Delta \phi))^2} \\ & \approx -\frac{e(\Delta r)^2(n_+ |_{j,s}^n - n_- |_{j,s}^n)}{\epsilon_0} \end{aligned} \quad (3.33)$$

or

$$\begin{aligned} & \left(1 - \frac{1}{2j}\right) V|_{j-1,s}^n + \frac{1}{(j\Delta \phi)^2} V|_{j,s-1}^n - 2 \left[1 + \frac{1}{(j\Delta \phi)^2}\right] V|_{j,s}^n \\ & + \frac{1}{(j\Delta \phi)^2} V|_{j,s+1}^n + \left(1 + \frac{1}{2j}\right) V|_{j+1,s}^n \\ & \approx -\frac{e(\Delta r)^2}{\epsilon_0} (n_+ |_{j,s}^n - n_- |_{j,s}^n), \end{aligned} \quad (3.34)$$

where  $j = 1, 2, 3, \dots, N-1$ ;  $s = 1, 2, 3, \dots, N'$ ;  $r_1$  is the radius of the inner cylinder;

and  $N_1 = \frac{r_1}{\Delta r}$ . Note that the boundaries are at  $j = 0$  and  $j = N+1$ , that is,  $V|_{0,s}^n = 0$

and  $V|_{N+1,s}^n = V_0$ . Eqs. 3.34 can be written at the time  $t = n\Delta t$ .

$$A\vec{V} = \vec{M}, \quad (3.35)$$

where

$$\vec{V} = \begin{pmatrix} V |_{1,1}^n \\ \cdot \\ \cdot \\ \cdot \\ V |_{2,1}^n \\ \cdot \\ \cdot \\ \cdot \\ V |_{N,1}^n \\ \cdot \\ \cdot \\ \cdot \\ V |_{N,N'}^n \end{pmatrix} \quad (3.36)$$

$$\vec{M} = -\frac{e (\Delta r)^2}{\epsilon_0} \begin{pmatrix} (n_+ |_{1,1}^n - n_- |_{1,1}^n) \\ (n_+ |_{1,2}^n - n_- |_{1,2}^n) \\ \cdot \\ \cdot \\ (n_+ |_{1,N'}^n - n_- |_{1,N'}^n) \\ \cdot \\ \cdot \\ (n_+ |_{N,1}^n - n_- |_{N,1}^n) \\ \cdot \\ \cdot \\ (n_+ |_{N,N'}^n - n_- |_{N,N'}^n) \end{pmatrix}. \quad (3.37)$$

$$A = \begin{pmatrix} B|_{1,s}^n & C|_{1,s}^n & 0 & 0 & 0 & 0 & \cdot & \cdot & \cdot & 0 & 0 \\ A|_{2,s}^n & B|_{2,s}^n & C|_{2,s}^n & 0 & 0 & 0 & \cdot & \cdot & \cdot & 0 & 0 \\ 0 & A|_{3,s}^n & B|_{3,s}^n & C|_{3,s}^n & 0 & 0 & \cdot & \cdot & \cdot & 0 & 0 \\ 0 & 0 & A|_{4,s}^n & B|_{4,s}^n & C|_{4,s}^n & 0 & \cdot & \cdot & \cdot & 0 & 0 \\ 0 & 0 & 0 & A|_{5,s}^n & B|_{5,s}^n & C|_{5,s}^n & \cdot & \cdot & \cdot & 0 & 0 \\ \cdot & \cdot & \cdot & \cdot & \cdot & \cdot & \cdot & \cdot & \cdot & \cdot & \cdot \\ \cdot & \cdot & \cdot & \cdot & \cdot & \cdot & \cdot & \cdot & \cdot & \cdot & \cdot \\ \cdot & \cdot & \cdot & \cdot & \cdot & \cdot & \cdot & \cdot & \cdot & \cdot & \cdot \\ 0 & 0 & 0 & 0 & 0 & 0 & \cdot & \cdot & \cdot & A|_{N,s}^n & B|_{N,s}^n \end{pmatrix}, \quad (3.38)$$

where

$$A|_{j,s}^n = \begin{pmatrix} \left(1 - \frac{1}{2j}\right) & 0 & 0 & \cdot & \cdot & \cdot & 0 \\ 0 & \left(1 - \frac{1}{2j}\right) & 0 & \cdot & \cdot & \cdot & 0 \\ 0 & 0 & \left(1 - \frac{1}{2j}\right) & \cdot & \cdot & \cdot & 0 \\ \cdot & \cdot & \cdot & \cdot & \cdot & \cdot & \cdot \\ \cdot & \cdot & \cdot & \cdot & \cdot & \cdot & \cdot \\ \cdot & \cdot & \cdot & \cdot & \cdot & \cdot & \cdot \\ 0 & 0 & 0 & \cdot & \cdot & \cdot & \left(1 - \frac{1}{2j}\right) \end{pmatrix} \quad (3.39)$$

$$C|_{j,s}^n = \begin{pmatrix} \left(1 + \frac{1}{2j}\right) & 0 & 0 & \cdot & \cdot & \cdot & 0 \\ 0 & \left(1 + \frac{1}{2j}\right) & 0 & \cdot & \cdot & \cdot & 0 \\ 0 & 0 & \left(1 + \frac{1}{2j}\right) & \cdot & \cdot & \cdot & 0 \\ \cdot & \cdot & \cdot & \cdot & \cdot & \cdot & \cdot \\ \cdot & \cdot & \cdot & \cdot & \cdot & \cdot & \cdot \\ \cdot & \cdot & \cdot & \cdot & \cdot & \cdot & \cdot \\ 0 & 0 & 0 & \cdot & \cdot & \cdot & \left(1 + \frac{1}{2j}\right) \end{pmatrix}. \quad (3.40)$$

$$B |_{j,s}^n = \begin{pmatrix} -2 \left[ 1 + \frac{1}{(j\Delta\phi)^2} \right] & \frac{2}{(j\Delta\phi)^2} & 0 & \cdot & \cdot & \cdot & 0 \\ \frac{1}{(j\Delta\phi)^2} & -2 \left[ 1 + \frac{1}{(j\Delta\phi)^2} \right] & \frac{1}{(j\Delta\phi)^2} & \cdot & \cdot & \cdot & 0 \\ 0 & \frac{1}{(j\Delta\phi)^2} & -2 \left[ 1 + \frac{1}{(j\Delta\phi)^2} \right] & \cdot & \cdot & \cdot & 0 \\ \cdot & \cdot & \cdot & \cdot & \cdot & \cdot & \cdot \\ \cdot & \cdot & \cdot & \cdot & \cdot & \cdot & \cdot \\ \cdot & \cdot & \cdot & \cdot & \cdot & \cdot & \cdot \\ 0 & 0 & 0 & \cdot & \cdot & \cdot & -2 \left[ 1 + \frac{1}{(j\Delta\phi)^2} \right] \end{pmatrix} \quad (3.41)$$

We can solve Eq. 3.34 for the potential distributions in the space between two cylindrical electrodes. We also have the relationship between the electric field and potential<sup>15</sup> as follows

$$\mathbf{E}(\mathbf{r}, \phi) = -\nabla V = -\frac{\partial V}{\partial r} \hat{r} - \frac{1}{r} \frac{\partial V}{\partial \phi} \hat{\phi}. \quad (3.42)$$

By evaluating Eq. 3.42 at the grid-point  $(j, s, n)$ , we then get

$$E_r(r, \phi) |_{j,s}^n = -\frac{\partial V}{\partial r} |_{j,s}^n. \quad (3.43)$$

It is easy to calculate the radial distribution of the electric fields based on the following relation using the central difference approximation to the first order potential derivative with respect to both  $r$  and  $\phi$  at the particular time  $t = n\Delta t$ .

$$E_r |_{j,s}^n = -\frac{V |_{j+1,s}^n - V |_{j-1,s}^n}{2(\Delta r)} + O((\Delta r)^2), \quad (3.44)$$

where  $j = 1, 2, 3, \dots, N$  and  $s = 1, 2, 3, \dots, N'$ . By dropping the term of  $O((\Delta r)^2)$

from Eq. 3.44, an explicit finite difference equation is obtained

$$E_r|_{j,s}^n \approx -\frac{V|_{j+1,s}^n - V|_{j-1,s}^n}{2(\Delta r)}. \quad (3.45)$$

Now, we use the electric field close to the inner cylinder ( $E_r|_{1,s}^n$ ) to calculate the surface charges induced by the moving laser-produced charges on the inner cylinder using Gauss' law at given time  $t_n = n\Delta t$  as follows

$$\oint_{all-surface} \mathbf{E} \cdot d\mathbf{a} = \frac{Q_{enclosed}}{\epsilon_0}, \quad (3.46)$$

$$Q|_j^n = \sum_{s=1}^{s=N'} L(r_1 + j\Delta r) (\Delta\phi) E_r|_{j,s}^n, \quad (3.47)$$

or

$$Q|_1^n = 2 \sum_{s=1}^{s=N'} L(r_1 + \Delta r) (\Delta\phi) E_r|_{1,s}^n, \quad (3.48)$$

where  $L$  is the length of the cylinder,  $j$  is from 1 to  $N$ ,  $s$  is from 1 to  $N'$ , and  $\phi$  is from 0 to  $\pi$ . Similarly, we can calculate the induced charges on the surface of the inner cylinder at the time  $t = (n+1)\Delta t$

$$Q|_1^{n+1} = 2 \sum_{s=1}^{s=N'} L(r_1 + \Delta r) (\Delta\phi) E_r|_{1,s}^{n+1}. \quad (3.49)$$

The current induced by moving charges from  $t_n = n\Delta t$  to  $t_{n+1} = (n+1)\Delta t$  is

$$i_{inner} = \frac{Q|_1^{n+1} - Q|_1^n}{\Delta t}. \quad (3.50)$$

The induced charges on the surface of the outer cylinder are calculated through using Eq. 3.46 at  $t = n\Delta t$ . If we choose the Gaussian surface within the outer

cylinder that is a perfect conductor, then we get

$$\oint_{all-surface} \mathbf{E} \cdot d\mathbf{a} = 0 = \frac{Q_{enclosed}}{\epsilon_0}, \quad (3.51)$$

$$Q_{enclosed}^n = Q_{inner}^n + Q_{between-cylinder}^n + Q_{outer}^n = 0, \quad (3.52)$$

or

$$Q_{outer}^n = -Q_{inner}^n - Q_{between-cylinder}^n, \quad (3.53)$$

where  $Q_{between-cylinder}^n = en_+^n - en_-^n$ . The current flowing out from the outer cylinder from  $t = n\Delta t$  to  $t = (n+1)\Delta t$  is

$$i_{outer}^n = \frac{Q_{outer}^{n+1} - Q_{outer}^n}{\Delta t}. \quad (3.54)$$

The total current is given

$$i_{total}^n = i_{inner}^n - i_{outer}^n. \quad (3.55)$$

Appendix D contains the source-listing of the Matlab program, based on Eq. 3.34.

This program is written to keep track of how the current induced by laser-produced charges changes with time.

### 3.5. Comparison of Numerical Results to Experimental Waveforms

Figures 3.6-3.10 show the computed current induced by the positive and negative ions, compared to the experimental waveforms, for laser positions of 1 mm, 2 mm, 3 mm, 4 mm, and 4.5 mm from the center of the cylinder. For the first figure, at 1 mm from the center, the positive styrene molecules move only 0.95 mm (radius of inner cylinder: 0.05 mm) to reach the grounded electrode while the negative ions travel a much longer distance (4 mm) to arrive at the positive electrode (outer cylinder). The current induced by the positive ions reaches a maximum in a very

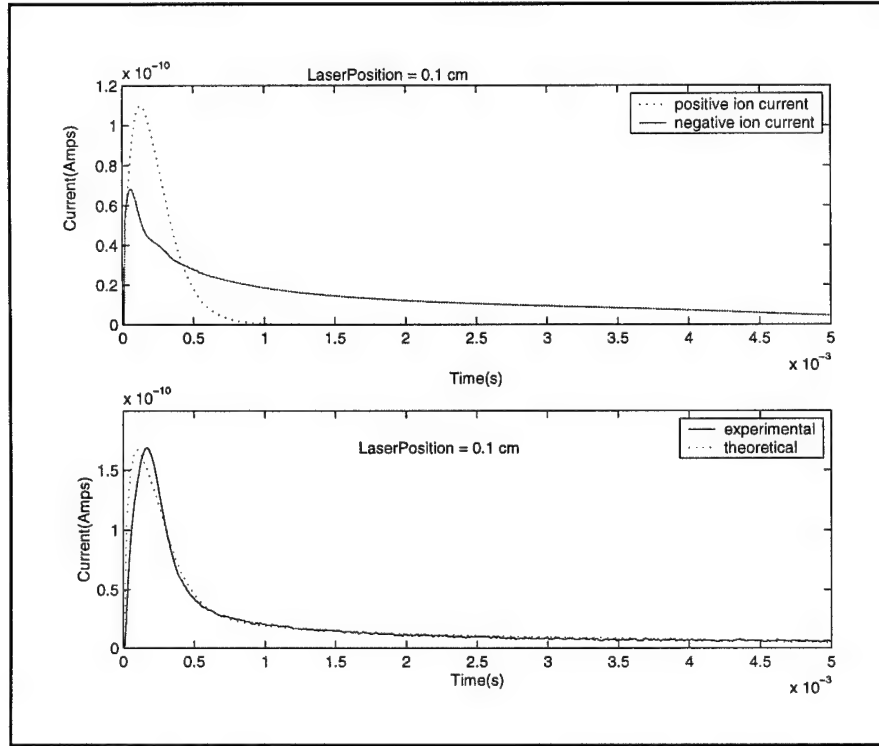


Figure 3.6. The positive ion and negative ion currents computed numerically at initial laser position of 1 mm are shown in the top figure. The lower figure compares the total induced current calculated numerically to that measured at ambient pressure with a 100 V bias for the initial laser position of 1 mm. The calculation parameters were  $c_0 = 0.25$ ,  $\mu_+ = 1.36 \text{ volt}^{-1} \text{ cm}^2 \text{ sec}^{-1}$ ,  $\mu_- = 1.82 \text{ volt}^{-1} \text{ cm}^2 \text{ sec}^{-1}$ ,  $D_+ = 0.032 \text{ cm}^2 \text{ sec}^{-1}$ , and  $D_- = 0.040 \text{ cm}^2$ .



short time and then goes to zero. Since the electric field increases as  $\frac{1}{r}$  approaching the inner cylinder and the drift velocity is proportional to the electric field, it is seen that the magnitude of the positive ion current is greater than that of the negative ion current, and the increase of the positive ion current is faster than the decrease of the negative ion current. As the laser is moved away from the inner cylinder, the positive ions travel farther, and the positive ion current is delayed in time. For Figures 3.9 and 3.10, the total current first drops slowly. The shapes of the induced current curves in Figures 3.6-3.10 are determined by the combined effects of the mobilities and the radially dependent electric field. As seen in these figures, the numerical model gives a good, qualitative interpretation of the experimental waveforms. The physical process of the induced current is nicely illustrated by Figures 3.6-3.10 where the positive ion current, the negative ion current, and the total current between the cylindrical electrodes are plotted according to calculations based on equations related to the induced current (Chapter 2).

It must also be emphasized that several parameters, such as the mobilities, diffusion coefficients of both positive and negative ions, and laser width, are not precisely known. In Figure 3.11, it is observed that the current slopes decrease with an increase of the diffusion coefficients in the same manner as the parallel configuration. Figure 3.12 shows how different values of the positive and the negative mobilities affect the shape of the induced current curve. As the mobilities increase, the drift velocities also increase, resulting in a narrower peak with a larger maximum current. For Figure 3.13, as the laser width varies, the width of the induced current peak varies proportionately as expected. Since experiments have been done in nearly the same conditions for both parallel and cylindrical configurations, the same values of these parameters, mobilities, diffusion coefficients, laser width, and amplitude of the initial ion distribution, as those applied in the parallel case (Chapter 2) are

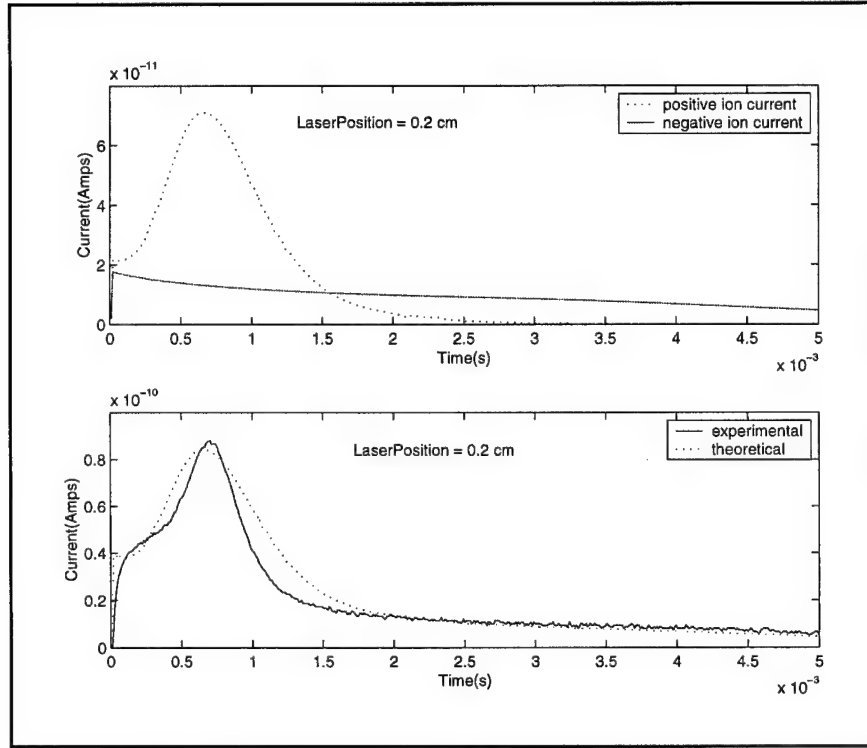


Figure 3.7. The positive ion and negative ion currents computed numerically at initial laser position of 2 mm are shown in the top figure. The lower figure compares the total induced current calculated numerically to that measured at ambient pressure with a 100 V bias for the initial laser position of 2 mm. The calculation parameters were  $c_0 = 0.25$ ,  $\mu_+ = 1.36 \text{ volt}^{-1} \text{ cm}^2 \text{ sec}^{-1}$ ,  $\mu_- = 1.82 \text{ volt}^{-1} \text{ cm}^2 \text{ sec}^{-1}$ ,  $D_+ = 0.032 \text{ cm}^2 \text{ sec}^{-1}$ , and  $D_- = 0.040 \text{ cm}^2$ .

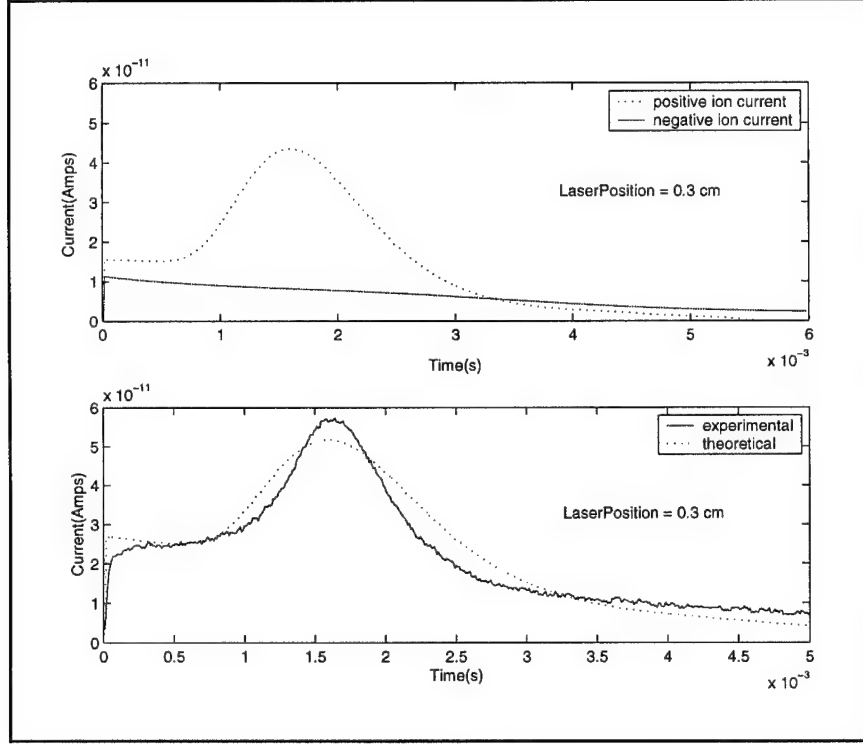


Figure 3.8. The positive ion and negative ion currents computed numerically at initial laser position of 3 mm are shown in the top figure. The lower figure compares the total induced current calculated numerically to that measured at ambient pressure with a 100 V bias for the initial laser position of 3 mm. The calculation parameters were  $c_0 = 0.25$ ,  $\mu_+ = 1.36 \text{ volt}^{-1} \text{ cm}^2 \text{ sec}^{-1}$ ,  $\mu_- = 1.82 \text{ volt}^{-1} \text{ cm}^2 \text{ sec}^{-1}$ ,  $D_+ = 0.032 \text{ cm}^2 \text{ sec}^{-1}$ , and  $D_- = 0.040 \text{ cm}^2$ .

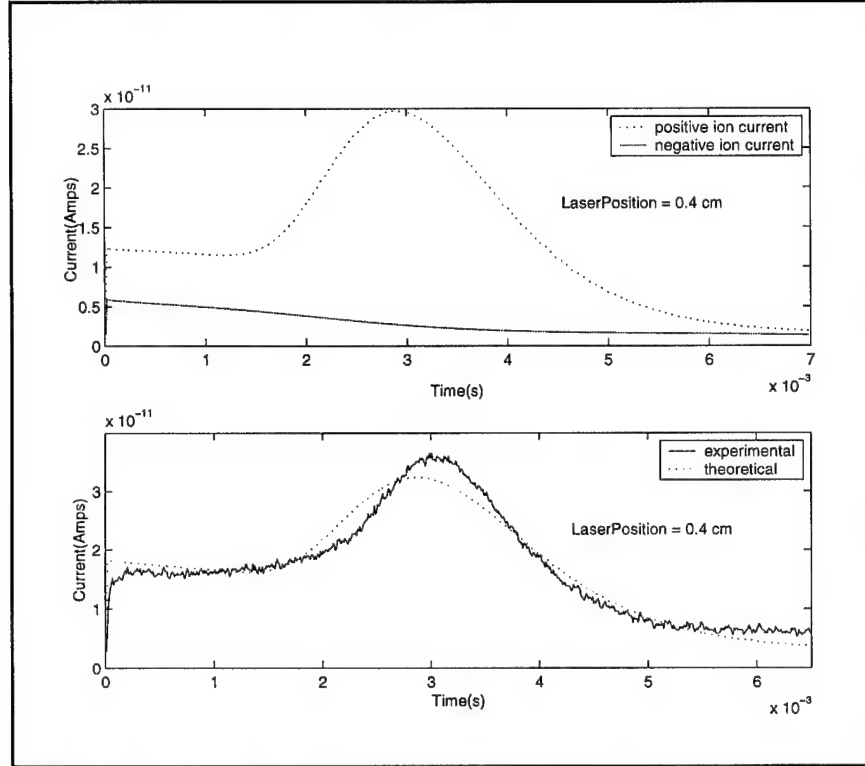


Figure 3.9. The positive ion and negative ion currents computed numerically at initial laser position of 4 mm are shown in the top figure. The lower figure compares the total induced current calculated numerically to that measured at ambient pressure with a 100 V bias for the initial laser position of 4 mm. The calculation parameters were  $c_0 = 0.25$ ,  $\mu_+ = 1.36 \text{ volt}^{-1} \text{ cm}^2 \text{ sec}^{-1}$ ,  $\mu_- = 1.82 \text{ volt}^{-1} \text{ cm}^2 \text{ sec}^{-1}$ ,  $D_+ = 0.032 \text{ cm}^2 \text{ sec}^{-1}$ , and  $D_- = 0.040 \text{ cm}^2$ .

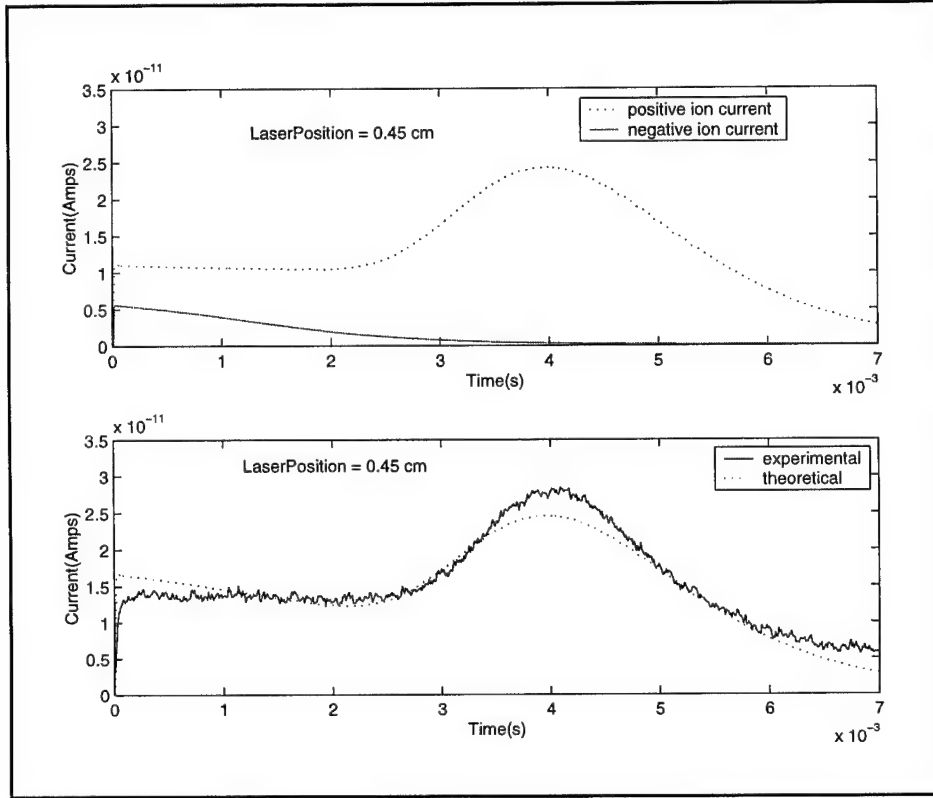


Figure 3.10. The positive ion and negative ion currents computed numerically at initial laser position of 4.5 mm are shown in the top figure. The lower figure compares the total induced current calculated numerically to that measured at ambient pressure with a 100 V bias for the initial laser position of 4.5 mm. The calculation parameters were  $c_0 = 0.25$ ,  $\mu_+ = 1.36 \text{ volt}^{-1} \text{ cm}^2 \text{ sec}^{-1}$ ,  $\mu_- = 1.82 \text{ volt}^{-1} \text{ cm}^2 \text{ sec}^{-1}$ ,  $D_+ = 0.032 \text{ cm}^2 \text{ sec}^{-1}$ , and  $D_- = 0.040 \text{ cm}^2$ .

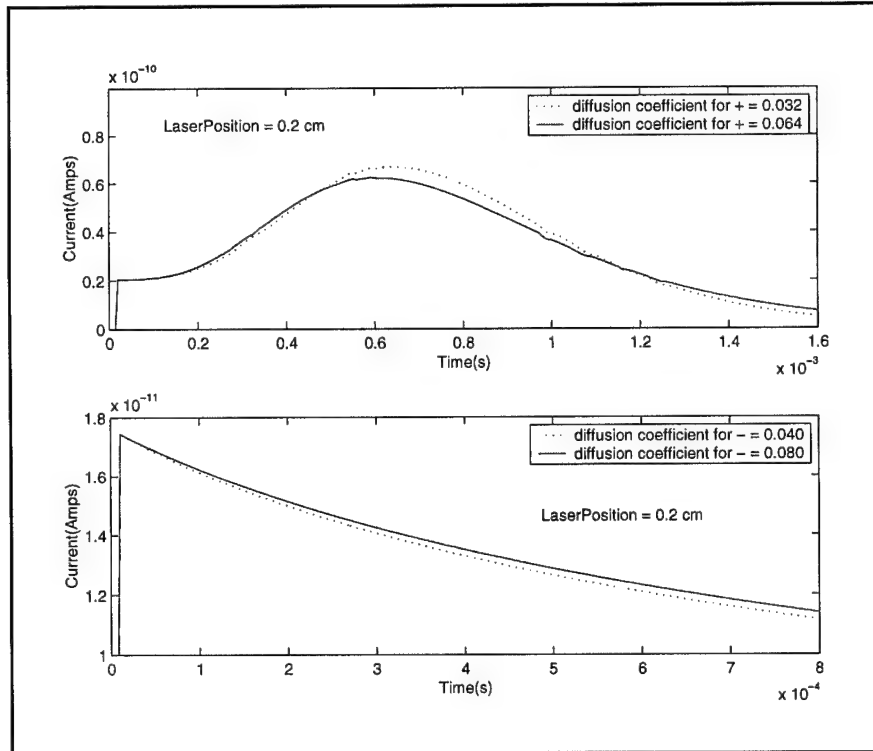


Figure 3.11. Same as Figure 3.7 showing the influence of choosing different diffusion coefficients on the induced current.

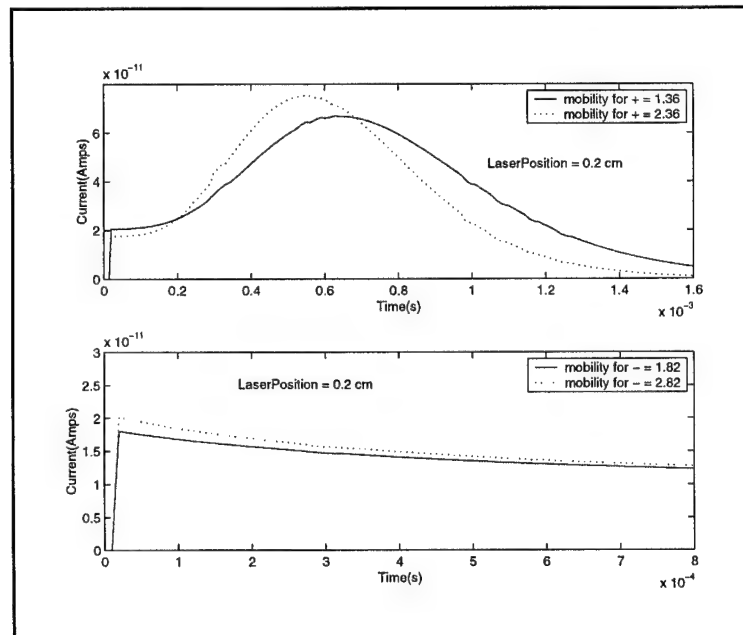


Figure 3.12. Same as Figure 3.7 showing the influence of choosing different mobilities on the induced current.

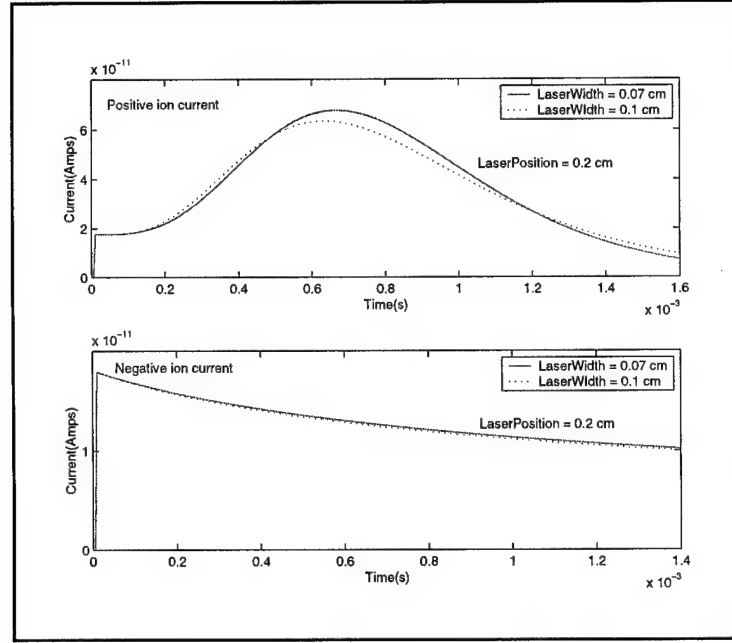


Figure 3.13. The influence of choosing different laser widths on the induced current.

chosen; that is,

$$\begin{aligned}
 \mu_+ &= 1.36 \text{ cm}^2 \text{V}^{-1} \text{s}^{-1} \\
 D_+ &= 0.032 \text{ cm}^2 \text{s}^{-1} \\
 \mu_- &= 1.82 \text{ cm}^2 \text{V}^{-1} \text{s}^{-1} \\
 D_- &= 0.04 \text{ cm}^2 \text{s}^{-1} \\
 \sigma &= 0.1 \text{ cm} \\
 c_0 &= 0.25.
 \end{aligned}
 \tag{3.56}$$

These parameters may be dependent on the operating conditions. For example, the mobility for negative oxygen molecules has been measured,<sup>6,12</sup> but the effective mobility in the experiments may differ. When negative oxygen molecules are present in the cell, a reaction may take place where the  $O_2^-$  ions form clusters; that is, water molecules stick to  $O_2^-$  to form  $(H_2O)_n O_2^-$ , where  $n$  represents the number of water

molecules sticking to  $O_2^-$ . The extent of water molecule clustering that happens under our experimental conditions is not clear; however, the values of the parameters used in modeling are in a reasonable range.<sup>3,6,8,12</sup> Hayhurst et al.<sup>19</sup> reported two mobilities of  $2.38 \text{ cm}^2 \text{ V}^{-1} \text{ s}^{-1}$  and  $2.27 \text{ cm}^2 \text{ V}^{-1} \text{ s}^{-1}$  for negative ion oxygen at room temperature ( $25^\circ\text{C}$ ) under dry and wet conditions. Kolaitis and Lubman<sup>20</sup> measured, analyzed, and compared the ion mobilities using both radioactive and laser ion sources to ionize the molecules in a gas. After the ions produced by laser are formed, they could react with the components of a gas to form other ions at ambient pressure. For example, positive styrene ions ( $M^+$ ) in air could react with the components of air to form other ions, such as  $MH^+$ ,  $(M-H)^+$ , and  $(M-2H)^+$ . These combinations would result in different values of mobilities for the styrene ions. However, generally, the difference between these different ions is not large. We have measured the mobility for styrene ion in a drift tube as approximately  $1.70 \text{ cm}^2 \text{ V}^{-1} \text{ s}^{-1}$  at  $25^\circ\text{C}$  in atmospheric pressure air. In future work, we will measure the mobilities and diffusion coefficients of the positive styrene molecules as well as the negative oxygen molecules.



## CHAPTER 4

### DISCUSSION AND CONCLUSION

#### 4.1. Discussion

The numerical approach described in Chapters 2 and 3 is the explicit finite difference method.<sup>14,15</sup> At the new time level,  $t = (n + 1)\Delta t$ , the finite difference equations (Eqs. 2.34 and 3.24) contain the one unknown value,  $n_{\pm} |^{n+1}$ , which is calculated explicitly from values known at previous time levels. This approach is easy to program and requires few computations to determine the values of  $n_{\pm} |^{n+1}$  at each new time level. Unfortunately, this method is restricted to very small time steps,  $\Delta t$ . In general, this approach is not very stable.<sup>14,15</sup> In ongoing work, we intend to use the implicit finite difference in order to make the numerical computation more stable.

We considered this model in two different cases, the parallel and the cylindrical electrode configurations. In both cases, it is reasonable to neglect the influence of ionization due to ion collisions and recombination in a gas on the induced current in an ideal situation in which  $E/P$  ( $E$ : electric field between two electrodes and  $P$ : gas pressure) is low and the laser-induced ion number density is small. However, in general, this ideal situation is not satisfied, and we will include the effect of ionization and recombination due to ion collisions in future work.

In addition, since the time scale for electron attachment<sup>21</sup> is nanoseconds and the time scale for the measured ion drift is microseconds, we can make the assumption that, as soon as a free electron is available, it immediately attaches to an oxygen molecule to form a negative ion.

For modeling the motion of the distributions of laser-induced ions in the parallel

configuration, the mathematical description is simplified by reducing the three dimensions to one.<sup>5</sup> However, in the cylindrical case, two dimensions were applied to the numerical model.

In both parallel and cylindrical configurations, we assumed that the laser-generated ion number density is small enough to ignore the effect of the electric field produced by the space charges between the two electrodes while we calculate the ion number densities,  $n_+$  and  $n_-$ . Under this assumption,  $\mathbf{E}$  of Eqs. 2.16, 2.17, and 3.13 is equal to the external electric field. However,  $\mathbf{E}$  is equal to the superposition of the external electric field and the electric field induced by space charges between the two electrodes.

The space charge effects seen in the experimental parallel data of Figure 4.1 can be explained qualitatively as follows.

**Region A** For a very short time (from 0 to approximately 0.1 ms), the positive ion and negative ion swarms are overlapped. If we assume that charge is distributed uniformly throughout the volume of the infinitely long swarm cylinders, then the electric field in the overlap region is given by

$$E = \frac{1}{2\epsilon_0} \rho d, \quad (4.1)$$

where  $d$  is the distance between the centers of the swarm cylinders and  $E$  opposes the external field. For our conditions, it ranges from 0  $V/cm$  at time 0 to 80  $V/cm$  at time 0.1 ms ( $d = 0.9$  mm) when they barely overlap compared to the applied external field of 300  $V/cm$ . Since the directions of the electric field induced by the ion swarms and the applied external field are opposite, the total electric field is reduced in the overlap region. Consequently, the drift velocities of the positive and negative ions decrease, resulting in the reduction of the induced current (Eq. 2.10).

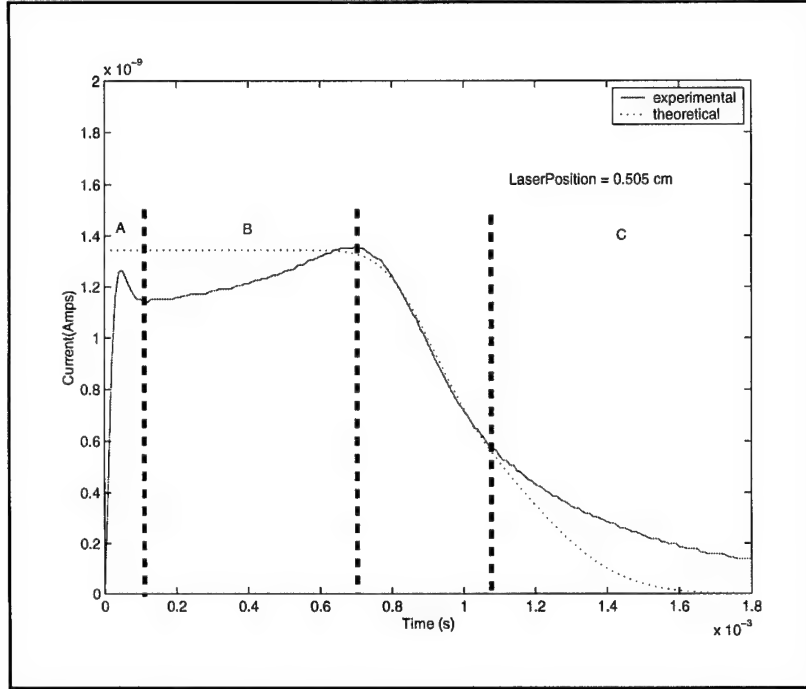


Figure 4.1. This figure compares the total induced current calculated numerically to that measured at ambient pressure with a 300 V bias for the initial laser position of 5.05 mm. The calculation parameters were  $c_0 = 0.25$ ,  $\mu_+ = 1.36 \text{ volt}^{-1} \text{ cm}^2 \text{ sec}^{-1}$ ,  $\mu_- = 1.82 \text{ volt}^{-1} \text{ cm}^2 \text{ sec}^{-1}$ ,  $D_+ = 0.032 \text{ cm}^2 \text{ sec}^{-1}$ , and  $D_- = 0.040 \text{ cm}^2$ .

**Region B** After separation, the electric field due to one swarm at the center of the other will be

$$E = \frac{\rho R^2}{2\epsilon_0 d}, \quad (4.2)$$

where  $R$  is the radius of ion swarm cylinders. Since this electric field, which has a value of  $25 \text{ V/cm}$  at  $d = 1 \text{ mm}$  and  $5.6 \text{ V/cm}$  at  $d = 0.44 \text{ cm}$ , is opposite to the external electric field and decreasing with time, the total electric field is increasing. Consequently, the drift velocities of the positive and negative ions are now slowly increasing, causing an increase of the induced current.

**Region C** Within the swarm, the electric field at point  $r$  due to the other charges in the swarm is given by

$$E = \frac{\rho r}{2\epsilon_0}. \quad (4.3)$$

The value of this electric field varies from 0 at the center of the swarm to  $49 \text{ V/cm}$  at  $r = 0.5 \text{ mm}$ . This electric field within the swarms results in broadening of the swarm in addition to the diffusion effect. In other words, the slope in Figure 4.1C becomes smaller.

We plan to incorporate additional effects into the model, including recombination, space charge, and free electron attachment rate. We further plan to measure the mobility and the diffusion coefficients of the positive and the negative ions by optimizing the numerical model fit to experimental data.

## 4.2. Conclusion

We have developed a model for the behavior of laser-produced ion distributions and for the subsequent induced current flow in an external circuit connected to the biased electrodes. This model allowed the quantitative determination of the time evolution of the induced current and the laser-generated ion distributions in the

presence of an applied electric field. The numerical solutions provided the picture of the laser-induced charge distributions moving in a gas between parallel plates as well as cylindrical electrodes and the measured induced current behavior with time. A numerical model was first established to describe the laser-induced charge distributions,  $n_+$  and  $n_-$ , and dynamics of the positive and negative ions between the parallel plate and cylindrical electrodes.

We described the model in two different cases, parallel and cylindrical configuration. In the first case, both the analytical and numerical approaches are used to solve for the charge distribution and consequent induced current. They showed good agreement with the experimental results. In the second one, the numerical method was applied to calculate the charge distributions and induced current as a function of time. It is also shown that the variation of the total current induced by the laser-generated positive and negative ions results mainly from the positive current. The modeling was greatly simplified by making the assumptions mentioned above; however, the theoretical results demonstrated good agreement with experimental results.

## REFERENCES CITED

- [1] O.F. Swenson, G.D. Gillispie, and C.J. Walls, *Trends in Optics and Photonics Series* **8**, 1996.
- [2] D.H. Parker, *Laser Ionization Spectroscopy and Mass Spectrometry in Ultrasensitive Laser Spectroscopy* edited by D. S. Kliger (Academic Press, New York, 1983).
- [3] J.J. Lowke, *Aust. J. Phys.* **15**, 39, 1962.
- [4] K. Giles and E. P. Grimsrud, *J. Phys. Chem.* **96**, 6680-6687, 1992.
- [5] J.C. Travis and Gregory C. Turk, *Laser-Enhanced Ionization Spectrometry* (John Wiley & Sons, Inc., New York, 1996).
- [6] L. G. H. Huxley, *Aust. J. Phys.* **25**, 523-527, 1972.
- [7] E. Nasser, *Fundamentals of Gaseous Ionization and Plasma Electronics* (John Wiley & Sons, Inc., New York, 1971).
- [8] G.A. Eiceman and Z. Karpas, *Ion Mobility Spectrometry* (CRC Press, Inc., New York, 1972).
- [9] L.G. Christophorou, *Atomic and Molecular Radiation Physics* (John Wiley & Sons, Inc., New York, 1971).
- [10] J. D. Jackson, *Classical Electrodynamics* 3<sup>rd</sup> ed., (John Wiley & Sons, Inc., New York, 1975).
- [11] L. Lapidus and G.F. Prinder, *Numerical Solution of Partial Differential Equations in Science and Engineering* (John Wiley & Sons, Inc., New York, 1982).
- [12] C. Shumate, R.H. St. Louis, and H.H. Hill, *Journal of Chromatography* **373**, 141-173, 1986.
- [13] M. Ikawa, *Hyperbolic Partial Differential Equations and Wave Phenomena* (American Mathematical Society, Providence, R.I., 2000).
- [14] G.D. Smith, *Numerical Solution of Partial Differential Equations - Finite Difference Methods* (Clarendon Press, New York, 1978).

- [15] J. Noye, *Numerical Solutions of Partial Differential Equations* (University of Adelaide, Australia, 1981)
- [16] L. Von Rosenberg, *Methods for the Numerical Solution of Partial Differential Equations* (American Elsevier Pub. Co., New York, 1969).
- [17] Symposium on the numerical solution of partial differential equations, *Numerical Solution of Partial Differential Equations* (Academic Press, New York, 1986).
- [18] I. Fried, *Numerical Solution of Differential Equations* (Academic Press, New York, 1979).
- [19] C.J. Hayhurst, P. Watts, and A. Wilders, *International Journal of Mass Spectrometry and Ion Processes* **121**, 127-139, 1992.
- [20] L. Kolaitis and D.M. Lubman, *Analytical Chemistry* **58**, 9, August 1986-1995.
- [21] L.G.H. Huxley and R.W. Crompton, *The Diffusion and Drift of Electrons in Gases* (John Wiley & Sons, Inc., New York, 1974).
- [22] E. Zauderer, *Partial Differential Equations of Applied Mathematics* 2<sup>nd</sup> ed., (John Wiley & Sons, Inc., New York, 1988).

## APPENDIX A

### ANALYTICAL SOLUTIONS OF EQS. 2.16 AND 2.17

$$\frac{\partial n_+}{\partial t} = -\frac{\partial}{\partial x} \left( +\mu_+ E n_+ - D_+ \frac{\partial n_+}{\partial x} \right) \quad (\text{A.1})$$

$$\frac{\partial n_-}{\partial t} = -\frac{\partial}{\partial x} \left( +\mu_- E n_- - D_- \frac{\partial n_-}{\partial x} \right) \quad (\text{A.2})$$

Laser ionization is assumed to create equal Gaussian distributions of positive and negative ions at time  $t = 0$ .

$$n_+(x, t = 0) = c_0 e^{-\frac{4(x-x_l)^2}{\sigma^2}}, \quad (\text{A.3})$$

where  $c_0$  represents the amplitude of the ion distribution at  $t = 0$ .

The Fourier Transform,<sup>22</sup>  $N_+(\lambda, t)$ , of  $n_+(x, t)$  is defined as

$$N_+(\lambda, t) = \frac{1}{\sqrt{2\pi}} \int_{-\infty}^{\infty} e^{i\lambda x} n_+(x, t) dx. \quad (\text{A.4})$$

Multiply both sides of Eq. A.1 by  $\frac{1}{\sqrt{2\pi}} e^{i\lambda x}$ , and integrate with respect to  $x$  from  $-\infty$  to  $\infty$  to obtain

$$\begin{aligned} \frac{1}{\sqrt{2\pi}} \int_{-\infty}^{\infty} e^{i\lambda x} \frac{\partial n_+(x, t)}{\partial t} dx &= \frac{1}{\sqrt{2\pi}} \int_{-\infty}^{\infty} D_+ e^{i\lambda x} \frac{\partial^2 n_+(x, t)}{\partial x^2} dx \\ &\quad - \frac{1}{\sqrt{2\pi}} \int_{-\infty}^{\infty} \mu_+ E e^{i\lambda x} \frac{\partial n_+(x, t)}{\partial x} dx \end{aligned} \quad (\text{A.5})$$

or

$$\frac{\partial}{\partial t} N_+(\lambda, t) = -\lambda^2 D_+ N_+(\lambda, t) + \mu_+ E \lambda N_+(\lambda, t) i \quad (\text{A.6})$$



or

$$\frac{dN_+}{N_+} = (-\lambda^2 D_+ + \mu_+ E i \lambda) dt. \quad (\text{A.7})$$

The Fourier Transform of the positive number density is

$$N_+(\lambda, t) = N_+(\lambda, t=0) e^{(-D_+ \lambda^2 + \mu_+ E i \lambda) t}, \quad (\text{A.8})$$

where  $N_+(\lambda, t=0)$  is the Fourier Transform of  $n_+(x, t=0)$  (A.3); that is,

$$N_+(\lambda, t=0) = \frac{1}{\sqrt{2\pi}} \int_{-\infty}^{\infty} e^{i\lambda x} n_+(x, t=0) dx, \quad (\text{A.9})$$

where  $n_+(x, t=0) = c_0 e^{-\frac{4(x-x_l)^2}{\sigma^2}}$ .

To solve for  $n_+(x, t)$ , we take the inverse the Fourier Transform of Eq. A.4

$$\begin{aligned} n_+(x, t) &= \frac{1}{\sqrt{2\pi}} \int_{-\infty}^{\infty} e^{-i\lambda x} N_+(\lambda, t) d\lambda \\ &= \frac{1}{\sqrt{2\pi}} \int_{-\infty}^{\infty} N_+(\lambda, t=0) e^{-i\lambda x} e^{(-D_+ \lambda^2 + \mu_+ E i \lambda) t} d\lambda \\ &= \frac{c_0}{2\pi} \int_{-\infty}^{\infty} \int_{-\infty}^{\infty} e^{i\lambda s} n_+(s, t=0) e^{-i\lambda x} e^{(-D_+ \lambda^2 + \mu_+ E i \lambda) t} d\lambda ds \\ &= \frac{c_0}{2\pi} \int_{-\infty}^{\infty} \int_{-\infty}^{\infty} e^{i\lambda s} e^{-\frac{4(s-x_l)^2}{\sigma^2}} e^{-i\lambda x} e^{(-D_+ \lambda^2 + \mu_+ E i \lambda) t} d\lambda ds \\ &= \frac{c_0}{2\pi} \int_{-\infty}^{\infty} e^{-\frac{4(s-x_l)^2}{\sigma^2}} \left( \int_{-\infty}^{\infty} e^{i\lambda(s-x)} e^{(-D_+ \lambda^2 + \mu_+ E i \lambda) t} d\lambda \right) ds \\ &= \frac{c_0}{2\pi} \int_{-\infty}^{\infty} e^{-\frac{4(s-x_l)^2}{\sigma^2}} \left( \int_{-\infty}^{\infty} e^{-D_+ t \lambda^2} e^{i[(s-x) + \mu_+ E t] \lambda} d\lambda \right) ds \\ &= \frac{c_0}{2\pi} \int_{-\infty}^{\infty} e^{-\frac{4(s-x_l)^2}{\sigma^2}} \left( \int_{-\infty}^{\infty} e^{-(\sqrt{D_+ t})^2 \lambda^2} e^{i[(s-x) + \mu_+ E t] \lambda} d\lambda \right) ds. \end{aligned} \quad (\text{A.10})$$

To evaluate the inner integral, let  $a = \sqrt{D_+ t}$  and  $b = i[(s-x) + \mu_+ E t]$ ; that is,

$$\int_{-\infty}^{\infty} e^{-D_+ t \lambda^2} e^{i[(s-x) + \mu_+ E t] \lambda} d\lambda = \int_{-\infty}^{\infty} e^{-a^2 \lambda^2} e^{b \lambda} d\lambda. \quad (\text{A.11})$$

Let  $\int_{-\infty}^{\infty} e^{-a^2 \lambda^2} e^{b\lambda} d\lambda = I$ ; then,

$$\begin{aligned}
I &= \int_{-\infty}^{\infty} e^{-a^2(\lambda^2 - \frac{b}{a^2})} d\lambda \\
&= \int_{-\infty}^{\infty} e^{-a^2(\lambda - \frac{b}{2a^2})^2} e^{\frac{b^2}{4a^2}} d\lambda \\
&= \frac{\sqrt{\pi}}{a} e^{\frac{b^2}{4a^2}}.
\end{aligned} \tag{A.12}$$

Eq. A.11 now becomes

$$I = \frac{\sqrt{\pi}}{a} e^{\frac{b^2}{4a^2}} = \frac{\sqrt{\pi}}{\sqrt{D_+ t}} e^{\frac{(i(s-x) + \mu_+ Et)^2}{4D_+ t}} = \frac{\sqrt{\pi}}{\sqrt{D_+ t}} e^{-\frac{((s-x) + \mu_+ Et)^2}{4D_+ t}}. \tag{A.13}$$

By inserting Eq. A.13 into Eq. A.10, we obtain

$$\begin{aligned}
n_+(x, t) &= \frac{c_0}{2\pi} \frac{\sqrt{\pi}}{\sqrt{D_+ t}} \int_{-\infty}^{\infty} e^{-\frac{((s-x) + \mu_+ Et)^2}{4D_+ t} - \frac{4(s-x_l)^2}{\sigma^2}} ds \\
&= \frac{c_0}{2\pi} \frac{\sqrt{\pi}}{\sqrt{D_+ t}} \int_{-\infty}^{\infty} e^{-\frac{(s-x)^2 + s\mu_+ Et + \mu_+^2 E^2 t^2}{4D_+ t}} e^{-\frac{4(s^2 - 2sx_l + x_l^2)}{\sigma^2}} ds \\
&= \frac{c_0}{2\pi} \frac{\sqrt{\pi}}{\sqrt{D_+ t}} \int_{-\infty}^{\infty} e^{-\frac{(x-\mu_+ Et)^2}{4D_+ t} - \frac{4x_l^2}{\sigma^2}} e^{-\frac{s^2 - 2xs + 2\mu_+ Ets}{4D_+ t}} e^{-\frac{4s^2 - 8sx_l}{\sigma^2}} ds \\
&= \frac{c_0}{2\pi} \frac{\sqrt{\pi}}{\sqrt{D_+ t}} \int_{-\infty}^{\infty} e^{-\frac{(x-\mu_+ Et)^2}{4D_+ t} - \frac{4x_l^2}{\sigma^2}} e^{-(\frac{1}{4D_+ t} + \frac{4}{\sigma^2})s^2} e^{(\frac{2(x-\mu_+ Et)}{4D_+ t} + \frac{8x_l}{\sigma^2})s} ds \\
&= \frac{c_0}{2\pi} \frac{\sqrt{\pi}}{\sqrt{D_+ t}} e^{-\frac{(x-\mu_+ Et)^2}{4D_+ t} - \frac{4x_l^2}{\sigma^2}} \int_{-\infty}^{\infty} e^{-(\frac{1}{4D_+ t} + \frac{4}{\sigma^2})s^2} e^{(\frac{2(x-\mu_+ Et)}{4D_+ t} + \frac{8x_l}{\sigma^2})s} ds.
\end{aligned} \tag{A.14}$$

Since  $\int_{-\infty}^{\infty} e^{-a^2 \lambda^2} e^{b\lambda} d\lambda = \frac{\sqrt{\pi}}{a} e^{\frac{b^2}{4a^2}}$ , Eq. A.14 becomes

$$\begin{aligned}
n_+(x, t) &= \frac{c_0}{2\pi} \frac{\sqrt{\pi}}{\sqrt{D_+ t}} \frac{\sqrt{\pi}}{\sqrt{\frac{1}{4D_+ t} + \frac{4}{\sigma^2}}} e^{-\frac{(x-\mu_+ Et)^2}{4D_+ t} - \frac{4x_l^2}{\sigma^2}} e^{\frac{[\frac{(x-\mu_+ Et)}{2D_+ t} + \frac{8x_l}{\sigma^2}]^2}{4(\frac{1}{4D_+ t} + \frac{4}{\sigma^2})}} \\
&= \frac{c_0}{2\pi} \frac{\sqrt{\pi}}{\sqrt{D_+ t}} \frac{\sqrt{\pi}}{\sqrt{\frac{1}{4D_+ t} + \frac{4}{\sigma^2}}} e^{-\frac{4}{\sigma^2 + 16D_+ t} ((x-\mu_+ Et)^2 - 2x_l(x-\mu_+ Et) + x_l^2)} \\
n_+(x, t) &= \frac{\sigma c_0}{\sqrt{\sigma^2 + 16D_+ t}} e^{-\frac{4(x-x_l-\mu_+ Et)^2}{\sigma^2 + 16D_+ t}}.
\end{aligned} \tag{A.15}$$

Similarly, the solution for a negative charge distribution is

$$n_{-}(x, t) = \frac{\sigma c_0}{\sqrt{\sigma^2 + 16D_{-}t}} e^{-\frac{4(x-x_l+\mu_{-}Et)^2}{\sigma^2+16D_{-}t}}. \quad (\text{A.16})$$

## APPENDIX B

### NUMERICAL SOLUTIONS OF EQS. 2.16 AND 2.17

#### B.1. Consistency

A finite difference equation (Eq. 2.34) is said to be *consistent* with a partial differential equation (Eq. 2.16) if, in the limit as the grid spacing tends to zero, the difference equation becomes the same as the partial differential equation at each point in the solution domain. We wish to determine how closely Eq. 2.34 corresponds to Eq. 2.16 at the (j,k) grid-point, that is, how close it is to

$$\frac{\partial n_+}{\partial t} \Big|_j^k + \mu_+ E \frac{\partial n_+}{\partial x} \Big|_j^k = D_+ \frac{\partial^2 n_+}{\partial^2 x} \Big|_j^k. \quad (\text{B.1})$$

Evaluating Eq. 2.16 at the (j,k) grid-point using the Finite Difference techniques, we obtain the solution as follows:

$$n_+ \Big|_j^{k+1} = \left( S + \frac{1}{2}C \right) n_+ \Big|_{j-1}^k + (1 - 2S) n_+ \Big|_j^k + \left( S - \frac{1}{2}C \right) n_+ \Big|_{j+1}^k. \quad (\text{B.2})$$

The truncation error for this approach is usually  $O [(\Delta t)^2, (\Delta t)(\Delta x)^2]$ .

Substitution of the Taylor series expansion about the (j,k) grid-point for each term

of Eq. B.2 gives

$$\begin{aligned}
& \left( n_+ |_j^k + \Delta t \frac{\partial n_+}{\partial t} |_j^k + \frac{(\Delta t)^2}{2!} \frac{\partial^2 n_+}{\partial t^2} |_j^k + \frac{(\Delta t)^3}{3!} \frac{\partial^3 n_+}{\partial t^3} |_j^k + \dots \right) = \\
& \left( S + \frac{1}{2}C \right) \left( n_+ |_j^k - \Delta x \frac{\partial n_+}{\partial x} |_j^k + \frac{(\Delta x)^2}{2!} \frac{\partial^2 n_+}{\partial x^2} |_j^k - \frac{(\Delta x)^3}{3!} \frac{\partial^3 n_+}{\partial x^3} |_j^k + \dots \right) + \\
& \left( S - \frac{1}{2}C \right) \left( n_+ |_j^k + \Delta x \frac{\partial n_+}{\partial x} |_j^k + \frac{(\Delta x)^2}{2!} \frac{\partial^2 n_+}{\partial x^2} |_j^k + \frac{(\Delta x)^3}{3!} \frac{\partial^3 n_+}{\partial x^3} |_j^k + \dots \right) + \\
& (1 - 2S) n_+ |_j^k,
\end{aligned} \tag{B.3}$$

where  $C = \frac{\mu_+ E \Delta t}{\Delta x}$  and  $S = \frac{D_+ \Delta t}{(\Delta x)^2}$ .

Upon simplifying, using  $C = \frac{\mu_+ E \Delta t}{\Delta x}$  and  $S = \frac{D_+ \Delta t}{(\Delta x)^2}$ , Eq. B.29 becomes

$$\frac{\partial n_+}{\partial t} |_j^k = -\mu_+ E \frac{\partial n_+}{\partial x} |_j^k + D_+ \frac{\partial^2 n_+}{\partial x^2} |_j^k - \frac{\Delta t}{2} \frac{\partial^2 n_+}{\partial t^2} |_j^k + O((\Delta t)^2, (\Delta x)^2). \tag{B.4}$$

Since  $n_+$  is the solution to Eq. 2.16, it follows that

$$\frac{\partial}{\partial t} (n_+) = - \left( -\mu_+ E \frac{\partial}{\partial x} - D_+ \frac{\partial^2}{\partial x^2} \right) n_+, \tag{B.5}$$

$$\frac{\partial^2}{\partial t^2} (n_+) = \left( \frac{\partial}{\partial t} \right)^2 n_+ = \left( \mu_+^2 E^2 \frac{\partial^2}{\partial x^2} - 2\mu_+ E D_+ \frac{\partial^3}{\partial x^3} + D_+^2 \frac{\partial^4}{\partial x^4} \right) n_+. \tag{B.6}$$

By substituting Eq. B.6 into Eq. B.4, we obtain

$$\begin{aligned}
\frac{\partial n_+}{\partial t} |_j^k &= -\mu_+ E \frac{\partial n_+}{\partial x} |_j^k + D_+ \frac{\partial^2 n_+}{\partial x^2} |_j^k + O((\Delta t)^2, (\Delta x)^2) \\
&\quad - \frac{\Delta t}{2} \left( \mu_+^2 E^2 \frac{\partial^2 n_+}{\partial x^2} |_j^k - 2\mu_+ E D_+ \frac{\partial^3 n_+}{\partial x^3} |_j^k + D_+^2 \frac{\partial^4 n_+}{\partial x^4} |_j^k \right)
\end{aligned} \tag{B.7}$$

or

$$\frac{\partial n_+}{\partial t} |_j^k = -\mu_+ E \frac{\partial n_+}{\partial x} |_j^k + \left( D_+ - \widetilde{D}_+ \right) \frac{\partial^2 n_+}{\partial x^2} |_j^k + O(\Delta t, (\Delta x)^2), \tag{B.8}$$

where  $\widetilde{D}_+ = \frac{1}{2} \mu_+^2 E^2 \Delta t$ . For negative charges, we obtain the same result as the

positive charges; that is,

$$\frac{\partial n_-}{\partial t} \big|_j^k = \mu_- E \frac{\partial n_-}{\partial x} \big|_j^k + (D_- - \widetilde{D}_-) \frac{\partial^2 n_-}{\partial^2 x} \big|_j^k + O(\Delta t, (\Delta x)^2), \quad (\text{B.9})$$

where  $\widetilde{D}_- = \frac{1}{2}\mu_-^2 E^2 \Delta t$ .

It is obvious that Eq. 2.34 is consistent with Eq. 2.16 as

$$\begin{aligned} \widetilde{D}_+ &< D_+ \\ \widetilde{D}_- &< D_- \end{aligned} \quad (\text{B.10})$$

or

$$\begin{aligned} \Delta t &< \frac{2D_+}{\mu_+^2 E^2} \\ \Delta t &< \frac{2D_-}{\mu_-^2 E^2} \end{aligned} \quad (\text{B.11})$$

or

$$\Delta t < \min \left( \frac{2D_+}{\mu_+^2 E^2}, \frac{2D_-}{\mu_-^2 E^2} \right). \quad (\text{B.12})$$

If  $\Delta t$  and  $\Delta x$  ( $\Delta t \sim 10^{-5}$  and  $\Delta x \sim 10^{-3}$ ) become smaller, then the numerical solution is closer to the analytical solution (shown in Figure 2.9). The numerical approach used here has decreased the effect of the diffusion term,  $D_{\pm} \frac{\partial^2 n_{\pm}}{\partial x^2}$ , in Eq. 2.16 by an amount  $\frac{1}{2}\mu_{\pm}^2 E^2 \Delta t \frac{\partial^2 n_{\pm}}{\partial^2 x}$ ,<sup>18</sup> which can be large if  $\mu_{\pm}$ ,  $E$  and  $\Delta t$  are large.

## APPENDIX C

### SOURCE CODE FOR PARALLEL PLATES

This program models the behavior of positive and negative ion distributions under the influence of an applied electric field for parallel configuration. By using the explicit finite difference approach, we obtain the positive and negative ion number densities,  $n_+(x, t)$  and  $n_-(x, t)$ , at every time step. From Chapter 2, the charges induced by a point charge,  $q$ , on the surfaces of both electrodes are given

$$\begin{aligned} q_1 &= -q\left(\frac{L_0 - x_Q}{L_0}\right) \\ q_2 &= -q\left(\frac{x_Q}{L_0}\right), \end{aligned} \tag{C.1}$$

where  $q_1$  is the charge induced on the cathode,  $q_2$  is the charge induced on the anode, and  $x_Q$  is the initial position of point charge  $q$ . Since the charge is now a distribution rather than a point charge, the total induced charges on each electrode are an integral over the distance between two electrodes. Then, the induced current is  $I = \frac{dq}{dt}$ . The only reason why I wrote this program using  $C++$  as well as MatLab is that I want to make sure the programming is correct.

#### C.1. Code Written in C++

```
#include < sys/types.h >
#include < iostream.h >
#include < string.h >
#include < math.h >
#include < stdlib.h >
```

```

#include < stdio.h >
#include < io.h >
struct times { int number1; number2 }
times T;
times1 T1;
void SaveFile(double [],int,int);
void main()
{
    FILE*outfile;
    FILE*file;
    double n1[200],n2[200],n1_new[200],n2_new[200];
    //number density of total charges
    double v=300,//applied potential
           xlas,//the position of laser
           wl; //laser width
    double dt=3e-6;
    double q10=0.0,q_10=0.0,q20=0.0,q_20=0.0,q=0.0,
           q_new=0.0,q1=0.0,
           q1_new=0.0,a0=1.6e-19,t;
    double m=1.36,d=0.032+0.5*m*m*E*E*dt;
    double m1=1.82,d1=0.04+0.5*m1*m1*E*E*dt;
    double E=-300;
    cout<<"Enter Laser position(0;XL;1.0):";
    cin>>xlas;
    cout<<"Enter Laser Width(WL;XL/2):";
    cin>>wl;
    if (( outfile = fopen( "CURRENT`DATA.m", "wb" )) == NULL)
    {
        fprintf(stderr, "can't open output file %s / n");
        exit(1);
    }
    if (( file = fopen( "TIME`DATA.m", "wb" )) == NULL)
    {

```



```

        fprintf(stderr, "can't open output file s / n");
        exit(1);
    }
    double x;
    double dx=0.005;
    int nx,i;
    nx=int(1/dx);
    double a1,a2;
    a1=(2*d)/(m*m*v*v);
    a2=(dx*dx)/(2*d);
    for(i=0;i<nx;i++)
    {
        x=i*dx;
        n1[i]=0.25*exp((-4*(x-xlas)*(x-xlas))/(wl*wl));
        n2[i]=0.25*exp((-4*(x-xlas)*(x-xlas))/(wl*wl));
        q10=q10+n1[i]*dx*(1-i*dx);
        q20=q20+n2[i]*dx*(1-i*dx);
        q_10= q_10 + n1[i]*dx*i*dx;
        q_20=q_20+n2[i]*dx*i*dx;
    }
    double current;
    double T=1/(m*v);
    for(t=0;t<T;t=t+dt)
    {
        double c1=(m*E*dt)/(2*dx),c2=(m1*E*dt)/(2*dx); //multiply by E
        double s1=(d*dt)/(dx*dx),s2=(d1*dt)/(dx*dx);
        double l,Q,l1,Q1;
        Q=q10;
        Q1=q20;
        Q_new=q_10;
        Q_1=q_20
        for(int k=0;k<nx;k++)
        {

```

```

        n1_new[k]=(s1-c1)*n1[k+1]+(s1+c1)*n1[k-1]+(1-2*s1)*n1[k];
        n2_new[k]=(s2+c2)*n2[k+1]+(s2-c2)*n2[k-1]+(1-2*s2)*n2[k];
        q=q+n1_new[k]*dx*(1-k*dx);
        q1=q1+n2_new[k]*dx*(1-k*dx);
        q_new=q_new + n1_new[k]*dx*k*dx;
        q1_new=q1_new+n2_new[k]*dx*k*dx;
    }
    l=a0*(q-Q)/dt;
    l1=a0*(q1-Q1)/dt;
    l_new=a0*(q_new-Q_new)/dt;
    l_1=a0*(q1_new-Q_1)/dt;
    lp=l + l_new;
    ln=l1+l_1;
    current=lp+ln;
    q10=q;
    q20=q1;
    q_10=q_new;
    q_20=q1_new;
    for(int i=0;i<nx;i++)
    {
        n1[i]=n1_new[i];
        n2[i]=n2_new[i];
    }
    fwrite(&current,sizeof(double),1,outfile);
}
fclose(outfile);
fclose(file);
}

```

```

void SaveFile(double n[],int num,int s)
{
    FILE *fp;
    int fh;

```

```

char buf[6];
char filename[30];
if(s==1)
{
    strcpy(filename,"pos`dist");
    strcat(filename,".m");
    fh=_creat(filename,'S`IREAD — .S`IWRITE');//create a file
    if((fp=fopen(filename,"wb+"))!=NULL)
    {
        for(int i=0;i<200;i++)
            fwrite(&n[i],sizeof(double),1,fp);
    }
    rewind(fp);
    fclose(fp);
}
else if(s==-1)
{
    strcpy(filename,"neg_dist");
    strcat(filename,"_");
    strcat(filename,_itoa(T1.number2,buf,10));
    strcat(filename,".m");
    fh=_creat(filename,_S`IREAD — `S`IWRITE);//create a file
    if((fp=fopen(filename,"wb+"))!=NULL)
    {
        for(int i=0;i<200;i++)
            fwrite(&n[i],sizeof(double),1,fp);
    }
    rewind(fp);
    fclose(fp);
}
if(num==1)
    T1.number1=T1.number1+1;
else if(num==2)

```

```
T1.number2=T1.number2+1;
```

```
}
```

## C.2. Code Written in Matlab

```
v=-300; %voltage
E=v;
m1=1.36; %mobility of positive charge
d1=0.032; %diffusion coefficient of positive charge
m2=1.82; %mobility of positive charge
d2=0.040; %diffusion coefficient of positive charge

laser=input('Enter laser position:', 's'); % enter the position of laser
xlas=str2num(laser);
wl=0.1; %laser width
dx=0.005; %space step of grid
t1=2*d1/((m1^2)*(v^2));
t2=(dx^2)/(2*d1);
N=1/dx;
num=600;
q10=0;
q_10=0;
q20=0;
q_20=0;
q1=0;
q_1=0;
q2=0;
q_2=0;
e0=1.6e-19;
if t1 > t2
    dt=t2;
```

```

else
    dt=t1;
end
dt
for i=1:N
    x=i*dx;
    n1(i)=0.25*exp(-4*(x-xlas)^2/(wl^2));%initial positive distribution
    n2(i)=0.25*exp(-4*(x-xlas)^2/(wl^2));%initial negative distribution
    q10=q10+n1(i)*dx*(1-i*dx);    %initial induction charges
    q_10= q_10 + n1(i)*dx*i*dx;
    q20=q20+n2(i)*dx*(1-i*dx);
    q_20=q_20+n2(i)*dx*i*dx;
end
for t=dt:dt:num*dt
    c1=(m1*v*dt)/(2*dx);
    s1=(d1*dt)/(dx^2);
    c2=(m2*v*dt)/(2*dx);
    s2=(d2*dt)/(dx^2);
    q10_new=q10;
    q_10_new=q_10;
    q20_new=q20;
    q_20_new=q_20;
    pos_charge(1)=q10;
    neg_charge(1)=q20;
    for k=1:N
        if k==1
            n1_new(1)=(s1-c1)*n1(2)+(1-2*s1)*n1(1);%n1(0)==0
            n2_new(1)=(s2+c2)*n2(2)+(1-2*s2)*n2(1);%n2(0)==0
        elseif k==N
            n1_new(N)=(s1+c1)*n1(N-1)+(1-2*s1)*n1(N);%n1(N+1)==0
            n2_new(N)=(s2-c2)*n2(N-1)+(1-2*s2)*n2(N);%n2(N+1)==0
        else
            n1_new(k)=(s1-c1)*n1(k+1)+(s1+c1)*n1(k-1)+(1-2*s1)*n1(k);

```

```

    n2_new(k)=(s2+c2)*n2(k+1)+(s2-c2)*n2(k-1)+(1-2*s2)*n2(k);
end
q1=q1+n1_new(k)*dx*(1-k*dx);
q_1=q_1 + n1_new(k)*dx*k*dx;
q2=q2+n2_new(k)*dx*(1-k*dx);
q_2=q_2+n2_new(k)*dx*k*dx;

end
index1=fix(t/dt);
pos_charge(index1+1)=q10;
neg_charge(index1+1)=q20;
I1(index1)=e0*(q1-q10_new)/dt;
I_1(index1)=e0*(q_1-q_10_new)/dt;
I2(index1)=e0*(q2-q20_new)/dt;
I_2(index1)=e0*(q_2-q_20_new)/dt;
Ip(index1)=I1(index1) + I_1(index1);
In(index1)=I2(index1) + I_2(index1);
current(index1)=Ip(index1)+In(index1);
for l=1:N
    n1(l)=n1_new(l);
    n2(l)=n2_new(l);
end
q10=q1;
q_10=q_1;
q20=q2;
q_20=q_2;
end
T=[dt:dt:num*dt];
plot(T,Ip,'r')
hold on
plot(T,In,'y')
hold on
plot(T,current,'r')

```

*xlabel('Time')*

*ylabel('total induced current')*

## APPENDIX D

### SOURCE CODE FOR CYLINDRICAL PLATES

This script file is written with *MatLab* to compute how charge distribution changes with time, angle, and position for the cylindrical case. This program is to solve the non-linear second-order partial differential equations for the positive and negative ion distribution,  $n_+(r, \phi, t)$  and  $n_-(r, \phi, t)$ , and then find the potential distributions,  $v(r, \phi, t)$ , using the Poisson equation. Finally, the electric field corresponding the potentials are calculated. By using Gauss Law, we can compute the charges induced by the space charge on the surfaces of two electrodes. It is easy to calculate the induced current by the positive and negative ions between the electrodes through the definition of current,  $I = \frac{dq}{dt}$ .

```

v=-100; %voltage
dt=3e-6; %time step
m2=1.82; %mobility for negative ion
d2=0.032 + 0.5*m2*m2*E*E*dt; %diffusion coefficient for negative ion
L=1; %the length of cylinder
m1=1.36; %mobility for positive ion
d1=0.04+0.5*m1*m1*E*E*dt; %diffusion coefficient for positive ion
rlas=0.2; %the position of laser
wl=0.1; %laser width
dr=0.01; %space step
da=0.1; %angle step
num=31; %number of angle steps
angle_step=31;%number of angle steps
c0=(1.6e-19)*dr*dr/(8.85e-14); % constant
N=50; %number of space steps

```



```

N1=0.05/dr;
space_step=50; %number of space steps
q_temp1=0.0;
q_temp2=0.0;
loop_No=200; %number of time steps
a00=2;
for i=1:N
    r2=idr+(0.1/2);
    for j=1:num
        n1(i,j)=0.25 * exp(-4*(r2^2-2*rlas*r2*cos((j-1)*da)...
            +(rlas)^2)/(wl^2));%initial positive distribution
        n2(i,j)=0.25*exp(-4*(r2^2-2*rlas*r2*cos((j-1)*da)...
            +rlas*rlas)/(wl^2));%initial negative distribution
    end
end
for t=0:5e-6:loop_No*5e-6
    k1=d1-(m1*v/3.0); %constant for negative
    c1=(k1*dt)/(2*dr);%constant for negative
    sr1=(d1*dt)/(dr^2);%for negative
    sa1=(d1*dt)/(da^2);%for negative

    k2=d2+(m2*v/3.0); %constant for positive
    c2=(k2*dt)/(2*dr);%constant for positive
    sr2=(d2*dt)/(dr^2);%for positive
    sa2=(d2*dt)/(da^2);%for positive
    index1=fix(t/(5e-6));%get unsigned integers
    index=index1+1
    if t==0
        for i=1:N
            r2=i*dr+(0.1/2);
            for j=1:num
                n1(i,j)=0.25*exp(-4*(r2^2-2*rlas*r2*cos((j-1)*da)+...
                    (rlas)^2)/(wl^2));%initial positive distribution

```

```

n2(i,j)=0.25*exp(-4*(r2^2-2*rlas*r2*cos((j-1)*da)+...
    rlas*rlas)/(wl^2));%initial negative distribution
end
end
else
%calculate the charge number densities of positive and negative
%ions at time t=t0 + dt
for k=1:N
    r1=k*dr+(0.1/2);
    for n=1:num
        if n==1
            if k==1
                n_new1(1,1)=(sr1+(c1/r1))*n1(2,1)+...
                    (1-2*sr1-(2*sa1/(r1^2)))*n1(1,1)+... %n1(0,1)=0
                2*(sa1/(r1^2))*n1(1,2);%n1(1,0)=n1(1,2)
                n_new2(1,1)=(sr2+(c2/r1))*n2(2,1)+... %n2(0,1)=0
                (1-2*sr2-(2*sa2/(r1^2)))*n2(1,1)+...
                2*(sa2/(r1^2))*n2(1,2);%n1(1,0)=n1(1,2)
            elseif k==N
                n_new1(N,1)=(sr1-(c1/r1))*n1(N-1,1)+... %n1(N+1,1)=0
                (1-2*sr1-(2*sa1/(r1^2)))*n1(N,1)+...
                2*(sa1/(r1^2))*n1(N,2);%n1(N,2)=n1(N,0)
                n_new2(N,1)=(sr2-(c2/r1))*n2(N-1,1)+... %n1(N+1,1)=0
                (1-2*sr2-(2*sa2/(r1^2)))*n2(N,1)+...
                2*(sa2/(r1^2))*n2(N,2);%n1(N,2)=n1(N,0)
            else
                n_new1(k,1)=(sr1+(c1/r1))*n1(k+1,1)+...
                    (sr1-(c1/r1))*n1(k-1,1)+...
                    (1-2*sr1-(2*sa1/(r1^2)))*n1(k,1)+...
                    2*(sa1/(r1^2))*n1(k,2);%n1(k,2)=n1(k,0)
                n_new2(k,1)=(sr2+(c2/r1))*n2(k+1,1)+...
                    (sr2-(c2/r1))*n2(k-1,1)+...
                    (1-2*sr2-(2*sa2/(r1^2)))*n2(k,1)+...

```

```

    2*(sa2/(r1^2))*n2(k,2);%n1(k,2)=n1(k,0)
end
elseif n==num
    if k==1
        n_new1(1,num)=(sr1+(c1/r1))*n1(2,num)+...
            (1-2*sr1-(2*sa1/(r1^2)))*n1(1,num)+...
            (sa1/(r1^2))*n1(1,num-1);
        %n1(0,num)=0,n1(1,num+1)=0
        n_new2(1,num)=(sr2+(c2/r1))*n2(2,num)+...
            (1-2*sr2-(2*sa2/(r1^2)))*n2(1,num)+...
            (sa2/(r1^2))*n2(1,num-1);
        %n1(0,num)=0,n1(1,num+1)=0
    elseif k==N
        n_new1(N,num)=(sr1-(c1/r1))*n1(N-1,num)+...
            (1-2*sr1-(2*sa1/(r1^2)))*n1(N,num)+...
            (sa1/(r1^2))*n1(N,num-1);
        %n1(N,num+1)=0,n1(N+1,num)=0
        n_new2(N,num)=(sr2-(c2/r1))*n2(N-1,num)+...
            (1-2*sr2-(2*sa2/(r1^2)))*n2(N,num)+...
            (sa2/(r1^2))*n2(N,num-1);
        %n1(N,num+1)=0,n1(N+1,num)=0
    else
        n_new1(k,num)=(sr1+(c1/r1))*n1(k+1,num)+...
            (sr1-(c1/r1))*n1(k-1,num)+...
            (1-2*sr1-(2*sa1/(r1^2)))*n1(k,num)+...
            (sa1/(r1^2))*n1(k,num-1);%n1(k,num+1)=0
        n_new2(k,num)=(sr2+(c2/r1))*n2(k+1,num)+...
            (sr2-(c2/r1))*n2(k-1,num)+...
            (1-2*sr2-(2*sa2/(r1^2)))*n2(k,num)+...
            (sa2/(r1^2))*n2(k,num-1);%n1(k,num+1)=0
    end
end
elseif
    if k==1

```

```

n_new1(1,n)=(sr1+(c1/r1))*n1(2,n)+...%n1(0,n)=0
(1-2*sr1-(2*sa1/(r1^2)))*n1(1,n)+...
(sa1/(r1^2))*(n1(1,n+1)+n1(1,n-1));
n_new2(1,n)=(sr2+(c2/r1))*n2(2,n)+...%n1(0,n)=0
(1-2*sr2-(2*sa2/(r1^2)))*n2(1,n)+...
(sa2/(r1^2))*(n2(1,n+1)+n2(1,n-1));
elseif k==N
n_new1(N,n)=(sr1-(c1/r1))*n1(N-1,n)+...
(1-2*sr1-(2*sa1/(r1^2)))*n1(N,n)+...
(sa1/(r1^2))*(n1(N,n+1)+n1(N,n-1));
n_new2(N,n)=(sr2-(c2/r1))*n2(N-1,n)+...
(1-2*sr2-(2*sa2/(r1^2)))*n2(N,n)+...
(sa2/(r1^2))*(n2(N,n+1)+n2(N,n-1));
else
n_new1(k,n)=(sr1+(c1/r1))*n1(k+1,n)+...
(sr1-(c1/r1))*n1(k-1,n)+...
(1-2*sr1-(2*sa1/(r1^2)))*n1(k,n)+...
(sa1/(r1^2))*(n1(k,n+1)+n1(k,n-1));
n_new2(k,n)=(sr2+(c2/r1))*n2(k+1,n)+...
(sr2-(c2/r1))*n2(k-1,n)+...
(1-2*sr2-(2*sa2/(r1^2)))*n2(k,n)+...
(sa2/(r1^2))*(n2(k,n+1)+n2(k,n-1));
end
end
q_temp1=q`temp1 + n_new1(k,n)...
*da*dr*dr*L*(N1+1)*1.6e-19;
q_temp2=q`temp2 + n_new2(k,n)...
*da*dr*dr*L*(N1+1)*1.6e-19;
q1(index,1)=q`temp1;
q2(index,1)=q`temp2;
end
end
for i=1:N

```

```

for j=1:num
    n1(i,j)=n_new1(i,j);
    n2(i,j)=n_new2(i,j);
    %B=sum(n1');
end
end
%%%%%%%%%%%%%%%%%%%%%%%%%%%%%%%%%%%%%%%%%%%%%%%%%%%%%%%%%%%%%%%%%%%%%%%%
% SOLVE A SET OF LINEAR EQUATIONS:
%[matrix]*[variables]=[matrix].
%By using the charge number
%densities of positive and
%negative ions, n1 and n2,
%that are calculated with
%the continuity equation,
%I am going to create a
%matrix, M, with the sparse
% matrix (command:spdiags).
%%%%%%%%%%%%%%%%%%%%%%%%%%%%%%%%%%%%%%%%%%%%%%%%%%%%%%%%%%%%%%%%%%%%%%%%
%create the term: [(n+) - (n-)]
for ii5=1:space_step-1
    for jj5=1:angle_step
        temp1(ii5,jj5)=n1(ii5,jj5);
        temp2(ii5,jj5)=n2(ii5,jj5);

    end
end
den`temp1=reshape(temp1',(space_step-1)*angle_step,1);
density1=-c0 den_temp1;
for ii6=1 angle`step
    density1(angle_step*(space_step-2)+ii6)...
    =density1(angle`step*(space_step-2)+ii6)...
    - (1 + (1/(2*space_step)))*v;
end

```

```

den_temp2=reshape(temp2',(space_step-1)*angle_step,1);
density2 = -c0 dentemp2;
for ii6=1:angle_step
    density2(angle_step*(space_step-2)+ii6)...
        =density2(angle_step*(space_step-2)+ii6)...
        - (1 + (1/(2*space_step)))*v;
end
%%%%%%%%%%%%%%%%%%%%%%%%%%%%%%%%%%%%%%%%%%%%%%%%%%%%%%%%%%%%%%%%%%%%%%%%
%create a matrix using sparse matrix.
%%%%%%%%%%%%%%%%%%%%%%%%%%%%%%%%%%%%%%%%%%%%%%%%%%%%%%%%%%%%%%%%%%%%%%%%
for i1=1:space_step-1
    for j1=1:angle_step
        D_ab(i1,j1)=1/(((i1+N1)^2)*(da^2));% *2* %
        D_main(i1,j1)=-2*(1+(1/((da^2)*((i1+N1)^2))));
        %create main diagonals
    end
end
temp=D'ab';
%%%%%%%%%%%%%%%%%%%%%%%%%%%%%%%%%%%%%%%%%%%%%%%%%%%%%%%%%%%%%%%%%%%%%%%%
for i2=1:space_step-1
    for j2=1:angle_step
        D12(i2,j2)=1+(1/(2*(i2+N1)));
        D21(i2,j2)=1-(1/(2*(i2+N1)));
        %create a set of diagonals in row=1,column=2,...
    end
end
%%%%%%%%%%%%%%%%%%%%%%%%%%%%%%%%%%%%%%%%%%%%%%%%%%%%%%%%%%%%%%%%%%%%%%%%
%Sparse matrix is applied
% to create a matrix in which
%most elements are zeros
%Function:spdiags(), zeros()
%First, create
%(space_step,space_step) blocks

```

```

%%%%%%%%%%%%%%%%%%%%%%%%%%%%%%%%%%%%%%%%%%%%%%%%%%%%%%%%%%%%%%%%%%%%%%%%
for i3=1:space_step-1
    %temp1=flipud(temp(:,i3));
    %temp2=temp(:,i3);
    x11=spdiags([temp(:,i3) (D`main(i3,:))'...
        temp(:,i3)],-1:1,angle`step,angle`step);
    x12=spdiags([D12(i3,:)'],0,angle`step,angle`step);
    x21=spdiags([D21(i3,:)'],0,angle`step,angle`step);
    %create 51 blocks which contain 31 by 31 matrix
    eval(['A',int2str(i3),'=x11']);
    eval(['B',int2str(i3),'=x12']);
    eval(['C',int2str(i3),'=x21']);
    %assign each block to a different variable
    % like A1,A2,...A51
end

```

```

%%%%%%%%%%%%%%%%%%%%%%%%%%%%%%%%%%%%%%%%%%%%%%%%%%%%%%%%%%%%%%%%%%%%%%%%
%It is the stupid way to
%change the value
%of particular elements
%%%%%%%%%%%%%%%%%%%%%%%%%%%%%%%%%%%%%%%%%%%%%%%%%%%%%%%%%%%%%%%%%%%%%%%%
A1(1,2)=a00*A1(1,2);%
A1(angle_step,angle_step-1)=2*A1(angle_step,angle_step-1);
A2(1,2)=a00*A2(1,2);%
A2(angle_step,angle_step-1)=2*A2(angle_step,angle_step-1);
A3(1,2)=a00*A3(1,2);%
A3(angle_step,angle_step-1)=2*A3(angle_step,angle_step-1);
A4(1,2)=a00*A4(1,2);%
A4(angle_step,angle_step-1)=2*A4(angle_step,angle_step-1);
A5(1,2)=a00*A5(1,2);
A5(angle_step,angle_step-1)=2*A5(angle_step,angle_step-1);
A6(1,2)=a00*A6(1,2);
A6(angle_step,angle_step-1)=2*A6(angle_step,angle_step-1);

```

$A7(1,2)=a00*A7(1,2);$   
 $A7(\text{angle\_step},\text{angle\_step}-1)=2*A7(\text{angle\_step},\text{angle\_step}-1);$   
 $A8(1,2)=a00*A8(1,2);$   
 $A8(\text{angle\_step},\text{angle\_step}-1)=2*A8(\text{angle\_step},\text{angle\_step}-1);$   
 $A9(1,2)=a00*A9(1,2);$   
 $A9(\text{angle\_step},\text{angle\_step}-1)=2*A9(\text{angle\_step},\text{angle\_step}-1);$   
 $A10(1,2)=a00*A10(1,2);$   
 $A10(\text{angle\_step},\text{angle\_step}-1)=2*A10(\text{angle\_step},\text{angle\_step}-1);$   
 $A11(1,2)=a00*A11(1,2);$   
 $A11(\text{angle\_step},\text{angle\_step}-1)=2*A11(\text{angle\_step},\text{angle\_step}-1);$   
 $A12(1,2)=a00*A12(1,2);$   
 $A12(\text{angle\_step},\text{angle\_step}-1)=2*A12(\text{angle\_step},\text{angle\_step}-1);$   
 $A13(1,2)=a00*A13(1,2);$   
 $A13(\text{angle\_step},\text{angle\_step}-1)=2*A13(\text{angle\_step},\text{angle\_step}-1);$   
 $A14(1,2)=a00*A14(1,2);$   
 $A14(\text{angle\_step},\text{angle\_step}-1)=2*A14(\text{angle\_step},\text{angle\_step}-1);$   
 $A15(1,2)=a00*A15(1,2);$   
 $A15(\text{angle\_step},\text{angle\_step}-1)=2*A15(\text{angle\_step},\text{angle\_step}-1);$   
 $A16(1,2)=a00*A16(1,2);$   
 $A16(\text{angle\_step},\text{angle\_step}-1)=2*A16(\text{angle\_step},\text{angle\_step}-1);$   
 $A17(1,2)=a00*A17(1,2);$   
 $A17(\text{angle\_step},\text{angle\_step}-1)=2*A17(\text{angle\_step},\text{angle\_step}-1);$   
 $A18(1,2)=a00*A18(1,2);$   
 $A18(\text{angle\_step},\text{angle\_step}-1)=2*A18(\text{angle\_step},\text{angle\_step}-1);$   
 $A19(1,2)=a00*A19(1,2);$   
 $A19(\text{angle\_step},\text{angle\_step}-1)=2*A19(\text{angle\_step},\text{angle\_step}-1);$   
 $A20(1,2)=a00*A20(1,2);$   
 $A20(\text{angle\_step},\text{angle\_step}-1)=2*A20(\text{angle\_step},\text{angle\_step}-1);$   
 $A21(1,2)=a00*A21(1,2);$   
 $A21(\text{angle\_step},\text{angle\_step}-1)=2*A21(\text{angle\_step},\text{angle\_step}-1);$   
 $A22(1,2)=a00*A22(1,2);$   
 $A22(\text{angle\_step},\text{angle\_step}-1)=2*A22(\text{angle\_step},\text{angle\_step}-1);$   
 $A23(1,2)=a00*A23(1,2);$



$A23(\text{angle\_step}, \text{angle\_step}-1) = 2 * A23(\text{angle\_step}, \text{angle\_step}-1);$   
 $A24(1,2) = a00 * A24(1,2);$   
 $A24(\text{angle\_step}, \text{angle\_step}-1) = 2 * A24(\text{angle\_step}, \text{angle\_step}-1);$   
 $A25(1,2) = a00 * A25(1,2);$   
 $A25(\text{angle\_step}, \text{angle\_step}-1) = 2 * A25(\text{angle\_step}, \text{angle\_step}-1);$   
 $A26(1,2) = a00 * A26(1,2);$   
 $A26(\text{angle\_step}, \text{angle\_step}-1) = 2 * A26(\text{angle\_step}, \text{angle\_step}-1);$   
 $A27(\text{angle\_step}, \text{angle\_step}-1) = 2 * A27(\text{angle\_step}, \text{angle\_step}-1);$   
 $A27(1,2) = a00 * A27(1,2);$   
 $A28(\text{angle\_step}, \text{angle\_step}-1) = 2 * A28(\text{angle\_step}, \text{angle\_step}-1);$   
 $A28(1,2) = a00 * A28(1,2);$   
 $A29(\text{angle\_step}, \text{angle\_step}-1) = 2 * A29(\text{angle\_step}, \text{angle\_step}-1);$   
 $A29(1,2) = a00 * A29(1,2);$   
 $A30(\text{angle\_step}, \text{angle\_step}-1) = 2 * A30(\text{angle\_step}, \text{angle\_step}-1);$   
 $A30(1,2) = a00 * A30(1,2);$   
 $A31(\text{angle\_step}, \text{angle\_step}-1) = 2 * A31(\text{angle\_step}, \text{angle\_step}-1);$   
 $A31(1,2) = a00 * A31(1,2);$   
 $A32(\text{angle\_step}, \text{angle\_step}-1) = 2 * A32(\text{angle\_step}, \text{angle\_step}-1);$   
 $A32(1,2) = a00 * A32(1,2);$   
 $A33(1,2) = a00 * A33(1,2);$   
 $A33(\text{angle\_step}, \text{angle\_step}-1) = 2 * A33(\text{angle\_step}, \text{angle\_step}-1);$   
 $A34(1,2) = a00 * A34(1,2);$   
 $A34(\text{angle\_step}, \text{angle\_step}-1) = 2 * A34(\text{angle\_step}, \text{angle\_step}-1);$   
 $A35(1,2) = a00 * A35(1,2);$   
 $A35(\text{angle\_step}, \text{angle\_step}-1) = 2 * A35(\text{angle\_step}, \text{angle\_step}-1);$   
 $A36(1,2) = a00 * A36(1,2);$   
 $A36(\text{angle\_step}, \text{angle\_step}-1) = 2 * A36(\text{angle\_step}, \text{angle\_step}-1);$   
 $A37(1,2) = a00 * A37(1,2);$   
 $A37(\text{angle\_step}, \text{angle\_step}-1) = 2 * A37(\text{angle\_step}, \text{angle\_step}-1);$   
 $A38(1,2) = a00 * A38(1,2);$   
 $A38(\text{angle\_step}, \text{angle\_step}-1) = 2 * A38(\text{angle\_step}, \text{angle\_step}-1);$   
 $A39(1,2) = a00 * A39(1,2);$   
 $A39(\text{angle\_step}, \text{angle\_step}-1) = 2 * A39(\text{angle\_step}, \text{angle\_step}-1);$

```

A40(1,2)=a00*A40(1,2);
A40(angle_step,angle_step-1)=2*A40(angle_step,angle_step-1);
A41(1,2)=a00*A41(1,2);
A41(angle_step,angle_step-1)=2*A41(angle_step,angle_step-1);
A42(1,2)=a00*A42(1,2);
A42(angle_step,angle_step-1)=2*A42(angle_step,angle_step-1);
A43(1,2)=a00*A43(1,2);
A43(angle_step,angle_step-1)=2*A43(angle_step,angle_step-1);
A44(1,2)=a00*A44(1,2);
A44(angle_step,angle_step-1)=2*A44(angle_step,angle_step-1);
A45(1,2)=a00*A45(1,2);
A45(angle_step,angle_step-1)=2*A45(angle_step,angle_step-1);
A46(1,2)=a00*A46(1,2);
A46(angle_step,angle_step-1)=2*A46(angle_step,angle_step-1);
A47(1,2)=a00*A47(1,2);
A47(angle_step,angle_step-1)=2*A47(angle_step,angle_step-1);
A48(1,2)=a00*A48(1,2);
A48(angle_step,angle_step-1)=2*A48(angle_step,angle_step-1);
A49(1,2)=a00*A49(1,2);
A49(angle_step,angle_step-1)=2*A49(angle_step,angle_step-1);
%%%%%%%%%%%%%%%%%%%%%%%%%%%%%%%%%%%%%%%%%%%%%%%%%%%%%%%%%%%%%%%%%%%%%%%%%%

%%%%%%%%%%%%%%%%%%%%%%%%%%%%%%%%%%%%%%%%%%%%%%%%%%%%%%%%%%%%%%%%%%%%%%%%%%
%This is the stupid way to
%create the big matrix.
%I will figure out the
%short way to do this later on.
%%%%%%%%%%%%%%%%%%%%%%%%%%%%%%%%%%%%%%%%%%%%%%%%%%%%%%%%%%%%%%%%%%%%%%%%%%

Z=zeros(angle_step); %create 31 by 31 zero matrix
M1=[A1,B1,Z,Z,Z,Z,Z,Z,Z,Z,Z,Z,Z,Z,Z,Z,Z,Z,Z,Z,Z,...
     Z,Z,Z,Z,Z,Z,Z,Z,Z,Z,Z,Z,Z,Z,Z,Z,Z,Z,Z,Z];
M2=[C2,A2,B2,Z,Z,Z,Z,Z,Z,Z,Z,Z,Z,Z,Z,Z,Z,Z,Z,Z,Z,Z,...
     Z,Z,Z,Z,Z,Z,Z,Z,Z,Z,Z,Z,Z,Z,Z,Z,Z,Z,Z,Z];

```



$Z,Z,Z,Z,Z,Z,Z,Z,Z,Z,Z,Z,Z,Z,Z,Z,Z,Z,Z$ ;  $M_{20}=[Z,Z,Z,Z,Z,Z,Z,Z,Z,Z,Z,Z,Z,Z,C_{20},A_{20},B_{20},Z,\dots Z,Z]$ ;  $M_{21}=[Z,Z,Z,Z,Z,Z,Z,Z,Z,Z,Z,Z,Z,Z,Z,Z,Z,Z,C_{21},A_{21},B_{21},Z,\dots ,Z]$ ;  $M_{22}=[Z,Z,Z,Z,Z,Z,Z,Z,Z,Z,Z,Z,Z,Z,Z,Z,Z,Z,C_{22},A_{22},B_{22},\dots Z,Z]$ ;  $M_{23}=[Z,C_{23},A_{23},\dots B_{23},Z]$ ;  $M_{24}=[Z,C_{24},A_{24},\dots B_{24},Z]$ ;  $M_{25}=[Z,C_{25},\dots A_{25},B_{25},Z]$ ;  $M_{26}=[Z,C_{26},\dots A_{26},B_{26},Z,Z,Z,Z,Z,Z,Z,Z,Z,Z,Z,Z,Z,Z,Z,Z,Z,Z]$ ;  $M_{27}=[Z,C_{27}\dots ,A_{27},B_{27},Z,Z,Z,Z,Z,Z,Z,Z,Z,Z,Z,Z,Z,Z,Z,Z,Z,Z]$ ;  $M_{28}=[Z,\dots C_{28},A_{28},B_{28},Z,Z,Z,Z,Z,Z,Z,Z,Z,Z,Z,Z,Z,Z,Z,Z]$ ;  $M_{29}=[Z,\dots Z,C_{29},A_{29},B_{29},Z,Z,Z,Z,Z,Z,Z,Z,Z,Z,Z,Z,Z,Z,Z]$ ;  $M_{30}=[Z,\dots Z,Z,C_{30},A_{30},B_{30},Z,Z,Z,Z,Z,Z,Z,Z,Z,Z,Z,Z,Z,Z]$ ;  $M_{31}=[Z,\dots Z,Z,Z,C_{31},A_{31},B_{31},Z,Z,Z,Z,Z,Z,Z,Z,Z,Z,Z,Z,Z,Z]$ ;  $M_{32}=[Z,\dots Z,Z,Z,Z,C_{32},A_{32},B_{32},Z,Z,Z,Z,Z,Z,Z,Z,Z,Z,Z,Z,Z]$ ;  $M_{33}=[Z,\dots Z,Z,Z,Z,C_{33},A_{33},B_{33},Z,Z,Z,Z,Z,Z,Z,Z,Z,Z,Z,Z,Z]$ ;  $M_{34}=[Z,\dots Z,Z,Z,Z,C_{34},A_{34},B_{34},Z,Z,Z,Z,Z,Z,Z,Z,Z,Z,Z,Z,Z]$ ;  $M_{35}=[Z,\dots Z,Z,Z,Z,C_{35},A_{35},B_{35},Z,Z,Z,Z,Z,Z,Z,Z,Z,Z,Z,Z,Z]$



```

% this matrix for solving potential distribution
%if size(M)~= [space`step*angle`step,...
    space`step*angle`step]
% disp('there is something wrong with the size of...
    the huge matrix')
%else
%%%%%%%%%%%%%%%%%%%%%%%%%%%%%%%%%%%%%%%%%%%%%%%%%%%%%%%%%%%%%%%%%%%%%%%%
%calculate the potential distribution in the space
%between two cylindrical electrodes due to the
%production of laser-induced ions
V1=M/density1;
V2=M/density2;
%V = gmres(M,density);

%%%%%%%%%%%%%%%%%%%%%%%%%%%%%%%%%%%%%%%%%%%%%%%%%%%%%%%%%%%%%%%%%%%%%%%%
%Now compute the electric field on the surface of j=1
for i4=1:angle_step
    E1(i4)=-(1/(dr))*(V1(i4,1));

    E2(i4)=-((1/(dr))*V2(i4,1));

end
Q1(index,1)=1e-12*da*L*(0.05+dr)*sum(E1);
Q2(index,1)=1e-12*da*L*(0.05+2*dr)*sum(E2);

total2(index,1)=(q1(index,1));
total3(index,1)=(q2(index,1));
end
end
%%%%%%%%%%%%%%%%%%%%%%%%%%%%%%%%%%%%%%%%%%%%%%%%%%%%%%%%%%%%%%%%%%%%%%%%
for i9=1:(loop_No-2)
    I1(i9)=(Q1(i9+1,1)-Q1(i9,1))/dt;

```

```

I2(i9)=(Q2(i9+1,1)-Q2(i9,1))/dt;

I12(i9)=(total2(i9+1,1)-total2(i9,1))/dt;
I13(i9)=(total3(i9+1,1)-total3(i9,1))/dt;
end
plot(I1+I12)
hold on
plot(I2+I13,':')
hold on
plot(I1+I12+I2+I13,'r')

```

## APPENDIX E

### INDUCED CHARGES ON PARALLEL PLATES

In this section, we find the solution to the problem of figuring out the induced charges on the two infinite parallel plates due to the point charge between the plates. There is a wide variety of approaches that can be used to solve this problem, such as the Green function solution and image charges. For simplicity, we use the Green Reciprocity Theorem to solve the problem of a point charge between two parallel conducting plates.

We treat situation 1 and situation 2 shown in Figure E.1 as equivalent. The reason why we do this way is that  $V_0$  does not affect the charges induced by point charge  $q$  between the two parallel plates under the condition that point charge  $q$  is small enough that the effect on the external electric field is neglected. In other words, we just calculate the induced charges in situation 1.  $Q_{x_1}$ ,  $V_{x_1}$ ,  $Q_{x_2}$ , and  $V_{x_2}$  denote the charges and potentials at the positions of the point charge in Figure E.1, respectively.

#### E.1. Green Reciprocity Theorem

Suppose a charge distribution,  $\rho_1(\mathbf{r})$ , produces a potential,  $V_1(\mathbf{r})$ , and some other charge distribution  $\rho_2(\mathbf{r})$  produces a potential,  $V_2(\mathbf{r})$ . Green Reciprocity Theorem<sup>15</sup> is given by

$$\int_{allspace} \rho_1 V_2 d\tau = \int_{allspace} \rho_2 V_1 d\tau. \quad (\text{E.1})$$

Note that  $\rho_1$  and  $\rho_2$  have nothing in common.



## E.2. Induced Charges

We use the Green Reciprocity Theorem to compute the induced charges due to the point charge between the two plates. Both plates are grounded, and the point charge is placed at distance  $x$  from plate 1 as shown in Figure E.1. The plate separation is  $L_0$ . We assume that  $Q_1$  and  $Q_2$  are induced charges of the left and right plates, respectively. In situation 1,

$$\int_{allspace} \rho_1 V_2 d\tau = V_{l_2} Q_{l_1} + V_{r_2} Q_{r_1} + V_{x_2} Q_{x_1}. \quad (\text{E.2})$$

Since  $V_{l_2} = 0$ ,  $V_{r_2} = V_0$ ,  $Q_{x_1} = q$ ,  $Q_{r_1} = Q_2$ , and  $V_{x_2} = \frac{xV_0}{L_0}$ , Eq. E.2 becomes

$$\int_{allspace} \rho_1 V_2 d\tau = \left(\frac{xV_0}{L_0}\right)q + V_0 Q_2. \quad (\text{E.3})$$

In situation 2,

$$\int_{allspace} \rho_2 V_1 d\tau = V_{l_1} Q_{l_2} + V_{r_1} Q_{r_2} + V_{x_1} Q_{x_2}. \quad (\text{E.4})$$

Substituting  $V_{l_1} = 0$ ,  $V_{r_1} = 0$ ,  $Q_{x_2} = 0$ , and  $Q_{r_1} = Q_2$  into Eq. E.4, we obtain

$$\int_{allspace} \rho_2 V_1 d\tau = 0. \quad (\text{E.5})$$

By using the Green Reciprocity Theorem (Eq. E.1), the induced charges can be calculated:

$$\begin{aligned} \int_{allspace} \rho_1 V_2 d\tau &= \int_{allspace} \rho_2 V_1 d\tau \\ \left(\frac{xV_0}{L_0}\right)q + V_0 Q_2 &= 0. \end{aligned} \quad (\text{E.6})$$

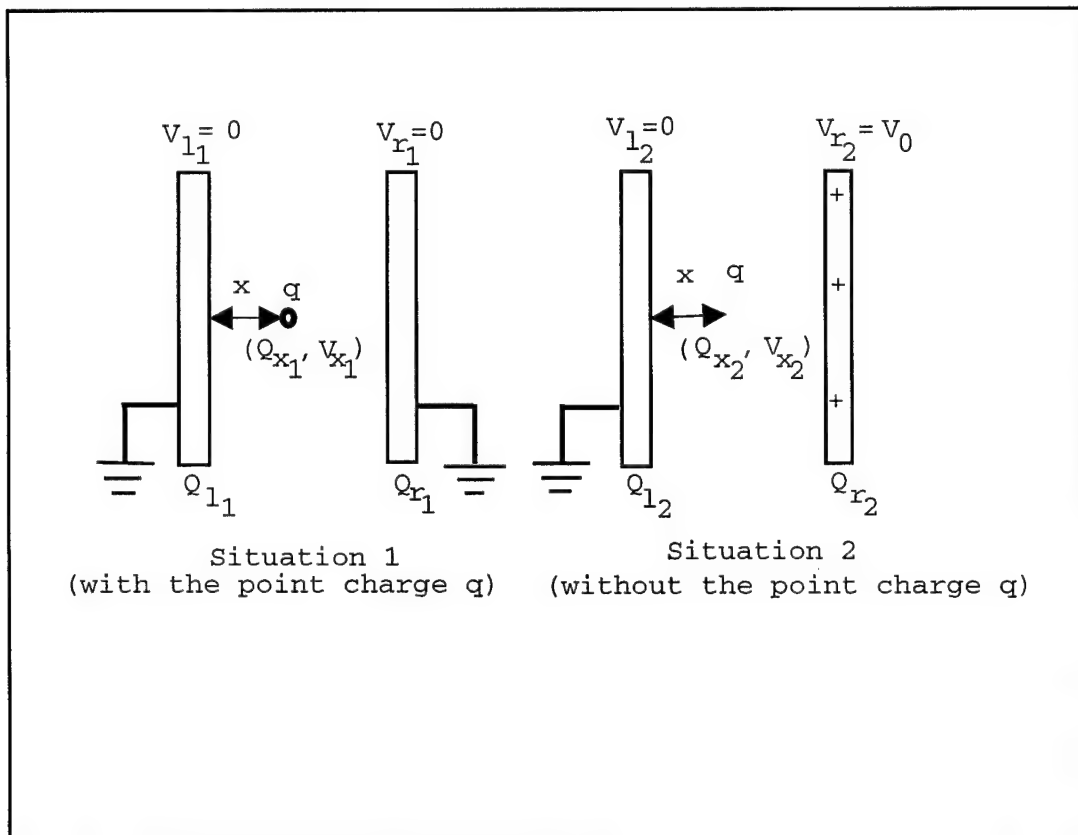


Figure E.1. Two situations: (1) both grounded, a point charge at  $x$ . (2) right plate at  $V_0$  and left plate at  $V_0 = 0$ , no point charge at  $x$ .

The induced charge of the right plate shown in Figure E.1 is

$$Q_2 = -q \left( \frac{x}{L_0} \right). \quad (\text{E.7})$$

According to charge conservation law, the relationship between the point charge and the induced charges is

$$Q_1 + Q_2 = -q, \quad (\text{E.8})$$

so the induced charge of the left plate is

$$Q_1 = -q - Q_2 = -q \left( 1 - \frac{x}{L_0} \right). \quad (\text{E.9})$$

## APPENDIX B

RESONANCE ENHANCED MULTIPHOTON IONIZATION SPECTROSCOPY OF  
INDENE AT AMBIENT CONDITIONS

A Thesis  
Submitted to the Graduate Faculty  
of the  
North Dakota State University  
of Agriculture and Applied Science

By

Maxwell Ryan Lucci

In Partial Fulfillment of the Requirements  
for the Degree of  
MASTER OF SCIENCE

Major Department:  
Chemistry

June 1999

Fargo, North Dakota

North Dakota State University  
Graduate School

---

Title

Resonance Enhanced Multiphoton Ionization  
Spectroscopy of Indene at Ambient Conditions

---

By

Maxwell Ryan Lucci

---

The Supervisory Committee certifies that this disquisition complies with North Dakota State University's regulations and meets the accepted standards for the degree of

MASTER OF SCIENCE

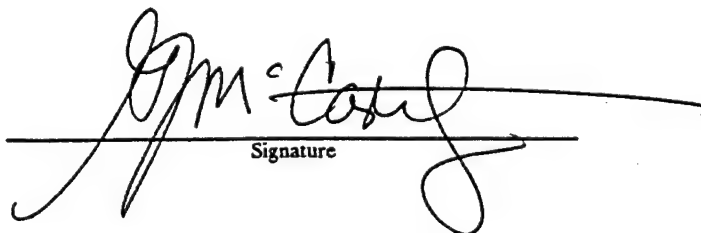
SUPERVISORY COMMITTEE:

Gregory D. Killipie  
Chair  
David J. Swenson  
John F. Hershberger  
Michael R.

---

Approved by Department Chair:

23 May 2000  
Date

  
Signature

## ABSTRACT

Lucci, Maxwell Ryan, M.S., Department of Chemistry, College of Science and Mathematics, North Dakota State University, June 1999. Resonance Enhanced Multiphoton Ionization Spectroscopy of Indene at Ambient Conditions. Major Professor: Dr. Gregory D. Gillispie.

The room temperature 1+1 and 2+2 resonance enhanced multiphoton ionization (REMPI) spectra of gas-phase indene,  $C_9H_8$ , near the origin of the first electronic transition at 287.86 nm are reported. This work relates to chemically specific measurements of trace organic species in ambient air. The 1+1 REMPI spectrum for indene at 50 ppbv concentration in ambient air qualitatively agrees with absorbance spectra obtained for much longer pathlength and higher sample concentration. Extensive sequence band structure is observed near the origin. The typical rotational contour consists of a narrow, nearly symmetric feature and a less intense broad sideband shaded to the red. The narrow feature at 287.86 nm in the high-resolution 1+1 REMPI spectrum is not as narrow as in the highest resolution vapor absorption spectrum; this difference can not be fully explained by power (intensity) saturation effects, pressure broadening, or laser bandwidth. Indene was also detected in the headspace over the multicomponent mixtures of coal tar and creosote.

## ACKNOWLEDGMENTS

I would like to thank the members of my Advisory and Examination Committee, Dr. Gregory D. Gillispie, Dr. Orven F. Swenson, Dr. John Hershberger, and Dr. Michael Page, for their time and support. I wish to express my sincere gratitude to my co-advisors, Dr. Gregory D. Gillispie and Dr. Orven F. Swenson, for their guidance, and critical review of the work presented in this thesis. Special thanks to Harlan Isensee and Joe Carriere for their technical assistance on the experimental apparatus used in this thesis. In addition, the financial support provided by the United States Air Force is greatly appreciated.

I would also like to thank the following people: Mike Remington, Tim Zensen, Chris Walls, Paul Jarski, Dr. Erik Hagestuen, and Dr. Tom Gonnella. They are my friends, as well as my colleagues, who made my graduate school experience at North Dakota State University a memorable one.

Above all, the patience and support of my parents, Michael and Deborah Lucci, as well as my sister and her family, Carmen, Rob, and Ryan Reuhl, is sincerely appreciated.



## TABLE OF CONTENTS

ABSTRACT .....	iii
ACKNOWLEDGMENTS .....	iv
LIST OF TABLES .....	vii
LIST OF FIGURES .....	viii
LIST OF SYMBOLS/ABBREVIATIONS .....	x
I. INTRODUCTION .....	1
A. Absorbance Spectroscopy .....	1
B. Multiphoton Processes: Historical Background .....	5
C. Gas-Phase MPI .....	6
D. Time-of-Flight Mass Spectrometry (TOFMS) .....	12
E. Jet Spectroscopy .....	13
F. Ambient Pressure REMPI .....	14
II. EXPERIMENTAL .....	18
A. Pump Laser .....	18
B. Dye Laser .....	18
C. Experimental Apparatus .....	19
D. Absorbance Experiments .....	25
E. Reagents .....	25
F. Power-Dependence and Pressure Broadening Experiments .....	25
III. RESULTS AND DISCUSSION .....	28
A. Ambient Pressure REMPI Waveforms .....	28

## TABLE OF CONTENTS (Continued)

B. The 1+1 REMPI Spectra of Indene in Ambient Air.....	30
C. Line Broadening Factors .....	35
D. REMPI versus Conventional Absorbance.....	43
E. Indene Detection in Chemical Mixtures.....	43
F. The 2+2 REMPI Spectra of Indene in Ambient Air.....	45
IV. CONCLUSIONS .....	52
V. REFERENCES CITED .....	54

## LIST OF TABLES

<u>Table</u>	<u>Page</u>
1. Spectral data for aromatic hydrocarbons.....	4
2. Indene sequence band comparison between the Hollas vapor absorption spectrum and high-resolution 1+1 REMPI spectrum.....	33

## LIST OF FIGURES

<u>Figure</u>	<u>Page</u>
1. Simplified energy-level diagram for a molecule undergoing a non-resonant MPI process.....	7
2. Simplified energy-level diagram for a molecule undergoing a 1+1 REMPI process.....	9
3. Simplified energy-level diagram for a molecule undergoing a 2+2 REMPI process.....	11
4. Schematic diagram of the experimental apparatus used for ambient pressure REMPI measurements.....	20
5. Schematic diagram of the ambient pressure REMPI cell and peripheral components .....	23
6. Corrected 1+1 REMPI spectrum of 100 ppbv styrene in ambient air.....	27
7. Ion current-time waveforms for 1+1 REMPI of 50 ppbv indene in ambient air at laser wavelengths of 287.83 nm and 287.86 nm.....	29
8. Corrected 1+1 REMPI spectrum of 50 ppbv indene in ambient air.....	31
9. High-resolution 1+1 REMPI spectra of 50 ppbv indene in ambient air .....	32
10. The 1+1 REMPI signal amplitude as a function of laser pulse energy .....	34
11. The 1+1 REMPI power-dependence on the rotational contour of the indene origin band.....	36
12. The 1+1 REMPI pressure broadening effects on the rotational contour of the indene origin band.....	39
13. The 1+1 REMPI pressure broadening effects on the rotational contour of the indene origin band.....	40
14. The 1+1 REMPI pressure broadening effects on the rotational contour of the indole origin band.....	41
15. The 1+1 REMPI and conventional absorbance spectra of indene in atmospheric pressure air.....	44
16. Detection of indene in chemical mixtures via 1+1 REMPI .....	46

## LIST OF FIGURES (Continued)

<u>Figure</u>	<u>Page</u>
17. Corrected 2+2 REMPI spectrum of 30 ppmv indene in ambient air.....	48
18. Corrected 2+2 REMPI spectrum of 30 ppmv indene in ambient air.....	49
19. The 2+2 REMPI signal amplitude as a function of laser pulse energy .....	50
20. The 1+1 and 2+2 REMPI spectra of indene in atmospheric pressure air.....	51

## LIST OF SYMBOLS/ABBREVIATIONS

<u>Term</u>	<u>Definition</u>
$\lambda$ .....	wavelength
$^{\circ}\text{C}$ .....	degrees Celsius
$l$ .....	lines
A.....	ampere
AC .....	alternating current
atm.....	atmosphere
BNC.....	bayonet nut connector
BTEX .....	benzene, toluene, ethylbenzene, xylenes
cm.....	centimeter ( $10^{-2}$ m)
$\text{cm}^{-1}$ .....	wavenumber
DSO.....	digital storage oscilloscope
eV .....	electron volt
FWHM .....	full width at half maximum
ft .....	foot
GPIB.....	general purpose interface bus
HPLC.....	high performance liquid chromatography
Hz .....	hertz
IBM .....	International Business Machines
IE .....	ionization energy
in. ....	inch
J .....	joule
KDP.....	potassium dihydrogen phosphate
KTP .....	potassium trihydrogen phosphate
kV.....	kilovolt ( $10^3$ V)
L .....	liter
m.....	meter
<u>M</u> .....	molar (mol/L)
MHz.....	megahertz ( $10^6$ Hz)

## LIST OF SYMBOLS/ABBREVIATIONS (Continued)

<u>Term</u>	<u>Definition</u>
mJ .....	millijoule ( $10^{-3}$ J)
mL .....	milliliter ( $10^{-3}$ L)
mm.....	millimeter ( $10^{-3}$ m)
mM.....	millimolar ( $10^{-3}$ M)
mol.....	mole
MPI.....	multiphoton ionization
ms .....	millisecond ( $10^{-3}$ s)
mtorr.....	millitorr ( $10^{-3}$ torr)
Nd:YAG.....	neodymium: yttrium aluminum garnet
NIR.....	near-infrared
nm.....	nanometer ( $10^{-9}$ m)
ns .....	nanosecond ( $10^{-9}$ s)
PID .....	photoionization detector
ppbv.....	parts per billion by volume
ppmv.....	parts per million by volume
psi .....	pounds per square inch
REMPL.....	resonance enhanced multiphoton ionization
s .....	second
S <sub>1</sub> .....	first excited singlet state
S <sub>1</sub> ←S <sub>0</sub> .....	first singlet transition
S <sub>2</sub> ←S <sub>0</sub> .....	second singlet transition
TOFMS .....	time-of-flight mass spectrometry
TPA .....	two-photon absorption
μL .....	microliter ( $10^{-6}$ L)
UV .....	ultraviolet
V .....	volt
VIS .....	visible
W .....	watt

## I. INTRODUCTION

### A. Absorbance Spectroscopy

Conventional absorbance spectroscopy probes state-to-state molecular transitions via the wavelength-dependent attenuation of an incident light beam. One molecule is excited (raised to a higher energy state) for every photon absorbed and the energy of the absorbed photon equals the energy difference between the initial and final molecular states of the transition. The spectra are interpreted with the aid of various quantum mechanical models such as the harmonic oscillator or rigid rotor. The characteristic nature of the absorbance spectra has qualitative analysis applications. The presence of a given species in a mixture may be inferred from its characteristic spectral features in the absorbance spectrum of the mixture. The term fingerprinting is sometimes used in this context, particularly in infrared spectroscopy.

Absorbance spectra are quantitatively interpreted in terms of Beer's Law, which states that the absorbance is proportional to the product of the concentration of the absorbing species, the path length of the light through the sample, and a fundamental parameter known as the molar absorptivity. The absorbance is defined as the negative logarithm of the transmittance (the fraction of light that gets through the sample). If both the molar absorptivity and path length are known, then the concentration is inferred from the absorbance value. As is well known, sensitive absorbance measurements involve measuring a small difference between two relatively large light signals.

Many applications in environmental science and air quality monitoring involve concentrations too low to measure with conventional absorbance techniques. A strong electronic transition in the ultraviolet (UV) or visible (VIS) region may have a molar



absorptivity of  $10^3$ - $10^4$  L/mol-cm. An absorbance value of 0.01 for a path length of 10 cm corresponds to a concentration of  $10^{-6}$ - $10^{-7}$  mol/L. At room temperature, the corresponding partial pressure range is  $2.5$ - $25 \times 10^{-6}$  atm (atmosphere) or 2.5-25 ppmv (parts per million by volume).

Fluorescence excitation spectroscopy is often more sensitive than absorbance for probing upward molecular transitions because it is effectively a zero-background measurement, i.e., the signal appears against a weak background. With appropriate corrections, the fluorescence excitation spectrum is equivalent to the absorbance spectrum.

Resonance enhanced multiphoton ionization (REMPI), the topic of this thesis, combines favorable attributes of conventional linear absorbance and fluorescence spectroscopy. To a first approximation, the REMPI spectrum is identical to the conventional absorbance spectrum but the measurement itself is ideally zero-background in nature, which makes it more sensitive than direct absorbance. This higher sensitivity is advantageous for probing the optically thin samples encountered in supersonic jet expansions, which constitute the vast majority of REMPI applications. Time-of-flight mass spectrometry (TOFMS), which requires even lower pressures, is often used in combination with the supersonic expansion to mass analyze ions generated in REMPI processes. Thus, it is not surprising that REMPI is sometimes considered as an inherently low-pressure technique.

However, there are no fundamental factors that preclude ambient pressure REMPI measurements. Once the oppositely charged species created by the ionization process have separated, pressure does not affect the efficiency of the charge collection at the biased electrodes, just the time interval. Various ion-molecule reactions may occur as the ions

drift to the electrodes, but no charge need be lost in a properly designed cell. It should also be recognized that the flame ionization and photoionization detectors, which are widely used in gas chromatography and ion mobility spectrometers, rely on ion collection and quantitation at near atmospheric pressure.

Relatively little REMPI spectroscopic work performed under ambient pressure conditions has been reported. Small molecules such as nitric oxide, nitrogen dioxide, and acetaldehyde have been studied in the most detail. Aromatic species such as benzene, toluene, aniline, styrene, and naphthalene have also been characterized. Spectral congestion, often a factor associated with higher molecular weight species, may have served as a deterrent to studying molecules at ambient pressure via REMPI.

A major issue that needs to be examined deals with how much specificity can be obtained without the cost and complexity associated with jet cooling and TOFMS. Consequently, our research group is pursuing REMPI at ambient pressure and temperature as the basis for real-time chemical analysis. There are many different gas-phase species that could be detected under ambient pressure REMPI conditions. The need to identify the most appropriate target species, the optimal spectral ranges, and possible interferences exists.

For single ring aromatic molecules, the onset wavelength of significant UV absorbance often corresponds to a photon energy that is close to half the molecule's ionization energy. Data are given for representative species in Table 1. The first singlet transition ( $S_1 \leftarrow S_0$ ) in each case lies at a sufficiently short wavelength to allow efficient 1+1 REMPI detection.

Table 1. Spectral data for aromatic hydrocarbons

Molecule	IE (eV)	Maximum $\lambda$ for 1+1 REMPI (nm)	Onset $\lambda$ (nm)
Benzene	9.24	268.4	260.0 (strong) 267.0 (weak)
Toluene	8.82	281.2	267.0
Ethylbenzene	8.76	283.1	267.0
Xylenes	8.44 (p)	293.8	272.0
	8.56 (o, m)	289.7	270.0 (m)
Aniline	7.70	322.1	291.2
Styrene	8.47	292.8	287.8
Phenol	8.51	291.4	275.0
Indene	8.14	304.6	287.9

Key: IE = ionization energy; eV = electron volt;  $\lambda$  = wavelength; nm = nanometer; o = ortho; m = meta; p = para.

The resonant photon absorption that initiates a 1+1 REMPI event has the same cross-section as conventional one-photon absorbance. The wavelength selectivity of the subsequent photon transition from the resonant state to the ionization continuum is expected to be low in most cases. Thus, the action spectrum of ion current versus wavelength in a one-color experiment should resemble the conventional absorbance spectrum, but this assumption has not been rigorously tested to our knowledge. The optically thin nature of free jet expansions or molecular beams makes a direct absorbance measurement difficult, and too little REMPI work has been done in the ambient pressure regime.

Our investigation of indene, C<sub>9</sub>H<sub>8</sub>, under ambient pressure REMPI conditions gives us the opportunity to examine the validity of this assumption. Indene is an excellent candidate molecule for ambient pressure REMPI study for many reasons: it is a polycyclic aromatic hydrocarbon, which allows us to examine the issue of spectral congestion; the room temperature vapor pressure (ca. 2 torr) of indene means the molecule is amenable to

headspace analysis; the molecule can be efficiently ionized in the wavelength region of its first singlet transition via a 1+1 REMPI process, and consequently the durable and efficient rhodamine class of laser dyes can easily supply the requisite visible output needed for frequency-doubling into this wavelength region; the gas-phase UV-VIS absorption spectrum of indene exhibits relatively narrow features. All these factors make indene a suitable molecule for investigation. The room temperature 1+1 and 2+2 REMPI spectra of indene in ambient air are reported here for the first time. The 1+1 REMPI spectrum for a supersonic jet expansion has been partially analyzed by Kendler et al.<sup>1</sup>

## **B. Multiphoton Processes: Historical Background**

Multiphoton spectroscopy involves the simultaneous absorption of two or more photons, generally in the visible or ultraviolet regions. Vibronic and electronically excited states not seen in single-photon spectroscopy can be observed owing to different selection rules and transition probabilities. Although simultaneous two-photon absorption (TPA) was theorized by Goeppert-Mayer<sup>2</sup> in 1931, experimental observation of TPA (the lowest-order multiphoton process) in molecules had to await the advent of high-intensity pulsed lasers in the late 1960s. Conventional non-laser sources (discharge lamps) were unable to induce TPA in molecules due to the high-intensity conditions that must be satisfied in multiphoton transitions. Compared to a typical single-photon cross-section ( $10^{-18} \text{ cm}^2$ ), multiphoton cross-sections for two-photon and three-photon processes are typically  $10^{-51} \text{ cm}^4 \cdot \text{s}$  and  $10^{-82} \text{ cm}^6 \cdot \text{s}^2$ , respectively.<sup>3</sup> Thus, the laser provides the high-photon flux needed to overcome these low multiphoton cross-sections.

Gas-phase multiphoton ionization (MPI) was first demonstrated as a spectroscopic technique in 1975. Johnson et al.<sup>4,5</sup> and Dalby et al.<sup>6</sup> reported the initial observations of

MPI in the molecular systems of nitric oxide, benzene, and iodine, respectively. The ionization cell configuration in many of these early experiments was a thin wire axially positioned in a cylindrical metal tube and positively biased at 100 V. The laser was focused into a cell filled with the analyte vapor at a few torr pressure. Free electrons created in the MPI process were collected at the positively biased wire. The resulting current was amplified and the signal displayed on a chart recorder. Alternatively, the thin axial wire and cylindrical tube can be replaced with two parallel plate electrodes.

Reviews on the development of multiphoton spectroscopy can be found in the literature.<sup>3,7,8</sup> Although MPI spectroscopy has been applied to samples in the solid and liquid phases, our primary interest lies in the investigation of gas-phase molecules. The next section will describe various MPI processes that may occur for molecules in the gas phase.

### C. Gas-Phase MPI

MPI spectroscopy is based upon the ionization of an excited state formed by a multiphoton transition. Thus, the final state reached optically in a MPI process is an ionization continuum rather than a bound energy state. A simplified molecular energy-level diagram is shown in Figure 1. In this example, the molecule has sufficiently low ionization energy that ionization can occur through the simultaneous absorption of two photons. The first step is sometimes simplistically considered to involve excitation of the molecule to a short-lived ( $10^{-15}$  s) virtual state, followed by absorption of the second (ionizing) photon. This ionization process, referred to as non-resonant MPI, is inefficient. A tightly focused laser beam is commonly used to provide the high-photon flux needed for these multiphoton transitions, and the non-resonant process provides limited selectivity

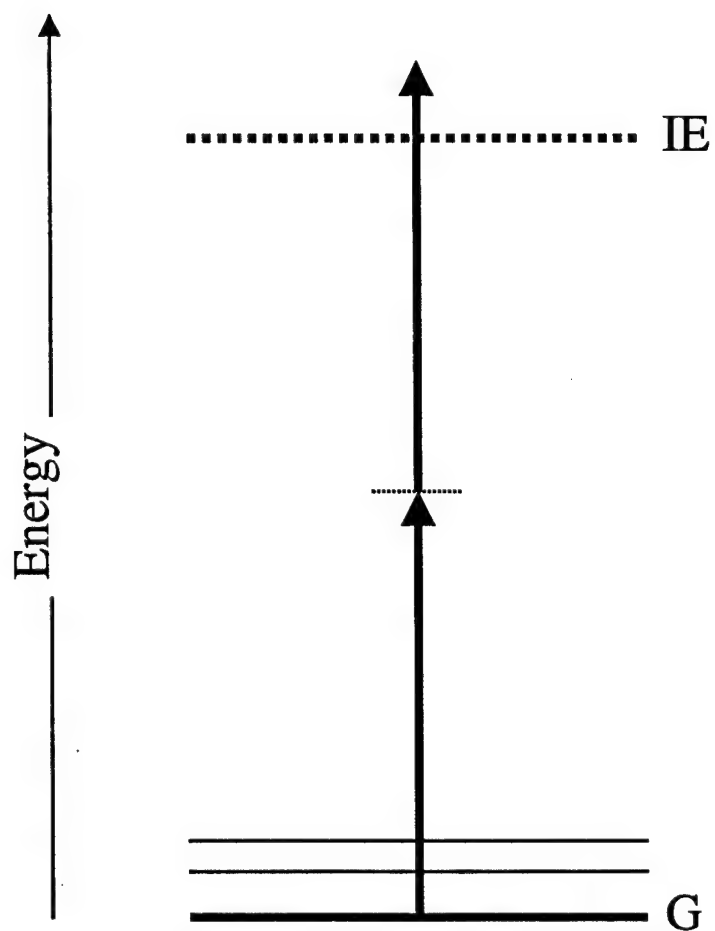


Figure 1. Simplified energy-level diagram for a molecule undergoing a non-resonant MPI process. Key: G = ground electronic state; IE = ionization energy. The small dashed line represents a virtual state.

since all molecules with sufficient ionization energies can be ionized with similar efficiencies.

Enhanced selectivity can be obtained through a two-photon (the easiest and most efficient case) ionization process that utilizes a real intermediate (resonant) electronic state as a "stepladder" towards ionization. The ionization efficiency of this process, termed resonance enhanced multiphoton ionization (REMPI), is several orders of magnitude greater than non-resonant MPI processes. Conventional terminology is to refer to  $m+n$  REMPI, where  $m$  is the number of photons that must be absorbed to reach the intermediate excited state (the resonance), and  $n$  the additional number of photons that must be absorbed to ionize the molecule. In the REMPI processes described here, the photons are of identical wavelength (single color).

It is interesting to note that REMPI is essentially a laser-based elaboration of the familiar single-photon photoionization detector (PID) commonly found in gas chromatographs and organic vapor analyzers.<sup>9,10</sup> Conventional PIDs use low-intensity discharge lamps that provide continuous broadband light in the vacuum ultraviolet region. Molecules that absorb the short-wavelength lamp photons are ionized, and the ion current is measured. The ionization process in this case is practically non-selective; all species whose ionization energy is less than the photon energy of the light source are ionized.

In contrast, the light source for the REMPI process is a pulsed laser, ideally one whose wavelength can be tuned in the ultraviolet or visible spectral region. A simplified molecular energy-level diagram depicting a 1+1 REMPI process is shown in Figure 2. In this ionization procedure, the first photon absorbed by the molecule excites an intermediate

electronic state. In most molecules, the lifetime of the intermediate state is on the order of

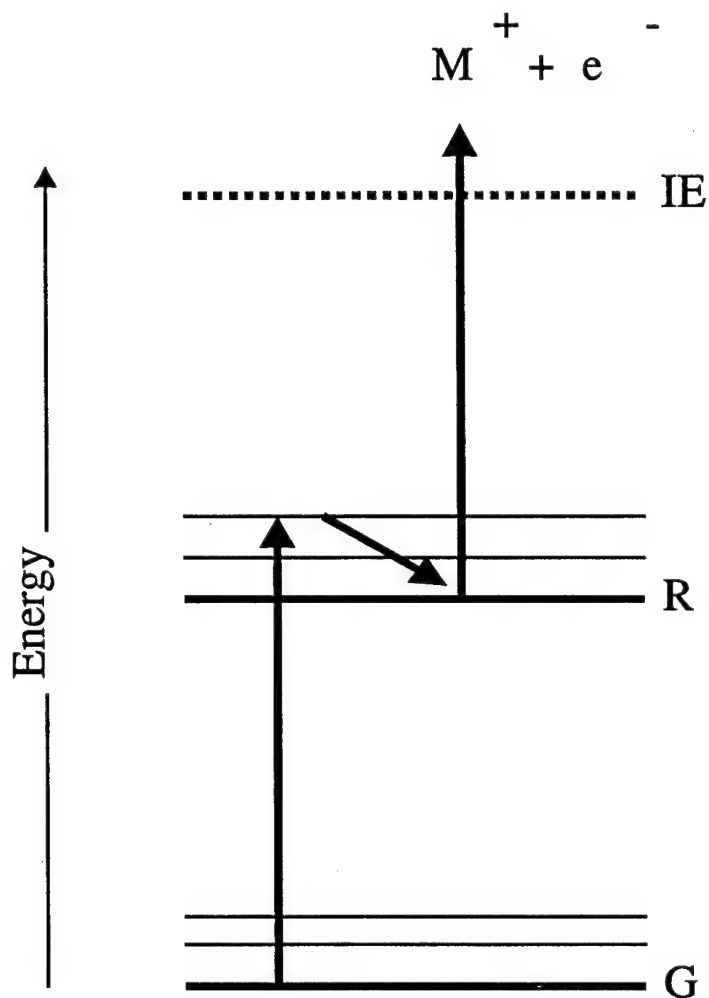


Figure 2. Simplified energy-level diagram for a molecule undergoing a 1+1 REMPI process. Key: G = ground electronic state; R = intermediate (resonant) electronic state; IE = ionization energy; M<sup>+</sup> = molecular ion; e<sup>-</sup> = electron.



a typical dye laser pulse ( $10^{-8}$ - $10^{-9}$  s) so that absorption of the second photon raises the molecule into the ionization continuum. The relatively long excited state lifetime relaxes the high laser power requirements that are typical in non-resonant MPI processes. The high selectivity of the REMPI process follows from the structured UV-VIS absorption spectrum of the neutral molecule. Thus, by tuning the laser wavelength to selectively populate resonant states in molecules of interest, one can obtain selective ionization.

In addition to 1+1 REMPI excitation, higher-order multiphoton processes can be used to probe molecular species. A simplified energy-level diagram depicting a 2+2 REMPI process is shown in Figure 3. In this ionization procedure, two photons must be simultaneously absorbed to reach the intermediate electronic state, followed by the successive absorption of two additional photons to ionize the molecule. Since detection via 2+2 REMPI incorporates non-resonant (virtual) states, the transition probability is lower compared to a 1+1 REMPI excitation scheme. Usually, a focused laser beam is used to provide the high-photon flux required for the 2+2 REMPI process. In addition, much higher sample concentrations are used, which reduces the overall sensitivity of the 2+2 REMPI process.

The transition probability and therefore the ion yield in a REMPI process is clearly dependent on the intensity of the laser light. In general, the  $i$ -photon transition probability is proportional to the  $i^{\text{th}}$  power of the laser intensity. This relationship is called the formal intensity law for the multiphoton transition. One can determine the order of the multiphoton transition from the slope of a bi-logarithmic plot of ion yield versus laser intensity. For REMPI processes, the intensity law holds at low to moderate laser photon flux. Optical (absorption) and geometric (focusing) saturation effects that are common

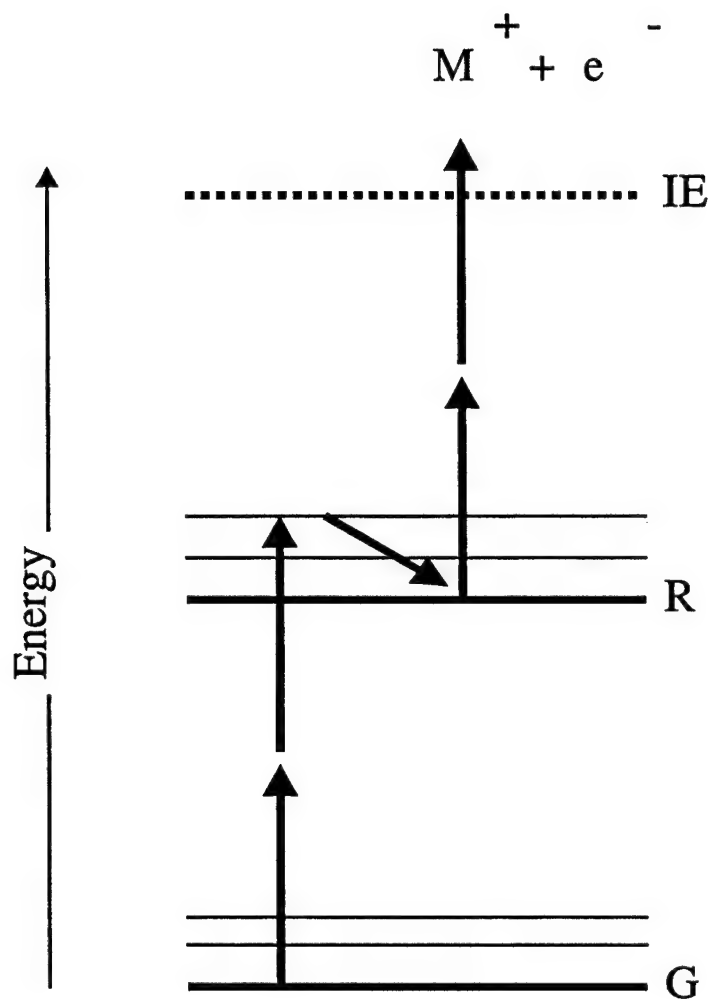


Figure 3. Simplified energy-level diagram for a molecule undergoing a 2+2 REMPI process. Key: G = ground electronic state; R = intermediate (resonant) electronic state; IE = ionization energy;  $M^+$  = molecular ion;  $e^-$  = electron.

under high laser intensity conditions will often lead to a significant deviation from the intensity law.

By limiting the laser intensity to  $10^4$ - $10^6$  W/cm<sup>2</sup>, the absorption of photons in a REMPI process will result in the exclusive formation of molecular ions. Since absorption of photons by the molecular ions is negligible at this low laser light intensity, no fragmentation takes place. The formation of only molecular ions is commonly referred to as a soft ionization procedure. In a hard ionization process, which occurs at higher laser intensity, additional photons are absorbed by the molecular ions, which then follow the energetically and kinetically most favored fragmentation pathway.<sup>11</sup> At sufficient laser intensities, the total destruction of a molecule into its atomic particles is possible. A discussion of this absorption-fragmentation mechanism can be found in the literature.<sup>12,13</sup> Thus, the extent of fragmentation can be controlled in a REMPI process by the choice of laser intensity. The next section will describe a mass-selective detection scheme that is commonly applied in tandem with REMPI.

#### **D. Time-of-Flight Mass Spectrometry (TOFMS)**

Time-of-flight mass spectrometry (TOFMS) takes advantage of the small-volume, pulsed ion production by REMPI.<sup>14,15</sup> The fundamental components of a time-of-flight mass spectrometer are an ion source, a differentially pumped drift tube, and an ion detector. In a typical experiment, a gaseous sample is ionized with a pulsed laser that is passed between two parallel grids. A negative bias between the grids causes the nascent ions to be accelerated at equal kinetic energies in the direction of the differentially pumped drift tube. The ions enter the collision-free (high vacuum) drift tube at velocities that are dependent upon their respective masses. Thus, ions can be physically separated according to their

mass. From the reference frame of the ion detector, the ions are separated in time with the lighter ions arriving first. Hence, mass-to-charge ratios for ionized species can be determined from the flight times. In general, the flight time is inversely proportional to the square root of the mass.

The time-of-flight mass spectrometer is an efficient mass-selective detector. In addition to its low cost and simplistic design, the instrument is capable of detecting an entire mass spectrum with each ionizing laser pulse. The combination of REMPI and TOFMS results in a two-dimensional analysis technique with the parameters of laser wavelength and ion mass. Reviews on the theory and development of REMPI/TOFMS can be found in the literature.<sup>11,16,17</sup> The next section presents a discussion of another common experimental technique used in REMPI.

#### **E. Jet Spectroscopy**

The gas-phase UV-VIS absorption spectra of polyatomic molecules at room temperature exhibit generally broad and relatively unstructured bands owing to the large number of vibrational and rotational states that are populated per the Boltzmann distribution. The spectral selectivity inherent in the REMPI process is reduced. Jet spectroscopy is a low-temperature, gas-phase technique that provides great spectral simplification.<sup>18</sup>

In a typical jet experiment, the molecule of interest is "seeded" in a noble carrier gas and expanded through a small orifice or nozzle into a high vacuum. This process, referred to as a supersonic jet expansion, translationally cools the gas mixture. A series of two-body collisions between the cold carrier gas atoms and the seed molecules results in the relaxation of molecular internal degrees of freedom. Hence, the seed molecules

become cooled translationally, rotationally, and to a lesser extent, vibrationally. The seed molecules do not condense because they are isolated from one another by the carrier gas. Rotational cooling sharpens the molecule's spectral features from typically nanometer widths to hundredths or even thousandths of a nanometer.<sup>19</sup>

In many jet experiments, a skimmer is placed in the supersonic expansion, which results in the formation of a molecular beam. These molecular beam techniques produce "spectroscopically" cold molecules that possess a narrow velocity distribution. Ionized species produced under these conditions are amenable to mass analysis via TOFMS. Thus, jet spectroscopic techniques inherently provide increased spectral and mass resolution in REMPI processes. Hollas and Phillips<sup>20</sup> provide an excellent review on current jet spectroscopic techniques.

#### **F. Ambient Pressure REMPI**

Jet-REMPI/TOFMS has become a popular laboratory research technique owing to its outstanding combination of sensitivity and selectivity. A variety of molecules have been studied via jet-REMPI/TOFMS, where the usual emphasis is on the wavelength dependence of the molecular transitions to obtain fundamental spectroscopic properties. However, supersonic cooling and TOFMS require high vacuum conditions that make them unsuitable for real-time chemical analysis. From an analytical perspective, the benefits of cooling obtained in jet or molecular beam techniques are partially offset by the reduction in analyte number density. REMPI could serve a wide range of applications in environmental analysis, indoor/outdoor air quality, and leak detection, but the complexity and cost of the requisite high-vacuum systems has hampered progress. It is interesting to note the common misconception that REMPI ion collection requires high vacuum conditions. With

the exception of a few groups, relatively little work has been devoted to ambient pressure REMPI detection methods. The following paragraphs will provide a brief discussion of those groups who have carried out ambient pressure REMPI experiments.

The first report of ambient pressure REMPI was in 1979 by Brophy and Rettner,<sup>21</sup> who studied 1+1 REMPI of aniline in air. They used a simple ionization cell in which the UV output from a pulsed frequency-doubled dye laser was focused between two parallel copper plates biased at 10 V. The resulting ion current was measured with an electrometer. The 1+1 REMPI spectrum exhibited significant structure. The concentration of aniline was in the ppmv range.

In the late 1970s and early 1980s, a group at the Aerospace Corporation (Los Angeles, CA) conducted a series of experiments that demonstrated the sensitivity of ambient pressure REMPI. Naphthalene vapor at concentrations below  $10^7$  molecules/cm<sup>3</sup> could be detected in buffer gases of argon, nitrogen, and air at atmospheric pressure.<sup>22</sup> The naphthalene detection limit in nitrogen was estimated at  $5 \times 10^4$  molecules/cm<sup>3</sup>.<sup>23</sup> In these experiments, the focused frequency-doubled output of a Nd:YAG (neodymium: yttrium aluminum garnet) pumped dye laser was used to measure the 1+1 REMPI spectrum in the vicinity of naphthalene's second singlet transition ( $S_2 \leftarrow S_0$ ) at 279 nm. Ion generation was monitored through the use of a proportional counter detector. The ionization cell was also coupled to a conventional gas chromatograph and mass detection limits on the order of 10 picograms were obtained for anthracene, phenanthrene, benzanthracene, acenaphthene, naphthalene, and various halonaphthalenes.<sup>24</sup>

In the early 1990s, researchers at the University of Glasgow (Glasgow, UK) used 1+1 REMPI to selectively detect trace quantities of nitric oxide photolyzed from nitrogen

dioxide in air at atmospheric pressure.<sup>25</sup> A detection limit for nitrogen dioxide was estimated at 150 ppbv (parts per billion by volume). In addition, nitrobenzene and ortho-nitrotoluene were detected in ambient air via 1+1 REMPI at concentrations in the ppmv range.<sup>26</sup> These nitroaromatic compounds are the main substituents in explosives. Benzene vapor was also detected in ambient air via 1+1 REMPI at a sensitivity of 25 ppbv.<sup>27</sup> In these REMPI experiments, the excitation source was an excimer pumped dye laser that was frequency-doubled to provide focused UV light in the 224-264 nm wavelength region. The ionization cell was a metal box that housed two parallel copper plates biased at 100 V. The ion current was collected with a pre-amplifier and subsequently digitized for data analysis.

During the same time period, Ogawa et al.<sup>28,29,30</sup> studied laser two-photon ionization detection of aromatic molecules on liquid and metal surfaces in ambient air. In their experiments, a pulsed nitrogen laser at 337 nm was focused onto an adsorbed sample or liquid droplet. A positively biased (2.5 kV) electrode was used to collect photoelectrons released by the two-photon ionization process. The entire assembly was housed within a metal box at atmospheric pressure. The generated ion current was collected with a pre-amplifier and sent to a digital storage oscilloscope (DSO) for data analysis. Ogawa's results indicated that the photoionization signal was approximately linear with respect to solute concentration. Although these experiments were performed under ambient-pressure conditions, the fixed wavelength excitation could not exploit the inherent spectral selectivity of REMPI.

Similarly, Schechter et al.<sup>31,32</sup> used a single wavelength (248 nm) from a krypton fluoride excimer laser to ionize organic molecules (demonstrated with benzene) in a vacuum via non-resonant MPI. To the time-resolved ion current data, they applied

chemometric techniques to extract information on the ion masses and number of ions.<sup>33</sup>

Although their method was touted as an ambient-pressure detection scheme, examination of their experimental procedure clearly shows that high vacuum conditions ( $10^{-6}$  torr) were employed. In addition, the spectral selectivity of REMPI was not utilized. Using an experimental apparatus similar to Ogawa's group, Schechter et al. also detected pyrene in droplets<sup>34</sup> and soil<sup>35,36</sup> samples in ambient air.

More recently, Gillispie, Swenson, and co-workers have detected aniline, styrene, acetaldehyde, and BTEX (benzene, toluene, ethylbenzene, xylenes) species via 1+1 REMPI in atmospheric pressure air.<sup>37,38,39</sup> Detection limits of less than 1 ppbv have been obtained. In their experiments, REMPI spectra were collected by scanning the light from a frequency-doubled dye laser into a simple ionization cell under ambient conditions. The main focus of their REMPI work was obtaining limits of detection for chemical species that are of interest to the United States Air Force. The next chapter will provide a description of the experimental apparatus that was for our REMPI measurements at ambient conditions.



## II. EXPERIMENTAL

### A. Pump Laser

The pump laser for these experiments is the second harmonic of a 50 Hz Big Sky Laser Technology CFR-200 Nd:YAG laser. The laser head contains a Q-switched Nd:YAG oscillator and KTP (potassium trihydrogen phosphate) frequency-doubling module that is connected by umbilical cables to a rack-mountable control unit and cooling system. The pump laser provides a pulse energy of 50 mJ at 532 nm. The pulse width is 10 ns at full width at half maximum (FWHM).

The control unit is powered by 110 V AC and provides the high voltage required to flash-pump the laser rod, as well as manage the system timing, safety interlocks, and synchronization of the laser system. The laser head is pressurized with 5 psi of dry nitrogen to prevent condensation on the optics. An oven mounted in the resonator enclosure keeps the KTP crystals dry and stabilizes the frequency-doubled output. The Nd:YAG laser uses a distilled water cooling system with a liquid-to-air heat exchanger to cool the flashlamp and laser rod.

### B. Dye Laser

The dye laser oscillator consists of a commercial Littman grazing incidence dye laser (Lumonics Hyperdye-300) that has been modified by replacing its flowing dye cell with a Bethune prism cell.<sup>40</sup> The prism beam expander has also been eliminated, which increases the visible linewidth to  $0.4 \text{ cm}^{-1}$ . The visible linewidth is degraded upon removal of the prism beam expander because the irradiated length along the diffraction grating is reduced. A second Bethune prism cell is used as a single-stage amplifier. The oscillator

and amplifier cells each have a bore diameter of 2 mm and a length of 25 mm. A centrifugal dye pump circulates a 0.3 mM rhodamine 590 dye solution through both prism cells from a 500 mL reservoir. The dye circulation system is made from 6.35 mm (0.25 in.) diameter tubing that incorporates Swagelok and quick-connect components. The return dye lines pass through a small refrigerator (Avanti) in order to cool the dye, which improves long term amplitude stability.

The scan control unit (SCU) provides wavelength scanning of the Hyperdye-300 dye laser. It can be operated either through a remote keypad or the acquisition computer (serial port). The SCU drives a worm-and-wheel mirror-stage stepper-motor that uses an incremental shaft encoder and an optoelectronic home sensor to electronically record the mirror angle. The central processing unit of the SCU then converts the tuning mirror angle into wavelength units. An optogalvanic cell<sup>41</sup> is used to calibrate the dye laser and measure the laser linewidth of the visible dye output. Software routines written in Quick Basic are used to control the SCU from the acquisition computer.

### **C. Experimental Apparatus**

A schematic of the ambient pressure REMPI set-up is shown in Figure 4. The apparatus is mounted on a 4 ft (1.2 m) by 8 ft (2.4 m) Newport optical table. The optical components are oriented to avoid focused reflections from entering the laser head and oscillator cavity. A supported plywood roof that is attached with plastic curtains covers the breadboard. The plastic curtains protect the optical components from dust and block stray reflections.

A 20% reflective (at 45°) beamsplitter (BS1, Figure 4) is used to supply the oscillator (OSC, Figure 4) with 20% of the Nd:YAG pump beam (Big Sky, Figure 4). The

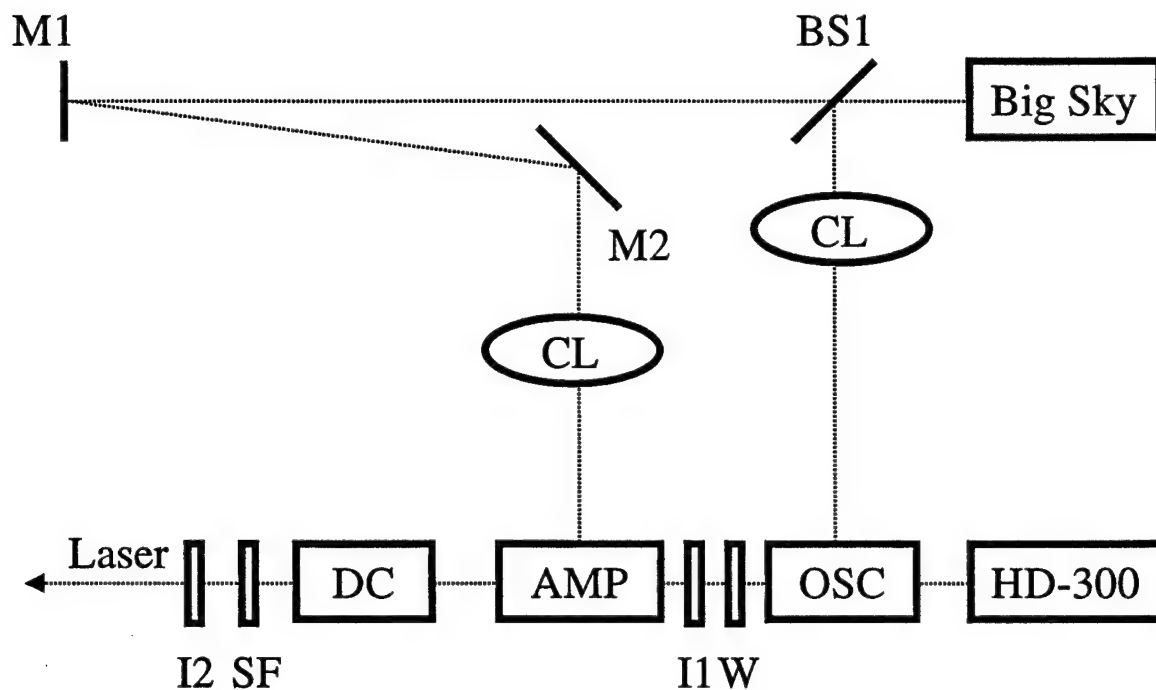


Figure 4. Schematic diagram of the experimental apparatus used for ambient pressure REMPI measurements. Key: Big Sky = Nd:YAG pump laser; BS1 = 20% at 45° beamsplitter; M1 = 100% at 0° dichroic mirror; M2 = 100% at 45° mirror; CL = 15 cm cylindrical lens; HD-300 = Hyperdye-300 tuning system; OSC = Bethune oscillator; W = BK-7 wedge; I1 = 3 mm iris; AMP = Bethune amplifier; DC = KDP doubling crystal; SF = Schott UG-11 filter; I2 = adjustable iris.

remainder is delayed by approximately four nanoseconds before reaching the amplifier (AMP, Figure 4). The optical delay line consists of a 100% reflective (at  $0^\circ$ ) dichroic mirror (M1, Figure 4) and a 100% reflective (at  $45^\circ$ ) mirror (M2, Figure 4). Delaying the pumping of the amplifier with respect to the oscillator reduces amplified spontaneous emission. With the pump beam delay, the amplifier will not provide gain until the oscillator has reached threshold. Therefore, amplification of the initial broadband fluorescence in the oscillator is minimized.<sup>42</sup>

For both prism cells, the 5 mm diameter pump beam is broadened by passing through the focal point of a 15 cm cylindrical lens (CL, Figure 4) and diverging to fill the 25 mm long bore. This optical arrangement ensures that the entire 25 mm wide faces of the Bethune prism cells are irradiated with the pump beam. This focusing condition results in a 2 mm (bore diameter) by 25 mm (length) cylindrical gain region of excited dye molecules with each pulse of the pump beam.

A BK-7 wedge (W, Figure 4) is used as the output coupler to reflect 4% of the excited dye molecule emission back through the active gain region. The amplified feedback beam is incident on the 2400 //mm holographic diffraction grating at near grazing incidence ( $86^\circ$ ). The dispersed beam from the grating is reflected back by the tuning mirror positioned at variable angles with a stepper motor controlled rotation stage (HD-300, Figure 4).

The visible oscillator beam passes through a 3 mm iris (I1, Figure 4) before it is amplified to several millijoules in a second Bethune prism cell. The amplified beam is frequency-doubled into the ultraviolet region with an Inrad KDP (potassium dihydrogen phosphate) doubling crystal (DC, Figure 4). The phase matching angle of the doubling

crystal must be precisely adjusted as the wavelength is scanned to maintain doubling efficiency. The correct angle is obtained by a stepper motor driven rotation stage. Software routines written in Quick Basic and MatLab are used to drive the rotation stage and calibrate the doubling crystal to the wavelength scanning mechanism of the Hyperdye-300.

A Schott UG-11 filter (SF, Figure 4) is positioned after the doubling crystal to block the residual visible light. Ultraviolet pulse energies of a few hundred microjoules in the 282-295 nm range are routinely generated in this fashion. The unfocused UV laser light is then directed into the REMPI cell. An adjustable iris (I2, Figure 4) is used to prevent ultraviolet reflections off of the cell windows from propagating back through the optical train.

A schematic of the ambient pressure REMPI cell and its peripheral components is shown in Figure 5. For 1+1 REMPI measurements, the unfocused frequency-doubled output is passed between copper parallel plate electrodes 2 cm in diameter and separated by 1.5 cm. The copper electrodes, supported by BNC feedthrough flanges (Ceramaseal, Inc.), are housed within the opposite ends of a stainless steel four-way cross (MDC Manufacturing, Inc.) and biased with a 300 V battery (VB, Figure 5). The electric field between the electrodes is 200 V/cm. Plexiglas cell mounts are used to insulate the REMPI cell from the optical table to reduce radio frequency noise produced by the laser power supply. The laser beam passes through fused silica windows sandwiched between Viton gaskets.

A fused silica beam splitter (BS2, Figure 5) positioned after the REMPI cell is used to reflect 8% of the transmitted laser energy into a rhodamine-B quantum counter (QC,

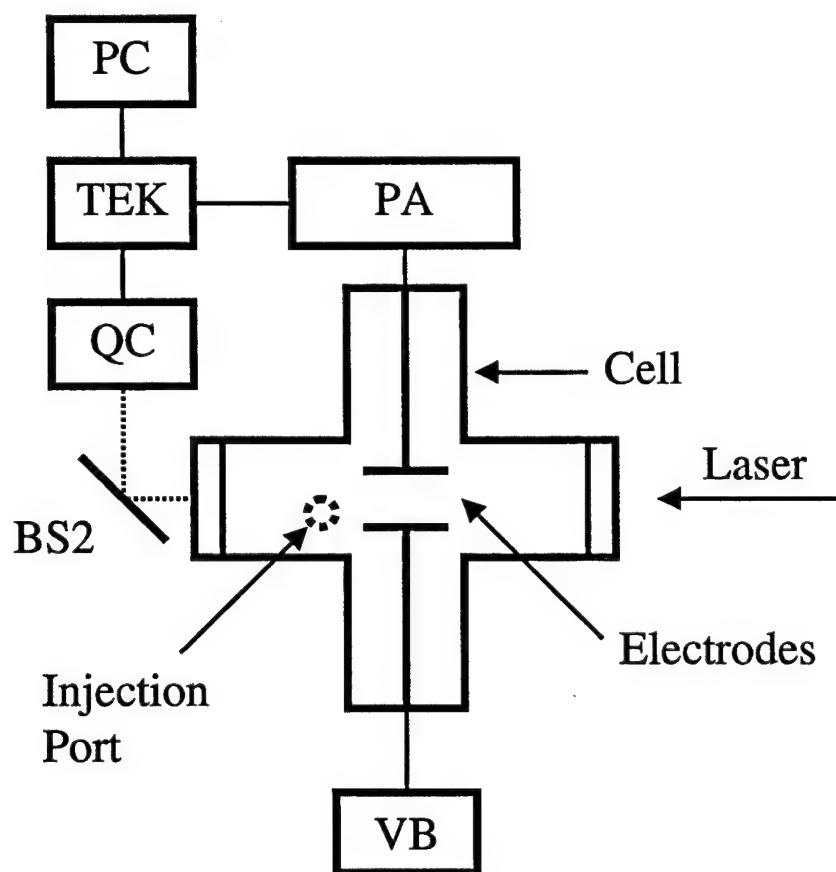


Figure 5. Schematic diagram of the ambient pressure REMPI cell and peripheral components. Key: VB = 300 V battery; BS2 = 8% at 45° beamsplitter; QC = rhodamine B quantum counter; PA =  $10^8$  V/A pre-amplifier; TEK = Tektronix 2440 DSO; and PC = 33 MHz 486 IBM personal computer.

Figure 5). The remainder is dumped into a graphite block. The quantum counter is used to correct the REMPI signal for variations of the dye laser pulse energy as the wavelength is scanned. For 2+2 REMPI measurements, a 10 cm lens is used to focus the amplified visible output into the center of the REMPI cell. A Molectron J-25 joulemeter is used to measure laser energy for 2+2 REMPI experiments.

Vapor taken from the headspace over the neat liquid or solid is injected through a septum on the REMPI cell using a gas chromatography (Hamilton) or tuberculin (B-D Glaspak) syringe. The REMPI cell is filled with ambient laboratory air at room temperature. The internal volume of the REMPI cell is approximately 250 mL. Alternatively, a small crystal of the analyte can be deposited into the REMPI cell and allowed to equilibrate at room temperature. In order to eliminate residual aromatic background interference, a vacuum oven (VWR Scientific Products 1400E) is used to bake all cell components at 110°C for several hours.

A REMPI spectrum consists of the integrated ion current (hence total charge collected) as a function of laser wavelength. The small REMPI ion currents undergo a  $10^8$  V/A current-to-voltage conversion in a home-built pre-amplifier (PA, Figure 5). The amplified voltage versus time waveforms are displayed, digitized (1024 data points), and averaged over 32 or 64 shots in a 200 MHz Tektronix 2440 DSO (TEK, Figure 5). The integrated area under the waveform is proportional to the number of ions created by the REMPI process. A photodiode is used to ensure stable triggering of the DSO.

All signal data recorded by the oscilloscope (REMPI, quantum counter) are downloaded to a 33 MHz 486 IBM compatible personal computer (PC, Figure 5) for permanent storage and data processing. A GPIB card (National Instruments) housed within

the acquisition computer is used to communicate with the DSO. Software routines written in MatLab are used to integrate and graph both REMPI and quantum counter waveforms. Unless otherwise noted, the integrated REMPI signal is divided by the square of the integrated quantum counter response in order to normalize for the laser power.

#### **D. Absorbance Experiments**

Medium-resolution (0.03 nm bandwidth) absorbance spectra of indene are measured with a Cary 500 UV-VIS-NIR spectrophotometer (Varian, Inc.).

#### **E. Reagents**

Unless otherwise stated, all chemicals were purchased from their respective manufacturers and used without further purification. Indene (99%), indole (90%), and styrene (98%) were purchased from Aldrich. HPLC-grade methanol was purchased from E.M. Science. Rhodamine 590 dye was purchased from Exciton. Helium was purchased from GenEx. Coal tar, creosote, and diesel fuel samples were obtained from Dakota Technologies, Inc.

#### **F. Power-Dependence and Pressure Broadening Experiments**

For 1+1 REMPI power-dependence experiments, a Newport 935-3 variable beam attenuator is placed after the Schott UG-11 visible-blocking filter. This optical component allows one to attenuate the frequency-doubled output without changing the temporal or spatial characteristics of the beam profile. For pressure broadening experiments, the REMPI cell is evacuated to 5 mtorr with a mechanical vacuum pump (Welch Scientific Company) that incorporates Swagelok fittings. The cell is then filled with one atmosphere of helium or maintained at reduced air pressure. The REMPI signal observed is generated



from indene that is left over from previous 2+2 REMPI experiments. In addition, the 300 V battery is replaced with a variable (0-2.1 kV), high-voltage power supply (Fluke 412B) to prevent saturation of the pre-amplifier.

#### **G. Styrene 1+1 REMPI Spectrum**

The ambient pressure REMPI spectrum of styrene,  $C_8H_8$ , near the origin of its first singlet transition has been re-examined to assess apparatus improvements made since our previous study.<sup>37</sup> The corrected 1+1 REMPI spectrum of 100 ppbv styrene in air at atmospheric pressure is shown in Figure 6. The higher signal-to-noise and reduced wavelength step (0.005 nm) reveals considerably more structure in the spectra. The complex pattern of features arises from a combination of extensive sequence band structure and partially resolved rotational contours. Repeat high-resolution scans taken over this same 1 nm range agree very well with the spectrum shown in Figure 6. The next chapter will discuss the results obtained for our REMPI studies at ambient conditions.

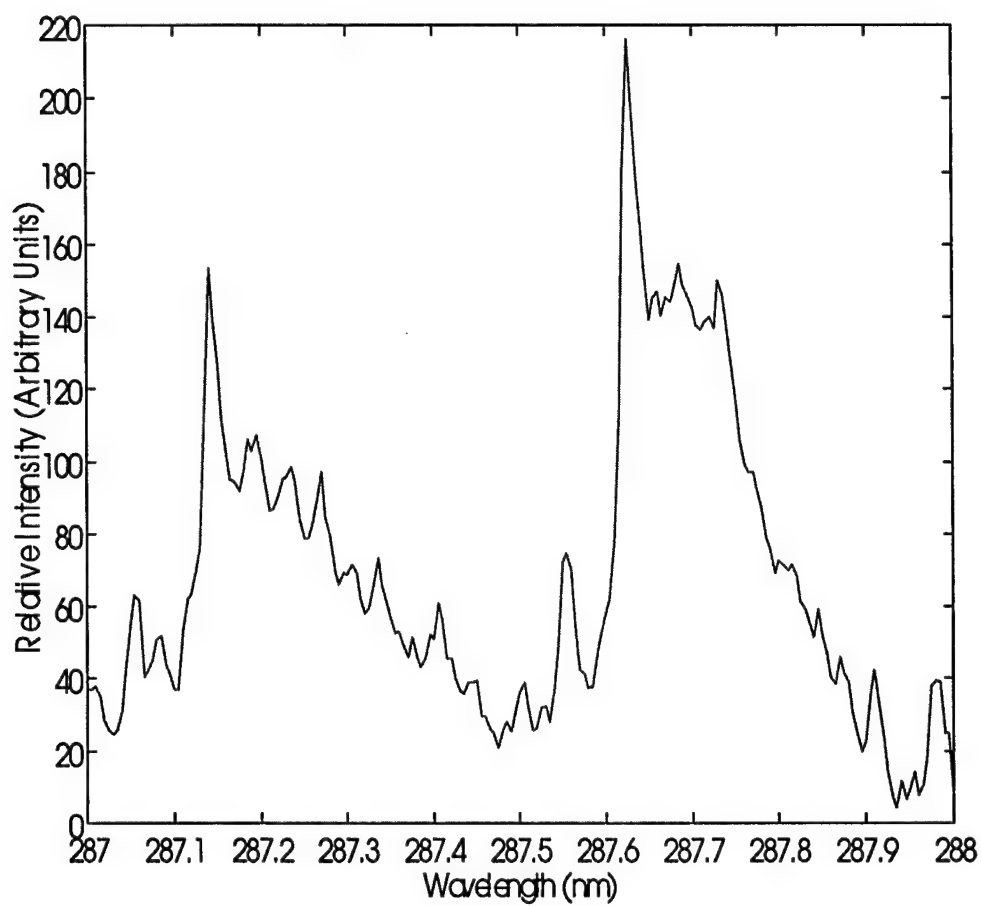


Figure 6. Corrected 1+1 REMPI spectrum of 100 ppbv styrene in ambient air. Step size = 0.005 nm.

### III. RESULTS AND DISCUSSION

#### A. Ambient Pressure REMPI Waveforms

As stated previously, a REMPI spectrum consists of the integrated ion current as a function of laser wavelength. Figure 7 depicts typical ion current-time waveforms taken from a 1+1 REMPI spectrum of 50 ppbv indene in ambient air. The normalized waveforms acquired at different laser wavelengths are essentially identical in shape. The band origin of the first singlet transition in indene has an intensity maximum at 287.86 nm (top waveform, Figure 7). It is interesting to note the difference in signal amplitude that occurs with only a 0.03 nm shift in laser wavelength.

The waveform shapes in Figure 7 are attributed to the creation by REMPI of electron-positive ion pairs that then drift to the electrodes due to the electric field as they collide with ambient air molecules. The electrons produced in the REMPI process are expected to quickly attach to the abundant oxygen molecules to form oxygen anions. These oxygen anions can then further react with water and other atmospheric constituents.<sup>43</sup> After diffusing through the air, the anions are collected at the positive electrode and the cations are collected at the negative electrode. When a charged particle moves between the electrodes, it induces a varying charge on the electrode surfaces resulting in a current that flows through a circuit connecting the electrodes. This induced current, which is measured with a pre-amplifier, appears when the charge is created and continues until the charged particles strike the electrode. The cations approaching the negative electrode and the anions approaching the positive electrode are both recorded by the pre-amplifier as a positive current flowing from the negative electrode to the positive

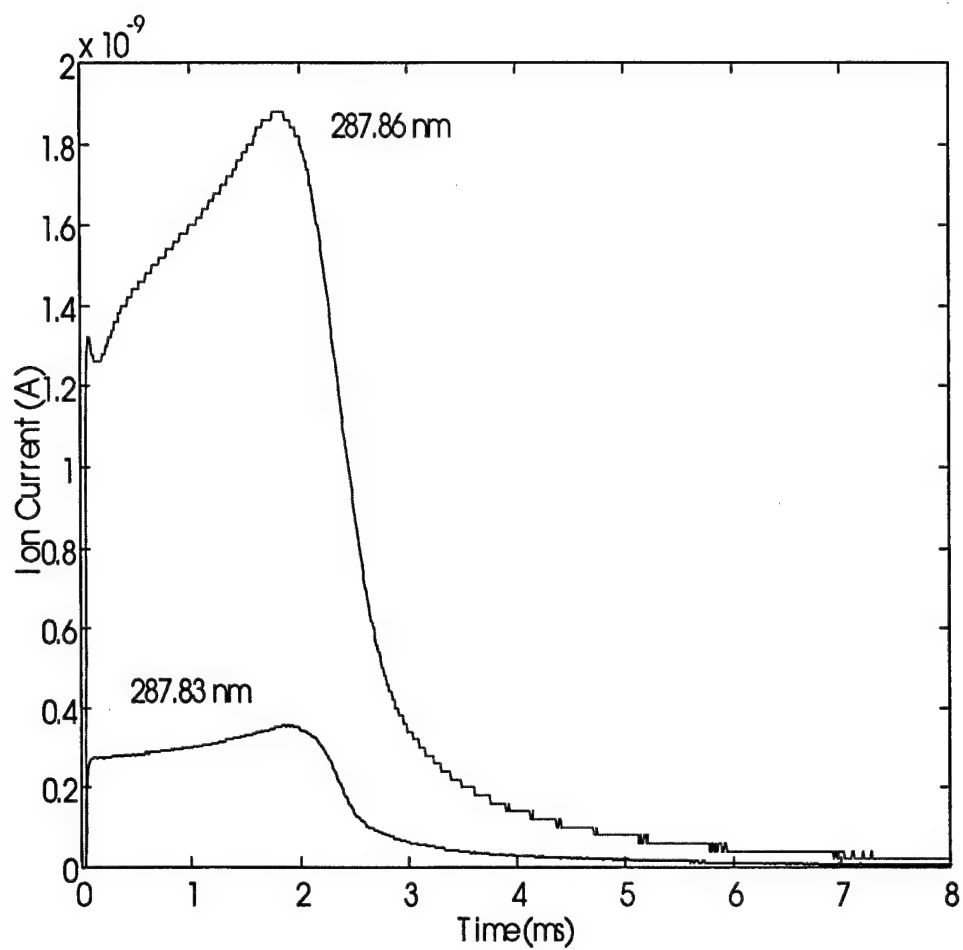


Figure 7. Ion current-time waveforms for 1+1 REMPI of 50 ppbv indene in ambient air at laser wavelengths of 287.83 nm and 287.86 nm.

electrode. Thus, the anion and cation contributions to the current are superimposed. The next section will discuss the 1+1 REMPI results for indene in ambient air.

### **B. The 1+1 REMPI Spectra of Indene in Ambient Air**

The survey 1+1 REMPI spectrum (step size = 0.05 nm) of 50 ppbv indene in ambient air is shown in Figure 8. This spectrum qualitatively agrees with the gas-phase absorbance spectrum recorded photographically by Byrne and Ross.<sup>44</sup> The electronic origin lies near 287.9 nm (vide infra) and the lowest in-plane vibrational frequency in indene<sup>45</sup> is 379.6 cm<sup>-1</sup>. The corresponding wavelength interval in this spectral region is 3.2 nm. Thus, the bands to the shorter wavelength side of 286 nm in Figure 8 are assigned to S<sub>1</sub> (first excited singlet state) fundamental vibrations active in the electronic transition from the ground electronic state. The pattern around the origin band arises from hot band sequence transitions.

Figure 9 displays high-resolution 1+1 REMPI spectra (step size = 0.005 nm) of 50 ppbv indene. The spectra have been vertically offset for clarity purposes. The scans were acquired over a 1 nm range in the vicinity of the electronic origin. The sequence-band structure and partially resolved rotational structure are now seen more clearly. The origin band of the first singlet transition in indene has a peak maximum at 287.86 nm, compared to 287.6 nm in styrene. Apparently, the second ring in indene has a negligible effect on the amount of pi-electron conjugation. Also, note how well the quantum counter correction (trace b, Figure 9) has reduced the noise associated with shot-to-shot variation in the laser power, as well as accounting for the overall laser power changes over the gain profile of the dye.

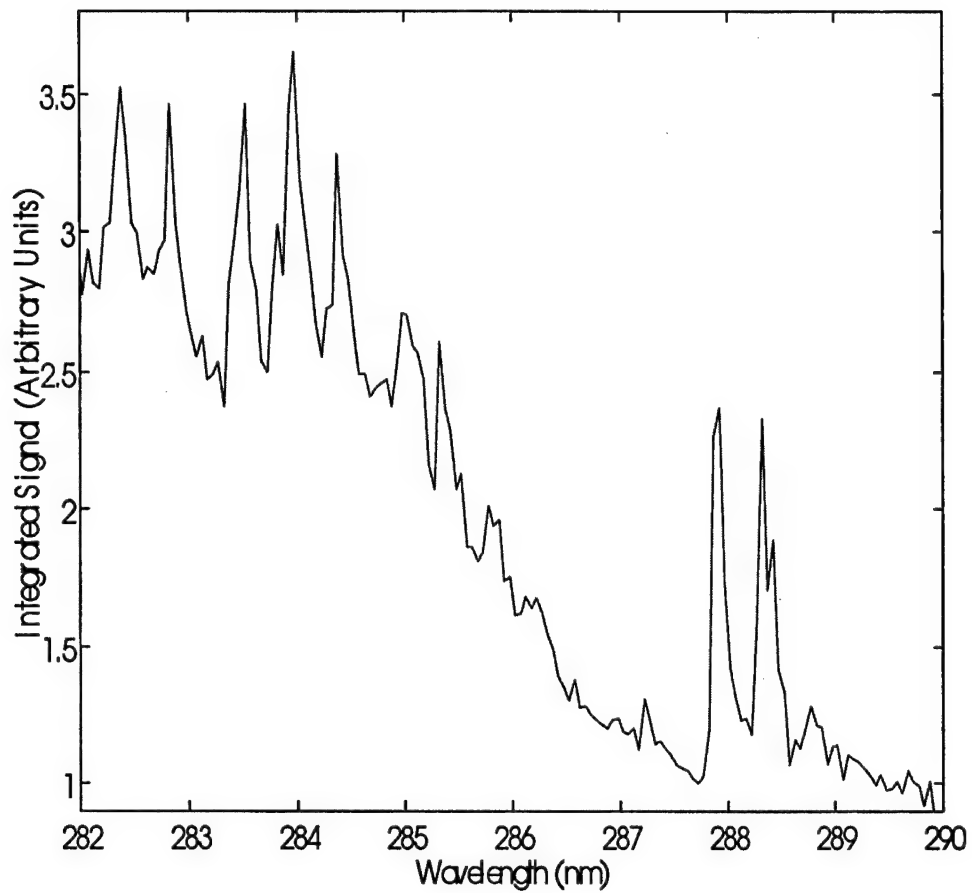


Figure 8. Corrected 1+1 REMPI spectrum of 50 ppbv indene in ambient air. Step size = 0.05 nm.

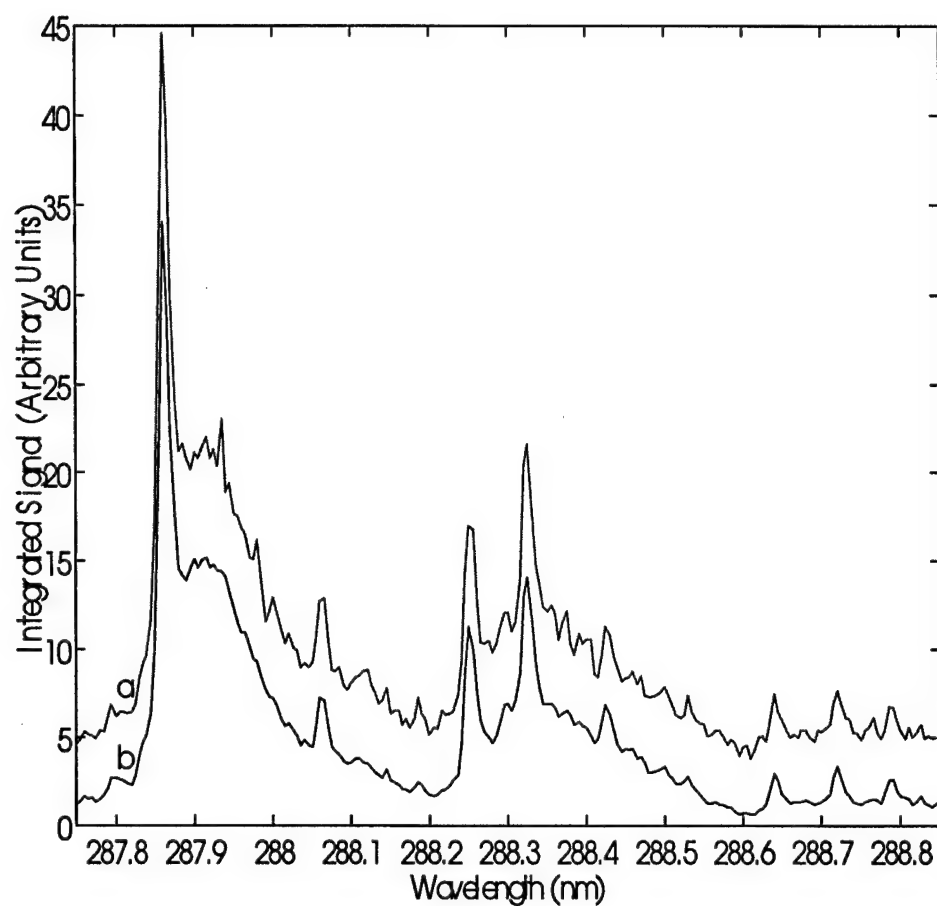


Figure 9. High-resolution 1+1 REMPI spectra of 50 ppbv indene in ambient air. Step size = 0.005 nm. Key: a = raw spectrum and b = raw spectrum divided by the square of the quantum counter response.

Repeat runs of the corrected 1+1 REMPI spectrum in this 1 nm region showed that the sequence band structure in Figure 9 is extremely repeatable. It should be emphasized that the power normalized spectrum in Figure 9 has not been smoothed in any fashion and the data acquisition time per point is just over one second. The signal-to-noise is excellent for a pulsed dye laser experiment. Although a full analysis was not attempted, the sequence band structure from the high-resolution 1+1 REMPI spectrum in Figure 9 is in good agreement with the vapor absorption spectrum recorded by Hollas.<sup>46</sup> This comparison is shown in Table 2.

Table 2. Indene sequence band comparison between the Hollas vapor absorption spectrum and high-resolution 1+1 REMPI spectrum

Assignment <sup>a</sup>	Absorption Shift <sup>a</sup> (cm <sup>-1</sup> )	REMPI Shift <sup>b</sup> (cm <sup>-1</sup> )
e(1,1)	24.5	24.1
b(1,1)	47.2	47.0
a(1,1)	56.5	56.6
c(1,1)	68.4	68.6
b(2,2)	93.7	93.9
a(1,1)·b(1,1)	103.6	103.5
a(2,2)	112.3	111.9

<sup>a</sup>Reference 46; <sup>b</sup>This work; cm<sup>-1</sup> = wavenumber.

Since the indene ground-state vibrational frequencies have been characterized in detail<sup>45</sup>, it should be possible to determine many of the low frequency vibrations in S<sub>1</sub>, and how they pair up with the corresponding vibrations of the ground state. This experiment could be accomplished by recording the sequence-band structure at a few different temperatures. Note that this opportunity does not exist for supersonic jet expansions because the cooling process collapses the population distribution to the lowest vibrational level.



To verify the two-photon nature of the 1+1 REMPI process, the power dependence of the integrated REMPI signal was measured. The fit of the integrated REMPI signal versus laser pulse energy is shown in bi-logarithmic form in Figure 10. Three averaged waveform acquisitions were taken for each pulse energy setting and are plotted to indicate the signal-to-noise characteristics. The slope of 1.9 is very close to the expected value of 2. Thus, under these experimental conditions the formal intensity law holds.

Figure 11 shows the rotational contour of the origin band recorded at the highest (a) and lowest (b) laser pulse energies in the power-dependence study. This contour analysis corresponds to over an order of magnitude difference in laser pulse energy. The surprising degree of rovibronic structure obtained under these ambient conditions makes indene an excellent candidate for on- and off-resonance measurements. Less than a 0.03 nm shift in the ultraviolet laser wavelength changes the REMPI intensity by over an order of magnitude. The high-resolution 1+1 REMPI spectra in Figure 11 are nearly identical after the quantum counter normalization has been applied and are qualitatively consistent with the high-resolution vapor absorption spectrum reported by Hartford and Lombardi.<sup>47</sup> However, the narrow feature at 287.86 nm is over  $2\text{ cm}^{-1}$  wide (FWHM) in our spectrum, compared to  $0.3\text{ cm}^{-1}$  (FWHM) in their work. The next section will discuss the factors that may contribute to this discrepancy between the high-resolution 1+1 REMPI spectrum and Lombardi's high-resolution vapor absorption spectrum.

### C. Line Broadening Factors

The rotational contour of the origin band in the high-resolution 1+1 REMPI spectrum may be broader than in the Lombardi high-resolution vapor absorption spectrum for one or more of the following reasons: power (intensity) saturation, pressure broadening,

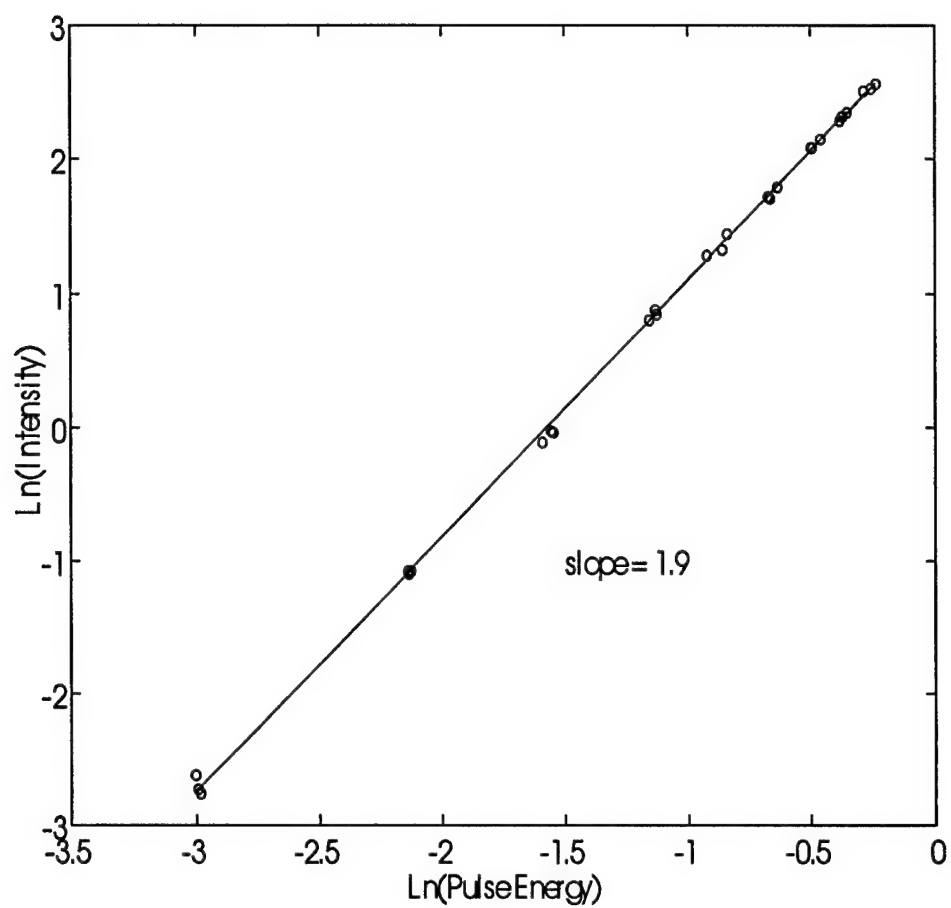


Figure 10. The 1+1 REMPI signal amplitude as a function of laser pulse energy.

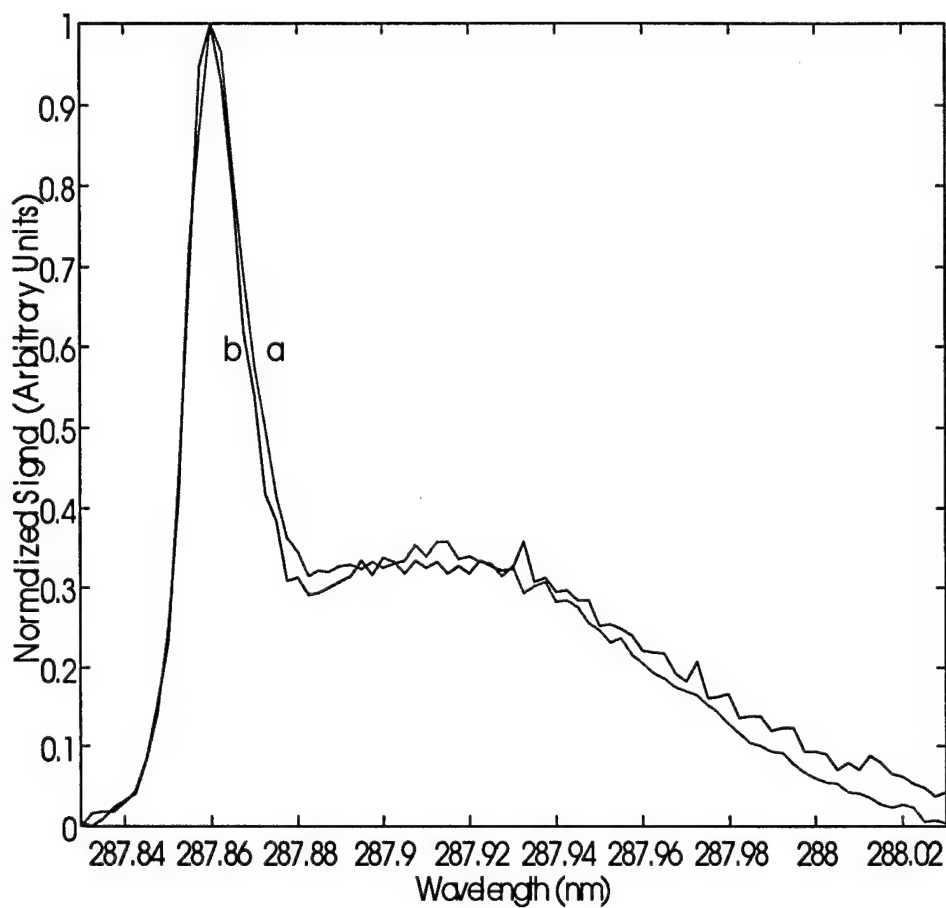


Figure 11. The 1+1 REMPI power-dependence on the rotational contour of the indene origin band. Key: a = highest laser energy; b = lowest laser energy.

or laser bandwidth versus spectrophotometer resolution. The following paragraphs will discuss the importance of these three factors. The natural linewidth broadening and Doppler broadening are negligible by comparison and are not discussed here.

Spectral broadening owing to power (intensity) saturation is a potential concern when using a high-intensity light source such as a pulsed dye laser. In a 1+1 REMPI process, power saturation may occur if the absorption cross-section to the excited intermediate state is much larger than the absorption cross-section to the ground ionic state, which is a characteristic common to many aromatic molecules.<sup>48</sup> If careful attention to laser power is not paid, it is possible to deplete the ground state population. From a REMPI perspective, power saturation could lead to a significant deviation from the formal intensity law. However, Figure 11 shows that the spectral shape of the rotational contour is virtually unchanged over an order of magnitude range in laser power. These spectra, in combination with the slope of 1.9 from Figure 10, show that optical and geometric saturation effects are not significant under our experimental conditions.

One might expect that the most probable factor affecting the REMPI transition linewidth is pressure broadening since our data are collected at atmospheric pressure, whereas the Lombardi high-resolution absorbance measurements were performed for pressures less than or equal to the indene room temperature vapor pressure (ca. 2 torr). A rough estimate for the pressure broadening in small molecules is 10 MHz/torr.<sup>49</sup> At atmospheric pressure, the broadening would be  $0.3 \text{ cm}^{-1}$ , but the REMPI transition linewidth is much larger than this estimate. However, indene ( $\text{C}_9\text{H}_8$ ) is not a "small" molecule, and it is important to note that pressure broadening is sensitive to the

intermolecular forces between the molecule undergoing the spectroscopic transition and the collision partner. Therefore, it is important to examine this issue further.

Figure 12 shows the rotational contour of the origin band in ambient air and at a reduced air pressure of 100 mtorr. Both spectra have been normalized to their most intense feature at 287.86 nm. The 100 mtorr pressure is significantly lower than the saturated vapor pressure of indene (ca. 2 torr). It is evident that some narrowing does occur, but probably not to the extent that pressure broadening is the sole factor involved in the broadening of the REMPI transition linewidth. Figure 13 shows the rotational contour of the origin band in ambient air and 1 atm of helium. Both spectra have been normalized to their most intense feature at 287.86 nm. This experiment was done in order to verify the initial pressure broadening results, and also to determine if the helium buffer gas would have a greater effect than that observed at reduced air pressure. As before, some narrowing does occur, but not to the extent that one would assume if the high-resolution 1+1 REMPI and Lombardi absorbance spectra were identical.

The fundamental interest in what pressure broadening effects can reveal about intermolecular forces is of secondary interest to us. We want to collect the data at ambient pressure, regardless of the effect of air on the REMPI transition linewidth. For the nonpolar molecule indene, the pressure broadening is discernable, but small. However, other molecules that are suitable for analysis via ambient pressure REMPI may contain functional groups such that intermolecular forces play a larger role in pressure broadening. For example, Figure 14 shows the 1+1 REMPI rotational contour (origin band) of indole,  $C_8H_7N$ , in ambient air and at a reduced air pressure of 100 mtorr. Both spectra have been normalized to the intensity maximum at 283.75 nm ( $S_1 \leftarrow S_0$ ). It is evident that the degree

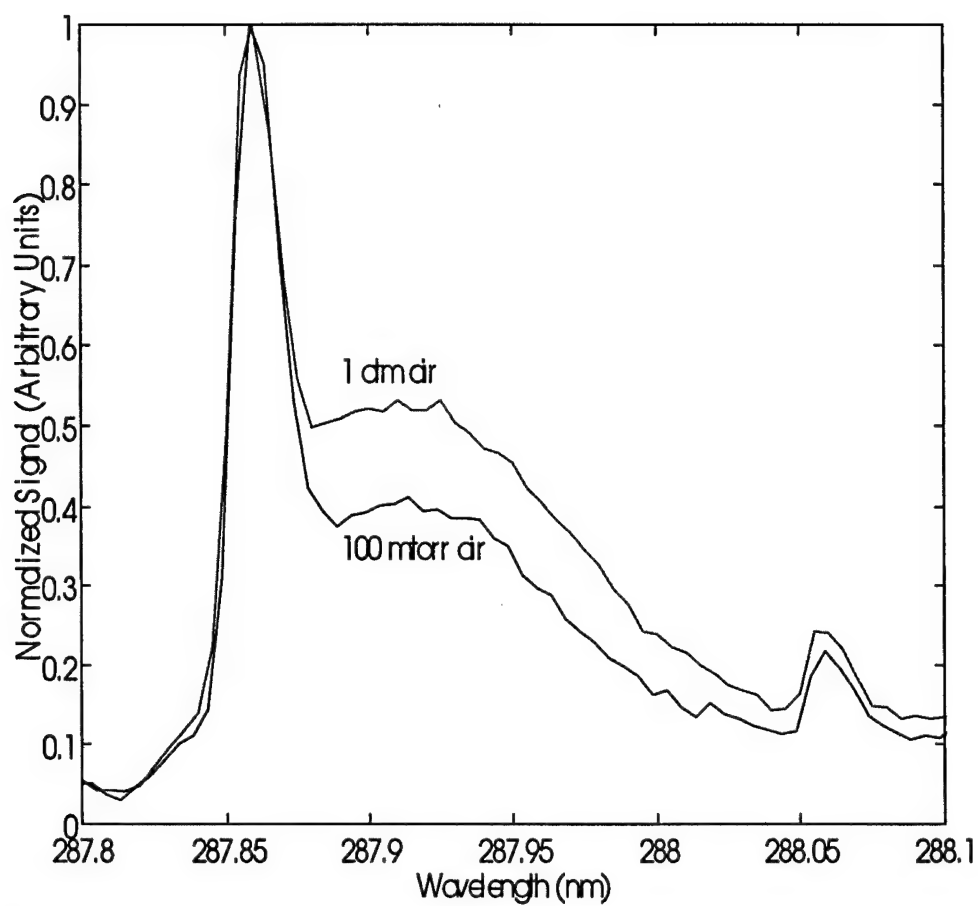


Figure 12. The 1+1 REMPI pressure-broadening effects on the rotational contour of the indene origin band. Upper trace = indene in 1 atm air; lower trace = indene in 100 mtorr air.

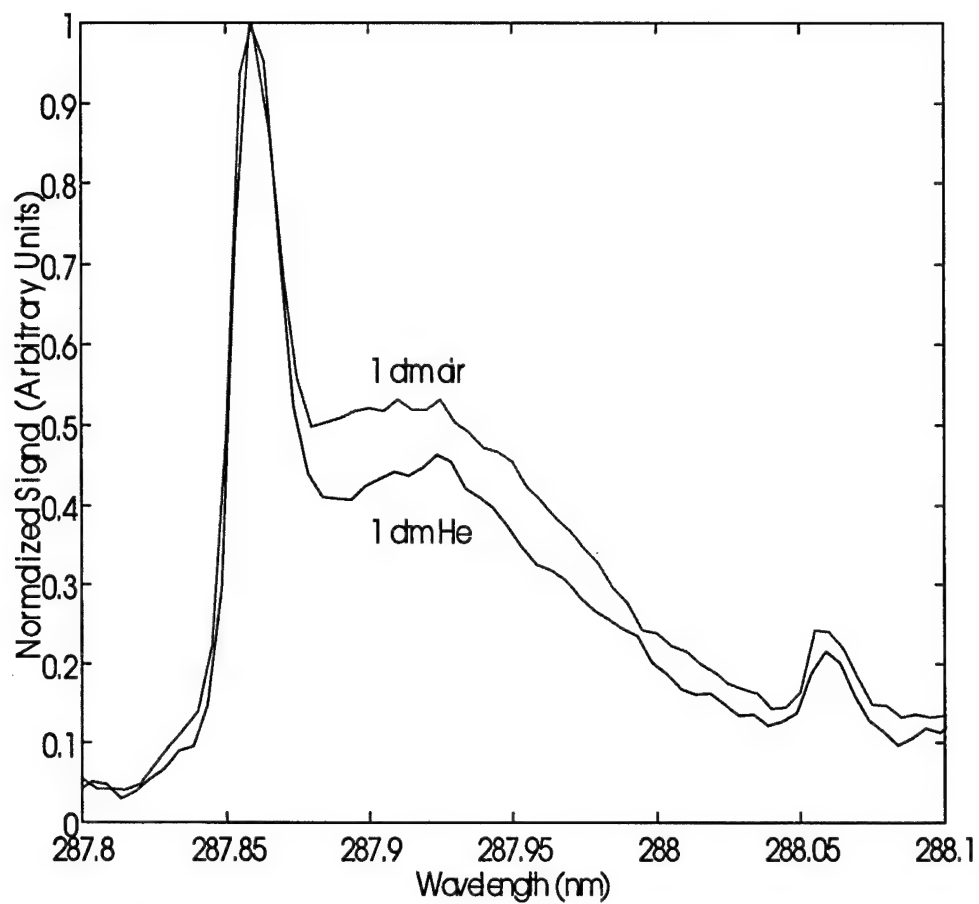


Figure 13. The 1+1 REMPI pressure broadening effects on the rotational contour of the indene origin band. Upper trace = indene in 1 atm air and lower trace = indene in 1 atm helium.

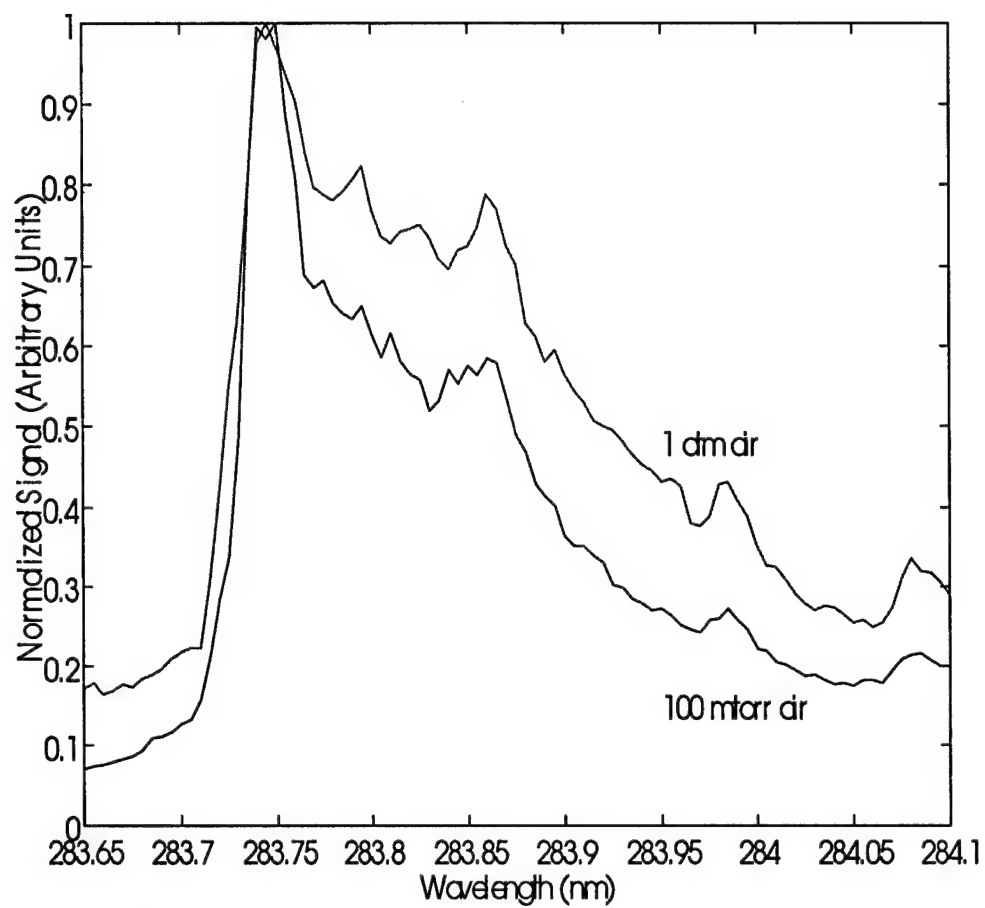


Figure 14. The 1+1 REMPI pressure-broadening effects on the rotational contour of the indole origin band. Upper trace = indole in 1 atm air and lower trace = indole in 100 mtorr air.



of broadening is substantially greater for indole, a N-heterocyclic, than for indene. This type of information may prove useful in the future for the mixture analysis of samples that have overlapping spectroscopic transitions and are prone to pressure broadening.

The laser bandwidth also accounts in part for the observed breadth in the high-resolution 1+1 REMPI spectrum when compared to Lombardi's high-resolution absorbance spectrum. The bandwidth in the visible region was measured to be  $0.4\text{ cm}^{-1}$  via the optogalvanic effect. The bandwidth in the ultraviolet region was not measured directly. Because the UV light is obtained by frequency-doubling, a linewidth of  $0.8\text{ cm}^{-1}$  might be expected. However, a linewidth of  $0.6\text{ cm}^{-1}$  could be predicted owing to the quadratic intensity dependence of frequency-doubling.

Both pressure broadening effects and laser bandwidth contribute to the slightly low resolution of the REMPI transition linewidth. The nature of the second absorption cross-section, which is associated with the photon transition from the resonant state to the ionization continuum, may also contribute. For a 1+1 REMPI process, the wavelength dependence of the second absorption cross-section is usually low. If this condition is true, then the 1+1 REMPI spectrum should resemble the conventional absorbance spectrum in a one-color experiment. However, if the photoionization cross-section is wavelength-dependent, then one could argue that the 1+1 REMPI spectrum would not be identical to the absorbance spectrum. In order to examine this issue for indene, a two-color 1+1 REMPI experiment at ambient conditions would be needed. This experiment would require two independent, tunable dye laser systems. The first laser would be fixed at  $287.86\text{ nm}$  ( $S_1 \leftarrow S_0$ ), which corresponds to the intensity maximum of indene's origin band. The second dye laser would then be scanned through  $S_1$ , and the ionization yield as a

function of laser wavelength would be recorded. If optimal conditions in the two-color experiment were maintained (line broadening factors comparable, sufficient temporal overlap of the dye laser pulses), then the one- and two-color 1+1 REMPI spectra of indene in ambient air could be analyzed in order to characterize the wavelength dependence of the photoionization cross-section.

#### **D. REMPI versus Conventional Absorbance**

The REMPI and conventional absorbance spectra of indene are compared in Figure 15. The bottom trace is the 1+1 REMPI spectrum of 100 ppbv indene in atmospheric-pressure air. The top trace is the saturated indene (2500 ppmv) absorption spectrum in air measured with a Cary 500 UV-VIS-NIR spectrophotometer (Varian, Inc.). The bandwidth of the spectrophotometer is 0.03 nm. Since the resolution of the laser is better than the Cary 500, the 1+1 REMPI spectrum is better resolved and its indene concentration is four orders of magnitude lower than in the absorbance measurement. Clearly, REMPI is much more sensitive than conventional absorbance techniques.

#### **E. Indene Detection in Chemical Mixtures**

Indene was selected as a target analyte to demonstrate 1+1 REMPI detection of single components in complex chemical mixtures. It is an excellent candidate molecule for several reasons: the substance's volatility (ca. 2 torr room temperature vapor pressure), its highly structured spectrum, and its known presence in some of the "heavier" fuels. For example, the composition of a #2 fuel oil was stated to be 0.022% indene and 1% total indenenes.<sup>50</sup> This preliminary study involved three petroleum-based samples: coal tar, creosote, and diesel fuel.

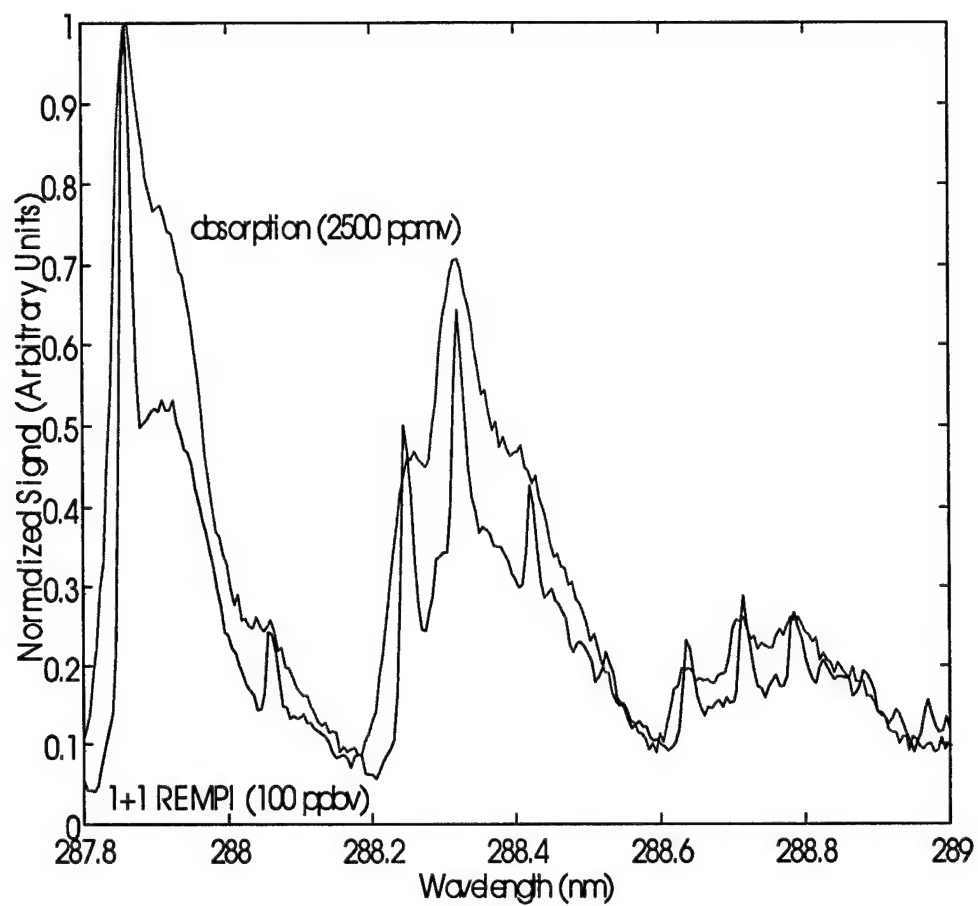


Figure 15. The 1+1 REMPI and conventional absorbance spectra of indene in atmospheric pressure air.

Gaseous samples taken from the headspace over the petroleum products at room temperature were injected into the REMPI cell. Before each experiment, the cell was baked overnight in a vacuum oven, which reduced background signals to a few hundred microvolts. The 1+1 REMPI spectra of the diluted headspace samples taken near the indene origin band are shown in Figure 16. The upper trace (a) is 50  $\mu\text{L}$  headspace of coal tar, the middle trace (b) is 100  $\mu\text{L}$  headspace of creosote, and the lower trace (c) is indene at 100 ppbv. The spectra have been normalized for the laser power, but are otherwise on the same scale.

The indene partial pressure after the 5000 fold dilution of the headspace sample in the REMPI cell is estimated as 2 ppbv. In the coal-tar headspace, the indene partial pressure is therefore approximately 10 ppmv (ca. 0.008 torr), corresponding to an indene mole fraction in the liquid of 0.004 according to Henry's Law. If the effective molecular weight of coal tar is comparable to the molecular weight of indene, a composition of 0.4% by mass indene in coal tar would be predicted. An improved estimate would require more information about the molecular weight distribution of the major components in coal tar. The amount of indene in the creosote sample is much less than in the coal tar. Indene could not be seen in the headspace over diesel fuel. However, most "heavier" fuels contain relatively small proportions of unsubstituted aromatic hydrocarbons. Most of the fuel mass is associated with alkylated hydrocarbons. The alkylated indenenes could account for the small baseline observed in Figure 16.

#### **F. The 2+2 REMPI Spectra of Indene in Ambient Air**

In addition to 1+1 REMPI experiments, 2+2 REMPI spectra of indene in ambient air have been measured. In these experiments, the indene concentration was increased to

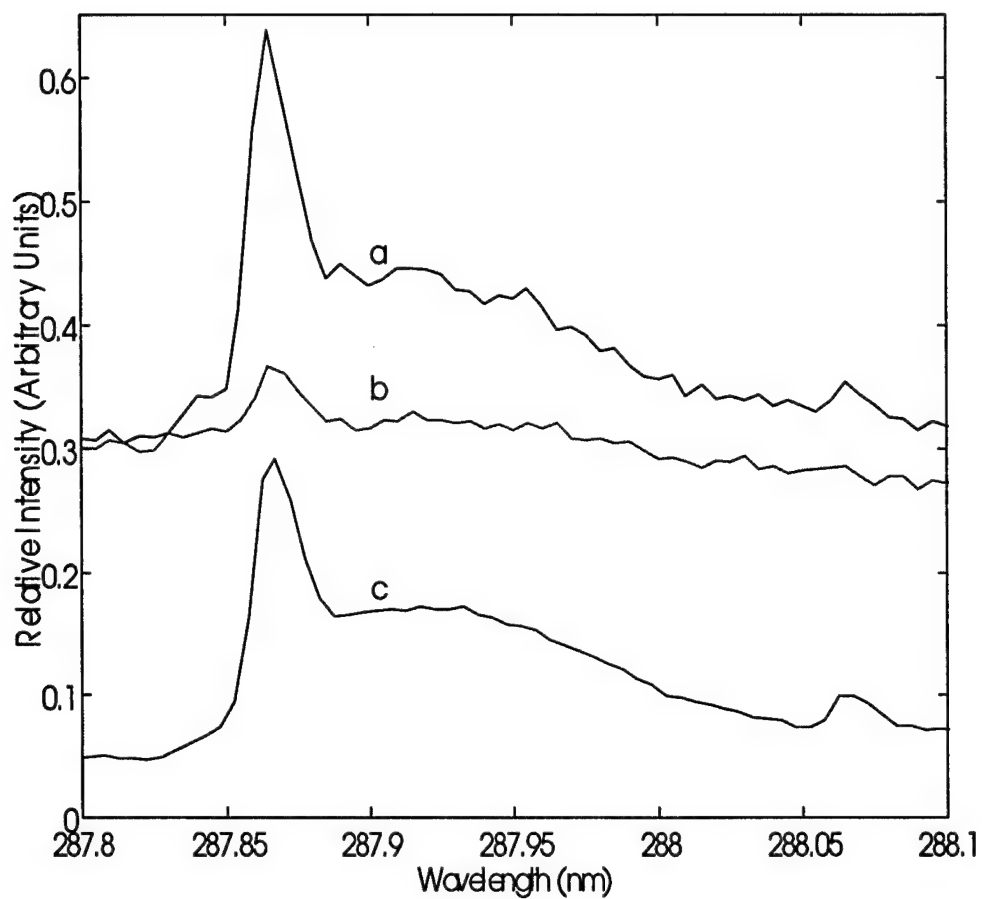


Figure 16. Detection of indene in chemical mixtures via 1+1 REMPI. Key: a = coal tar (50  $\mu\text{L}$  headspace); b = creosote (100  $\mu\text{L}$  headspace) and c = indene vapor (100 ppbv).

30 ppmv, the KDP doubling crystal was removed, and the visible light was focused into the center of the REMPI cell with a 10 cm lens. The corrected 2+2 REMPI spectra of indene in ambient air for 0.10 nm and 0.01 nm step size are shown in Figures 17 and 18, respectively.

In order to determine the *i*-photon nature of the 2+2 REMPI process, the power-dependence of the integrated REMPI signal was measured. The fit of the integrated REMPI signal versus laser pulse energy is shown in bi-logarithmic form in Figure 19. Three averaged, waveform acquisitions were taken for each pulse energy setting and are plotted to indicate the signal-to-noise characteristics. Although different from the expected value of 4, the experimental slope of 2.6 is reasonable since 2+2 REMPI processes usually involve tight-focusing conditions that tend to saturate the interaction volume. Thus, the resultant order is often skewed.

The 1+1 and 2+2 REMPI spectra of indene are compared in Figure 20. The 1+1 REMPI spectrum is reduced by a factor of 75 for display purposes. Differences between the two spectra are clearly evident. Qualitatively, it appears that the sharp features in the 1+1 REMPI spectrum have a corresponding, but much broader, feature in the 2+2 REMPI spectrum. Also, a few additional bands not seen in the 1+1 REMPI spectrum are observed in the 2+2 REMPI spectrum. It would be interesting to record the two-photon resonant spectra in circularly polarized light, as it is known that polarization can have a large effect on rotational contours in two-photon spectra.

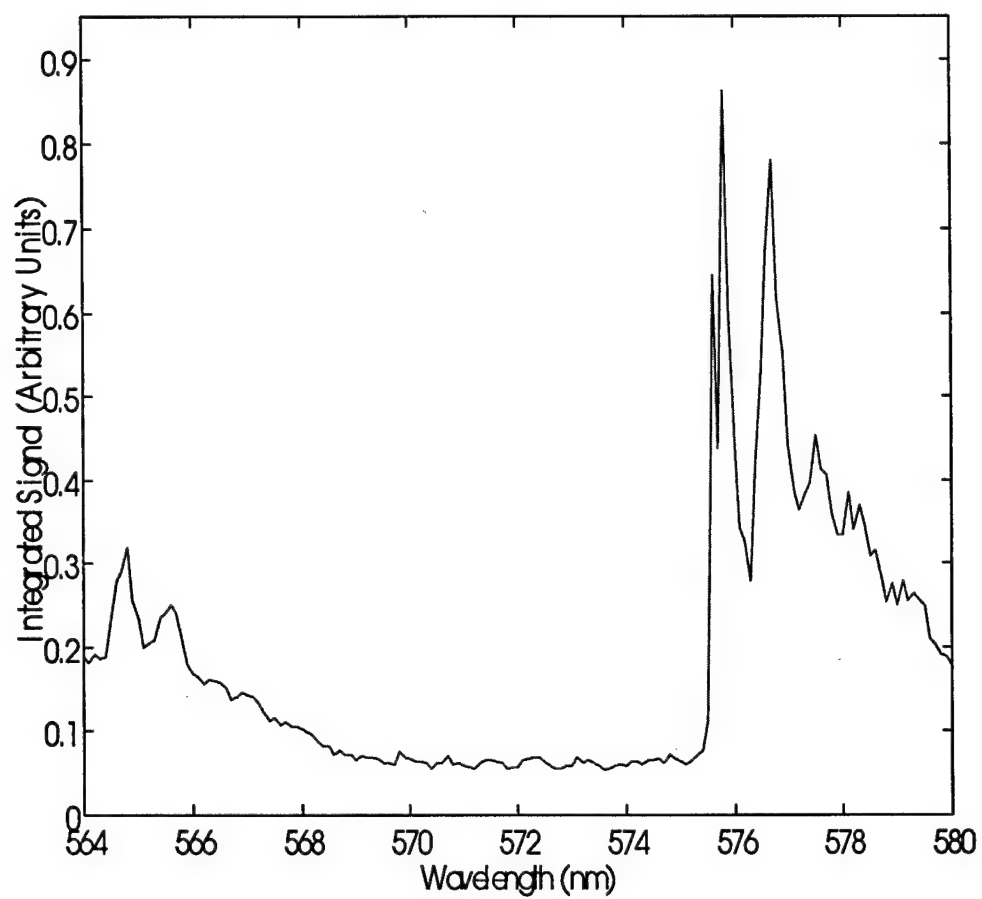


Figure 17. Corrected 2+2 REMPI spectrum of 30 ppmv indene in ambient air. Step size = 0.10 nm.

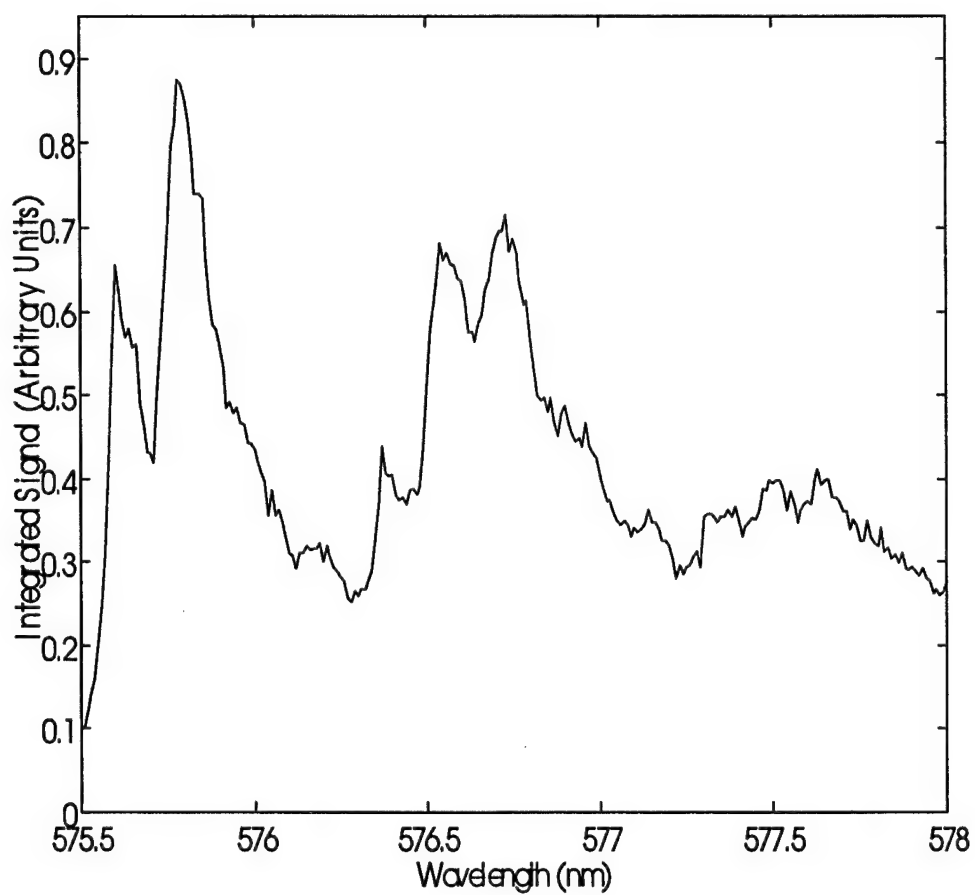


Figure 18. Corrected 2+2 REMPI spectrum of 30 ppmv indene in ambient air. Step size = 0.01 nm.



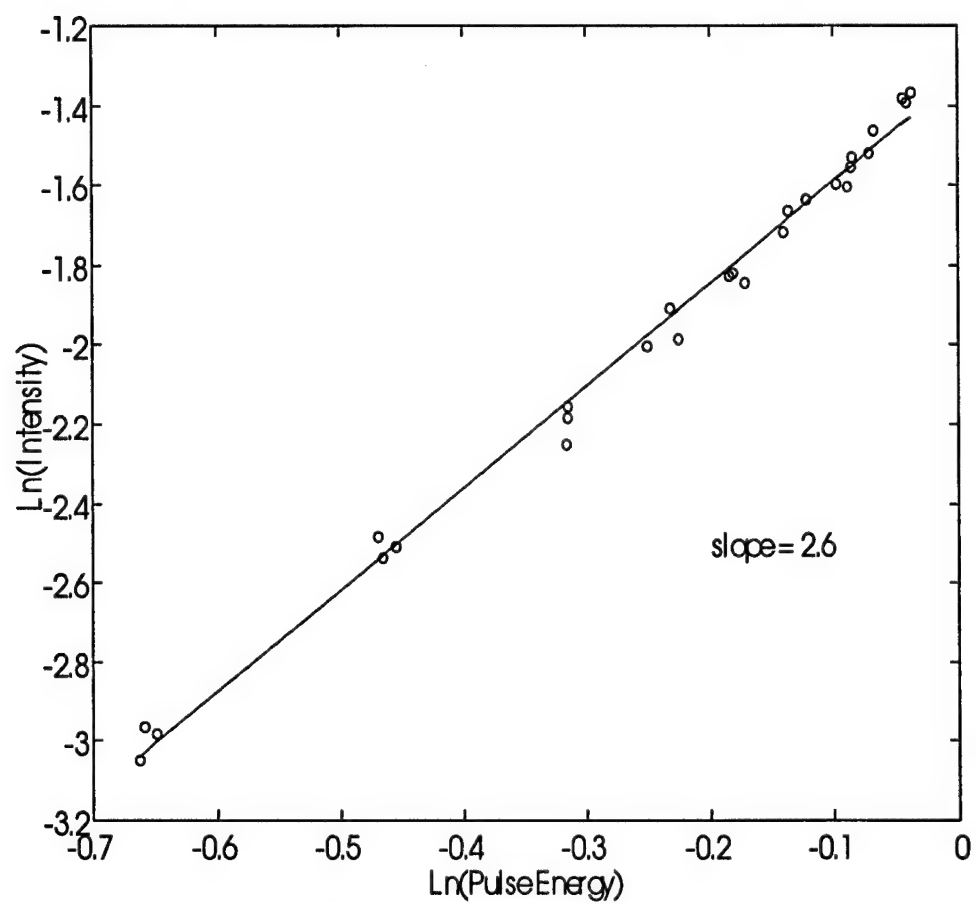


Figure 19. The 2+2 REMPI signal amplitude as a function of laser pulse energy.

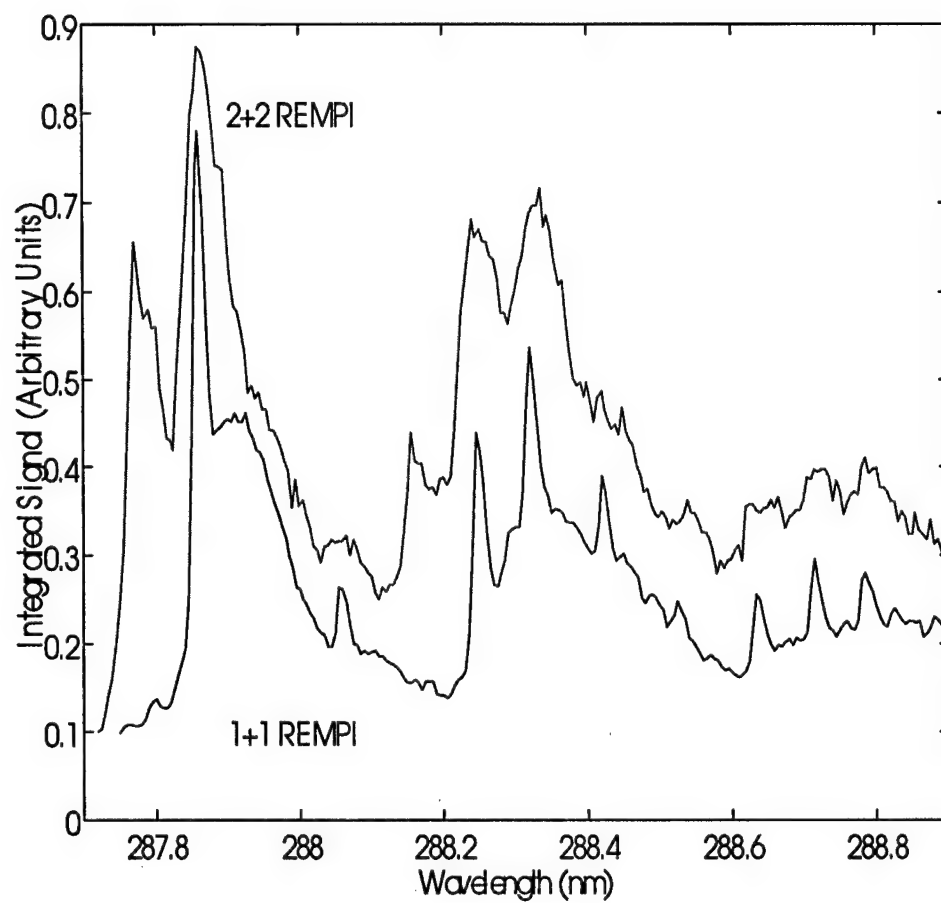


Figure 20. The 1+1 and 2+2 REMPI spectra of indene in atmospheric pressure air.

#### IV. CONCLUSIONS

This work is part of a larger project to examine the suitability of REMPI for real-time chemical analysis of organic species in ambient air. We have successfully demonstrated that very narrow features can be seen for indene, a polycyclic aromatic hydrocarbon, at ambient pressure and room temperature. The ambient pressure 1+1 REMPI spectrum of indene qualitatively agrees with the molecule's conventional one-photon absorbance spectrum; however, the REMPI spectrum is better resolved and significantly more sensitive when compared to the conventional absorbance spectrum.

One discrepancy we noted is that the rotational contour of the indene origin band in the high-resolution 1+1 REMPI spectrum is broader than in the Lombardi high-resolution vapor absorption spectrum. This breadth in the REMPI transition linewidth cannot be fully explained by power (intensity) saturation effects, pressure broadening, or laser bandwidth. Another contributing factor may deal with the wavelength dependence of indene's photoionization cross-section, which is associated with the photon transition from the resonant state to the ionization continuum. A two-color 1+1 REMPI experiment would be needed to study this potential factor, but this experiment is not feasible from a real-time, field-measurement perspective.

Regardless of the breadth in the REMPI transition linewidth, the rovibronic structure for indene at ambient conditions is sharp enough to make the molecule an excellent candidate for on- and off-resonance measurements to discriminate against other REMPI background signals. Consequently, ambient pressure 1+1 REMPI was demonstrated as a viable technique for the detection of indene in the headspace over the multicomponent mixtures of coal tar and creosote. In addition, the great sensitivity of

REMPI allowed for the measurement of the 2+2 spectrum of indene in ambient air. Future work will focus on expanding the spectral database of molecules that can be characterized via ambient-pressure REMPI.

## V. REFERENCES CITED

1. S. Kendler, S. Zilberg, and Y. Haas, *Chem. Phys. Lett.* **242**, 139 (1995).
2. M. Goeppert-Mayer, *Ann. Phys. Leipzig [5]* **9**, 273 (1931).
3. P.M. Johnson and C.E. Otis, *Ann. Rev. Phys. Chem.* **32**, 139 (1975).
4. P.M. Johnson, M.R. Berman, and D. Zakheim, *J. Chem. Phys.* **62**, 2500 (1975).
5. P.M. Johnson, *J. Chem. Phys.* **62**, 4562 (1975).
6. G. Petty, C. Tai, and F.W. Dalby, *Phys. Rev. Lett.* **34**, 1207 (1975).
7. S.H. Lin, Y. Fujimura, H.J. Neusser, and E.W. Schlag, *Multiphoton Spectroscopy of Molecules*, Academic Press, Orlando, (1984).
8. V.S. Letokhov, *Laser Photoionization Spectroscopy*, Academic Press, New York, (1987).
9. J.N. Driscoll and M. Duffy, *Chromatography Forum* **4**, 21 (1987).
10. J.N. Driscoll, in *Detectors for Capillary Chromatography, Chemical Analysis Series, Vol. 121*, Chapter 4, eds. H.H. Hill and D.G. McMinn, John Wiley & Sons, New York, (1992).
11. J. Grotemeyer and E.W. Schlag, *Angew. Chem. Int. Ed. Engl.* **27**, 447 (1988).
12. U. Boesl, H.J. Neusser, and E.W. Schlag, *Chem. Phys. Lett.* **87**, 1 (1982).
13. W. Dietz, U. Boesl, H.J. Neusser, E.W. Schlag, and S.H. Lin, *Chem. Phys.* **66**, 105 (1982).
14. W.C. Wiley and I.M. McLaren, *Rev. Sci. Instrum.* **26**, 1150 (1955).
15. D.M. Lubman, *Mass. Spectrom. Rev.* **7**, 535 (1988).
16. D.M. Lubman, *Mass. Spectrom. Rev.* **7**, 559 (1988).
17. D.M. Lubman, *Anal. Chem.* **59**, 31A (1987).
18. D.H. Levy, *Ann. Rev. Phys. Chem.* **31**, 197 (1980).
19. S.W. Stiller and M.V. Johnston, *Anal. Chem.* **59**, 567 (1987).

20. J.M. Hollas and D. Phillips, *Jet Spectroscopy and Molecular Dynamics*, Blackie Academic & Professional, London, (1995).
21. J.H. Brophy and C.T. Rettner, *Opt. Lett.* **4**, 337 (1979).
22. R. Frueholz, J.E. Wessel, and E. Wheatly, *Anal. Chem.* **52**, 281 (1980).
23. C.M. Klimcak and J.E. Wessel, *Appl. Phys. Lett.* **37**, 138 (1980).
24. C.M. Klimcak and J.E. Wessel, *Anal. Chem.* **52**, 1233 (1980).
25. A. Clark, R.M. Deas, C. Kosmidis, K.W.D. Ledingham, A. Marshall, J. Sandler, R.P. Singhal, M. Campbell, and R. Zheng, in *Sensors VI: Technology, Systems, and Applications*, pp. 57-61, ed. K.T.V. Grattan, Adam Hilger, Bristol, (1993).
26. A. Marshall, A. Clark, R.M. Deas, C. Kosmidis, K.W.D. Ledingham, W. Peng and R.P. Singhal, *Analyst* **119**, 1719 (1994).
27. A. Marshall, K.W.D. Ledingham, and R.P. Singhal, *Analyst* **120**, 2069 (1995).
28. T. Ogawa and T. Yasuda, *Anal. Chem.* **64**, 2615 (1992).
29. T. Inoue, K. Masuda, K. Nakashima, and T. Ogawa, *Anal. Chem.* **66**, 1012 (1994).
30. T. Ogawa, S. Sumi, and T. Inoue, *Anal. Sci.* **12**, 455 (1996).
31. I. Schechter, H. Schroder, and K.L. Kompa, *Anal. Chem.* **65**, 1928 (1993).
32. I. Schechter, H. Schroder, and K.L. Kompa, *SPIE* **2092**, 186 (1993).
33. I. Schechter, H. Schroder, and K.L. Kompa, *Anal. Chem.* **64**, 2787 (1992).
34. V.V. Gridin, M. Kadosh, and I. Schechter, *Anal. Chem.* **69**, 2098 (1997).
35. V.V. Gridin, A. Korol, V. Bulatov, and I. Schechter, *Anal. Chem.* **68**, 3359 (1996).
36. V.V. Gridin, A. Korol, V. Bulatov, and I. Schechter, *Anal. Chem.* **69**, 478 (1997).
37. O.F. Swenson, G.D. Gillispie, and C.J. Walls, *Trends in Optics and Photonics Series (TOPS), Vol. 8, Environmental Monitoring and Instrumentation*, pp. 20-24, Optical Society of America, (1996).
38. O.F. Swenson, G.D. Gillispie, W.F. Cooper, and M.A. Dvorak, *Trends in Optics and Photonics Series (TOPS), Vol. 8, Environmental Monitoring and Instrumentation*, pp. 14-19, Optical Society of America, (1996).

39. O.F. Swenson and G.D. Gillispie, *SPIE* **2835**, 144 (1996).
40. D.S. Bethune, *Appl. Opt.* **20**, 1897 (1981).
41. D.S. King, P.K. Schenck, K.C. Smyth, and J.C. Travis, *Appl. Opt.* **16**, 2617 (1977).
42. T.J. McKee, J. Lobin, and W.A. Young, *Appl. Opt.* **21**, 725 (1982).
43. G.A. Eiceman and Z. Karpas, *Ion Mobility Spectrometry*, CRC Press, Boca Raton, (1994).
44. J.P. Byrne and I.G. Ross, *Aust. J. Chem.* **24**, 1107 (1971).
45. T.D. Klots, *Spectrochim. Acta A* **51**, 2307 (1995).
46. J.M. Hollas, *Spectrochim. Acta* **19**, 753 (1963).
47. A. Hartford, Jr. and J.R. Lombardi, *J. Mol. Spectrosc.* **34**, 257 (1970).
48. U. Boesl, H.J. Neusser, and E.W. Schlag, *Chem. Phys.* **55**, 193 (1981).
49. P.F. Bernath, *Spectra of Atoms and Molecules*, Oxford University Press, Oxford, (1995).
50. [www.aehs.com/ASP/publications/tphables/2-83-02.html](http://www.aehs.com/ASP/publications/tphables/2-83-02.html), American Petroleum Institute, unpublished data, (1994).

## APPENDIX C



**PHOTOEMISSIVE ION MOBILITY SPECTROMETRY FOR  
DETECTION OF CHLORINATED VAPORS**

**Draft Thesis**

**By**

**Christopher J. Walls**

# **CHAPTER 1**

## **INTRODUCTION**

Chlorinated aliphatic compounds are ubiquitous pollutant threats to air and water. The Environmental Protection Agency has released a final Integrated Urban Air Toxics Strategy<sup>1</sup> that intends to assess and control emissions of 33 Hazardous Air Pollutants (HAPs) thought to pose the greatest public health risks in urban areas. Among 13 halogenated species on the list are 9 chlorinated aliphatic compounds including tetrachloroethylene (or perchloroethylene, PCE), trichloroethylene (TCE), carbon tetrachloride, and chloroform. Chlorinated aliphatic compounds also constitute pervasive and persistent threat to groundwater resources in the form of Dense Non-Aqueous Phase Liquids (DNAPLs)<sup>2</sup>, fluids that are poorly miscible with, and denser than, water. Principal DNAPL-forming substances are the cleaners and degreasers PCE, TCE, and 1,1,1-trichloroethane (TCA).

The physical nature and transport mechanisms of DNAPLs in the subsurface are not completely understood due to the lack of a real-time, high spatial resolution sensor for downhole applications. The demanding nature of subsurface monitoring constrains both sensor size and complexity. Clearly, the diameter of the sensor packaging must be small so that the sensor can be placed within a direct push probe. Also, because ruggedness and reliability are often more important than sensitivity in subsurface monitoring, rudimentary instrumentation is advantageous. As is true for subsurface monitoring technology, a satisfactory real-time sensor for chlorinated aliphatics in the atmosphere is not available.

Although demands on air quality sensor design are not as stringent as demands on subsurface monitoring equipment, durable, uncomplicated sensors would be beneficial.

Because the vapors of nearly all chlorinated aliphatic compounds readily capture free electrons to form stable anion products, ionization detectors equipped with low-energy electron sources are suitable candidate technologies for sensing applications in both environments. The electron capture detector (ECD), which measures the loss of thermal-energy electrons to vapor samples, responds strongly to most chlorinated vapors. Though many chlorinated species capture thermal-energy electrons most efficiently, ionization detectors that expose vapors to more energetic electrons also respond strongly to chlorinateds. The ion mobility spectrometer (IMS) capably measures ions resulting from electron capture in weak electric fields where mean electron energies are greater than thermal.

Measuring the anions formed by low-energy electron attachment provides a means to identify individual species attaching low-energy electrons in a vapor sample. In weak homogeneous electric fields at ambient pressure, ions attain stable, characteristic drift velocities that represent equilibria between energy acquired from the electric field and energy lost to collisions with gas molecules. The gas occupying the drift tube of the IMS therefore acts as a crude chromatographic medium to sort mixtures of ions into packets based, among other factors, on size and shape. If resolution is sufficient, the packets containing single ion species arrive separately for detection at a collector electrode. The ECD offers no equivalent means to speciate sample vapors.

Photoemissive sources are attractive when only low-energy electron attachment is required to ionize analyte vapor and have appeared frequently throughout the past century

in experimentation requiring low-energy electrons. Photoemissive sources generate low-energy electrons directly via the photoelectric effect. In contrast to radioactive sources frequently used with the IMS that produce ions of both polarities, photoemission produces no positive ions, so no electrons or anions produced by electron capture are lost to recombination. In addition, the number of electrons produced is readily adjusted by changing the intensity of the light source. Because radioactive sources are continuous, constantly supplying ionizing particles to the vapor sample, radioactive-source IMS units require ion shutters situated within the drift tube near the ionization source to admit pulses of product ions to the drift tube for separation. Ions are pushed toward the shutter in its closed state, then through the shutter to the drift space when the shutter is opened briefly. A photoemitter operated by a pulsed light source can accomplish this without an ion shutter, which simplifies instrumentation.

Beyond using photoemissive sources to eliminate ion shutters, the goal of this work was to reduce ion mobility instrumentation further and assess capabilities of the resulting hardware toward detection of chlorinated vapors in nitrogen, air, and in nitrogen in the presence of oxygen. The simplifications included operating exclusively at ambient temperature, not using a counterflowing or other continual purge gas, using relatively short ion drift distances less than 4 cm, in some cases operating without a formal drift tube between the electrodes.

## CHAPTER 2

### REVIEW

#### 2.1. Ion Mobility Spectrometry

##### 2.1.1. Gas phase ion mobility

At number densities lower than about  $10^7$  ions·cm<sup>-3</sup>, Coulombic repulsion is considered insignificant<sup>3</sup> and in the absence of external electric and magnetic fields, a collection of ions disperses in a gas by diffusion. Fast, random motion of gas molecules and ions carries ions toward decreasing concentration at a rate proportional to the magnitude of the concentration gradient. Diffusion proceeds until the ions become uniformly distributed throughout the gas.

Placing a similar swarm of ions in an electric field causes drift to superimpose on diffusion. While pushed through the gas, ions continuously acquire kinetic energy from the field and repeatedly lose much or all of it to collisions with neutral gas molecules. As the result of successive, directed accelerations through free paths between molecules and frequent, randomizing collisions with the molecules, ions drifting through a gas achieve a mean velocity along the field lines or perpendicular to equipotential surfaces within the electric field. Generally, mean velocity depends upon the ratio,  $E/N$ , of the electric field magnitude,  $E$ , to the number density of the gas,  $N$ . However, when  $E/N$  is less than about  $2 \times 10^{-17}$  V·cm<sup>2</sup> (or 2 *Townsend*, Td), the field is considered weak<sup>4</sup> and the energy acquired by ions from the field is negligible compared to thermal energy. In this situation, the mean velocity of the ion swarm is directly proportional to electric field magnitude as

$$\frac{l_d}{t_d} = v_d = KE \quad (2.1)$$

where  $K$  is ion mobility in  $\text{cm}^2 \cdot \text{V}^{-1} \cdot \text{s}^{-1}$ ,  $l_d$  is drift length in cm,  $t_d$  is drift time in seconds,  $v_d$  is ion drift velocity in  $\text{cm} \cdot \text{s}^{-1}$ , and  $E$  is electric field magnitude in  $\text{V} \cdot \text{cm}^{-1}$ . Electric field magnitudes less than  $500 \text{ V} \cdot \text{cm}^{-1}$  satisfy the weak-field condition in most gases at atmospheric pressure and weak-field mobilities of most ions fall between 1 and  $3 \text{ cm}^2 \cdot \text{V}^{-1} \cdot \text{s}^{-1}$ . Thus ion drift velocities in weak, homogeneous electric fields are usually less than  $1.5 \text{ m} \cdot \text{s}^{-1}$ , much slower than the mean ion or molecular speeds in the gas that exceed  $300 \text{ m} \cdot \text{s}^{-1}$ .

Ion mobility depends on the properties of an ion and the gas through which it drifts, varying approximately with the inverse of the collision cross section,  $\Omega_D^{-1}$ , for the ion with a neutral molecule of the gas<sup>4</sup>. As a result, a particular ion has different mobilities in different drift gases while different ions might exhibit different mobilities in the same drift gas. The Mason-Schaump equation, an expression for the mobility of ions drifting through a gas in an electric field derived from gas kinetic theory, is

$$K = \left( \frac{3e}{16N} \right) \sqrt{\left( \frac{2\pi}{\mu k T_{eff}} \right)} \left[ \frac{1 + \alpha}{\Omega_D(T_{eff})} \right] \quad (2.2)$$

where  $e$  is ion charge,  $N$  is gas number density,  $\mu$  is the reduced mass of the ion-neutral collision pair, and  $k$  is Boltzmann's constant. The term  $T_{eff}$  is the effective temperature of

the ion, which is approximately equal to the temperature of the gas under weak-field conditions,  $\Omega_D(T_{\text{eff}})$  is the ion-neutral collision cross section that depends on effective ion temperature, and  $\alpha$  is a significant, but small theoretical correction factor that adjusts the computed mobility by no more than a few percent. Ignoring  $\alpha$  and assuming ions of near thermal energies, the mobilities of different ions in the same gas at specified pressure and temperature vary as  $\mu^{-1/2} \cdot \Omega_D^{-1}$ . The mobilities of ions that are much more massive than the drift gas neutrals vary disproportionately with  $\Omega_D^{-1}$  because the reduced mass of a large ion-small neutral collision is approximately equal to the mass of the neutral.

To account for pressure and temperature variations between measurements made in a particular drift gas, ion mobility is customarily reported as standard or reduced ion mobility,

$$K_o = K \left( \frac{p}{760} \right) \left( \frac{273}{T} \right) \quad (2.3)$$

where  $K_o$  is reduced ion mobility in  $\text{cm}^2 \cdot \text{V}^{-1} \cdot \text{s}^{-1}$ ,  $p$  is gas pressure in torr, and  $T$  is gas temperature in degrees Kelvin. Equation 2.3 normalizes the  $K$  to the mobility in the gas at standard temperature and pressure.

#### 2.1.2. Development of the ion mobility spectrometer<sup>4</sup>

The ion mobility spectrometer appeared in the 1960s not as new or improved technology, but as a solution toward growing demands for simple, portable detectors for vapor sensing applications. Measurements of ion mobility, diffusion, and other ion behaviors in electric and magnetic fields had been performed using similar instrumentation

for over 65 years before the IMS was developed. Ion mobilities had even been used to separate and identify gaseous ions well beforehand. Broad knowledge of gas phase ion chemistry and physics applicable to ion mobility spectrometry including ionization processes, electron-molecule interactions, and ion-molecule reactions was available.

Though Rutherford discovered the relationship between ion drift velocity and electric field magnitude in gases and made the first measurements of ion mobility by 1897, the bulk of the early investigations of ion mobility are ascribed to Langevin. By 1905 he had measured ion drift velocities and developed theories describing ion formation and ion mobility in air at ambient pressure. Using a drift tube resembling in some ways the traditional ion mobility spectrometer, his measurements were able to show that air exposed to radioactive materials contained several ion species. Though rudimentary, his theoretical approach was adequate to describe the behavior of the small ions he studied.

Despite improvements made to instrumentation during the 1930s such as ion gates and shutters that enabled remarkable separations of small ions, Langevin's work was not built upon until much later. In the 1960s, drift tube/mass spectrometers produced superior measurements of ion mobilities while confirming identities through mass. These instruments operated drift tubes at pressures at least slightly below ambient to separate ions and measure mobilities prior to admission to mass spectrometers for identification. Although emphasis was to develop means of accurately measuring the drift velocities of ions in gases, not to create analytical sensors, the results refined ion mobility theory to its modern form. Mass spectrometry performed near the same time also yielded descriptions of ion formation chemistry applicable to the IMS. Chemical ionization/mass spectrometry (CI/MS) in particular identified the types of ions generated in air at atmospheric pressure



and established the ionization scheme known as atmospheric pressure chemical ionization (APCI). Interpretation of early results obtained with the IMS relied heavily upon APCI results when no mass analysis of product ions was performed.

Though it had little direct impact on development of IMS instrumentation, the electron capture detector provided the realization that simple ionization detectors responded to trace concentrations of atmospheric pollutants. The foundation for the ECD was the vapor anemometer developed by Lovelock in the 1950s to monitor air currents in medical settings for correlation with disease transmission. His instrument monitored positive ion current generated by a radioactive source between parallel electrodes, which depended on the velocity of cross-flowing air. Halocarbon vapors in particular were found to dramatically alter the response of the simple instrument and subsequent versions configured to monitor changes in negative ion or electron current were early electron capture detectors.

Numerous efforts were undertaken to create sensors that added specificity to the ECD while retaining its simplicity. As the ECD only observed the loss of electrons to vapor samples and thereby offered no means to identify electron-attaching species, it offered little as a stand-alone detector. Many ionization detectors arose in the late 1960s and early 1970s from research and development encouraged largely by military entities in the United States and Britain that desired reliable, portable devices for applications involving personnel activity and warfare chemical detection. Among these the IMS was attractive because it was sensitive to warfare gases and explosives vapors, offered tentative identification of vapors through ion mobilities, and could be miniaturized for field use.

### 2.1.3. The ion mobility spectrometer

Measurements of ion drift velocities in ambient pressure gases are performed with the ion mobility spectrometer. Countless variations of the hardware have appeared, but all designs consist of an ambient pressure ion drift tube terminated by an ion-collecting electrode (Faraday plate). A simplified example of an ion mobility spectrometer is shown in Figure 2.1. The drift tube is a series of evenly spaced guard rings attached to a voltage

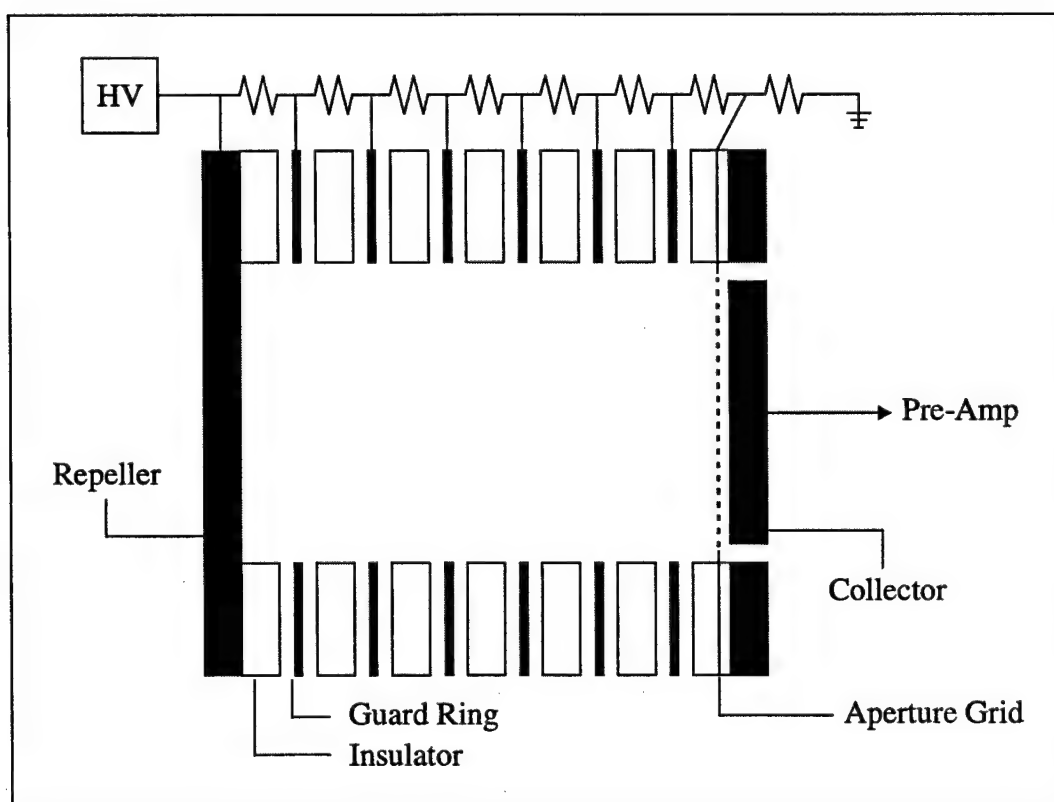


**Figure 2.1.** Schematic of an ion mobility spectrometer.

divider that maintains a homogeneous electric field through the drift space. During operation, the field pushes ions generated from a source located before, at, or behind the repeller through drift gas to the collector. An aperture grid, also connected to the voltage

divider, shields the collector from upfield ions that would otherwise induce current in the plate. The components form an airtight container or the device is encased to control gas contents. Most units deliver analyte to the ionization source in a carrier gas and purge the drift region with a counterflowing drift gas entering at the collector. Nearly all ion mobility spectrometry is performed at elevated temperature. As drift tubes are usually 4 to 10 cm long, ion drift times are on the order of  $10^{-3}$  s.

Numerous ionization sources have been paired successfully with the IMS, but ion mobility spectrometry traditionally and most frequently employs radioactive sources to ionize analyte vapor. While superior for reasons including high output stability, mechanical integrity, and noiseless operation, these produce both positive and negative ions and are continuous, requiring additional electronics in the form of ion shutters when used in the IMS. The most common radioactive source is  $^{63}\text{Ni}$ . Impacts of  $\beta$ -particles with nitrogen molecules in the carrier gas generate pairs of unstable cations and energetic secondary electrons<sup>5</sup>. Cations initiate a series of fast ion-molecule reactions that culminate in a reservoir of stable reactant cations dominated by hydrated protons. Secondary electrons generate additional ion pairs, but eventually thermalize. In air, these are captured rapidly to form a reservoir of stable reactant anions dominated by hydrated oxygen anions. When trace analyte vapor exists in the carrier gas, ion-molecule reactions between reactant ions and analyte neutrals generate product ions.

## 2.2 Photoemission from Metals

Photoemission from metals is treated as a sequence of three steps, including 1) absorption of photons by thermal electrons in the metal, 2) migration of excited electrons to the surface of the metal, and 3) escape of electrons from the metal surface<sup>6</sup>. A metal emits electrons only when the energy of incident photons exceeds a surface barrier called the work function of the metal, or

$$E_{\text{photon}} > \phi \quad (2.4)$$

where  $E_{\text{photon}}$  is the energy of the incident photon and  $\phi$  is the work function of the metal. Because work functions generally exceed 3.5 eV, photoemission from most non-alkaline metals requires wavelengths shorter than 350 nm. Photon energy in excess of the work function appears as kinetic energy in the emitted electrons. The photoemission current produced by illumination that satisfies Equation 2.4 depends linearly on light intensity.

The number of electrons emitted per incident photon, or the quantum yield for photoemission, is less than  $10^{-4}$  for metallic photoemitters due to high reflectivity in the visible and near ultraviolet and large losses due to scattering of excited electrons with abundant thermal electrons in metals. As a result, only electrons excited near the surface contribute to photoemission. The escape depths for photoelectrons from metals are as thin as several atomic layers. Escape depth increases with photon energy and for many metals absorption increases with photon energy so quantum efficiencies reach maxima at deep ultraviolet wavelengths.

Consideration of the escape depth of photoelectrons is necessary for proper construction of thin metal film photoemitters, which are produced by sputtering or depositing evaporated metal on various substrates including metal, quartz, or fused silica. These may be illuminated from the front side, or if the substrate transmits light, from the back side or underside of the film. In either case, the film thickness that provides optimal quantum efficiency is comparable to the escape depth of photoelectrons, as determined by photon energy and the mean free path for electron collisions in the metal. Optimal thicknesses for gold films for front or back illumination are 40-50 Å, or roughly the depth of 20 closest-packed layers of gold atoms. Losses due to reflectivity are larger for back illumination than front illumination, but accounting for the losses, quantum efficiencies are comparable. Films that are thicker than optimal produce ample electrons for many applications, provided light intensity is sufficient, while ensuring conductivity and durability. The quantum yield for gold-palladium films of thickness 300 Å is one-third that of the optimal 40 Å film.

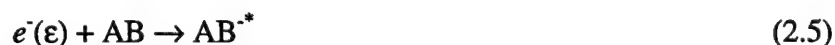
Several factors alter photoemission from metals in gases. Surface films of adsorbed gas molecules that are continually present alter the effective work functions of photoemitters. Electronegative gases such as oxygen tend to increase work functions while electropositive gases tend to produce the opposite. As a result, work functions for metals observed in gases can vary significantly from measurements performed in ultrahigh vacuum. Chemical changes on photoemissive surfaces such as surface oxidation that occurs on copper or aluminum during exposure to air also alter work functions, but shifts in these cases are due to the photoemissive properties of the metal oxides and not the base metal.

In gases, a portion of the photoemitted electrons is returned to the cathode by back diffusion, which lowers the effective quantum yield significantly versus measurements performed in vacuum. Losses are very large at low values of pressure-reduced electric field magnitude, decreasing as  $E/p$  increases. Measurements performed in nitrogen at pressures as high as 90 torr suggest losses at  $E/p = 0.2 \text{ V}\cdot\text{cm}^{-1}\cdot\text{torr}^{-1}$  in excess of 95 %. Quantum yields were found to vary in a similar way with  $E/p$  in early measurements of photoemission performed in atmospheric pressure gases including air.

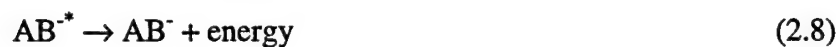
### 2.3. Electron-Molecule Interactions and Anion Formation

Due to the electric field, the distribution of electron energies generated within the IMS has mean value greater than thermal energy ( $E=3/2kT$ ), 0.04 eV at room temperature. The mean energy varies with the pressure-reduced electric field magnitude,  $E/p$ , where  $p$  is gas pressure in torr. At atmospheric pressure,  $E/p$  ratios for fields from 150 to 500  $\text{V}\cdot\text{cm}^{-1}$  typical of the IMS are 0.20 to 0.66  $\text{V}\cdot\text{cm}^{-1}\cdot\text{torr}^{-1}$ , which corresponds to mean electron energies in nitrogen from 0.28 to 0.58 eV and in air from 0.22 to 0.52 eV.

Under ambient conditions vapor molecules are predominantly in ground states and attachment of low-energy electrons can be summarized briefly. Unstable molecular anions are the initial result of low-energy electron attachment<sup>7</sup>. Collision of a low-energy electron with a ground state molecule may generate an excited molecular anion in its ground or in one of its excited states



where  $e^-(\epsilon)$  represents an electron of energy  $\epsilon$ , AB is a ground state molecule, and  $AB^*$  is a temporary negative ion (TNI) or negative ion resonance (NIR). The electron attachment cross section,  $\sigma_o(\epsilon)$ , describes the potential of molecule AB to attach electrons as a function of electron energy. The unstable NIR can react through one of three channels



where an asterisk in parentheses indicates a possible increase in internal energy, and  $e^-(\epsilon')$  is an electron of energy  $\epsilon'$  less than or equal to that of the incident electron,  $\epsilon$  (Equation 2.5).

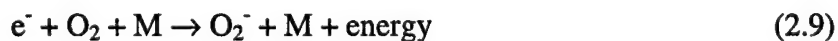
Equation 2.6 represents autodetachment or resonance electron scattering, which may be elastic or inelastic as determined by the energy of the scattered electron. The autodetachment lifetime,  $\tau_a$ , of the NIR is the period between attachment and loss of the electron. Equation 2.7 represents dissociative electron attachment, which occurs only if the state in which the NIR is created is dissociative and a stable fragment anion exists. The dissociative attachment lifetime,  $\tau_d$ , of species AB is the duration between electron attachment and dissociation of the molecule. The product of the electron attachment cross section by the probability that its NIR will react through Equation 2.7 versus the other channels is the dissociative attachment cross section,  $\sigma_{da}(\epsilon)$ , of molecule AB as a function of electron energy. Equation 2.8 represents associative electron attachment, which requires

a stable molecular anion and a stabilizing collision of the NIR with surrounding molecules within its autodetachment lifetime.

The electron affinity of a molecule, the energy difference between a neutral molecule and the molecular anion in ground electronic, vibrational, and rotational states, helps to predict whether its NIR will react through autodetachment (Equation 2.6) or associative electron attachment (Equation 2.8). Positive electron affinity indicates that the lowest level of the molecular anion ground state is energetically lower than that of the parent molecule and that the ground state molecular anion is stable. Conversely, the NIRs of molecules with negative electron affinity are subject to autodetachment as the lowest level of the molecular anion ground state lies energetically above that of the parent molecule.

#### 2.3.1 Attachment of low-energy electrons by molecular oxygen

Low-energy electron attachment by molecular oxygen ( $O_2$ ) has been studied extensively.<sup>8</sup> The electron affinity of the molecule is 0.44 eV and the only state of oxygen anion ( $O_2^-$ ) that lies energetically below the ground state of  $O_2$  is the  $O_2^-$  ground state. Thus attachment of low-energy electrons by oxygen occurs through NIRs in the ground state of oxygen anion, resonance energies ranging from slightly above thermal to beyond 1 eV. The autodetachment lifetimes of the resonances are on the order of  $10^{-12}$  s, less than the  $10^{-10}$  s between collisions in gases under ambient conditions. As a result, electron attachment by oxygen can be expressed as





a three-body electron attachment mechanism where M is a neutral molecule of the surrounding gas. Oxygen attaches the electron during collision with the third body, which removes excess energy and fixes the electron.

A three-body attachment rate coefficient ( $k_{3M}$ ) applies to Equation 2.9 and is strongly influenced by the identity of the third body. Third bodies pertinent to IMS are molecular nitrogen ( $N_2$ ) and molecular oxygen. Measurements of  $k_{3M}$  show that oxygen is a more efficient third body than nitrogen. For  $M=O_2$  and  $M=N_2$ , three-body attachment rate coefficients are approximately  $2.0 \times 10^{-30} \text{ cm}^6 \text{ s}^{-1}$  and  $0.2 \times 10^{-30} \text{ cm}^6 \text{ s}^{-1}$ , respectively. The utility of three-body attachment rate coefficients is limited, as  $k_{3M}$  applies to the condition of trace oxygen in a pure bath gas of the third body. However, electron attachment rate coefficients from measurements in air are of similar magnitude to  $k_{3M}$  measured with  $M=N_2$ .

### 2.3.2 Attachment of low-energy electrons by chlorinated aliphatic compounds

Low-energy electron attachment by chlorinated aliphatics is also well studied.<sup>9</sup> As a class, the species capture electrons dissociatively through NIRs of thermal energy to beyond 1 eV. The most heavily chlorinated species have electron affinities that are comparable to oxygen, 0.5 eV and 0.3 eV for PCE and TCE, respectively. Low-energy electron impact mass spectrometry has shown that low-energy electron attachment by chlorinated aliphatics leads to multiple fragment anions, chloride ion ( $Cl^-$ ) by far the most abundant. Electron swarm experiments have produced complementary results for trace

chlorinateds in atmospheric pressure nitrogen. The electron attachment rate constant for TCE is approximately  $5.5 \times 10^{-9} \text{ cm}^3 \cdot \text{s}^{-1}$  for electron energies 0.1 to 0.6 eV.

## **2.4 Photoemissive Ion Mobility Spectrometry**

Although photoemissive sources have existed for over a century and have been a key component of instrumentation for the study of gas phase electron-molecule interactions, only one ion mobility spectrometer using a photoemissive source has been reported. Simmonds, et. al.,<sup>10</sup> published the first and only report of ion mobility spectrometers paired with photoemissive sources. The devices used 1-cm inner diameter, 3.7-cm or 7.4-cm long drift tubes and did not use ion shutters. Photoemissive sources were 11-mm diameter (9-mm effective diameter) gold-coated fused silica discs driven by a pulsed xenon lamp operated at 30 to 50 Hz depending on drift length. Counterflowing air or nitrogen drift gas entered from the collector and air carrier gas was directed across the surface of the photoemitter. Both gases vented opposite the sample gas inlet. The instruments were operated at ambient temperature and pressure. Several relevant experimental results and conclusions were described.

### **2.4.1 Oxygen content of sample and drift gases**

One experiment varied the oxygen concentration in both the sample and drift streams in unison from 0 to 21% by volume oxygen. Resolution measured as drift time divided by peak width at half height was highest and steady above oxygen concentrations of 6% by volume but declined as oxygen level decreased. The resolution decrease was

accompanied by the growth of a leading edge shoulder on the ion mobility signatures measured for oxygen anions. The conclusion drawn from the observations was that electrons were able to travel longer distances before attachment in lower oxygen concentration and give rise to oxygen anions throughout the drift space producing ion current at all drift times. A similar experiment used nitrogen drift gas while varying the oxygen concentration of the carrier gas. In this case, resolution improved as the oxygen content of the carrier gas decreased, which was attributed to elimination of space-charge repulsion by production of fewer oxygen anions from the carrier gas.

#### 2.4.2. "Conventional flow" versus "sample in drift" modes

Experiments were performed with analyte embedded in air drift gas to create uniform concentration between the photoemitter and collector, which was termed "sample in drift" mode. Sensitivity enhancements for various species of 3 to 20 times, defined as ratios of peak heights, were observed for "sample in drift" mode versus "conventional flow" mode. However, the increased sensitivities caused the detectors to saturate at lower analyte concentrations. The conclusion drawn was that, versus conventional flow mode, the length of time for electron transfer from oxygen anions to the target species was longer in sample in drift mode. Product ion peaks were wider in sample in drift mode than in conventional flow mode, the peaks showed leading edge shoulders at low analyte concentration, and resolution was degraded. These observations supported the conclusion that reaction continued after the oxygen anions had drifted a significant distance down the drift tube in sample in drift mode, producing analyte ions at a range of drift distances and creating ion current over a range of drift times.

## CHAPTER 3

### ION MOBILITY INSTRUMENTATION

Three ion mobility cells were assembled to utilize three low-energy electron production schemes aimed at detection of chlorinated vapors. Each design was based on parallel electrode geometry and included an aperture grid before the anode, but details of electrode design, drift region construction, and cell housing varied. The first and second designs (*Cell A* and *Cell B*) did not include guard rings between the cathode and aperture grid and employed resonance-enhanced multiphoton ionization of aniline vapor and photoemission from laser illumination of copper cathodes as electron sources. *Cell A* featured movable electrodes such that the drift distance was adjustable. The third design (*Cell C*) included guard rings between the cathode and aperture grid and used photoemission from backside laser illumination of thin gold films as electron sources. Block diagrams of Cells A and B, which were electronically equivalent, and *Cell C* appear in Figures 1 and 2.

#### 3.1. Cell Using REMPI of Aniline Vapor as an Electron Source

*Cell A* was constructed within a cylindrical, stainless steel 4-way chamber, 2.75-inch nominal flange size, with removable lid and an internal volume of approximately 900 mL.

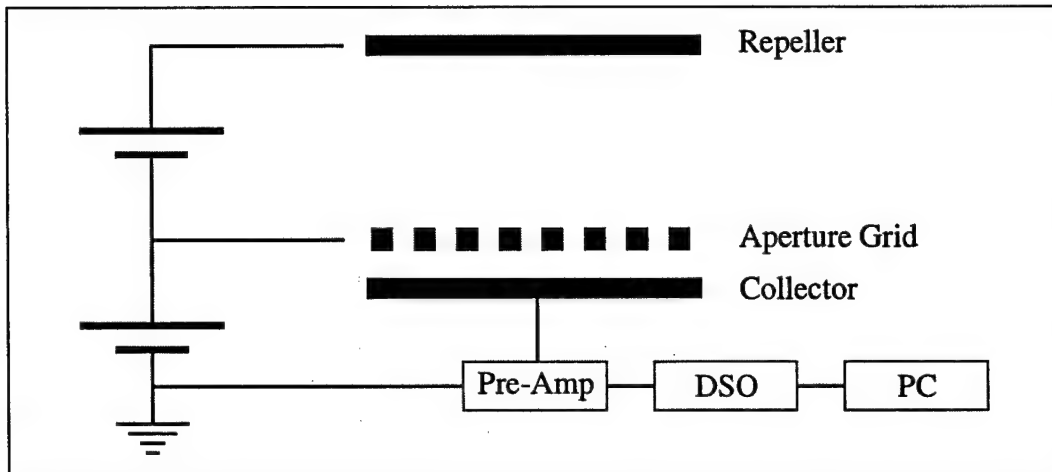


**Figure 3.1.** Block diagram of ion mobility cells using no guard rings (Cells A and B).

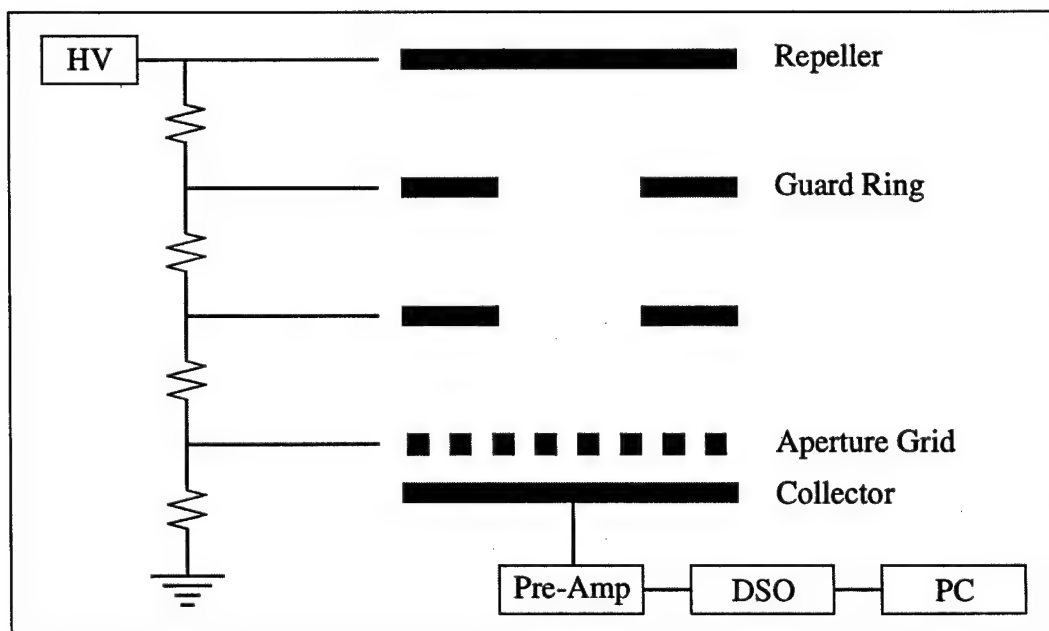


**Figure 3.2.** Block diagram of drift tube ion mobility spectrometer (Cell C).

The electrodes were mounted on lengths of thick-walled 0.375-inch glass tubing. The glass tubes were passed through Cajon o-ring feedthroughs mounted on opposite sides of the chamber so that the electrodes were easily moved through about 3.5 cm between the edge and center of the cell. Brewster windows were mounted on the perpendicular axis of the chamber and the repeller was positioned near the beam path. A 1.7-mm thick Teflon washer, a 2.1-mm thick metal ring, and an aperture grid cut from 60-mesh stainless steel screen were held against the collector by a tight-fitting PVC cap that reduced the exposed diameter of aperture grid and collector electrode to 4 cm. Tapped holes to either side of the anode feedthrough were used as ports for venting and sample introduction. Wiring was directed through the glass tubing to the electrodes and aperture grid with bias voltages to the repeller and aperture grid supplied by two 300 V batteries in series, as represented by Figure 3.1. Simply reversing the batteries changed the polarity of the voltage drop across the drift length.

### **3.2. Cell Using Front-Side Cathode Illumination**

Cell B was constructed within a nominal 2.75-inch stainless steel four-way cross of internal volume 200 mL. Electrodes consisting of 3-cm diameter copper blanks soldered to copper rods were mounted on BNC feedthrough flanges on opposing arms of the cross; the feedthrough on the anode arm was dual BNC. Electrodes were separated 2 cm and positioned such that laser pulses passed cleanly through flat fused silica windows terminating the perpendicular arms of the cross while striking the photocathode at a large incident angle. A 1.7-mm thick Teflon washer and an aperture grid cut from 60-mesh

stainless steel screen were pressed to the anode by a tight-fitting Nylotron cap that constricted the exposed diameter of the aperture grid and anode to 2 cm. Tapped holes in bored, double-sided flanges mounted between the cross and the BNC feedthroughs served as ports for venting and sample introduction. Bias voltages were supplied by two 300 V batteries connected in series as shown in Figure 3.1.

### **3.4. Drift Tube Ion Mobility Spectrometer Using Thin Film Photoemission**

Cell C was a drift tube ion mobility spectrometer constructed within a 2.75-inch nominal stainless steel nipple fitted at each end with bored, double-sided flanges. Two thin gold film photocathodes were used with the device. Both were 6.35-mm diameter fused silica windows sputter coated on one side, one with approximately 300 Å gold and the other with 10 Å chromium to improve adhesion then with 150 Å gold. These were supported within a 4.8-cm outer diameter, 6.35-mm inner diameter washer machined from a copper blank. Adhesion and electrical contact between the photoemitter and washer were made with silver epoxy. The photocathode was held to a double-sided flange at one end of the nipple within a flange machined from Corian. The drift tube consisted of a stack of 0.3-mm thick brass guard rings of 1.16-cm inner diameter obtained from a commercial source (Environmental Technologies Group, Inc., Edgewood, MD). Three holes distributed equatorially about the axial aperture were used to mount the guard rings, separated by 0.75-inch glass sleeves, on 3/16-inch glass rods. A 0.75-inch thick washer machined from Plexiglas, Corian, or machineable ceramic supported the ends of the glass rods at the entrance and exit of the drift tube. The terminal washer was affixed to a cap that held a 50-

mesh screen or a commercial aperture grid (Graseby Dynamics, Ltd., Watford, Herts, UK), a 0.82-mm thick insulating ring, and a 2-cm copper anode. The forward and rear washers maintained alignment of the drift axis with the center of the photoemissive surface.

The elements of the mobility spectrometer were connected through 0.5-W, 300 k $\Omega$  resistors. Bias voltage was applied directly to the back side of the photocathode and conducted to the first resistor inside the device through a small, circular piece of indium foil on a spring supported near the edge of the forward support washer. Contact with the aperture grid was made through a light wire loop fed through the side of the anode cap. Beyond this and a final resistor, the voltage divider terminated at one pin of a dual BNC feedthrough at the end of the nipple that was connected to high voltage supply ground. The anode was connected to the other. The total drift distance with four guard rings was 3.75 cm. When -2000 V bias was applied to the photocathode, the drift electric field magnitude was 444.4 V $\cdot$ cm<sup>-1</sup> and the aperture to collector field magnitude was 4065 V $\cdot$ cm<sup>-1</sup>.

Each of the double-sided flanges contained two 1/8-27 NPT tapped radial holes. During operation, one hole on each flange was capped. These were used between experiments to flush the cell. The other hole in the front flange was fitted with a Swagelok adapter and a short piece of Teflon tubing capped with a 5-mm NMR septum to serve as an injection port. The other hole in the rear flange fitted with valve served as cylinder gas inlet. The internal volume of the cell was 155 mL when completely assembled.



### 3.5. Laser Sources and Experimental Methods

The laser configuration implemented for electron production from aniline vapor by REMPI was a dye laser oscillator using a Bethune prism dye cell pumped by the second harmonic of a 10 Hz Quanta Ray DCR-11 Nd:YAG laser. Rhodamine 590 dye in methanol was selected to provide output between 574 and 588 nm. The dye laser output beam was directed to a KDP frequency-doubling crystal mounted on a manual rotation stage. The energy of the frequency-doubled output at 294.05 nm was about 500  $\mu\text{J}$  per pulse.

Wavelengths shorter than the fourth harmonic of Nd:YAG (266 nm) were necessary to produce photoemission from copper and gold photocathodes. Shorter wavelengths were produced by Raman shifting the fourth harmonic of the 10 Hz Quanta Ray DCR-11 Nd:YAG laser in 100 psi hydrogen. Both the first (AS1) and second (AS2) anti-Stokes lines at 239.53 nm and 217.85 nm, respectively, were used for photocathode illumination at pulse energies generally less than 30  $\mu\text{J}$  and usually around 10  $\mu\text{J}$ . AS1 provided ample photoelectron production from copper photocathodes while AS2 was used with gold thin films.

Analytes were delivered in a cyclohexane solution. Cyclohexane was found to not significantly alter photoemission, total ion charge collected, or waveform shapes produced in the mobility cells. Rarely analyte was delivered as headspace drawn over solutions of analyte with cyclohexane prepared following Raoult's Law, despite the likelihood that the species were not similar enough for this approach to be justified. All analyte samples were injected by microliter syringe and several minutes were allowed for evaporation and mixing of the sample in the cell. For experiments performed at relatively low oxygen

concentration, oxygen was introduced by injection of laboratory air using a 5 mL syringe assuming 21% by volume oxygen. All injections were performed through the sample inlet septum; large injections of air were performed with the gas outlet port loosely capped to prevent overpressure.

Measurements in nitrogen drift gas used 5.0 grade nitrogen, specified to contain less than 2 ppm water vapor and less than 1 ppm oxygen. Prior to introduction of sample vapor to nitrogen, the mobility cells were flushed with slowly flowing nitrogen beyond the disappearance of any slow ion current. Most measurements that used air as the drift gas were performed in laboratory air. Breathing grade compressed air was used for measurements of water vapor clustering with oxygen anions.

In all configurations, collector current caused by ions entering the volume between the aperture grid and striking the collector was amplified  $10^8 \text{ V}\cdot\text{A}^{-1}$  by a fast pre-amplifier and passed to a Tektronix 2440 or TDS series digital storage oscilloscope. An attached PC controlled waveform acquisition and downloading. Laser pulse energy measurements using various pyroelectric detectors were performed during many experiments, but extraction of accurate peak-to-peak voltages from pyroelectric waveforms was in most cases hampered by significant noise relative to the small waveform amplitudes. Normalizations for laser energy assuming linear photoemission with laser pulse energy were rarely found to improve data quality.

To overcome large electrical noise and large fluctuations in laser output, 32 to 256 laser shots were averaged for each acquisition. In some cases averages of replicate waveforms were taken. Ion mobility spectra are presented as ion current versus drift time in milliseconds. Ion current was calculated from voltage waveforms downloaded from the

oscilloscope by taking into account the  $10^8 \text{ V}\cdot\text{A}^{-1}$  pre-amplification. Integrals of ion current were taken in some cases to determine the charge collected. This was performed by summing the discrete current values under the portion of the ion mobility spectrum that was of interest then multiplying by the duration of the portion of the waveform

$$Q = \Delta t \cdot \{\Sigma i(t)\} \quad (3.1)$$

where  $Q$  is total charge in Coulombs,  $\Delta t$  is the time window of the integration, and  $\Sigma i(t)$  is the sum of the current at all times  $t$  between the start and end of the time window.

## CHAPTER 4

### RESULTS & DISCUSSION

#### 4.1. Ion Mobility Measurements Using REMPI of Aniline Vapor as Electron Source

Due to its relatively low vapor pressure and tendency to persist in ionization detectors at room temperature, aniline provides a convenient and reasonably stable source of free electrons. Multiphoton ionization of aniline vapor generates populations of aniline cations and free electrons that separate in the electric field between the repeller and aperture grid in Cell A as the ions drift toward electrodes of opposite polarity. Oxygen molecules quickly scavenge the free electrons and the oxygen anions created are susceptible to clustering with water vapor, carbon dioxide, and other neutrals found in laboratory air.

Figure 4.1 includes positive ion mobility spectra of approximately 500 parts-per-billion by volume (ppbv) aniline vapor in air measured on an ultraviolet absorption resonance of aniline at 294.05 nm and off the resonance at slightly longer wavelength. The electrical configuration of the cell (Figure 3.1) allows the pre-amplifier to register current due to ions approaching and striking the repeller in addition to those reaching the collector. In Figure 4.1, cations reaching the collector produce the slow signature in each spectrum while oxygen anions migrating toward and striking the repeller cause the sharp, fast signature and tail. The amplitude of the on-resonance spectrum is approximately 20 times that of the off-resonance spectrum, confirming ionization of aniline vapor at 294.05 nm.

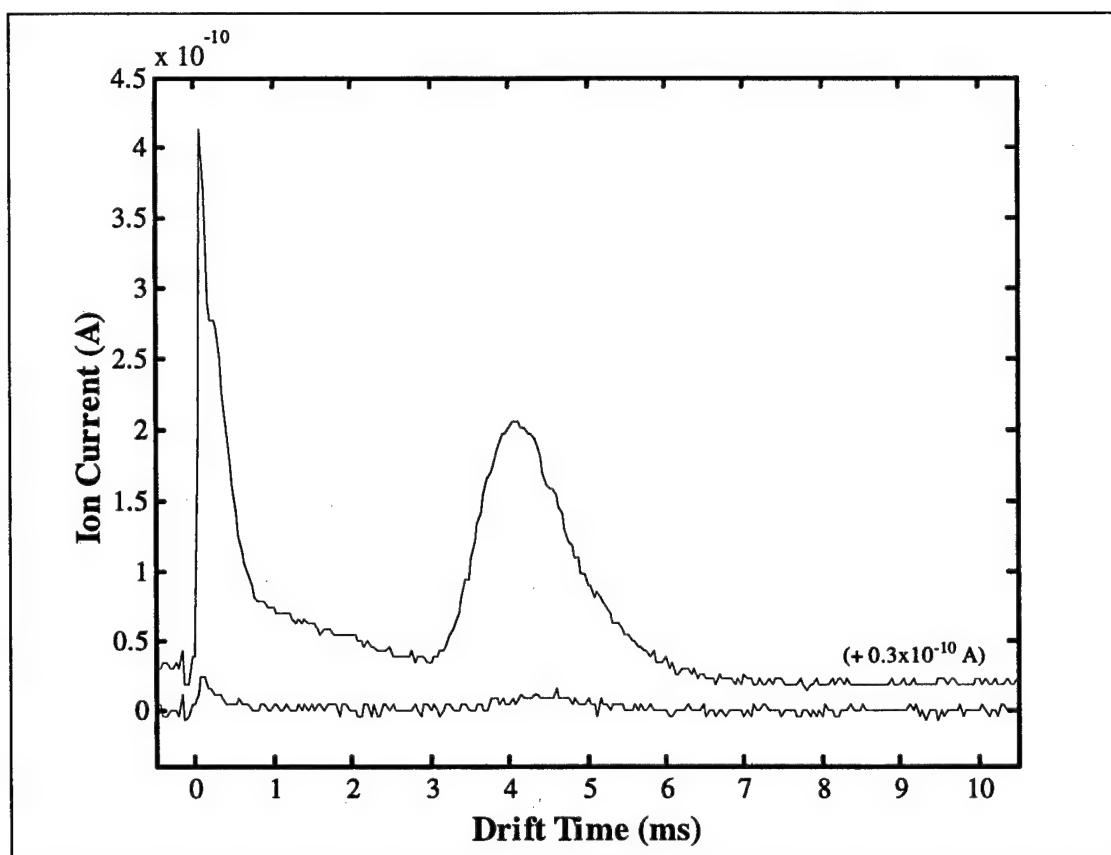


**Figure 4.1.** Positive ion mobility spectra produced by REMPI of approximately 500 ppbv aniline in air on-resonance at 294.05 nm (upper spectrum) and off-resonance at wavelength longer than 294.05 nm (lower spectrum). The spectra are 64-acquisition averages.

The on-resonance spectrum may be broadened or otherwise distorted by ion repulsion due to high ion densities produced in the laser path during measurement. Integrals of the slow peaks in the on- and off-resonance spectra are  $2.4 \times 10^{-13}$  C and  $1.1 \times 10^{-14}$  C, respectively, indicating that the collected signatures represent about  $1.5 \times 10^6$  and  $6.9 \times 10^4$  cations. Assuming that the aperture grid eliminates 80% of the ions passing through it, as discussed later (Section 4.2), the estimate of the number of aniline cations created for the on-resonance spectrum is  $7.5 \times 10^6$ . Assuming a beam diameter of 4 mm and an effective beam length of 4 cm (the diameter of exposed aperture grid and collector), the

ionization volume is  $0.5 \text{ cm}^3$ . Thus the number density of aniline cations in the beam path during the ionization pulse is approximately  $1.5 \times 10^7 \text{ cm}^{-3}$ , which may produce space-charge repulsion. The integrals of the prompt signatures in Figure 4.1, which are too fast for the detection electronics to be represented accurately, are  $1.8 \times 10^{-13} \text{ C}$  for the on-resonance spectrum and  $8.8 \times 10^{-15} \text{ C}$  for the off-resonance spectrum. Both values are approximately 20% lower than the areas of the corresponding aniline cation signatures.

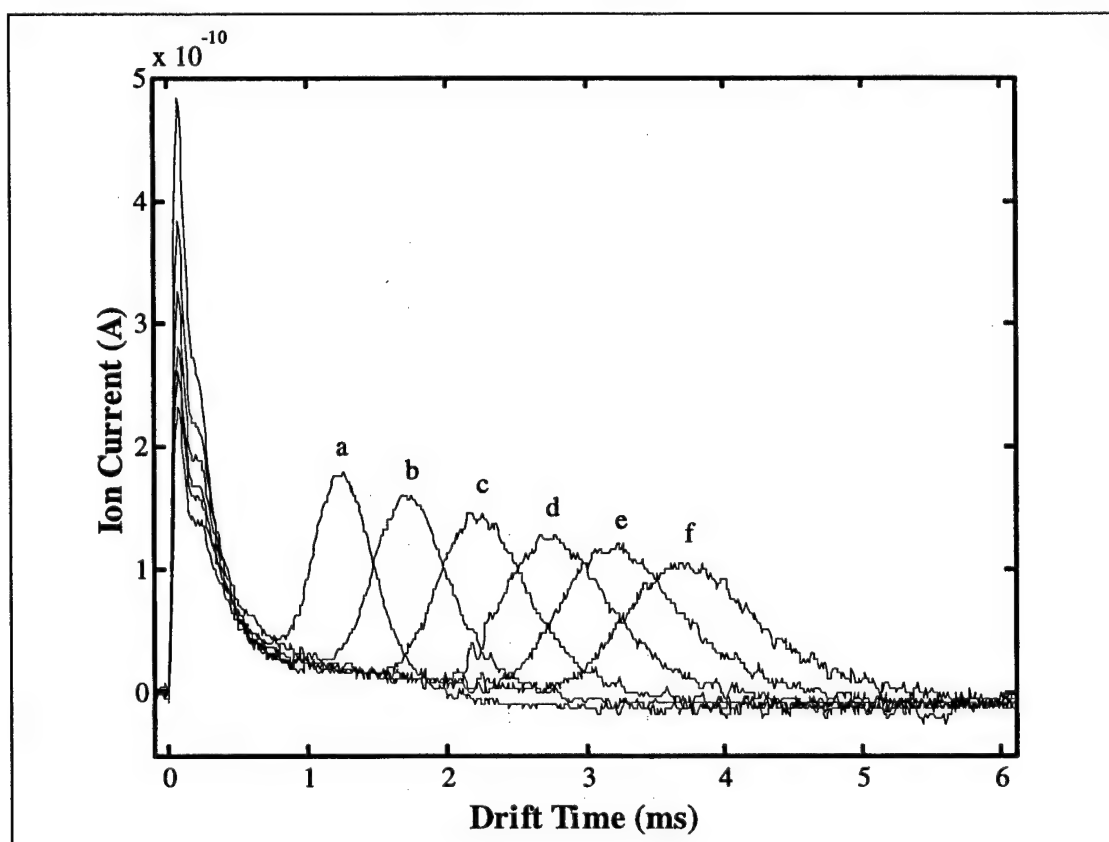


**Figure 4.2.** Positive ion mobility spectra produced by REMPI of approximately 500 ppbv aniline in air at plate separations increasing from approximately 1.0 cm, *a*, to 1.8 cm, *f*. The spectra are 64-acquisition averages measured at laser wavelength 294.05 nm.

Changing the position of the collector electrode at constant bias voltage changes the drift time and amplitude of the aniline cation signature, as demonstrated in Figure 4.2. Moving the collector in Cell A simultaneously changes drift length and electric field magnitude. Because ion drift times are proportional to the square of drift distance (Equation 2.1), the drift time of aniline cations more than triples as the plate separation is increased from around 1.0 to 1.8 cm.

The cation signature is tallest and narrowest at the shortest electrode separation, shrinking and broadening due to diffusion as the collector retreats. At shorter separations the cation signature is clearly superimposed on the tail of the anion signature, which alters the shape of the cation peak. Subtracting the anion components yields a consistent cation peak shape for all drift lengths, as shown in Figure 4.3, where the anion tails have been subtracted crudely from the spectra shown in Figure 4.2 by linearizing baselines about the cation peaks.

The difference between the drift times of aniline cations and oxygen anions formed by attachment of the liberated electrons is shown in Figure 4.3, which compares positive and negative ion mobility spectra of aniline in air at plate separation 2 cm and laser wavelength 291.2 nm. The drift times, taken as positions of maximum ion current of the slow signatures, are 3.38 ms and 3.86 ms for oxygen anions and aniline cations, respectively. The order of drift times agrees with published values of the mobilities of the ions. Flushing briefly with nitrogen removes all slow signal components from the negative ion mobility spectrum, but significant aniline remains as a continuing source of free electrons. In negative ion mode, electrons cross the drift distance rapidly and produce

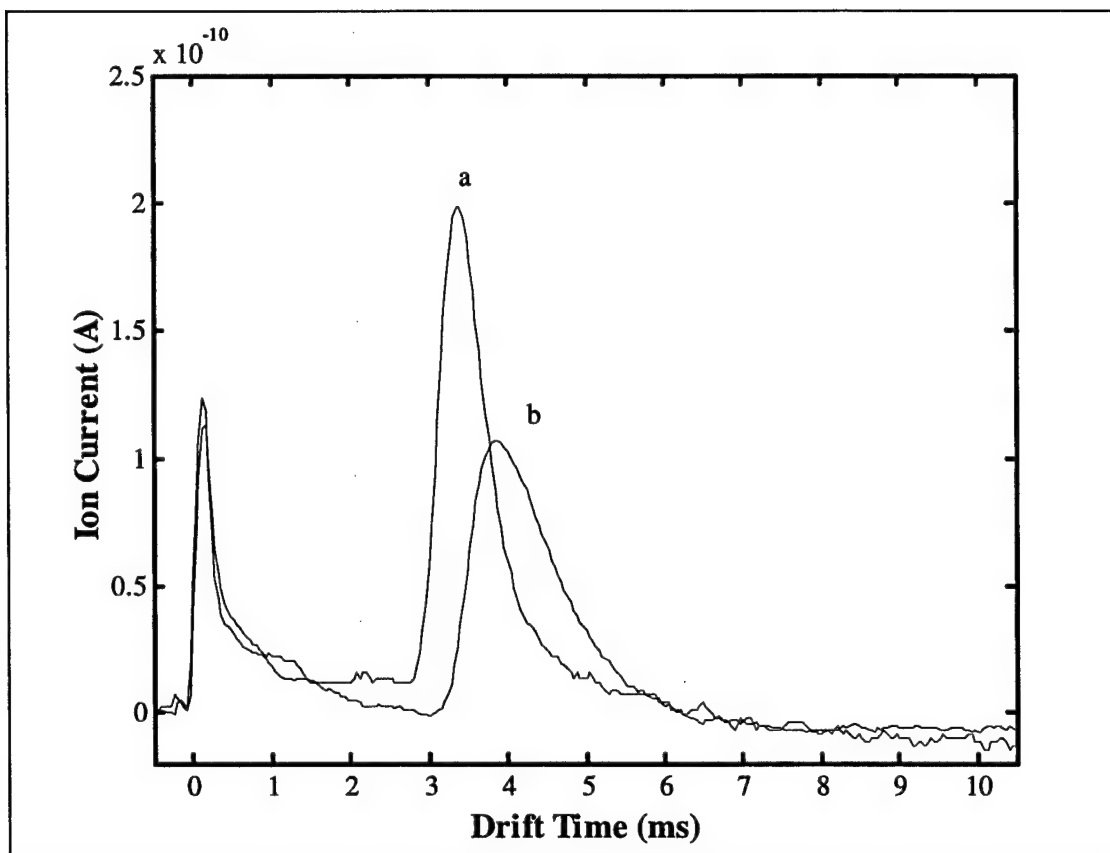


**Figure 4.3.** Negative ion mobility spectrum, *a*, and positive ion mobility spectrum, *b*, of aniline vapor at laser wavelength 291.2 nm.

a prompt, large signature as shown in Figure 4.4 for laser wavelength 287.0 nm and plate separation 2 cm. Ringing in the circuit follows the large free electron pulse. The amplitude of the free electron signature decreases and the slow signature reappears when an electron-attaching species such as oxygen or TCE is reintroduced.



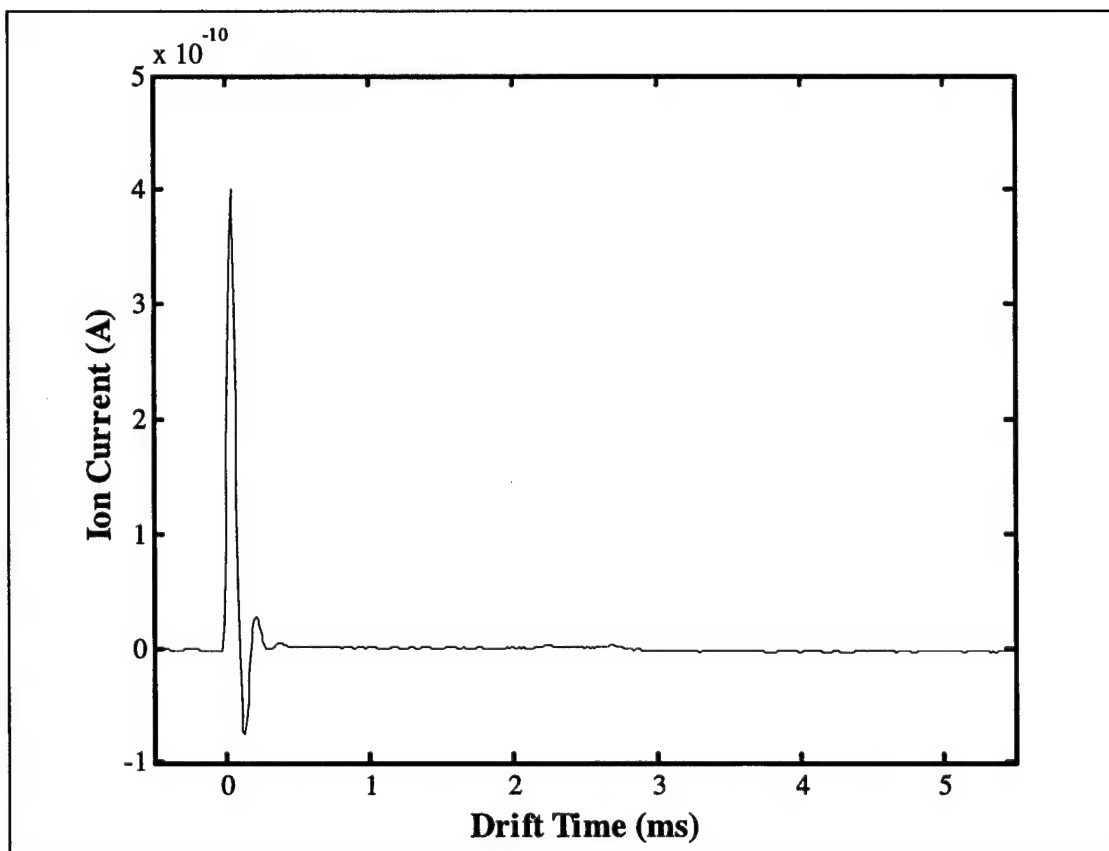


**Figure 4.4.** Negative ion mobility spectrum of nitrogen.

Figure 4.5 demonstrates detection of TCE at concentrations between 1 and 15 parts-per-million by volume (ppmv) in nitrogen using REMPI of aniline as a source of free electrons. Because electrons may be captured by TCE anywhere between the laser path and the collector, chloride ions arise and initiate drift throughout the drift space and arrive at the collector at all drift times. As attacher concentration increases, a prominent peak builds between 2.5 and 3.0 ms drift time. The peak shifts to longer drift times with increasing TCE concentration, which may be interpreted as shortening of the mean distance that the electrons travel before attachment but could also suggest cluster formation of chloride ions with TCE neutrals. Ion current prior to about 2.3 ms falls with increasing

TCE concentration, which is a hallmark of detector saturation. Saturation of the detector is supported by comparing the amplitudes of the free electron peaks not shown in Figure 4.5 which were 0.44, 0.16, 0.10, and 0.09 nA for TCE concentrations 1, 5, 10, and 15 ppmv (Figure 4.5, spectra a-d), respectively. The last two free electron amplitudes listed above are approximately equal to the amplitude of a noise spike that underlies the free electron signature. The initial free electron amplitude was 0.74 nA.

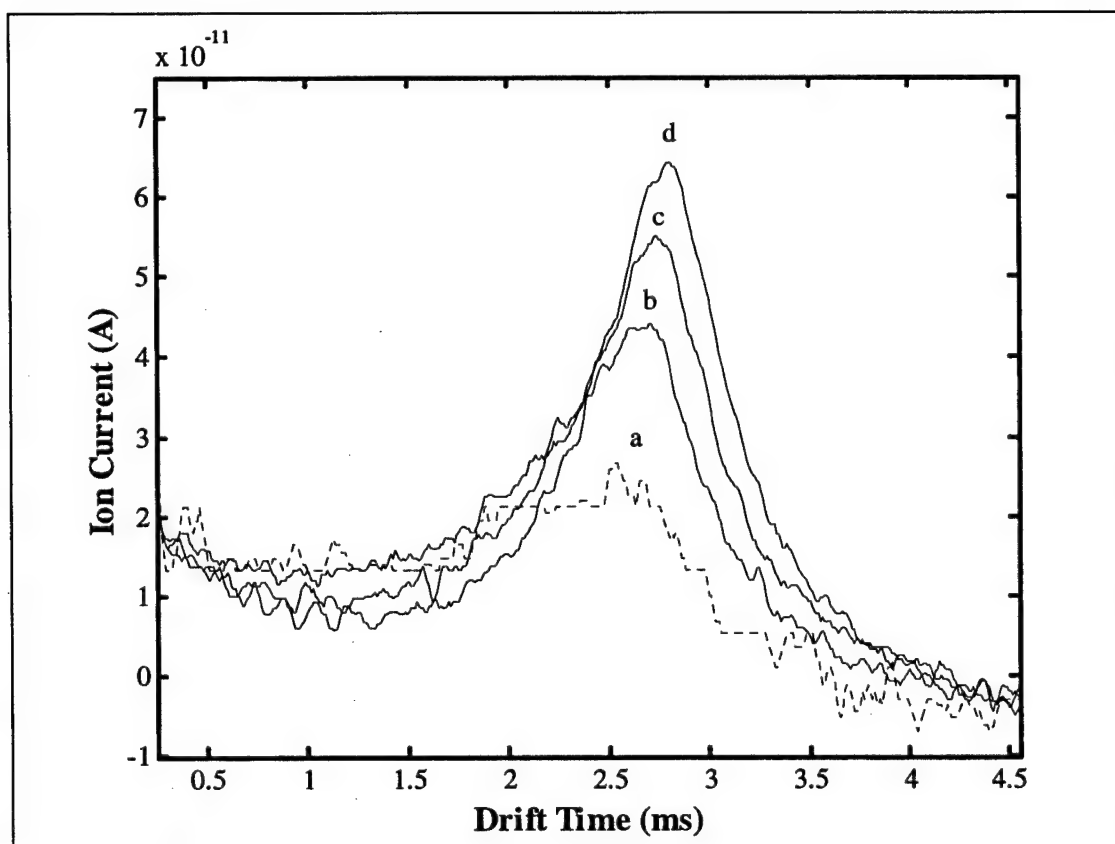


**Figure 4.5.** Ion mobility spectra in nitrogen of 1 ppmv TCE, *a*, 5 ppmv TCE, *b*, 10 ppmv TCE, *c*, and 15 ppmv TCE, *d*.

## 4.2. Ion Mobility Measurements Using Copper Photoemission as Electron Source

Photoemission from the copper photocathode of Cell B produces large numbers of free electrons from relatively weak laser pulses. For 10  $\mu\text{J}$  pulses of 239.53 nm hydrogen AS1, the amplitude of the fast free electron signature in nitrogen was typically 30 nA. The higher electron production improves TCE detection limits in nitrogen by at least an order of magnitude as shown by Figure 4.6. Ion current grows at all drift times with TCE concentration, which indicates that concentrations in the range 0.1 to 1.25 ppmv are below detector saturation, but slower growth of ion current between 0.75 ppmv (spectrum d) and

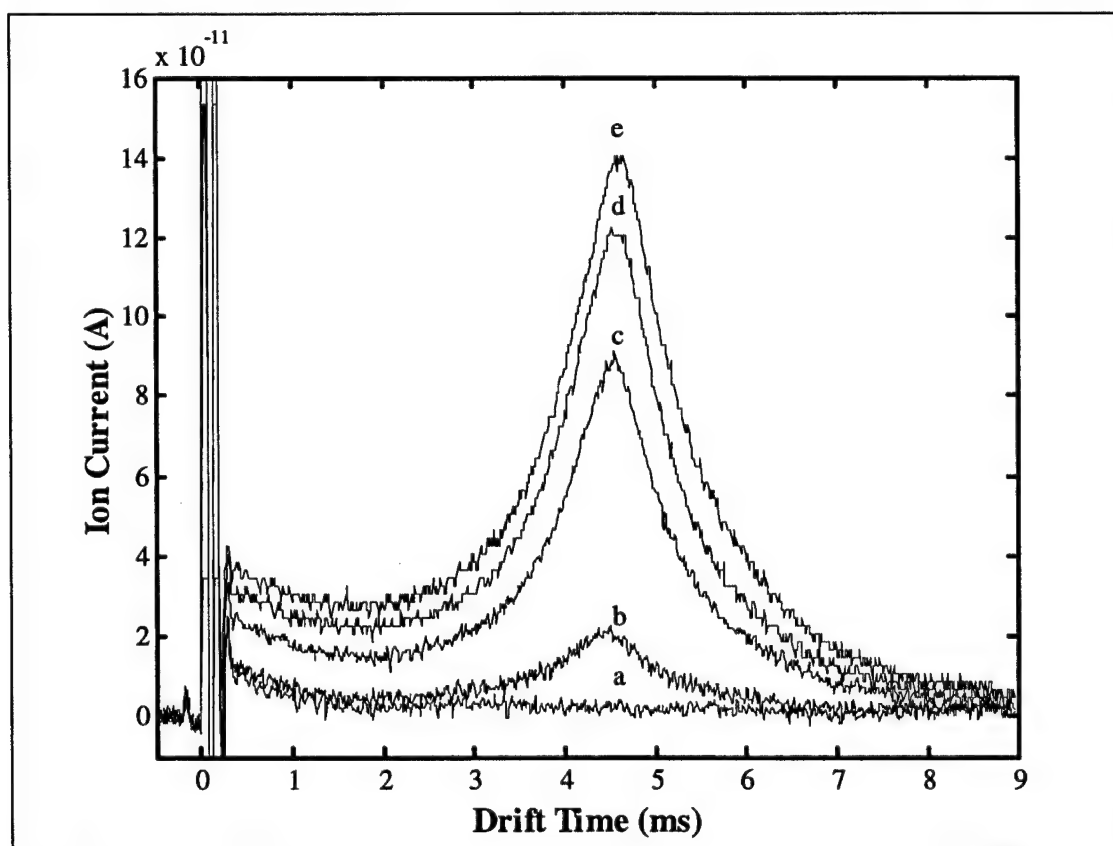


**Figure 4.6.** Ion mobility spectra of TCE in nitrogen at concentrations 0 ppmv, *a*, 0.1 ppmv, *b*, 0.5 ppmv, *c*, 0.75 ppmv, *d*, and 1.25 ppmv, *e*.

1.25 ppmv (spectrum e) compared with that between 0.5 ppmv (spectrum c) and 0.75 ppmv indicates an approach to saturation. This is confirmed in the calibration curve for TCE detection displayed in Figure 4.7, which shows that integrals of the chloride signatures or the chloride charge collected is quite linear with TCE concentration to about 0.75 ppmv TCE, sensitivity  $3.7 \times 10^{-13} \text{ C} \cdot \text{ppmv}^{-1}$ .

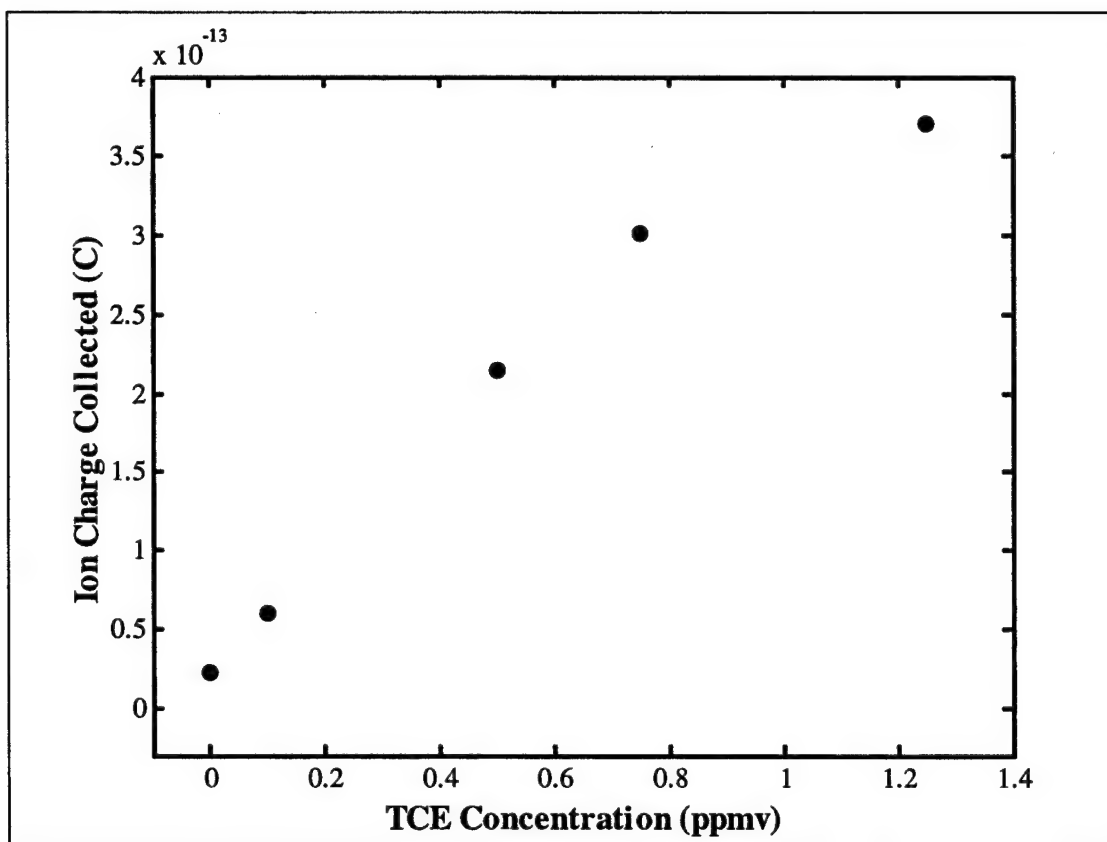


**Figure 4.7.** Calibration curve for detection of TCE vapor in nitrogen.

The aperture grid causes significant losses of ions in all ion mobility spectrometers. Figure 4.8 contains the ion mobility spectrum of air measured in normal operation and the same measured with the aperture grid electrically connected to the anode and -300 or -600

V applied to the repeller electrode. Comparison of the spectra shows the utility of the aperture grid, which is to prevent current induction in the anode until ions enter the short space between it and the aperture grid. In the absence of the grid spectra consist of continuous, more or less steady current that persists until all ions reach the anode.

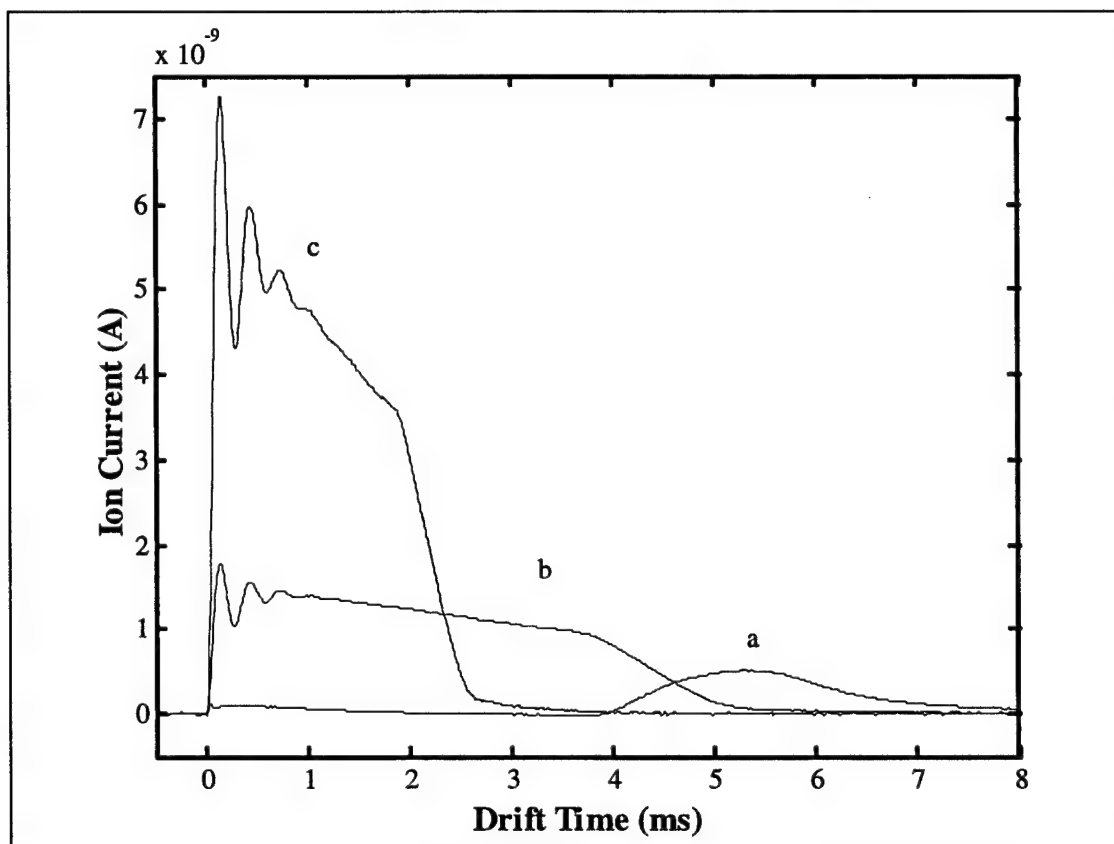


**Figure 4.8.** Ion mobility spectrum of air, *a*, ion current observed with the aperture grid and collector electrode connected with -300 V applied to the photocathode, *b*, and ion current observed with the aperture grid and collector electrode connected with -600 V applied to the photocathode, *c*.

Total charge values from the waveforms are 1.15, 4.32, and 10.00 pC for the normal configuration, anode tied to aperture grid using -300 V photocathode bias, and anode tied to aperture grid using -600 V bias, respectively. Since the electric field magnitude in the

normal configuration is comparable to that in the configuration where the aperture grid and anode are connected and bias voltage is  $-300$  V, approximately  $150 \text{ V}\cdot\text{cm}^{-1}$ , an estimate of ion loss to the aperture grid is 80%.

The other result shown by the ion loss measurements is that the magnitude of the photocathode bias voltage or drift electric field influences photoelectron yield through the extent of electron back diffusion to the photocathode. Doubling the bias voltage to  $-600$  V or field magnitude to  $300 \text{ V}\cdot\text{cm}^{-1}$  (Figure 4.8 spectra b versus c) reduces back diffusion and nearly doubles the ion charge collected.

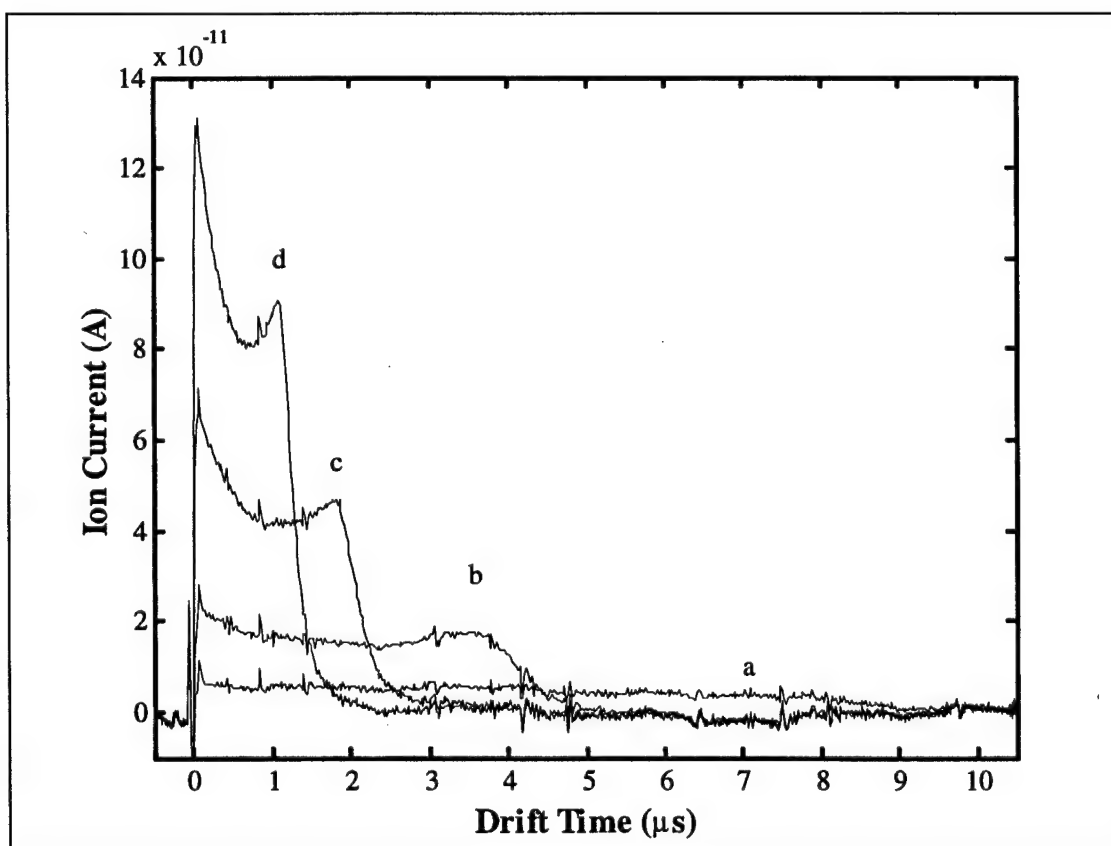


**Figure 4.9.** Electron current waveforms at electric field magnitudes  $75 \text{ V}\cdot\text{cm}^{-1}$ , *a*,  $150 \text{ V}\cdot\text{cm}^{-1}$ , *b*,  $300 \text{ V}\cdot\text{cm}^{-1}$ , *c*, and  $500 \text{ V}\cdot\text{cm}^{-1}$ , *d*.

Support for this result is obtained from direct measurements of electron production as a function of electric field magnitude. Figure 4.9 shows electron waveforms measured in nitrogen without the aperture grid or pre-amplifier using 2200  $\Omega$  oscilloscope input impedance. Electron charge collected is plotted in Figure 4.10 as a function of electric field magnitude.

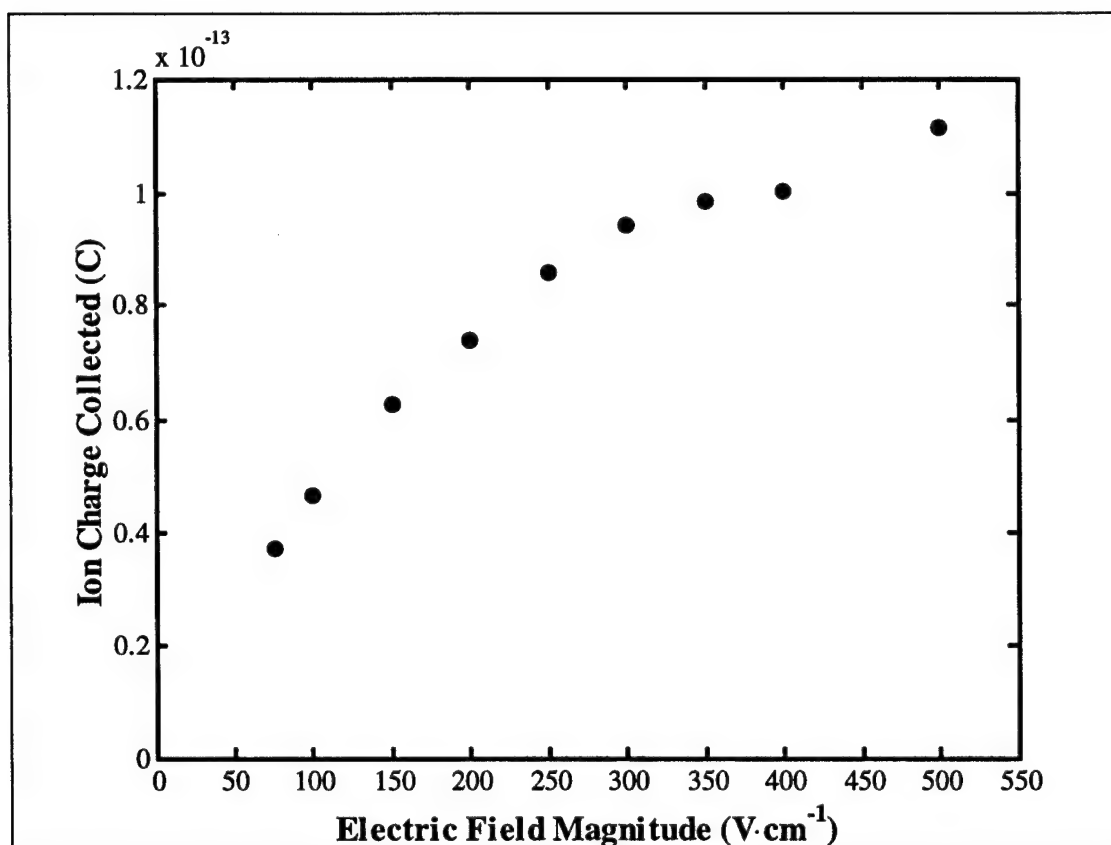


**Figure 4.10.** Electron charge collected in nitrogen as a function drift field magnitude.

### **4.3. Measurements Using Drift Tube with Thin Gold Film Photoemitter**

#### **4.3.1. Detection of TCE and PCE vapors using the drift tube IMS**

The PE-IMS is sensitive to TCE and PCE vapors. Ion mobility spectra obtained from several concentrations of PCE vapor, shown in Figure 4.11, and the accompanying concentration calibration curve shown in Figure 4.12 indicate PCE detectability slightly below 10 ppbv. Spectrum e of Figure 4.11 measured at 607 ppbv PCE shows some reduction of current at drift times less than 1 ms that may be attributed to detector saturation while the calibration curve suggests possible saturation below 200 ppbv PCE. The weakly linear initial portion of the calibration curve between 5 and 60 ppbv PCE suggests sensitivity near  $4.4 \times 10^{-16} \text{ C} \cdot \text{ppbv}^{-1}$ .

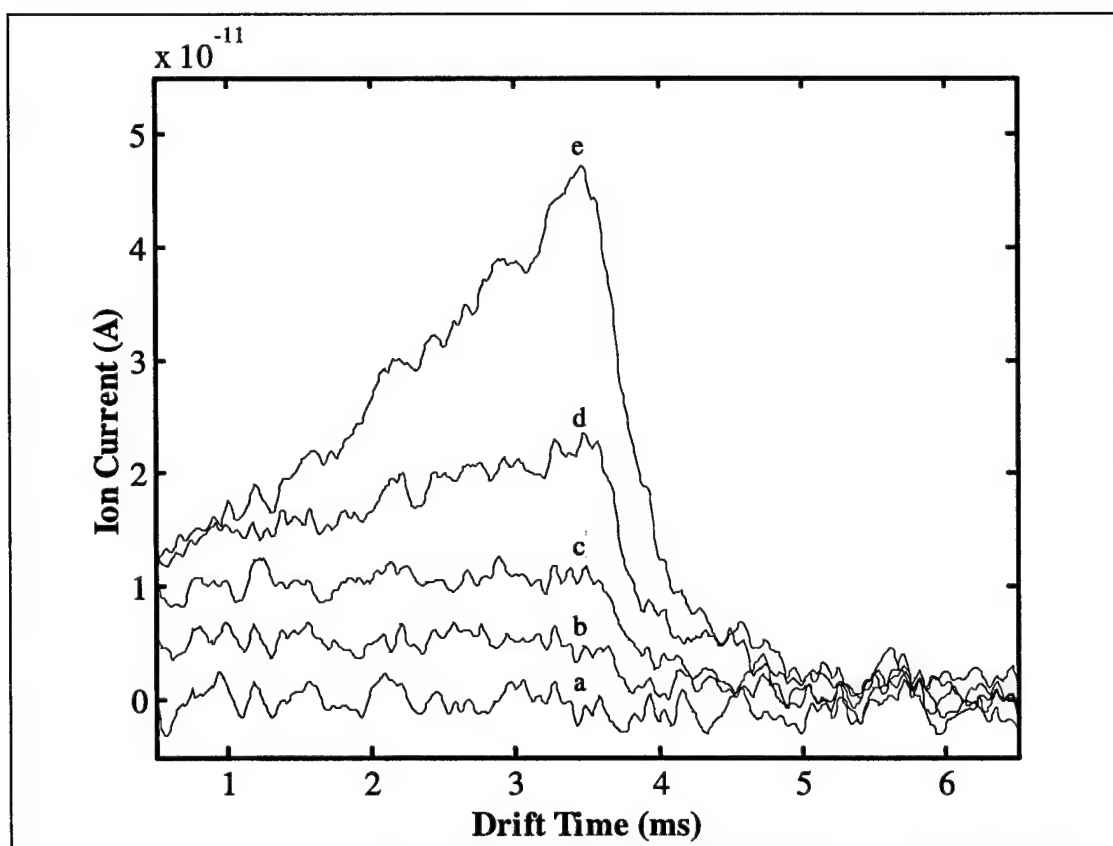


**Figure 4.11.** Ion mobility spectra of chloride ions generated from PCE. In the figure, *a* represents the background spectrum of nitrogen drift gas while *b*, *c*, *d*, and *e* represent spectra obtained at 4.63, 32.4, 236, and 607 ppbv PCE in nitrogen, respectively.



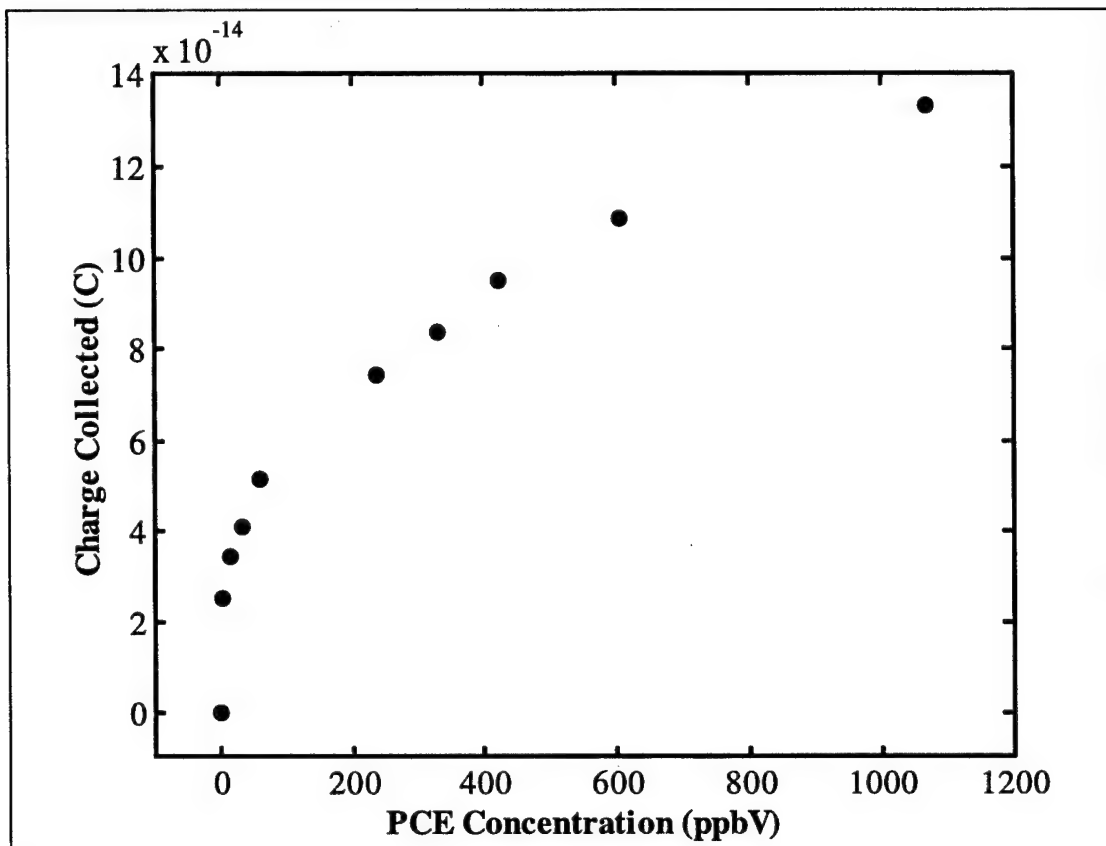


**Figure 4.12.** Concentration calibration curve for detection of PCE vapor.

Ion mobility spectra for TCE vapor shown in Figure 4.13 and the calibration curve in Figure 4.14 show detection of TCE at as low as 139 ppbv. From the spectra, the onset of detector saturation appears to begin at TCE concentration near 400 ppbv. The sensitivity to TCE, based only on the first two points of the calibration curve is around  $3 \times 10^{-16} \text{ C} \cdot \text{ppbv}^{-1}$ .

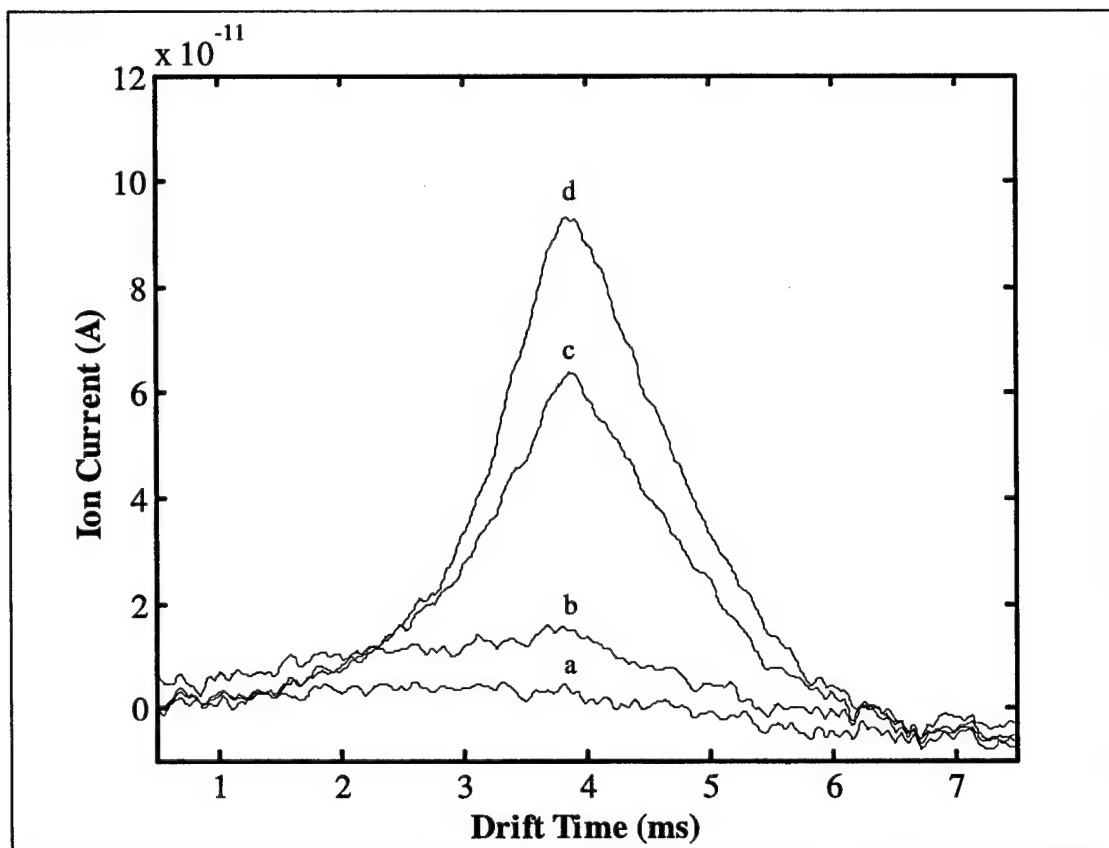


**Figure 4.13.** Ion mobility spectra of chloride ions generated from TCE. In the figure, *a* represents the background spectrum of nitrogen drift gas while *b*, *c*, and *d*, represent spectra obtained at 139, 418, and 697 ppbv TCE in nitrogen, respectively.

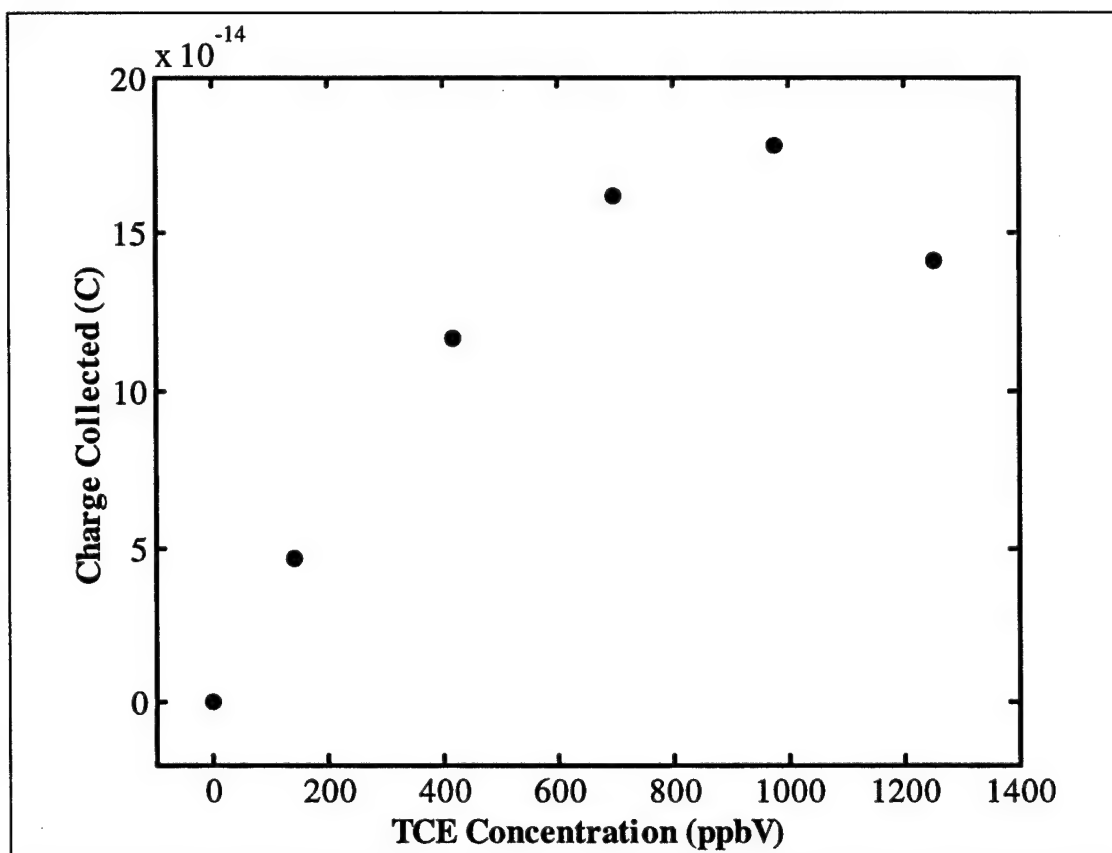


**Figure 4.14.** Concentration calibration curve for detection of TCE vapor.

#### 4.3.2. Detection of TCE in the presence of oxygen.

Detection of trace TCE in nitrogen is straightforward, but the same in air is difficult due to the magnitude of the free electron signature. The 20% oxygen content of air easily saturates the detector, capturing all free electrons. The results of several experiments conducted in Cells A and B not detailed here in which detection was attempted in air showed little reproducible change in the oxygen anion signature at TCE concentrations less than 10 ppmv. However, other results from these cells showed that if oxygen content was lowered below saturation (to less than 2% by volume), the detectors regained sensitivity to

low ppmv concentrations of TCE vapor. Figures 4.15 and 4.16 show ion mobility spectra

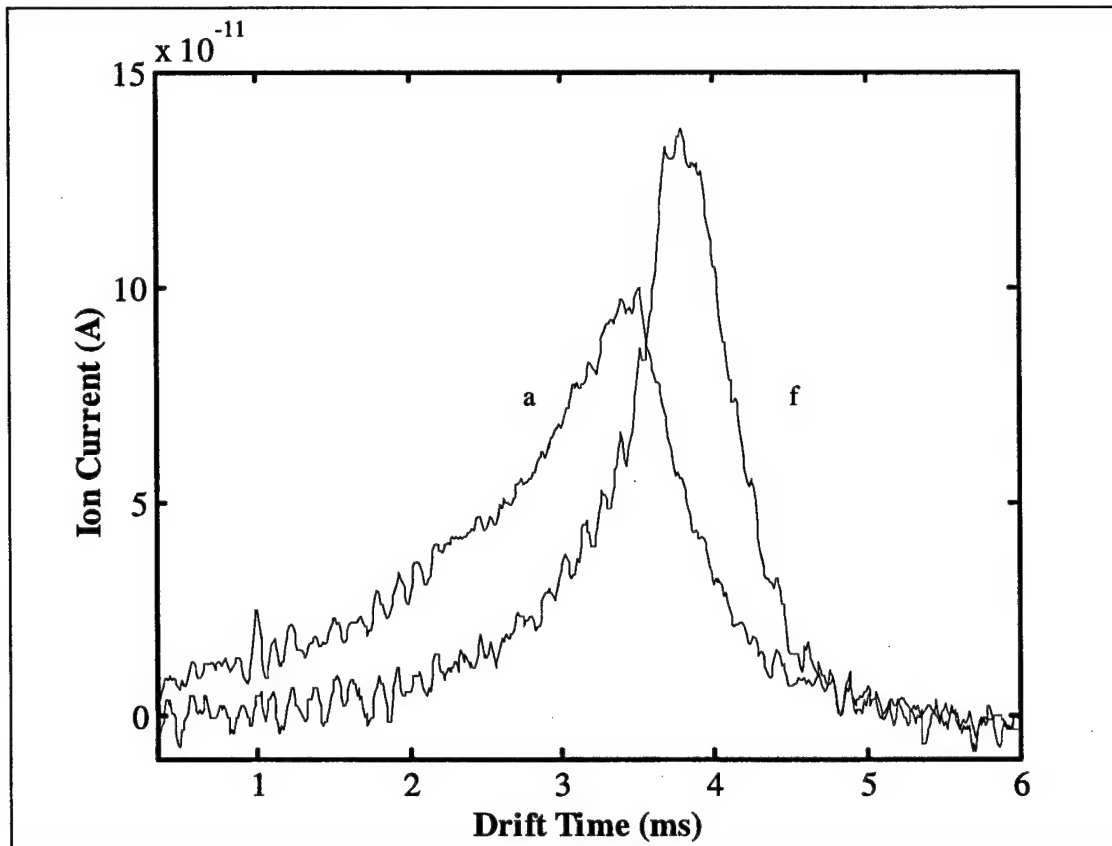


**Figure 4.15.** Ion mobility spectra of 0.67% oxygen in nitrogen, *a*, and 0.67% oxygen in nitrogen plus 1.25 ppmv TCE, *f*.

of approximately 0.67% by volume oxygen in nitrogen, added as part of laboratory air, and subsequent additions of TCE to that mixture. Figure 4.15 compares the spectra of 0.67% oxygen in nitrogen with and without 1.25 ppmv TCE and Figure 4.16 portrays the progression of the ion mobility spectrum from that of 0.67% oxygen plus 0.14 ppmv TCE to 0.67% oxygen plus 1.25 ppmv TCE. The additions of TCE, which place the detector in saturation, increase current at slow drift times at the expense of fast current and push the drift time of the maximum ion current from about 3.5 ms to nearly 3.9 ms.

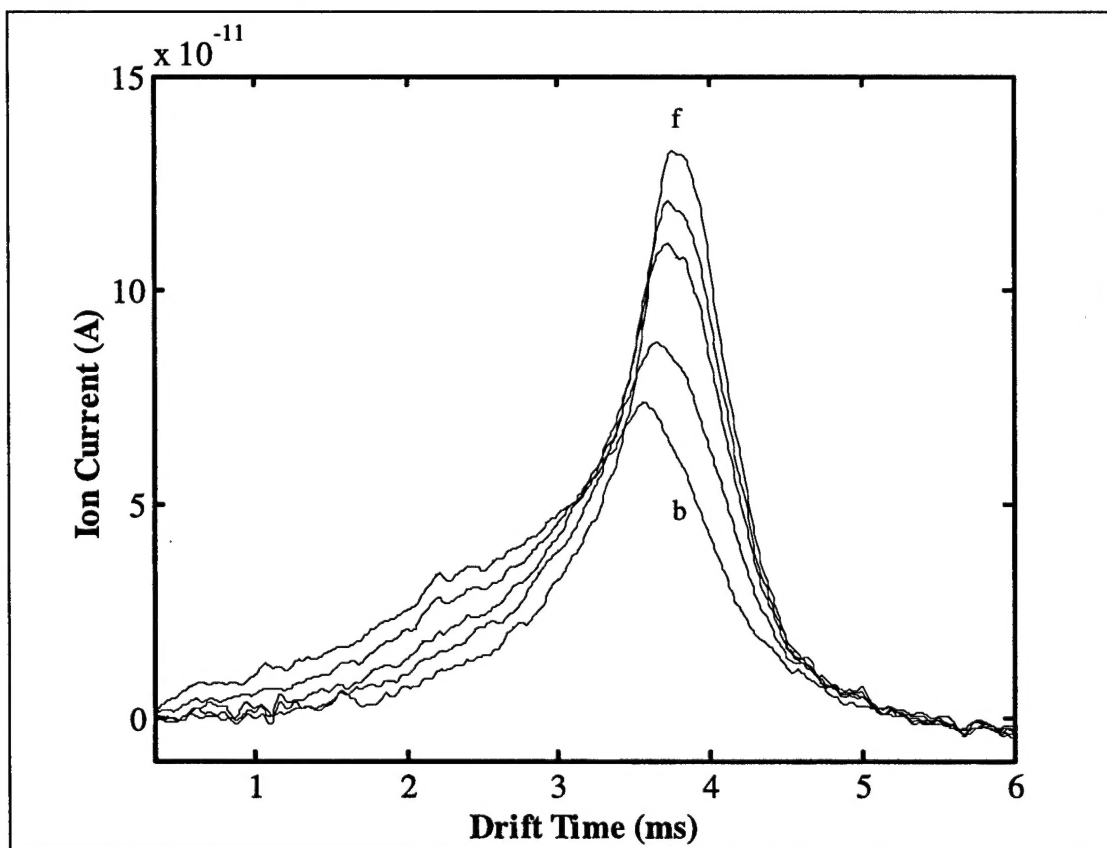


**Figure 4.16.** Progression of the ion mobility spectrum of 0.67% oxygen in nitrogen containing 0.14 ppmv TCE vapor, *b*, through intermediate concentrations 0.42, 0.70, and 0.98 ppmv TCE to final TCE concentration 1.25 ppmv, *f*.

## CHAPTER 5

### CONCLUSION

Unadorned photoemissive ion mobility detectors without amenities common in complete IMS units such as counterflowing drift gas and elevated temperature can ionize and detect chloride ions from chlorinated aliphatic compounds including TCE and PCE. These are easily detected in the absence of other electron-attaching species in nitrogen at ambient temperature. The detection limits estimated for the species are encouraging considering that other chlorinateds have higher electron affinities and attach electrons more efficiently. Detection in air is less successful, but when oxygen concentration is reduced sufficiently, ion mobility spectra respond noticeably to additions of chlorinated vapor in a repeatable fashion. The results for chlorinated detection in the presence of oxygen suggest that with some means to discriminate against oxygen, detection of chlorinateds in air at ambient temperature is possible.

Adding a counterflowing drift gas could increase the resolution of ion mobility spectra measured with the photoemissive ion mobility detectors. Counterflowing drift gases limit analyte vapor and most or all of the ionization chemistry to the space immediately surrounding the ionization source and provide a slab of clean gas for product ions to drift through to the collector. Ideally the drift gas prevents further electron transfer and clustering reactions involving product ions which can alter drift times and peak widths. For IMS with photoemissive sources, an electron transparent drift gas such as nitrogen would eliminate downfield electron capture that produces leading edge shoulders on ion mobility signatures.

Unfortunately, the addition of counterflowing drift gas would also decrease sensitivity. Heating the detectors may provide instant improvements to detection of chlorinateds in air without sacrificing the sensitivity enhancement attained by dispersing analyte throughout the drift region. In ion mobility spectrometry one benefit of heating is to reduce clustering that affects ion drift times and broadens ion signatures. However, the IMS and the oxygen-sensitized ECD have shown that enhanced ionization of chlorinated vapors is another important benefit of elevated temperature. In both cases enhancement results from improved electron transfer from oxygen anions to chlorinated species. The oxygen-sensitized ECD, which uses oxygen concentrations of up to a few percent by volume to improve sensitivity to various vapors with positive electron affinity, operates at elevated temperatures with the specific intent to make collisional detachment of electrons from oxygen anions competitive with associative electron attachment by oxygen molecules. Heightened sensitivity to chlorinateds in air at elevated temperature could also mitigate the loss of sensitivity caused by the use of counterflowing drift gas.

Although the mobilities of molecular anions can be used to identify analytes, identification of specific analytes from fragment anions is difficult or impossible because identical fragments can be generated from different molecules. Therefore identification of specific species in a mixture of chlorinated aliphatic compounds is impossible with ion mobility spectrometry, as all species dissociate to chloride ions. Despite this limitation, fragment anions can be analytically useful if the IMS is used as a class-specific detector, in which the fragment ion mobility signature becomes evidence that at least one member of a group of substances is present in the sample. Fragment ions are also acceptable when the IMS is used as a chromatography detector, where analytes arrive individually. Variations

of the photoemissive ion mobility instrumentation described, modified to reduce internal volume and accept continuous sample flow, could serve capably as gas chromatography detectors for vapors that have positive electron affinity.

#### Reference List

1. U. S. Environmental Protection Agency *Federal Register* **1999**, *64*, 38706-40.
2. Cherry, J. A. ; Pankow, J. E. *Dense chlorinated solvents and other DNAPLs in groundwater*, ed.; Waterloo Press: Portland, OR, 1996.
3. Busman, M.; Sunner, J.; Vogel, C. R. *J. Am. Soc. Mass Spectrom* **1991**, *2*, 1-10.
4. Eiceman, G. A.; Karpas, Z. *Ion Mobility Spectrometry*, ed.; CRC Press: Boca Raton, 1994.
5. Good, A.; Dueden, D. A.; Kebarle, P. *J. Chem. Phys.* **1970**, *52*, 212-21.
6. Vernier, P. J. *Progress in Optics XIV*, North-Holland: 1976.
7. Christophorou, L. G. *Atomic and Molecular Radiation Physics*, ed.; John Wiley & Sons Ltd: New York, 1971.
8. Illenberger, E. *Linking the Gaseous and Condensed Phases of Matter: The Behaviour of Slow Electons*, Christophorou, L. G.; Illenberger, E. Schmidt, W. F., Eds.; Plenum Press: New York, 1994.
9. Grimsrud, E. P. *Mass Spec. Rev.* **1992**, *10*, 457-89.
10. Begley, P.; Corbin, R.; Foulger, B. E.; Simmonds, P. G. *Journal of Chromatography* **1991**, *588*, 239-49.